

REPORT DOCUMENTATION PAGE				Form Approved OMB No. 0704-0188	
Public reporting burden for this collection of information is estimated to average 1 hour per response, including the time for reviewing instructions, searching existing data sources, gathering and maintaining the data needed, and completing and reviewing the collection of information. Send comments regarding this burden estimate or any other aspect of this collection of information, including suggestions for reducing the burden, to Department of Defense, Washington Headquarters Services, Directorate for Information Operations and Reports (0704-0188), 1215 Jefferson Davis Highway, Suite 1204, Arlington, VA 22202-4302. Respondents should be aware that notwithstanding any other provision of law, no person shall be subject to any penalty for failing to comply with a collection of information if it does not display a currently valid OMB control number. PLEASE DO NOT RETURN YOUR FORM TO THE ABOVE ADDRESS.					
1. REPORT DATE (DD-MM-YYYY) 24-06-2008		2. REPORT TYPE Final Report		3. DATES COVERED (From – To) 3 June 2005 - 03-Jan-08	
4. TITLE AND SUBTITLE Combined Attitude Control and Energy Storage For Small Satellites using Variable Speed Control Moment Gyroscopes			5a. CONTRACT NUMBER FA8655-05-1-3037		
			5b. GRANT NUMBER		
			5c. PROGRAM ELEMENT NUMBER		
6. AUTHOR(S) Dr. Vaios Lappas			5d. PROJECT NUMBER		
			5d. TASK NUMBER		
			5e. WORK UNIT NUMBER		
7. PERFORMING ORGANIZATION NAME(S) AND ADDRESS(ES) University of Surrey Guildford GU2 7XH United Kingdom			8. PERFORMING ORGANIZATION REPORT NUMBER N/A		
9. SPONSORING/MONITORING AGENCY NAME(S) AND ADDRESS(ES) EOARD Unit 4515 BOX 14 APO AE 09421			10. SPONSOR/MONITOR'S ACRONYM(S)		
			11. SPONSOR/MONITOR'S REPORT NUMBER(S) Grant 05-3037		
12. DISTRIBUTION/AVAILABILITY STATEMENT Approved for public release; distribution is unlimited.					
13. SUPPLEMENTARY NOTES					
14. ABSTRACT This report results from a contract tasking University of Surrey as follows: The Grantee will investigate three areas concerning energy storage and attitude control systems (ESACS) for small satellites: a.) Use of small satellite reference models to determine the relative scales for a combined variable speed control moment gyroscope (VSCMG) energy storage (ES) system. b.) Explore potential imbalances, derive mathematical descriptions of ESACS-imbalance systems and model the ESACS system in MATLAB/Simulink.. c.) Construct experimental hardware for power conversion demonstration: An experimental VSCMG system will be used to demonstrate combined attitude control and energy storage. The imbalances modeled in (b.) will be replicated in the experimental hardware. Derived control solutions to the imbalance problem will be implemented and validated in the experimental hardware.					
15. SUBJECT TERMS EOARD, Space Orientation, Control System, Energy Conversion, Astronautics					
16. SECURITY CLASSIFICATION OF:			17. LIMITATION OF ABSTRACT UL	18. NUMBER OF PAGES 249	19a. NAME OF RESPONSIBLE PERSON Brad Thompson
a. REPORT UNCLAS	b. ABSTRACT UNCLAS	c. THIS PAGE UNCLAS			19b. TELEPHONE NUMBER (Include area code) +44 (0)1895 616163



**Combined Attitude Control and Energy Storage For Small
Satellites using Variable Speed Control Moment Gyroscopes
Final Report to EOARD**

Principal Investigator
Vaios J. Lappas

Student
David J. Richie

Government Disclaimer

The views expressed in this article are those of the authors and do not reflect the official policy or position of the United States Air Force, Department of Defense, or the U.S. Government.

Acknowledgements

The authors gratefully acknowledge the contribution of Dr. Phil Palmer of the Surrey Space Centre for his supervision as well as project sponsorship from Dr. Barrett Flake of the US Air Force European Office of Advanced Research and Development, Dr. Brian Wilson of the Air Force Research Laboratory, and Dr. Jerry Fausz formerly of the Air Force Research Laboratory and currently employed by the National Aeronautics and Space Administration.

Summary

This work presents the first known energy storage and attitude control subsystem (ESACS) for small satellites, proving this technology to be viable, applicable to more complex, demanding space missions, and laden with substantial benefits, such as agile slewing, robust singularity avoidance, increased lifetime, mass savings, and favourable peak power density. In capturing the key features of this novel system, it investigates the design sizing, feasibility, mission utility, experimentation, and performance benefits for using variable-speed control moment gyroscopes (VSCMGs) to store and drain energy while controlling satellite orientation.

First, a novel optimal ESACS sizing algorithm is developed for a practical, miniature spotlight synthetic aperture RADAR (SAR) space mission. When given a set of small satellite agility and energy storage requirements, the design is cast as a constrained nonlinear programming problem using a performance index constructed from subsystem design margins including the attitude torque, peak power, energy capacity, and subsystem mass margins and solved using a reduced-order, gradient-based solver software code. The resulting method permits an efficient, structured approach to designing an optimally sized ESACS while enabling comparison of new technology performance to an existing system in order to identify the advantages and disadvantages of such new technology. The process shown generates point designs which are then compared via a design scoring process. Then, realistic usable energy capacity is studied, yielding a more practical system capable of meeting the desired requirements albeit with reduced mass savings benefits from theoretical levels. This factor, although presented in the early 1970s, is often overlooked in the literature.

Next, a novel ESACS gimbal steering law is derived to permit independent gimbal and wheel control of VSCMGs with continued singularity avoidance, a situation that allows direct incorporation of an ESACS into an existing small satellite energy storage (ES) subsystem. This law rejects the disturbances generated during independent ES wheel control which can be significant if the power is stored and drained rapidly, demanding high wheel deceleration/acceleration. Meanwhile, the separation of control renders simultaneous control law singularity avoidance through coordinated wheel torquing and gimbaling impossible, thus a conventional CMG gimbal singularity avoidance steering algorithm was also added to this new law. As it permits directly interfacing this small satellite ESACS into a conventional satellite, this novel, composite gimbal steering law is more immediately practical than pre-existing simultaneous steering laws.

Finally, a low-cost prototype using current off-the-shelf technology was effectively employed in the first known hardware-in-the-loop, three-axis, experimental demonstration of an ESACS. This is also the first known demonstration of VSCMGs for a small spacecraft scale ESACS. Key test results taken at moderate, less efficient wheel speeds show that a small ESACS can yield the depth-of-discharge and round-trip energy efficiencies near anticipated theoretical values while imparting attitude change, but have limitations in energy density due to the use of COTS motors. It is also shown that a resistive load can be powered from the flywheel system for a set time period (depending upon the resistive load), but drains energy much faster than a magnetically-levitated system would due to motor bearing friction. Nevertheless, these developments open the door for further practical advancement of these concepts and future employment on a small satellite.

Contents

Contents	vii
List of Figures	x
Nomenclature	xiii
1 Introduction	1
1.1 Motivation	1
1.2 Thesis Goal	2
1.3 Scope	3
1.4 Structure Of Thesis	4
1.5 Novel Work Undertaken	6
Acronym List	1
2 State-of-the Art Review	7
2.1 History and Description of Key ESACS Technology	8
2.1.1 Flywheel Energy Storage	8
2.1.2 CMGs/VSCMGs	14
2.1.3 Magnetic Levitation and Bearing Technology	15
2.1.4 Motor/Generator Design for High Speed Flywheels	18
2.1.5 Flywheel Rotor Structure	18
2.1.6 Flywheel Containment	19
2.1.7 VSCMGs for Energy Storage	20
2.1.8 Small Satellites	21
2.1.9 Design Optimization/Linear Programming	21
2.2 Contemporary Research	22
2.2.1 NASA	22
2.2.2 AFRL	24
2.2.3 SSC/SSTL Research	26

3	Mission Scenarios	28
3.1	Overview of Candidate Missions	28
3.2	Mission Design Requirements	30
3.3	Synthetic Aperture Radar Requirements	40
3.4	Power and Attitude Profiles	43
3.5	Mission Scenarios Requirements Summary	45
4	Attitude Control and Energy Storage Fundamentals	46
4.1	Attitude Control Subsystem	46
4.1.1	Disturbance Torques in Low Earth Orbit	48
4.1.1.1	Gravity Gradient	48
4.1.1.2	Earth's Magnetic Field	49
4.1.1.3	Solar Radiation Pressure	49
4.1.1.4	Aerodynamic Drag	50
4.1.1.5	Designing the Largest Spacecraft Facet	50
4.1.1.6	Numerical Example	51
4.1.2	Sizing Conventional Attitude Control Systems	53
4.1.3	Attitude Tracking Using VSCMGs	56
4.1.3.1	Singularity Problem	57
4.2	Power Subsystem	57
4.3	Flywheel Energy Storage	61
4.4	Summary of Fundamentals	62
5	Small Satellite ESACS Sizing/Optimization	63
5.1	Optimization Problem	63
5.1.1	Process Inputs	63
5.1.2	Optimal Sizing Theory	64
5.1.3	Optimization Logic	66
5.2	Trade Studies	69
5.2.1	Assumptions	69
5.2.2	Technology Trades	71
5.2.3	Sizing Results	71
5.2.4	Benefits & Scored Designs	78
5.3	Maximum Structural versus Usable Capacity Effects on Rotor Design	86
5.4	Numerical Example and Results	87
5.5	Gimbal Motor Sizing	91
5.6	Summary	93

6	Steering Laws	96
6.1	Literary Background	97
6.2	Vehicle Controllers	99
6.2.1	Lyapunov	99
6.2.2	Variable-Limiter PID	99
6.3	Simultaneous Steering	100
6.4	One-way Coupled Steering	101
6.4.1	Simultaneous Steering Law Example	106
6.4.2	One-way Coupled Steering Law Example	106
6.4.3	Simultaneous Steering Example	114
6.4.4	One-Way Coupled Steering Example	117
6.5	Summary	120
7	ESACS Hardware Design	121
7.1	Requirements Summary	121
7.2	Wheel Motor/Generator Design	124
7.3	Gimbal Motor Design	127
7.4	Mechanical Design	128
7.5	Electrical Design	130
7.6	Cluster Design	133
7.7	Proposed Design Changes for a Possible Flight Design	135
7.8	Summary	137
8	Practical Experimentation	138
8.1	Test Goals and Requirements	138
8.2	Integrated Testing	142
8.3	Experimental Results	144
8.4	Discussion of Results	145
8.5	Integrated Testing Summary/Proof of System Novelty	154
9	Conclusion	156
9.1	Summary of Results	156
9.2	Contribution to the Current State-of-the-Art	159
9.3	Summary of Publications	160
9.4	Proposed Future Work	161
9.5	Proof of Novelty	163

A	Impact of the Space Environment	182
A.1	Outgassing of Materials	182
A.2	Need for Bearing Lubrication	185
A.3	SEE and EMI/EMC	186
A.4	Thermal Impact on Motor Performance	187
A.5	Initial Start-up/Back-up Batteries and Bearings	188
A.6	Other Subsystem Assumptions	188
B	Motor Modelling	191
B.1	Power Balance	192
B.2	Calculating the ESACS Benefits Related to Motor Data	195
B.3	Comparison to Laboratory Data	196
B.4	BLDC Motor Thermal Heating in Space Vacuum	196
C	Testing Supplement	200
C.1	Test Article Design	200
C.2	Rotor Balancing	202
C.2.1	Need for Balancing	202
C.2.2	Defining the Key Balance Requirements	203
C.2.3	Balance Test Results	205
C.3	Sensor Calibration	207
C.4	Additional Test Results	209
C.4.1	Test Matrix	209
C.4.2	Test Run Procedure	211
C.4.3	Data Marking	211
C.4.4	Preliminary Attitude Performance Data	212
D	Attitude and Power Equations	217
D.1	Kinematics	217
D.2	Attitude Dynamics	218
D.2.1	Simplifying the Torque Equation	222
D.3	Proving Attitude Tracking Stability	224
D.4	Projected Power in Null Space of Q	225
D.5	Proving Power Tracking	226
E	Rotor Stress Analysis	227

List of Figures

1.1	Principles of Operation for an ESACS using VSCMGs	2
2.1	Conceptual Flywheel Spacecraft Battery, 1961 [1]	8
2.2	Advanced Technology Flywheel Concept, 1974 [2]	10
2.3	Conceptual Flywheel Design for Spacecraft Power System, 1983 [3]	12
2.4	IPACS Unit Design Concept, 1985 [4]	13
2.5	Magnetic Bearing and Candidate Flywheel Material Details	16
2.6	ESA/Teldix Magnetically Supported Momentum Wheel, 1995 [5]	17
2.7	Flywheel Battery for Space Station Experiment [6]	23
2.8	AF Research Laboratory's Agile Multi-Purpose Spacecraft Simulator (AMPSS) and Energy Storage CMGs [7]	25
2.9	SSC CMG Design	27
3.1	Top View - Spotlight SAR Collection Geometry	31
3.2	Side View - Spotlight SAR Roll Angle Coverage Area	32
3.3	Spotlight SAR Attitude Maneuver Calculation Process	32
3.4	Side View - Spotlight SAR Collection Geometry with Ground Swath	34
3.5	Spotlight SAR Parabolic Reflector Diameter Sizing	35
3.6	Spotlight SAR Power Calculations	37
3.7	Conceptual Design of a Small Spotlight SAR Satellite	38
3.8	Spotlight SAR Mechanical Dimensions	39
3.9	Spotlight SAR System Mass and Inertia Calculations	39
3.10	Bang-off-Bang Attitude Reference Maneuver and Power Profile	43
4.1	Block Diagram for Conventional Attitude Control Subsystem	47
4.2	Conventional Attitude Control Subsystem Sizing Process	54
4.3	Pyramid Cluster CMG and VSCMG Momentum Envelopes	58
4.4	Electrical Power Architectures	59

4.5	Conventional Energy Storage Subsystem Sizing Process	60
5.1	Bang-off-Bang Attitude Reference Maneuver and Power Profile	64
5.2	T1000G Carbon Fiber Radial and Tangential Stress Distributions	69
5.3	Basic Optimal Sizing Process	70
5.4	Key Variable-Speed CMG Technologies	72
5.5	Optimal Performance/Optimal Mass Results for Selected Rotor materials . .	73
5.6	Rotor Length versus Performance Indices J_a , J_b , and J_c for Three Alternatives at Optimal Performance and Optimal Mass	75
5.7	Rotor Length Versus Optimal Mass Savings	76
5.8	Maximum and Minimum Wheel Speed Comparisons with Other Decision Vari- ables for Three Alternatives at Optimal Performance (two plots at left) and Optimal Mass (three plots at right)	77
5.9	Maximum Gimbal Rate versus Rotor Length Comparisons by Maximum Wheel Acceleration for Alternatives #1 and #3 at Optimal Mass Savings	78
5.10	Selected Decision Variables Versus Energy and Power Density at Optimal Mass and Optimal Performance for All Three Alternatives	79
5.11	Spacecraft Mass Breakdown Before and After Combining Subsystems	80
5.12	Pyramid Cluster CMG and Superimposed VSCMG Momentum Envelopes . .	81
5.13	Depth-of-Discharge Versus Lifetime	82
5.14	Adjusted Technology Ragone Plot, Energy Density Versus Power Density . .	83
5.15	VSCMG-based ESACS Figures	90
5.16	Capacity Impact on Mass Savings	91
5.17	Gimbal Motor Sizing Process	93
6.1	Attitude Control Block ed Diagram with CMG Steering Architecture Inset .	97
6.2	Example 1 Angular Position	106
6.3	Example 1 Angular Position, Zoomed	107
6.4	Example 1 Angular Velocity	107
6.5	Example 1 Angular Velocity, Zoomed	108
6.6	Example 1 Singularity Index	108
6.7	Example 1 Power Plot	109
6.8	Example 1 Wheel Speed	109
6.9	Example 1 Wheel Speed, Zoomed	110
6.10	Example 1 Gimbal Angle	110
6.11	Example 2 Angular Position	111

6.12	Example 2 Angular Position, Zoomed In	111
6.13	Example 2 Angular Velocity	112
6.14	Example 2 Singularity Condition	112
6.15	Example 2 Power	113
6.16	Example 2 Wheel Speed	113
6.17	Example 2 Wheel Speed (Zoomed)	114
6.18	Example 2 Gimbal Angle	115
6.19	Example 2 Gimbal Angle (Zoomed)	115
6.20	Quaternion Error Max Magnitude	119
6.21	Power Tracking Error Magnitude	120
7.1	Candidate Motors for the Rev A Design	125
7.2	Rev A Gimbal Motor, Gearing, and Encoder	127
7.3	VSCMG Assembly Design	129
7.4	Wheel Assembly and Components	129
7.5	Rev A Design	131
7.6	Wheel and Gimbal DECV 50/5 Servo-Amplifier	132
7.7	SSC FES Board	134
7.8	VSCMG Cluster Images	135
8.1	Air Bearing Test Article	143
8.2	Wheel Speed Performance	145
8.3	Net Power History	146
8.4	Attitude Data Histories	147
8.5	Mechanical/Magnetic Bearing Discharge Comparison	152
8.6	Mechanical-/Magnetic Bearing Cycles	153
B.1	Net Load Power Data versus Model	197
B.2	Net Fit Data	197
C.1	Preliminary Rotor Balancing Concepts and Requirements	206
C.2	Rotor Balancing and Other Developmental Testing	215
C.3	Power and Attitude Calibration Curves	216
D.1	Variable Speed Control Moment Gyro	218
E.1	Wheel Rotor Representation	227
E.2	Rotor Differential Mass Free Body Diagram	228
E.3	Differential Mass Strain Diagram	230

Nomenclature

C	= storage capacity, $W \cdot hr$
dod	= depth of discharge, %
d_{ty}	= eclipse duty cycle, %
E	= elastic modulus
E_d	= energy density, $W \cdot hr/kg$
f_i	= equivalent performance constants
\hat{g}	= spin, transverse, gimbal axis unit vectors
h	= circular orbit altitude, km
I_T	= spacecraft principal-axis inertia, $kg \cdot m^2$
I_w	= control moment gyro wheel inertia, $kg \cdot m^2$
J_i	= candidate performance index a, b, or c
k_s	= rotor shape factor
l_{rot}	= rotor length, m
M	= attitude control + energy storage mass, kg
m_A	= component A mass based on parameters B,C
MS	= mass savings, %
N	= attitude torque, $N \cdot m$
N_{vc}	= number of cluster actuators
P	= instantaneous peak power, W
P_d	= power density, W/kg
T_e	= on-orbit eclipse duration, s
T_i	= design point score function a, b, or c
t_f	= slew maneuver time, s
t_{off}	= slew dead-band, s
t_{sp}	= wheel spoke thickness, m
t_{life}	= spacecraft lifetime, eclipse cycles
V_{bus}	= spacecraft power bus voltage, V
r	= generic radius, m
r_i	= rotor outer radius, m
r_o	= rotor inner radius, m
w	= scoring function weights
x_{msn}	= transmission efficiency, %
α_i	= rotor stress integration constants
β	= control moment gyro pyramid angle, rad
χ	= control moment gyro torque efficiency, %
δ	= gimbal angle, rad
$\dot{\delta}$	= maximum gimbal rate, rad/s
γ	= design margin weights
λ	= $(E_\theta/E_r)^{0.5}$

ν_{yx}	= rotor material poisson's ratio of contraction
	= in x-direction Due to Tension in y-direction
Ω	= wheel speed, rad/s or revolutions/minute
$\dot{\Omega}$	= maximum wheel acceleration, rad/s^2
ρ	= density, kg/m^3
σ	= rotor stress, N/m^2
θ_f	= slew maneuver angle, rad

Subscript

a	= actual
b	= baseline (comparison) system
dc	= Mark II Direct Current(DC) motor
g	= control moment gyro gimbal axis
i	= i_{th} actuator
m	= margin
m_j	= j_{th} wheel motor
max	= maximum
mb	= magnetic bearing
$mkii$	= Mark II Control Moment Gyroscope(CMG)
min	= minimum
oth	= miscellaneous actuator components
r	= required
R	= rotor radial direction
$real$	= realistic
rot	= wheel rotor
s	= control moment gyro spin axis
sc	= spacecraft (satellite)
sp	= spoke
$struct$	= structure
t	= control moment gyro transverse axis
ta	= total allowable
wh	= wheel (rotor + shaft + motor)
θ	= rotor tangential direction

Acronym List

AC	=	Alternating Current
ACS	=	Attitude Control Subsystem
AFRL	=	(United States) Air Force Research Laboratory
AMSAT	=	Amateur Satellite
BCR	=	Battery Charge Regulator
BLDC	=	Brushless DC PM Motor/Generator
CEACS	=	Combined Energy Storage and Attitude Control System
CMG	=	Control Moment Gyroscope
COTS	=	Commercial-off-the-Shelf
DC	=	Direct Current
DOD	=	Depth-of-Discharge
DoD	=	Department of Defense
DET	=	Direct Energy Transfer
DCM	=	Direction Cosine Matrix
DMC	=	Disaster Monitoring Constellation
DOF	=	Degree-of-Freedom
ECI	=	Earth Centred Inertial Coordinate Reference Frame
EOARD	=	European Office of Advanced Research and Development
EPS	=	Electrical Power Subsystem
ES	=	Energy Storage
ESACS	=	Energy Storage and Attitude Control System
ESCMG	=	Energy Storage Control Moment Gyroscope
FACETS	=	Flywheel Attitude Control, Energy Transmission and Storage
FES	=	Flywheel Energy Storage
F.S.	=	Factor-of-Safety
GRC	=	Glenn Research Center
GRG2	=	Generalised, Reduced-order Gradient Method #2
HTS	=	High-temperature Superconductor
IFC	=	In-flight Computer
IPACS	=	Integrated Power and Attitude Control System
ISS	=	International Space Station
LEO	=	Low Earth Orbit
MEMS	=	Micro Electro Mechanical Systems
MIT	=	Massachusetts Institute of Technology
MS	=	Mass Savings
MW	=	Momentum Wheel
NASA	=	(United States) National Aeronautics and Space Administration
NiCd	=	Nickel Cadmium
NLP	=	Nonlinear Programming Problem

OCPACS	=	One-way Coupled Power and Attitude Control System
OBC	=	On-board Computer
OCR	=	Open Core Rotator
PCB	=	Printed Circuit Board
PCM	=	Power Control Module
PM	=	Permanent Magnet
PPT	=	Peak Power Tracker
PSU	=	Pennsylvania State University
RADAR	=	Radio Detection and Ranging
RPM	=	Revolutions Per Minute
RW	=	Reaction Wheel
SAR	=	Synthetic Aperture RADAR
SSC	=	Surrey Space Centre
SSTL	=	Surrey Satellite Technology, Ltd.
SolarSim	=	Solar Simulator
SUV	=	Sport Utility Vehicle
SVD	=	Singular Value Decomposition
USAF	=	United States Air Force
US	=	United States
VSCMG	=	Variable-speed Control Moment Gyroscope

Chapter 1

Introduction

1.1 Motivation

Today's small satellites (less than 500 kg in mass) are increasingly considered for large satellite missions such as precision Earth imaging and Space RADAR [8–10]. Difficult hurdles face these small satellites' designers such as meeting stringent mass, power, and volume constraints which significantly impact cost. In order to mitigate costs, the Surrey Space Centre (SSC) in conjunction with Surrey Satellite Technology, Ltd. (SSTL) regularly uses commercial-off-the-shelf (COTS) components in satellite design [8–11]. Assuming that deleting mass eventually enables a change in launch vehicle class and thus, on average, reduces cost, an obvious method to reduce mass but maintain performance is to combine key satellite functions. For example, a satellite's Energy Storage (ES) function, usually achieved via rechargeable batteries, can be combined with its pointing system (i.e. the Attitude Control Subsystem (ACS)), forming an Energy Storage and Attitude Control System (ESACS) [12]. Such an ESACS consists of flywheel-based, three-axis stabilising, momentum exchange actuators such as Reaction Wheels (RWs), Momentum Wheels (MWs), Control Moment Gyroscopes (CMGs), or Variable-Speed CMGs (VSCMGs) doubling as energy storage devices. RWs provide zero-biased momentum through low spin rates thus are unrealistic for energy storage. In contrast, MWs have a momentum bias through non-zero nominal spin rate and thus the ability to store and drain flywheel energy, while CMGs operate at fixed flywheel speeds without freedom to store and drain energy. However, the CMG torque amplification property in which a small amount of CMG gimbal motor input torque results in a relatively large slewing torque gives it a distinct advantage over a MW-based system [13]. Fortuitously, VSCMGs combine these

CMG and MW advantages while eliminating well-known CMG gimbal-lock singularities by using the MW mode near singularity and therefore are the most logical ESACS alternative. Although, the ESACS concept for a space system has been investigated quite often in the literature, prior to the current work, a version for small satellites has never been built. Such an ESACS would bring substantial benefits to a small satellite system, such as significant mass savings, agile slewing, and increased power density, enabling the complex missions recently reserved for large satellites mentioned earlier, such as precision Earth imaging and Space RADAR.

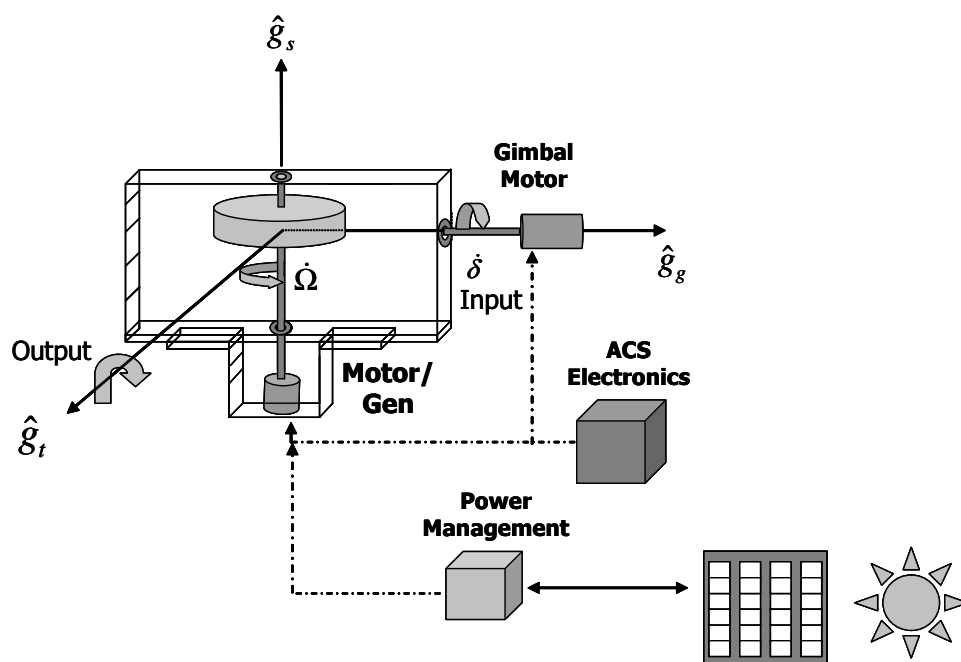


Figure 1.1: Principles of Operation for an ESACS using VSCMGs

1.2 Thesis Goal

In order to design, build, and test the first ever small satellite ESACS, this thesis proposes a new ESACS design based on optimal sizing of the system subject to practical constraints through employing cost COTS components. Specifically, the work aims to:

- Prove ESACS for small satellites
- Optimally size ESACS for a realistic, small Synthetic Aperture RADAR mission

- Design a practical ESACS system using COTS/low cost components
- Develop a novel, practical actuator steering law that decouples attitude and power tracking functions for immediate use on conventional satellites
- Prove flywheel energy can be stored/drained in small satellite ESACS context
- Test and analyze small satellite ESACS benefits

1.3 Scope

The research conducted centers on a few ground rules and assumptions. These are:

- Applicable/candidate ESACS missions require precision, agile slewing and high power density.
- Developed sizing algorithms provide a framework for selecting design points and comparing these designs to existing system for mass, power, and volume benefits given partially restricted dimensions (e.g. wheel rotor inner and outer radii, but not rotor length).
- A steering law is required that is practical, robust, and is based on conventional 4-CMG pyramid cluster logic. Experience/heritage shows that such conventional logic permits low risk software implementation. Note that associated singularities for such a law are important and heightened in the case of combined power and attitude tracking, but detailed investigation into the singularity space in employing this concept is outside the scope of the work.
- Instituting magnetic bearings to levitate the VSCMG flywheels in a small satellite concept is not yet feasible, especially in the context of a commercial-off-the-shelf miniature package. Although magnetic bearings are new to the flywheel industry, these magnetic bearings are primarily sized for much larger applications than envisioned here. Intuitively, one may think larger magnetic bearings are harder to produce, but issues in reducing the size involve electro-magnetic interference, heat, and power restrictions which make the miniaturization of magnetic bearings an advancement requiring further research prior to implementation. It is additionally noted that such bearings, although

virtually frictionless, still have losses such as eddy currents which contemporary literature has shown can limit amount of power producible during eclipse with such bearings. Nevertheless, comparison of design points implementing such bearings will be included in sizing algorithms to illustrate advantages possible once miniature magnetic bearings are commercially viable. In other words, the scope of the work involves employing mechanically levitated wheels in a such a manner to learn about ESACS and permit logical extensions to a system using miniature, magnetic bearings.

- Initial Demonstration of the VSCMG-based ESACS prototype will focus primarily on demonstrating the feasibility of storage and drain of power while imparting attitude change using a single, mechanically-levitated prototype with a conventional motor/generator but leave further advancement of the attitude control to be experimentally tested in follow-on work. For this reason, the experimental aim of the research is to show that this technology is possible and produces benefits that can be further refined for future implementation on a small satellite.

Therefore, the investigation will stay within the boundaries set forth here. Future research stemming from this first ever effort will build on the lessons learned through this study.

1.4 Structure Of Thesis

The thesis begins by identifying the motivation for a small satellite VSCMG-based ESACS in Chapter 1. Also in this chapter, the underlying goal of the thesis work is addressed along with the scope and novelty of the work presented in the thesis.

Next, Chapter 2 outlines the relevant literature pertaining to the ESACS and small satellite VSCMG topics. Most importantly, it highlights the void in the current state-of-the-art in these areas prior to inception of this research project. Therefore, this chapter pinpoints the significance of the novel advancements tackled in this work.

Third, Chapter 3 defines representative mission requirements for a mission relying on high peak power with simultaneous slewing agility envisioned for small satellites in the near future. Achieving these requirements will showcase the VSCMG-based ESACS technology and enable missions previously thought unrealistic.

Then, Chapter 4 outlines the fundamental mathematical and physical concepts behind attitude disturbance torques and attitude control for precision slewing. It also mentions the

necessity of steering momentum-exchange device actuators to achieve the desired full satellite commands which permit stable tracking of the desired attitude and attitude disturbance rejection. Also, this chapter presents standard electrical power topologies used on satellites based on conventional solar arrays as the primary source and rechargeable batteries as the secondary source. Then, it defines the basic energy concepts involved in flywheel batteries for power storage and drain.

Fifth, a novel optimal sizing algorithm is developed in Chapter 5 based on the applicable design margins of this system including the attitude torque, peak power, energy capacity, and subsystem mass margins. The algorithm uses a performance index crafted from these margins which also employs the margins of a baseline comparison system. This allows comparison of new technology performance to an existing system in order to identify the advantages and disadvantages of such new technology. The process shown in this chapter generates point designs which are then compared via a design scoring process. An additional topic covered in this chapter is that of realistic usable energy capacity and how using it yields a more practical system capable of meeting the desired requirements albeit with reduced mass savings benefits from theoretical levels. This factor, although presented in the early 1970s, is often overlooked in the related literature on flywheel batteries for energy storage.

Next, Chapter 6 develops and simulates a VSCMG actuator steering law that fulfills an immediately practical need. That is, employing a VSCMG based on commercial technology is more effective for use now when using its flywheel within an electrical power subsystem direct energy transfer or peak power tracking electronics loop while using the gimbal steering law crafted to reject disturbances caused by accelerating the wheel automatically in the aforementioned electronics loop. Plus, the gimbal steering law is also required to meet the desired slewing requirements of the spacecraft in addition to rejecting wheel disturbances. From this, this steering law is applied in the context of realistic attitude and power tracking algorithms based on a common set of parameters defined in previous work. Not only is this new algorithm applied, but it is contrasted in this chapter with a well-known simultaneous algorithm created in previous work by the author.

Then, Chapters 7 and 8 outline the first small satellite VSCMG prototype for an ESACS and capture the key test results from the hardware-in-the-loop, three-axis demonstration of this novel prototype on spherical air bearing platform. These tests show that even a less efficient, moderate speed below 10000 RPM, the small VSCMG ESACS can yield the depth-of-discharge and round-trip energy efficiencies near the predicted values while imparting attitude

change, but have limitations in energy density due to the limited wheel speeds. It is also shown that a resistive load can be powered from the flywheel system for a set time period (depending upon the resistive load), but runs down much faster than a magnetically-levitated system would due to motor bearing friction. These developments open the door for further practical advancement of these concepts and future employment in a small satellite context. Finally, Chapter 9 summarizes the key results from the thesis. Also, a summary of the novel contributions made advancing the current state-of-the-art is given. Finally, proposed future work is identified.

1.5 Novel Work Undertaken

As implied so far in this chapter, novel advancements to the current state-of-the-art will be made in the following areas:

- Sizing VSCMG components for a small satellite ESACS as published in the July/August 2007 edition of the American Institute of Aeronautics and Astronautics Journal of Spacecraft and Rockets [14]. The investigation of the current state of the art through the open literature reveals that this was not yet done prior to the current study.
- Developing a practical, immediately useful steering law for independent control of the gimbal and wheel motors for ESACS. Employing the flywheel battery consisting of VSCMG wheel motor/generators directly in an existing EPS architecture (i.e. in a passive electrical circuit) requires that the EPS be given exclusive command of the wheel motor/generator. This can affect the attitude and levies a requirement on the gimbal motor to be used solely for attitude control based on feedback of the attitude sensors and the wheel/motor generator states.
- Hardware-in-the-loop design, demonstration, and testing (performance evaluation) of the ESACS concepts (i.e. both energy storage/drain while changing the spacecraft's attitude) using a small satellite VSCMG cluster. The closest developments of this work either use counter-rotating momentum wheels (as demonstrated at NASA's Glenn Research center in 2004) or involve large satellite, custom-made magnetically-levitated wheels (as partially done in a program at the USAF Research Laboratory prior to its cancellation in early 2007).

Chapter 2

State-of-the Art Review

Since the United States' energy crisis in the early 1970's, using flywheels for satellite energy storage has been a well-studied problem along with combining such devices with a satellite's attitude control function. In fact, there is a rich design history of satellite flywheel energy storage actuators dating to the early 1960s. Sadly, due to technological limits in flywheel rotor materials, magnetic bearings, and motor/generator electronics, few flywheel energy storage systems have flown. Nevertheless, a couple magnetically suspended flywheels for attitude control have space flight heritage including those flown aboard the French SPOT satellite (1986) and the AMSAT Phase 3-D satellite (2000) [15,16]. Although the flown designs used magnetically suspended momentum wheels for attitude control, apparently none of these have been used as the key energy storage system for spacecraft power. Furthermore, very few past flywheel energy storage systems (and none of the magnetically-suspended flywheel systems) have used Control Moment Gyroscopes, although some have had minimal gyroscopic input ($< 20^\circ$) for gimbal actuation. Even flying CMGs onboard small satellites had not happened until recently [17]. Since then, there have been efforts to miniaturise both MWs and CMGs (e.g. [18]) using MEMS technology, but such designs require an expensive cryogenic cooling system to keep the system's magnetic materials within operating limits. This is not desirable for a COTS-based system. Therefore, a logical next step in the evolution of both CMG and FES technology, as enforced by the applicable literature and by contemporary achievement is to use a VSCMG-based ESACS comprised of COTS components on small satellites in the near future.

2.1 History and Description of Key ESACS Technology

The literary background along with descriptions of key technology for ESACS is best subdivided into Flywheel Energy Storage, CMGs and VSCMGs, magnetic levitation and bearing technology, flywheel rotor structural advances, rotor containment, VSCMGs for Energy Storage, Momentum Exchange Devices for Small Satellites, and design optimization/linear programming techniques. Much of the combined flywheel energy storage and attitude control history through the year 2000 is well-documented in a 45-page report by Hall [19] while past, present, and future technology developments and ideas is well addressed in the combined works given in Refs. [20,21]. The reader is referred to these works for more detail. Nevertheless, what follows is a representative sampling of this well-studied technology.

2.1.1 Flywheel Energy Storage

Roes first proposed satellite flywheel energy storage in 1961 [1] per the concept illustrated in Figure 2.1. Interestingly, his work details the energy storage process for a magnetically suspended, counter-rotating pair of flywheels, including launch stowage, initial wheel spin-up, and adverse “wheel configuration torque” avoidance. It even states that the electronic control circuitry drives this approach’s reliability [1]. The performance for this wheel was anticipated to have 17 W-hr/kg with an operating speed range of 9500 to 19000 RPM. With a 24 in diameter rotor, tip-speeds of 306 m/s to 612 m/s could be achieved [21]. Disappointingly, Roes’ article does not include using these wheels for attitude control.

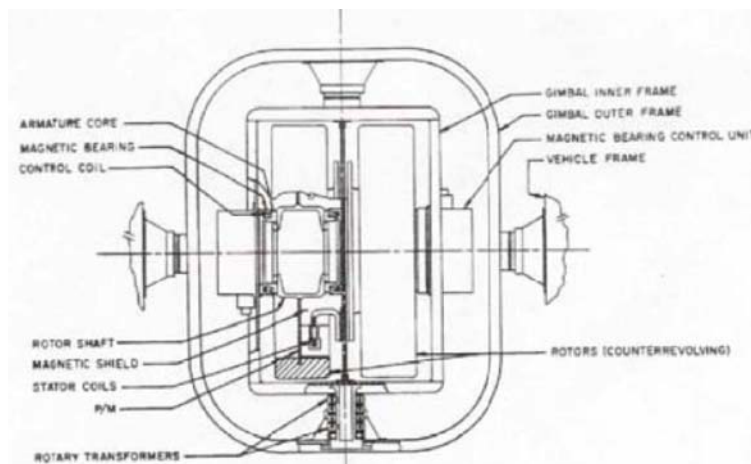


Figure 2.1: Conceptual Flywheel Spacecraft Battery, 1961 [1]

The idea became more prevalent as a sufficient alternative to fuel cells and secondary batteries during the aforementioned 1970s' energy crisis in which its popularity pervaded several industries, including automobiles, primary electrical power networks, and even combat aircraft [19,22,23]. However, spacecraft applications of flywheel energy storage did not catch on until Rabenhorst's work at Johns Hopkins University/Applied Physics Laboratory from 1969 through the 1970s [24]. Like Roes, Rabenhorst's early work mentioned flywheels for energy storage, but not for spacecraft attitude/momentum control. The attitude control idea did not catch on until the early 1970s when NASA engineers proposed coupling flywheel energy storage technology with this function (see for instance [25–27]).

Satellite ESACS interest grew during the period 1972-1979, with foundational works by Notti, Cormack, Klein, Kirk, Studer, Rodrigues, Will, Keckler, and Anderson [2, 26–34]. In fact, Anderson and Keckler were the first to use the term IPACS, referring to an Integrated Power and Attitude Control System, in 1973. Note that the IPACS concept is a subset of ESACS (which is also known by some authors as CEACS) and connotes a system where the attitude control actuation is controlled simultaneously with the power instead of treating the flywheel power actuation as a disturbance torque resolved by the ACS.

As mentioned in [20,21], the NASA-sponsored IPACS concepts studies in aforementioned work by Notti and Cormack (ref. [2]) “considered IPACS for seven possible NASA spacecraft/missions and proposed conceptual designs for two of them. Two technology levels were considered: conventional technology that was based on ball bearings and steel rotors and advanced technology that required development of composite rotors and magnetic bearings for the high spin speed regime” (See Figure 2.2). At the time, a conventional approach was preferred for a couple missions, but the advanced approach would push future flywheel technology.

Also during this time, there were two energy conferences and more than 550 works dedicated toward this technology [19], including a two-part series by Kirk and then Kirk and Studer, which summarises the state-of-the-art in 1976 and explains the value of a hollow-disk, composite wheel resting on magnetic bearings [28,34]. The consensus design amongst these researchers called for a magnetically levitated composite rotor flywheel spinning at 50-100K RPM, whilst a ball-bearing-levitated, steel/metal wheel design spinning at 25-50K RPM was already achievable. Interestingly, the effort by Adams in 1972 mentions using CMGs for Angular Momentum and/or Energy Storage [25] and the work by Notti in 1975 [26] investigates this concept further, detailing a CMG-related actuator known as a “Control Energy Momentum

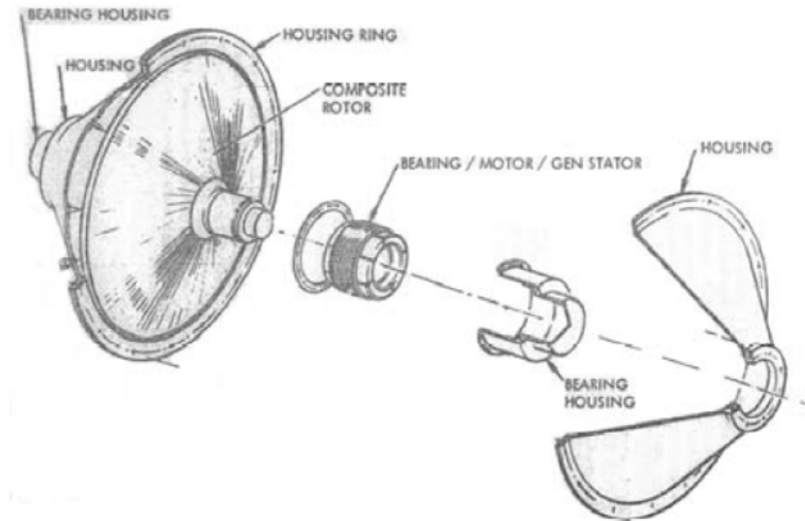


Figure 2.2: Advanced Technology Flywheel Concept, 1974 [2]

Gyroscope (CEMG),” either single- or double-gimballed, to meet the integrated functions. However, neither of these works address the governing nonlinear equations of motion nor the variable-speed, singularity avoidance control laws for such wheels, an advancement not made until Richie’s work, two and a half decades later [12].

As further mentioned in [20, 21],

two concurrent NASA Langley Research Center studies [33, 35, 36] presented experimental and simulation results of IPACS concepts for potential NASA missions. The objective of the experiments in Ref. [33] was to investigate the attitude control/power generation interactions. A double-rotor double-gimbal IPACS configuration was assumed. The experiments employed an IPACS scaled model with control moment gyro (CMG) units having a maximum momentum capacity of 1.78 N-m-sec. The report indicates that the experiment was essentially a table-top hardware-in-the-loop simulation with a spacecraft flying in a computer. In the other effort, [35, 36], a full scale IPACS unit was built and tested. The unit had a titanium constant stress rotor, a unit level energy density of 19 W-hr/kg, and an operating speed range of 17,500 to 35,000 RPM on ball bearings. The rotor diameter was 45.4 cm, and maximum rotor tip speed was 832 m/s at 35,000 RPM. These reports capture the IPACS state-of-the-art, state-of-the-experience, in the mid 1970s. References [33, 35, 36] are notable because they describe the first IPACS ground experiments. Until recently, these experiments were the most

comprehensive, integrated laboratory tests performed.

As previously mentioned, early flywheels were required to spin at very high speeds, yet faced two large barriers to implementation – rotor material strength and the flywheel suspension [27]. Spinning flywheels at high RPM (over 20K) would cause most 1970s-vintage materials to rupture. Strong materials, like metals, weighed too much for realistic spacecraft use. Also, spinning flywheels at this level quickly wore out conventional mechanical bearings. Thus, bearing inability to withstand high speeds over adequate lifetime limited this technology’s utility. The satellite community, then, put progress on-hold until sufficient composite materials and magnetic bearings could be realised [28,34].

After the 1970s surge, this concept waned until rejuvenated by MIT’s Draper Labs, Rockwell International, the University of Maryland, and NASA in the mid-1980s. Works by Eisenhaure, Downer, Oglevie, and others [3,4,37–49] characterised this period. The consensus design shifted toward a counter-rotating, magnetically-levitated momentum wheel-based system known as the CARES (Combined Attitude, Reference, and Energy Storage) system anticipated for ISS application. As mentioned in [21],

reference [3] identified and prioritized critical technologies as: (1) composite wheel development; (2) magnetic suspension; (3) motor/generator; (4) containment; (5) momentum control. A significant section on power system aspects is presented, including a comparison of energy storage efficiencies of flywheels with electrochemical systems for a LEO mission.

Figure 2.3 shows a conceptual flywheel design [3] from this work. As a short-term follow-on to this work, according to [21],

NASA reevaluated IPACS utility for space stations in Reference [4] since space station concepts evolved and technology panels recommended flywheel energy storage technology. This study concluded that an IPACS system has significant advantages over separate energy storage wheels and CMGs; however the study did not include electrochemical batteries in the trade. An array of five double gimbaled flywheel units (as shown in Figure 2.4) was preferred. The suggested design is notable because recent IPACS configurations have preferred single-gimbal units. Four composite material systems were identified for the rotor: (1) boron/epoxy; (2) graphite/epoxy; (3) boron/aluminum; (4) silicon car-

bide/aluminum. A large-angle magnetic bearing was proposed. The report also contains an excellent literature survey covering developments from the early 1970s. According to Reference [4], a 1983 US Air Force sponsored study [50] concluded that flywheel energy storage for spacecraft was not advantageous. Since none of the studies discussed involved actual hardware or missions, their conclusions depend on initial assumptions including wheel geometry, material strength, various efficiencies, and mission characteristics. In spite of all the promising study results, most government funding for flywheel energy storage systems was withdrawn in the mid 1980s, but work continued on a smaller, research-level scale. NASA's research support was continued primarily in magnetic bearings and also in flywheel momentum configurations [51].

Nevertheless, this work expanded the laboratory experimental base initiated in the 1970s and pushed the composite material and magnetic bearing technological advancement that emerged in the 1990s.

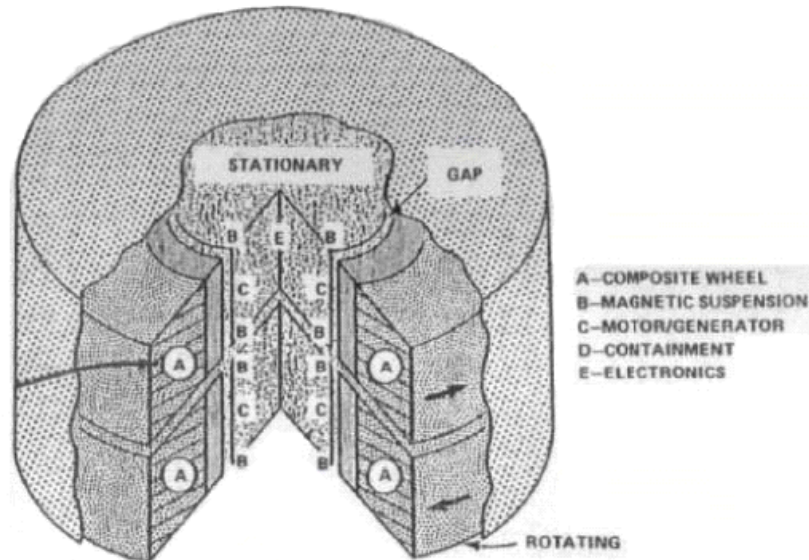


Figure 2.3: Conceptual Flywheel Design for Spacecraft Power System, 1983 [3]

In the mid-1990s, flywheel technology was reinvigorated with automobile industry-led advancement related to/sparking advancement in composite flywheel rotors and magnetic bearings. Commercial leader, AFS Trinity corporation, attributes much of its 1990s flywheel development to its automobile designs [52]. Also, [53] exemplifies one 1999 example of automotive interest in flywheel energy storage. Remarkably, automobile flywheel energy storage

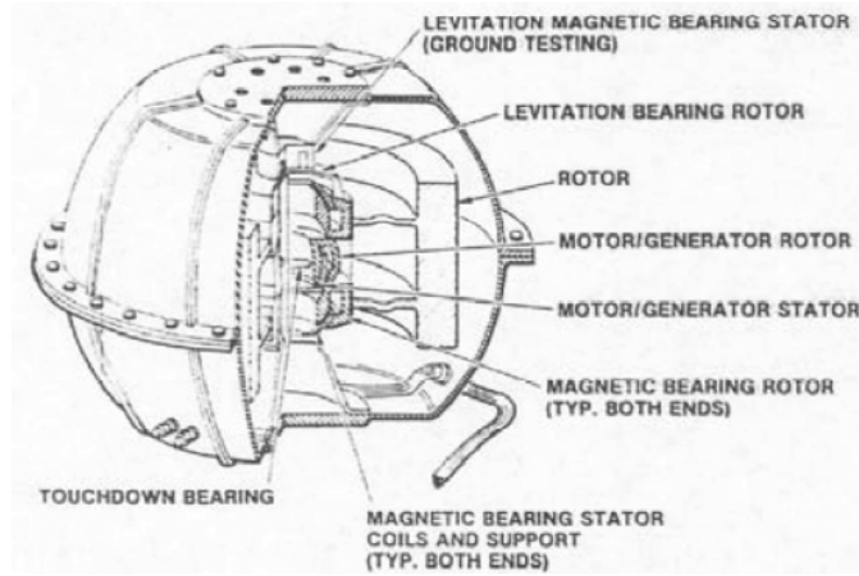


Figure 2.4: IPACS Unit Design Concept, 1985 [4]

dates to 1898 with German designer Dr. Ferdinand Porsche's second developed car, a hybrid using an internal combustion engine to spin a generator that supplied power to its electrical systems [54]. Since then, hybrid cars have relied on flywheel energy storage concepts to operate. In fact, hybrid car development the last 10 years has yielded successful products, such as the Honda Insight (the first US mass-marketed hybrid car), Toyota Prius, Honda Civic Hybrid (identical to its popular Civic), the Toyota Prius II (2004 Motor Trend Car of the Year), and Ford's Escape Hybrid (the first US hybrid SUV) [54]. In contrast, BMW scrapped its 1995 flywheel energy storage program after 3 employees were killed by flywheel shrapnel from its 2000 kg containment enclosure failure [55]. This illustrates inherent risks in high-speed flywheel development.

1990s automobile flywheel energy storage interest sparked the resurgence of satellite ESACS developments. Babuska et. al. [20] and Fausz et.al [21] mention that in 1994,

The NASA Glenn Research Center (then Lewis Research Center) began new efforts to develop flywheel systems on satellites. A cooperative effort was initiated with the Space Vehicles Directorate of the Air Force Research Laboratory (then Phillips Laboratory) to develop flywheel technology for satellite applications. Collaboration with TRW also was initiated [56] and yet another study of space station flywheel energy storage viability was performed [57]. The objective of this study was to examine the overall feasibility of using electromechanical flywheel systems

on the space station. The report included a conceptual design and deployment plan of a flywheel demonstrator experiment leading to a battery replacement option, life cycle cost analysis, a top-level development plan for critical flywheel technologies.

In the late 1990s, Hall published an essential article on flywheel energy storage and attitude control using “gyrostats” [58]. It outlines the gyrostat’s exact nonlinear equations of motion, developed by separating the ES and ACS functions through decomposing internal spacecraft torques via the SVD as well as shows a class of control laws for such a gyrostat-actuated system. This work is a cornerstone for much technical development. Key follow-on work to this effort was accomplished by Shen, Tsiotras, and Hall from 1998 to 2000 for simultaneous attitude control and energy storage using high-speed MWs [59–61]. No longer were counter-rotating flywheels necessary, but the full nonlinear equations of motion for a more conventional, redundant, 4-MW system were developed to track a desired 3-D attitude profile *and* a desired peak power demand profile. This work was the key enabler to the author’s further development of the theory prescribed in this report [12]. At this point, ESACS research did not end with Tsiotras’ work with Shen or Richie, but continued with Yoon and Tsiotras, Roithmayr, and Varatharjoo as later addressed in Subsections 2.1.5 and 2.1.8.

2.1.2 CMGs/VSCMGs

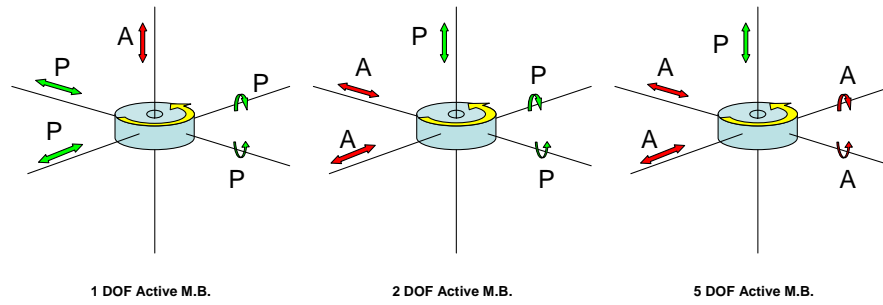
Like satellite flywheel energy storage technology, using CMGs for spacecraft attitude control, has its foundations in the early 1960s. Some of the first spacecraft used on-board gyroscopes to sense 3-dimensional vehicle attitude. During this time, as has been done in other satellite torque actuator developments, it was noted by White and Hansen that since these devices impart a small disturbance torque during operation, this torque could be harnessed and used for attitude control [62]. Thus, CMGs were born from this tiny disturbance torque. Ever since, CMGs have been used for key spacecraft programs, including Skylab, the Hubble Space Telescope, and the ISS [13,63]. Primarily, though, these devices have been used for medium to heavy/large satellites [13]. However, quite recently, CMGs have been designed and flown by SSTL and NASA for small satellites as is mentioned later in Subsections 2.2.1 and 2.2.3. Jacot and Liska (1966), Margulies and Aubrun (1978), and Oh and Vadali (1991), made contributions by capturing the exact nonlinear equations of satellite motion using CMGs, including single- and double-gimbal configurations, gimbal lock singularities, and CMG steering control

laws [64–66]. Further accomplishments in the late 1980s and early 1990s by Bedrossian, Paradiso, Bergmann, Rowell, Walker, and others described different CMG singularity avoidance methods [67–71]. This work enabled Ford and Hall’s efforts, who were the first to investigate the generic nonlinear equations of motion for momentum exchange devices (i.e. Reaction Wheels, Momentum Wheels, and CMGs) [72, 73]. Thus generalising the theory for these devices led directly to the work by Schaub, Junkins, and Vadali, which detailed, for the first time, the nonlinear dynamics behind single-gimbal VSCMGs and inherent singularity avoidance properties these actuators provide [74–77].

2.1.3 Magnetic Levitation and Bearing Technology

Magnetic bearings for flywheel rotor suspension has a rich literary base. No effort will be made to capture all of the past magnetic bearing works, but extensive investigations are undertaken in [1, 27, 28, 34] and works referenced therein. Nevertheless, magnetic bearing literature varies widely, but for flywheel energy storage, dates to the late 1960s/early 1970s.

As mentioned by countless sources, advantages of magnetic bearings include reduced friction (a requirement for high speed flywheels – high speeds are directly proportional to stored energy) through contact-less suspension, lubrication-free operation, and stiction-free zero speed operation, which also translates to effective operation over a long lifetime [15, 78, 79]. However, one should note, as Henrikson, Lyman, and Studer do in [27], “The development of magnetically suspended momentum wheels is just beginning.” Typically, in order to build magnetic bearings, both permanent and electro-magnets are combined using passive and active control principles to provide the typical 1-DOF, 2-DOF, or 5-DOF Active Magnetic Bearing suspension approaches [15, 78, 79]. These methods are illustrated in Figure 2.5(a) and their advantages /disadvantages are reflected in Table 2.5(b). It’s noted by [15] that 6-DOF systems cannot be realised under normal conditions as at least one axis requires active electromagnetic control. This is a result of Earnshaw’s Theorem in relation to electromagnetic stability of objects [15]. Although there is much written on magnetic bearings, there has been little conventional development on miniature versions of these devices for flywheel levitation. Perhaps the most development has been done by Scharfe and Varatharajoo [15, 78–83], but there are still several challenges in making it work for combined attitude control *and* energy storage as revealed in direct discussions with Scharfe [81]. Interestingly, much of this development has its roots in a 1995 ESA effort to develop low-noise momentum wheels [21]. Figure 2.6 shows one concept from this 1995 effort.



(a) Typical Magnetic Bearing Configurations. 'P' stands for passive, 'A' for active.

Active Control	Direction	Advantages	Disadvantages
1 DOF	Axial	Simple electronics low pwr consump.	high axial dim. awkward mech constr.
2 DOF	Both radial	High radial stiffness simple construction	3 DOF passive control
5 DOF	All except whl rot.	Vernier gimbaling cap	Complex, less reliable special precautions in 1 g

(b) Magnetic Bearing Active DOF Advantages and Disadvantages. Source: verbatim from Sharfe (1996)

Materials	Energy Density (Whr/lbf)	Energy Density (Whr/kg)
Maraging Steel	32	14.51
Kevlar-49	109	49.44
Music Wire	48	21.77
Boron/Magnesium	48	21.77
Steel/Epoxy	54	24.49
Future Music Wire	80	36.29
Beryllium Wire	84	38.10
Future Boron/Magnesium	90	40.82
Boron/Epoxy	98	44.45
HTS Glass/Epoxy	93	42.18
Present Graphite/Epoxy	109	49.44
Future Glass/Epoxy	143	64.86
Future Graphite/Epoxy	188	85.28
Theoretical Future	461	209.11
70% Graphite Whisker/Epoxy	565	256.28

(c) Energy Densities of a Few Interesting Materials [28]

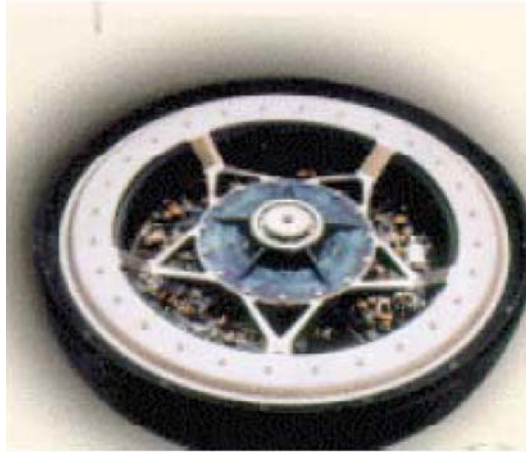


Figure 2.6: ESA/Teldix Magnetically Supported Momentum Wheel, 1995 [5]

One counterexample to this idea, though, is the work of Lee and Wilson [18, 84–91], wherein HTS magnetic bearings have been researched and developed. However, these systems require on-orbit cryogenic cooling, a distinct disadvantage to cheap small satellite systems predicated on COTS technology, such as SSTL/SSC provide.

As stated in [21],

A comparison of ball bearing and magnetic bearing static capacities is given in Table 2.1. The ball bearing radial static capacity is the load at which the bearing steel suffers load induced indentations. Since ball bearings have to support a rotor during launch, launch loads often drive the bearing selection. Operating radial loads (i.e. gimbaling loads) are usually much lower.

Table 2.1: Example of Magnetic and Ball Bearing Properties [21]

Bearing	ID (mm)	OD (mm)	Height (mm)	Radial Static Capacity(N)	Max Speed (RPM)
MB-R-25-205	25	98	52	205	58000
MB-R-280-25555	280	478	312	25555	8000
101 Hybrid	12	28	8	> 10675	40000
204 Hybrid	20	47	14	> 32472	25000
305 Hybrid	25	62	17	> 73396	6600

It is evident, then, that magnetic bearings have several advantages over mechanical bearings and enjoys an extensive literary base. However, this technology limits the present research (as will be addressed), but such limitation does not preclude future miniature magnetic bearings benefits for ESACS.

2.1.4 Motor/Generator Design for High Speed Flywheels

Several works addresses different flywheel energy storage motor/generator technologies. In fact, [27] mentions that “the [magnetic] suspension and drive system have often been in direct conflict in magnetically suspended momentum wheels ... the softness of the suspension precluded the use of conventional motors.” Many of the early satellite flywheel energy storage proposals include sections on motor/generator development and design in order to make such systems a success [27, 34, 38, 41, 45, 92]. Much of the literary background for motor/generator development is used in the present research for developing design approaches based on fundamental motor/generator design. Specifically, the book by Hanselman [93] in addition to a few other sources [94–103], describe the critical concepts for this development. For now, it suffices to say that there is extensive motor/generator discussion in the flywheel literature dating to the 1960s and 1970s as well as extensive knowledge in the electrical engineering community dating back to the 1800s and early 1900s [93, 104].

2.1.5 Flywheel Rotor Structure

The discussion now turns to developments in rotor design. Several references explain rotor limitations to supporting the extremely high wheel speeds necessary for energy storage [27, 28, 78, 79, 105]. This is a direct consequence from the wheel outer rim’s tangential velocity/acceleration (i.e. the force due to centripetal acceleration is limited by rotor tangential stress capacity). This leads to a material properties constraint on the maximum flywheel speed [28, 105]. In [28], it’s shown that a composite material pierced disk yields the largest energy density. Kirk also highlights representative material densities as reflected in Table 2.5(c). Although this list is relatively old, it’s important to understand technological advances have evolved it. Some of these materials are also explained in [78]. Energy density relates directly back to a material’s available storage capacity. In [78], Varatharajoo uses well known conventional materials, a couple not available in the 1970s, to illustrate the best rotor material for small satellites. Interestingly, as noted in [105], if rotor length to outside

diameter ratio is large as in a rod-shaped wheel, it is dynamically difficult to stabilise. [105] relates this ratio to the inner to outer wheel radius ratio. Choosing both ratios fixes the outer rotor radius, regardless of the mass.

Further composite materials work in miniaturising flywheels for small satellites was done by Charles Bakis at Penn State [106] which investigated 3 primary small satellite flywheel energy storage subsystems, including a high-strength, carbon fiber composite rotor rim; an actuator life-extending bearing system; and an OCR, permanent magnet motor/generator. Although the Penn State flywheels are designed to reach speeds of 150-300K RPM and store 100 W hrs of energy, the top speed achieved by 2004 in their laboratory was 18000 RPM due to rotor imbalance and reliance on mechanical bearings limits. Penn State also studied using Carbon nanotubes for flywheel rotor structural enhancement, but analysis shows this technology has no significant advantages. Instead, the standard filament wound carbon composite flywheels are best. Clearly, Penn State's work is fundamental to building high-speed, miniature flywheels.

2.1.6 Flywheel Containment

As emphasized in [21],

A major concern of high speed rotating machinery (flywheels, turbines, etc.) is containment of the test article in the event of a catastrophic failure. If such a failure occurs without containment, pieces of the rotor, or the whole rotor itself, may interfere with the test assembly and pose a great danger or cause significant damage. Certainly, if a catastrophic failure occurred on-orbit, the spacecraft would become space debris.

For this reason, the flywheel needs to be contained. Detailed study of such containment, although important, is beyond the scope of the thesis. Suffice it to say that the prototype presented in Chapter 7 and tested in Chapter 8 includes an Aluminium containment that is not optimal. It helps protect against catastrophic rotor failure from damaging the rest of the ESACS system, the test article itself, and any personnel involved with the test by providing a barrier to control a rotor blast that is quite close to the outer rim of the rotor. Excellent works further capturing the critical considerations associated with containment (of both the composite rotor and the entire test article) are detailed in [21]. Regardless, more advanced

containment design using composites (e.g. Kevlar) is a goal in the follow-on efforts to this work.

Here, it is also worth mentioning that an important advantage of the uni-directional fibers used in a composite flywheel are that they can be designed with a benign failure mode. In other words, the hoops of fibre connected with an imbedded binding material most likely will fail by unraveling the hoops radially outward. Releasing the kinetic energy in the structure this way means that a large blast of material acting similar to a kinetic-energy enriched projectile is a highly unlikely failure mode of the system. Even so, considering such an act helps focus the containment considerations.

2.1.7 VSCMGs for Energy Storage

As alluded to earlier, Shen, Tsiotras, and Hall evolved Hall's gyrostat-based, simultaneous ESACS nonlinear equations and controller design to a conventional, 4-MW, three-axis stabilized ACS and secondary battery ES (i.e. "simultaneous" in that the operations of combining attitude control actuation while storing energy are not decoupled, but instead "degrees of control freedom" are exploited to track instantaneous peak power demand requirements while simultaneously controlling attitude) [58–61]. This revolutionary work is the basis for the author's VSCMG theoretical work in 2000-2001. Combining the simultaneous ESACS concepts of Shen, Tsiotras, and Hall with that of Schaub, Junkins, and Vadali [66, 74–77], Richie, Tsiotras, and Fausz investigated using VSCMGs, with singularity avoidance advantages, as actuators for a simultaneous ESACS [12, 107, 108]. This work is one of two cornerstone efforts for the present investigation. In their work, the full nonlinear equations of motion for VSCMGs in *simultaneous* ESACS is developed and simulated. It shows that for a redundant set of n -VSCMGs (e.g. 4 arranged in a pyramid configuration), a satellite reference attitude profile can be tracked while maintaining a desired power profile [66–70, 74–77].

Continuing the work of Richie, Tsiotras, and Fausz further, in 2002, Yoon and Tsiotras developed a wheel speed equalisation technique through adaptive control principles which ensures the VSCMGs remain within adequate operating limits by keeping all the wheels at similar speeds (thus avoiding the case where one wheel becomes saturated) [109]. In 2004, Yoon and Tsiotras furthered the VSCMGs for ESACS efforts by examining the singularity space for cases where power demands are too high and redundancy in VSCMGs for ACS is too low [110]. This lays needed ground work for developing robust, fault-tolerant system

controllers.

Further continuing this work in late 2004, Rothmaier et al [111] investigated the generalised theory of gyrostats that use counter-rotating MWs in conjunction with CMGs, an approach somewhat similar to VSCMGs, but which requires much more mass due to the dual flywheels of each actuator. Plus, it addresses spacecraft reaction damping torque from such actuators, using a Kanesian dynamics analysis approach [112].

2.1.8 Small Satellites

Most successful small satellites (under 500 kg mass) have used secondary batteries such as NiCd to store energy [113, 114]. These systems, typically launched into Low Earth Orbit (LEO), require a rugged energy storage method due to frequent eclipse cycles. Therefore, LEO small satellites can greatly benefit from the robust aversion to component wear afforded by flywheel energy storage solutions. Nevertheless, contemporary small satellite programs endeavour to meet challenging missions previously reserved for large satellites. It is therefore useful to highlight the background of small satellite programs in this regime in terms of flywheel energy storage employment. It has already been mentioned that SPOT (1986) and AMSAT Phase 3-D (2000) flew 3 magnetically suspended momentum wheels [15, 16]. These missions form the small satellite flight heritage for magnetically suspended flywheels as attitude control actuators. Remarkably, in direct discussions Scharfe indicated using flywheel energy storage on small satellites is a risky, challenging proposition due to the wheel spin speed and stored energy magnitudes involved [81]. He emphasised that magnetically levitated flywheels for energy storage is a concept mentioned for AMSAT 3-D, but was only designed as a battery *emergency back-up* system and not the primary energy storage mechanism [15, 79–81]. Obviously, technology since the AMSAT 3-D flight should have advanced a long way by now, but wheel speed magnitudes limits and associated risks have hampered progress since 2000. Besides the flywheel energy storage employment aspect of a VSCMG-based ESACS, small satellites have used CMG technology as is addressed later in Subsection 2.2.3.

2.1.9 Design Optimization/Linear Programming

Another key area of research employed in the present investigation is that of parametric design optimisation. As it is a huge area with much advancement in the realm of mathematics and nonlinear programming, only a small portion is investigated here. Nevertheless, the works

by Bryson and Ho, Winston, and Lasdon et. al., and Berghen give plenty of theoretical background to direct the optimisation efforts in VSCMG actuator design [115–122]. The key result from these literary sources is that the Microsoft Excel Solver, used extensively in this research, is proprietary code based on Lasdon’s GRG2, but can be recreated from theory and computer algorithms spelled out by Bryson and Ho, Winston, and Berghen. In fact, the Bryson and Ho approach is most general and therefore more accurate than the GRG2 (although references [118–121] point out the GRG2’s relative accuracy as compared to a more general approach). It should be understood that GRG2 was primarily designed for coding efficiency on problems with well over 10000 decision variables vice the author’s problem with 150 or so parameters and just 5 decision variables. Regardless, the Bryson and Ho approach is based on a second-order, quadratic optimisation technique wherein a Lagrangian function (i.e. a function that combines a nonlinear performance index and the algebraic sum of Lagrange multiplier variables on the nonlinear constraints) is optimised.

2.2 Contemporary Research

Having presented the key VSCMG for ESACS literature, detailing current research in contemporary international laboratories is an important component to capturing the state-of-the-art. Herein, NASA, AFRL, and SSTL/SSC activities are described.

2.2.1 NASA

The bulk of contemporary satellite flywheel energy storage is led by NASA in 2 primary locations, Texas A & M University and the NASA Glenn Research Center (GRC) (formerly Lewis RC) in Ohio. Texas A & M’s work surrounds using HTS magnetic bearings for magnetic levitation. Eujeoung Lee, Thomas Wilson, and others began this effort in 1999 [18, 84–91]. It is the primary attempt at making nano-MWs and nano-CMGs for satellite ESACS, but relies on HTS bearings, which requires super-conducted materials to operate – a real challenge for low-cost, COTS-based small satellites.

Secondly, GRC sponsored Penn State’s flywheel miniaturisation work mentioned in Subsection 2.1.5. Also, GRC in-house work includes that of Kenny et.al.’s flywheel energy storage power system development and demonstration [123–128]. Kenny’s work is one of the first efforts to develop the electrical systems associated with ESACS, correctly noting that much

of the past ESACS developments in the literature focused on the ACS aspect of the problem. Its goals, according to [21], have been

performing system level experiments to develop multi-wheel systems and demonstrate ability to cycle while controlling torque, to define impacts of flywheel disturbances on attitude control, and address failure modes on both attitude control and power systems at the spacecraft level. The experiments involve single-axis airtable tests of two counter rotating flywheel modules, and two-axis, three-module tests are planned [129].

Much of the impetus for GRC's recent research was driven by anticipated future implementation on the ISS to replace the Nickel-Hydrogen secondary batteries on the International Space Station (ISS) [130]. An example concept of such a system is shown in Figure 2.7. As

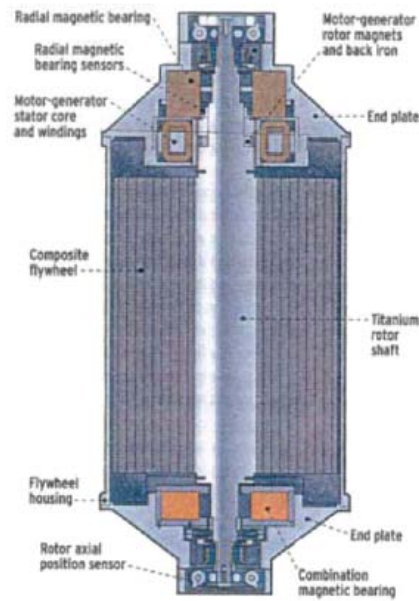


Figure 2.7: Flywheel Battery for Space Station Experiment [6]

stated in [21],

Two FES development units were built by U.S. Flywheel Systems for GRC, optimized for energy storage. The attitude control capability of these units was minimal at best (~ 1 N-m). One of these development units was able to achieve the technology goal of spinning at 60,000 RPM, the maximum design speed for

the units. Unfortunately, NASA funding cuts, especially for ISS, resulted in the ISS program office dropping the flywheel replacement option. However, NASA continues to develop these units in-house for a potential flight experiment on an ISS express pallet (2.7).

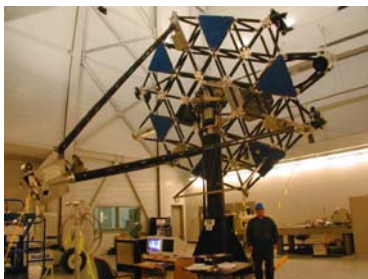
Ref. [131] revealed several observations in regards to NASA-related small satellite ESACS technology . First, tiny flywheel dynamics are strikingly similar to that of large flywheels except the speed is much faster. Thus, the technology can realistically be linearly scaled. The key lies in accounting for flywheel tip speeds. Second, NASA's is now more interested than before in applying small flywheel technology into dual-use systems (other than ESACS) such as in satellite boom deployment mechanisms and imbedded structures. This expands high-speed, mini-flywheel space application opportunities. Third, NASA's flywheel work has involved counter-rotating wheel concepts and not CMG-employment due to ISS ESACS plans to implement such counter-rotated flywheels. A program currently postponed, it's important to understand that much high-speed flywheel work for an ESACS over the last 20 years was dominated by NASA's ISS plans. However, as Beach confirmed, NASA's development direction is contrary to the author's research and is therefore wide-open for exploration.

2.2.2 AFRL

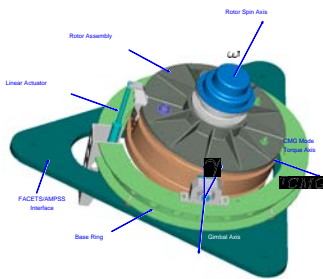
The "AFRL FACETS Grand Challenge" program, which was designed to "create the first 3-axis, spacecraft-scale, mission-traceable, ground demonstration of combined flywheel attitude control and energy storage by 2007" [7,132] encompassed AFRL's contemporary ESACS research. This program used a test article known as AMPSS, Agile Multi-Purpose Spacecraft Simulator, which rested on a hemispherical air bearing and employed 3 Honeywell-built Energy Storage CMGs (ESCMGs) as ESACS actuators [7,132]. Figure 2.8 illustrates the ESCMGs and AMPSS. Each ESCMG contained a 2 ft. (0.6 m) diameter, magnetically-levitated rotor and provided 1.4 kWhr usable energy.

More than 10 years in the making, perhaps the biggest limitation of this work is that it was geared for medium to large (and not small) satellite systems [133]. In addition, ref. [132] mentioned that "the flywheel battery transmits a disturbance reaction torque to the spacecraft when power commands are issued." In fact, the FACETS program can be thought of as a one-way coupled ESACS like that addressed later in Chapter 6. Therefore, although the FACETS program was designed to make incredible strides toward actualising a satellite

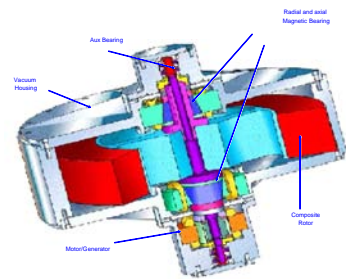
ESACS using CMGS, one can clearly see the need to resolve the one-way coupled-type disturbance problem as well as apply this technology to small satellites. These are both objectives of the present effort.



(a) AMPSS Photograph



(b) ESCMG Layout, Part 1



(c) ESCMG Layout, Part 2

Figure 2.8: AF Research Laboratory’s Agile Multi-Purpose Spacecraft Simulator (AMPSS) and Energy Storage CMGs [7]

The FACETS program dates back to the late 1980s and early 1990s with the Strategic Defense Initiative (SDI). As mentioned in [21],

Advancing from a space-based laser concept developed under the SDI, the Advanced Structures Experiment (ASTREX) conducted at Edwards Air Force Base, Calif., was used by AFRL to test control of large space structures. In 1992, the initial experiments at Edwards Air Force Base ceased. Eventually, the dormant ASTREX structure moved to the Space Vehicles Directorate at Kirtland Air Force Base, New Mexico. By 1997, it became the foundation for the FACETS concept.

Although the testing campaign for the AMPSS was estimated to occur in December 2006 with an expected completion and full-scale demonstration by the summer of 2007, this program slipped and was cancelled before completion. Thus, there was not an AFRL “3-axis, spacecraft-scale, mission-traceable, ground demonstration” of ESACS by 2007 as expected, but the disappointing void left by the AFRL FACETS program was filled by the experimental work documented in Chapter 8, the first “3-axis, spacecraft-scale, mission-traceable, ground demonstration” of ESACS.

2.2.3 SSC/SSTL Research

indent The SSC/SSTL research team has evolved its expertise in small satellite momentum exchange devices over the last decade. Much of this effort lies in its space-proven miniature RWs and MWs as well as its recent launch of mini-CMGs. The first two SSTL mini-MWs were launched along with a space-qualified Ithaco MW as part of the 325-kg UOSAT-12 in 1999 [11, 134]. UOSAT-12 was SSTL's first satellite with an active, 3-axis attitude determination and control capability [134], upon which its follow-on ACS designs are based. In 2000, SSTL supplemented its monumental UOSAT-12 achievements by flying the then smallest 3-axis stabilised satellite, the 6.5 kg SNAP-1 [135]. Although this mission did not use 3 separate wheels, it did employ a single, miniature pitch-axis momentum wheel that revolutionised small satellite ACS. Nevertheless, these accomplishments inspired the small CMG recently flown on Bilsat-1 [136]. Clearly, the SSC/SSTL team has much experience in developing momentum exchange devices for small satellites and is thus an ideal participant in realising a VSCMG-based ESACS.

The SSC approach to making CMGs for small satellite applications (shown in figure 2.9) via relatively simple and therefore low cost methods is addressed in [17]. The main disadvantages of CMG actuators are system complexity and gimbal-lock singularity potential. However, the SSC design shown in figure 2.9 permits torquing each flywheel by adjusting its speed, thereby creating a VSCMG. This has the advantage of singularity avoidance (as well as permitting energy storage, provided enough actuators are used).

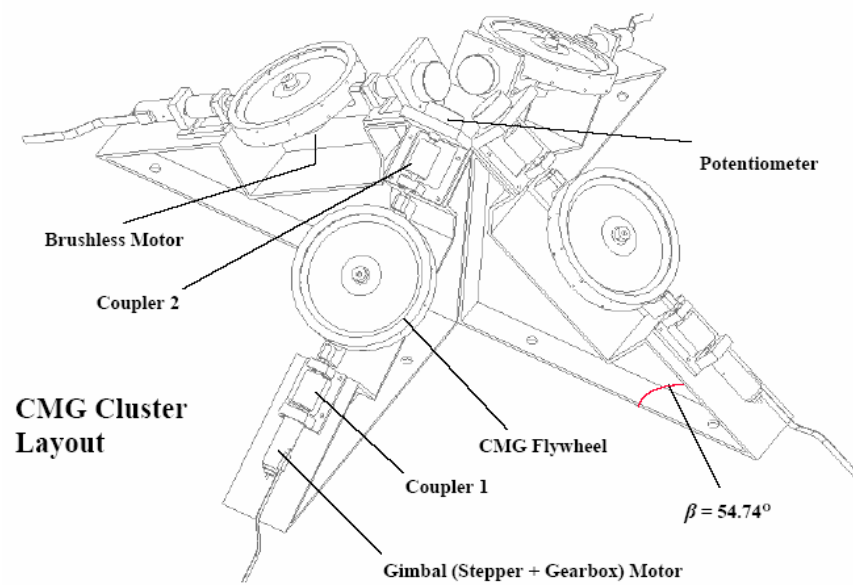


Figure 2.9: SSC CMG Design

Chapter 3

Mission Scenarios

This chapter defines representative mission and spacecraft requirements for a mission relying on high peak power with simultaneous slewing agility envisioned for small satellites in the near future. Achieving these requirements will showcase the ESACS technology and its potential to enabling missions previously thought unrealistic for these small satellites. The investigation begins with a brief discussion of candidate missions then moves into defining the key requirements for one of these missions, spotlight synthetic aperture radar (SAR). The attitude and power requirements are defined via a collection of a few individual processes. Example results from applying these processes is illustrated via a single scenario that yields a set of representative values. After establishing these static mission requirements, dynamic attitude and power reference profiles used to generate VSCMG-based ESACS control laws are described and presented.

3.1 Overview of Candidate Missions

Due to the instantaneous peak power density and agile spacecraft slewing benefits described later in the thesis, ESACS technology primarily aids systems requiring both agile slewing and high peak power. Agile slewing requires that the satellite rapidly change its attitude on a regular basis. This is much different from many conventional space missions which rely on a stable platform that maintains a constant orientation with respect to the Earth's surface whilst in orbit. Meanwhile, these rapidly slewing spacecraft also need high peak power in order to leverage ESACS benefits.

One such mission is that of TopSat, a high resolution, panchromatic earth imaging satellite

that provides data for disaster relief, news-gathering, and a variety of other applications quickly and at low cost [137]. In this situation, counter to conventional imaging systems, the satellite is rotated via a constant, backward pitch maneuver to keep the imaged ground area in focus (as opposed to scanning the camera) [138]. This maneuver is called a Time Delay Integration (TDI) maneuver [9, 114]. Note that the detailed data for today's more advanced cameras requires higher power to download images since the ground station pass times in LEO are no different than in the recent past. That is, the camera data needs to be sent at a very high data rate to get it all to the ground during a ground station pass such that the on-board data buffer is cleared for more imaging over the next orbit. Furthermore, the TDI maneuver is different from classical imager approaches since these approaches use the whisk-broom or push-broom techniques ([114]) where the camera is pointed to a fixed point on the earth and "dragged" along the desired area, requiring a stable, fixed attitude platform with respect to the Earth's surface.

Another mission that can be applied to small satellites yet requires rapid slewing with high peak power is that of spotlight synthetic aperture radar (SAR). The basic concept of SAR has been around since 1951 [139]. The synthetic aperture typically inferred through the term SAR arises when endeavouring to use either a single dish or phased array Radar to collect several consecutive images and then fuse these images together, thereby generating a consolidated image expected of a much larger radar system. This is the well-known "synthetic" connotation of SAR. Note that for low-cost small satellites, a single, non-scanning dish concept is more feasible than using a phased array or scanning dish due to the reduced complexity required. That is, in a phased array Radar, the array sections all move in close concert with each other while in a scanning dish, the dish moves with respect to the spacecraft. Each method relies on complex control/synchronization algorithms and actuation mechanisms, whereas in a scanning dish, the dish remains fixed, relying on the pointing/slewing capability of the satellite's ACS. However, the kind of SAR where several images are merged together of consecutive locations on the ground is known as strip-map SAR. This technique is identical to classical imager data in that the Radar antenna is pointed to the ground and dragged along it, with the collected images processed on board or on the ground. Note that in the case of strip-map SAR, although there is much data and required peak power is high, it relies on maintaining a fixed point on the ground and thus a stable platform assuming the satellite does not scan (i.e. have a moving orientation different to the satellite's orientation with respect to a sufficiently inertial reference). Although strip-mapping SAR requires a precision

attitude control system, it does not require rapid slewing.

However, another type of SAR mission that does require rapid slewing is that of spotlight SAR. In this case, the Radar dish points to a tracked object and maintains a centered focus on this target during a satellite's pass over head. In this case, although several images are collected of the same object, the host satellite's motion with respect to the ground permits several aspect angles of the target which helps build a more accurate characterization of the target. Similar to the TDI case, in order to maintain focus of the antenna on a target, one of two things needs to happen. Either the Radar is moved within the spacecraft to track the target or the entire satellite moves with respect to an inertial reference to keep the target in view of the Radar. The similarities in the TDI maneuver and spotlight SAR tracking mean that both such missions can exploit the benefits of ESACS. However, since spotlight SAR missions logically require more power to run the Radar, collect, and downlink mission data than TDI imaging, SAR is chosen as the representative mission example for this thesis.

3.2 Mission Design Requirements

Having determined that an ideal mission for exploiting ESACS benefits is small satellite spotlight SAR, further characteristics of this mission drive requirements for the ESACS. It is therefore necessary to define the calculation process used to ultimately capture the power and attitude requirements for such a mission. The mission assumes that a monostatic, parabolic reflector antenna that can fit on a small satellite (in the mini-satellite realm of 400 – 450 kg) will be used for this spotlight SAR mission. Thus, the SAR mission requirements are broken into these separate design processes: SAR geometry, SAR parabolic reflector diameter sizing, SAR transmitter link budget, and parabolic reflector plus spacecraft bus mass and inertia sizing.

Figures 3.1, 3.4, and 3.2 illustrate the mission geometry for a spotlight SAR concept [139–142]. In the limiting case depicted in Figure 3.1, the satellite first tracks the target at time t_1 where the spacecraft is its initial yaw angle, ψ_1 . The target then moves in the opposite direction of the satellite passing through its closest distance to the satellite ground trace at time t_2 until the satellite reaches its final yaw angle, ψ_3 at time t_3 . Since the target and satellite are moving with respect to the ground, the farthest ground distance between the satellite and target during the image collection period (t_f) is x_{sl_3} . x_{sl_3} is also the projection of the largest target range, R_{sl_3} , onto the ground neglecting the Earth's curvature. Superimposing

the viewing geometry for times t_1 and t_3 from the side, as depicted in Figure 3.2, one can find R_{sl_1} and R_{sl_3} from the circular orbit altitude, h , and the roll angle limits, ϕ_1 , and ϕ_3 . Reasons for selecting a circular orbit will be described along with other considerations in the sequel to this section. In addition, it's assumed that in the worst case, the satellite is at its roll angle limits at times t_1 and t_3 to match its yaw angle limits at these times. Added to this, the satellite constantly pitches to maintain its unrolled yaw axis along the Earth to satellite radius vector (i.e. nadir tracking). From this and the collection time, t_f , spanning from t_1 to t_3 , one can use the roll, pitch, and yaw requirements to capture an equivalent single-axis rotation maneuver about the Euler axis [143]. The process to calculate this attitude maneuver is summarized in Figure 3.3 while the equations are given in eqs. 3.1 through 3.24.

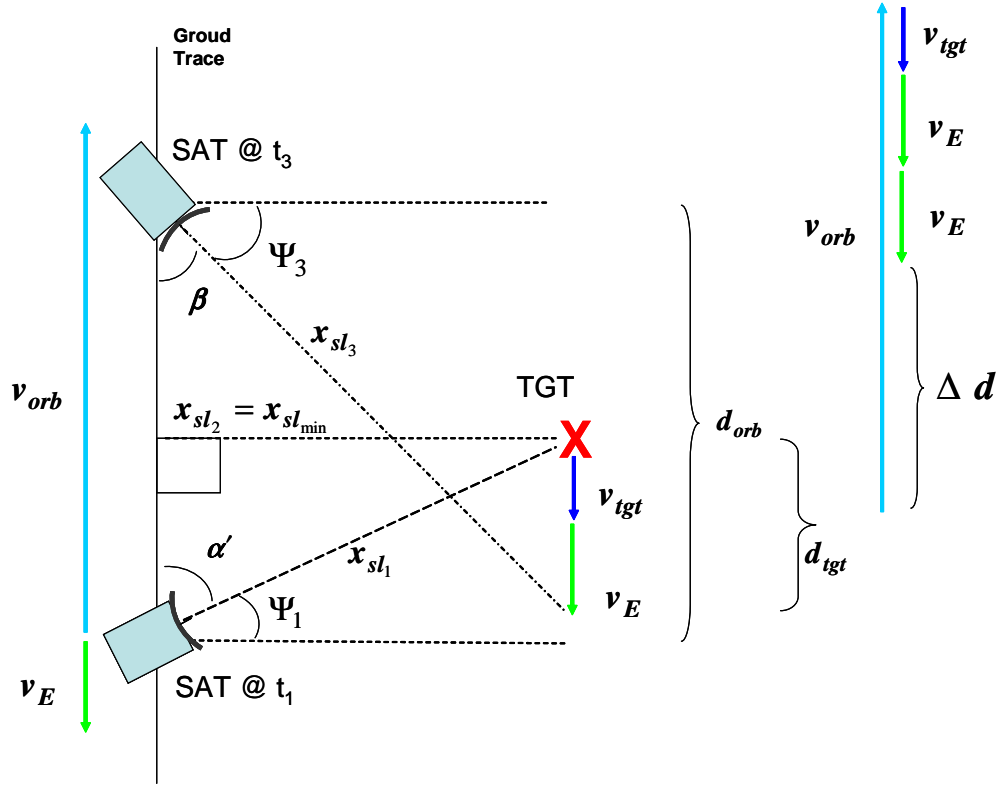


Figure 3.1: Top View - Spotlight SAR Collection Geometry

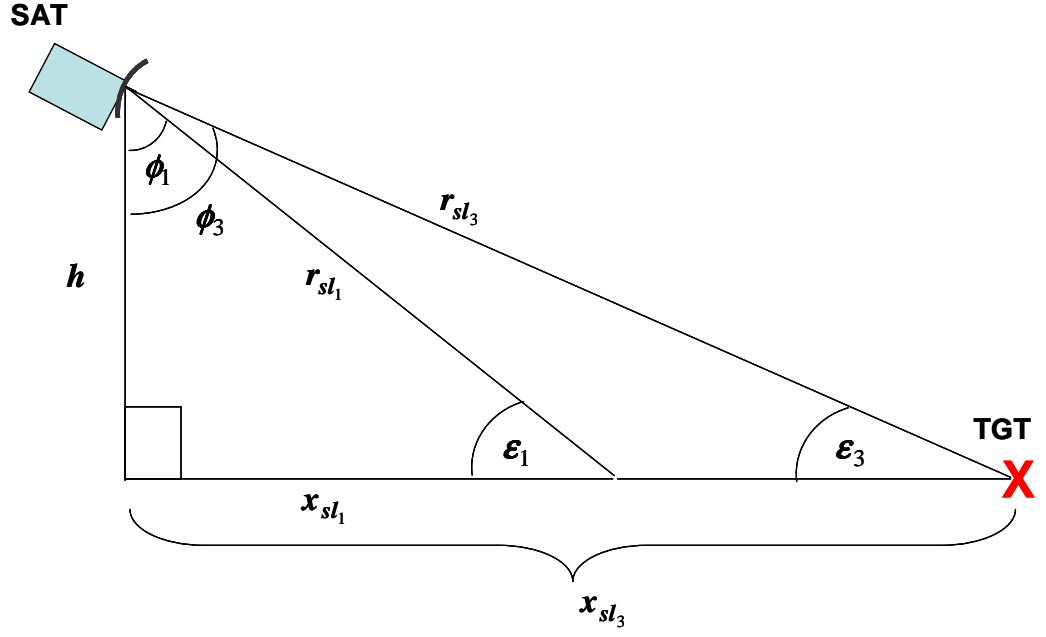


Figure 3.2: Side View - Spotlight SAR Roll Angle Coverage Area

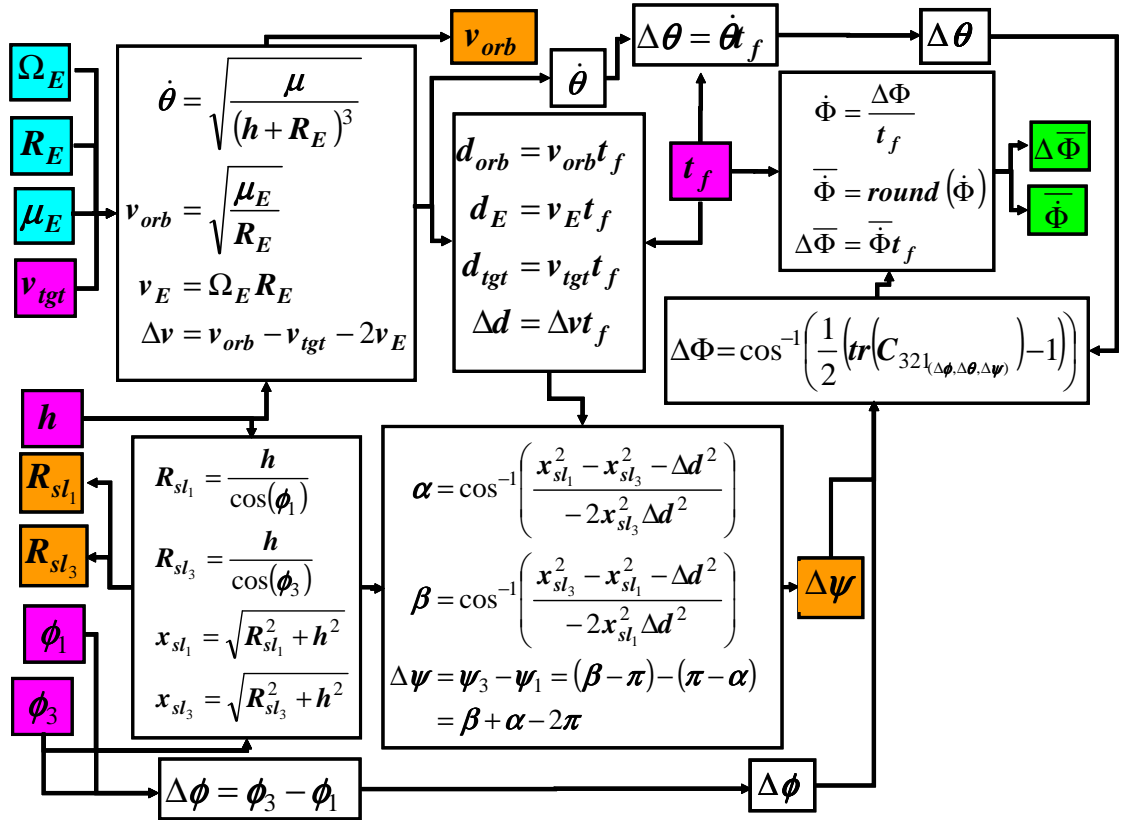


Figure 3.3: Spotlight SAR Attitude Maneuver Calculation Process

$$\dot{\theta} = \sqrt{\frac{\mu_E}{(h + R_E)^3}} \quad (3.1)$$

$$v_{orb} = \sqrt{\frac{\mu_E}{h + R_E}} \quad (3.2)$$

$$v_E = \Omega_E R_E \quad (3.3)$$

$$\Delta v = v_{orb} - v_{tgt} - 2v_E \quad (3.4)$$

$$d_{orb} = v_{orb} t_f \quad (3.5)$$

$$d_E = v_E t_f \quad (3.6)$$

$$d_{tgt} = v_{tgt} t_f \quad (3.7)$$

$$\Delta d = \Delta v t_f \quad (3.8)$$

$$R_{sl_1} = \frac{h}{\cos(\phi_1)} \quad (3.9)$$

$$R_{sl_3} = \frac{h}{\cos(\phi_3)} \quad (3.10)$$

$$x_{sl_1} = \sqrt{R_{sl_1}^2 + h^2} \quad (3.11)$$

$$x_{sl_3} = \sqrt{R_{sl_3}^2 + h^2} \quad (3.12)$$

$$\alpha = \cos^{-1} \left(\frac{x_{sl_1}^2 - x_{sl_3}^2 - \Delta d^2}{-2x_{sl_3}^2 \Delta d^2} \right) \quad (3.13)$$

$$\beta = \cos^{-1} \left(\frac{x_{sl_3}^2 - x_{sl_1}^2 - \Delta d^2}{-2x_{sl_1}^2 \Delta d^2} \right) \quad (3.14)$$

$$\psi_1 = \pi - \alpha \quad (3.15)$$

$$\psi_3 = \beta - \pi \quad (3.16)$$

$$\Delta\psi = \beta + \alpha - 2\pi \quad (3.17)$$

$$\Delta\theta = \dot{\theta} t_f \quad (3.18)$$

$$\Delta\phi = \phi_3 - \phi_1 \quad (3.19)$$

$$C_{321\Delta\phi\Delta\theta\Delta\psi} = \begin{pmatrix} c_{\Delta\theta}c_{\Delta\phi} & c_{\Delta\theta}s_{\Delta\phi} & -s_{\Delta\theta} \\ (-c_{\Delta\psi}s_{\Delta\phi} + s_{\Delta\psi}s_{\Delta\theta}c_{\Delta\phi}) & (c_{\Delta\psi}c_{\Delta\phi} + s_{\Delta\psi}s_{\Delta\theta}s_{\Delta\phi}) & s_{\Delta\psi}c_{\Delta\theta} \\ (s_{\Delta\psi}s_{\Delta\phi} + c_{\Delta\psi}s_{\Delta\theta}c_{\Delta\phi}) & (-s_{\Delta\psi}c_{\Delta\phi} + c_{\Delta\psi}s_{\Delta\theta}s_{\Delta\phi}) & s_{\Delta\psi}c_{\Delta\theta} \end{pmatrix} \quad (3.20)$$

$$\Delta\Phi = \cos^{-1} \left(\frac{1}{2} (\text{trace}(C_{321\Delta\phi\Delta\theta\Delta\psi}) - 1) \right) \quad (3.21)$$

$$\dot{\Phi} = \frac{\Delta\Phi}{t_f} \quad (3.22)$$

$$\bar{\Phi} = \text{round}(\dot{\Phi}) \quad (3.23)$$

$$\overline{\Delta\Phi} = \bar{\Phi} t_f \quad (3.24)$$

Next, the changing ground swath, S_a , for spotlight SAR shown by the side view in Figure 3.4 plus the yaw and roll angles found for the attitude maneuver are key inputs to determining the SAR parabolic reflector diameter, L_{pb} . The process for finding L_{pb} as well as the pulse repetition frequency (PRF), azimuth resolution, X_a , range resolution, X_r , synthesized antenna length, L_{synth} , and the effective azimuth area, A_{eff} , is illustrated in Figure 3.5 using the equations in set 3.25. Note that the key antenna sizing equations were derived from [139, 141, 144]

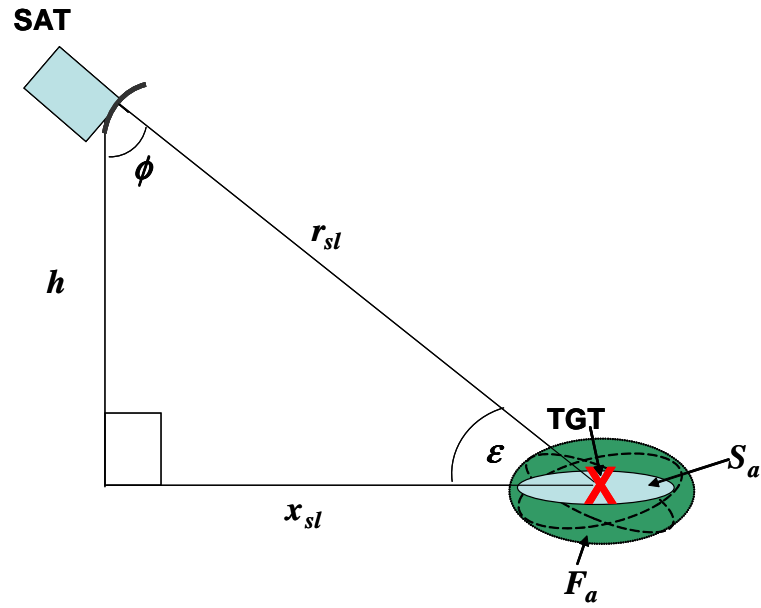


Figure 3.4: Side View - Spotlight SAR Collection Geometry with Ground Swath

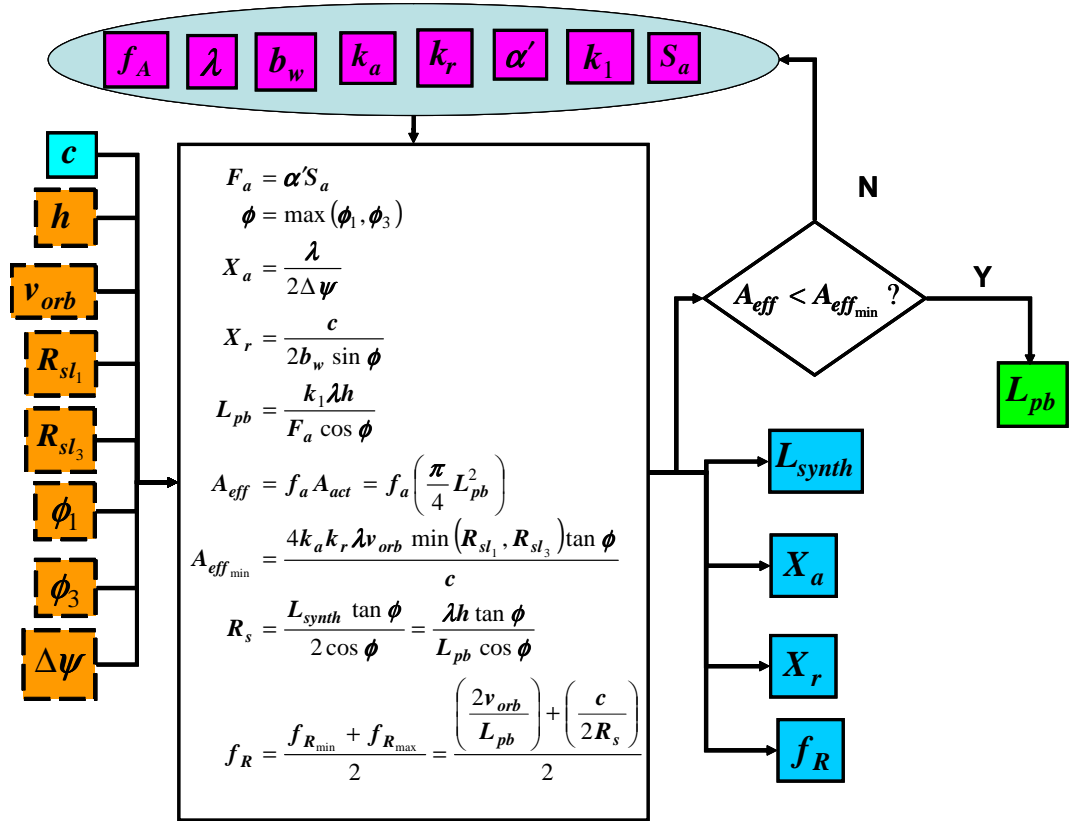


Figure 3.5: Spotlight SAR Parabolic Reflector Diameter Sizing

$$F_a = \alpha' S_a \quad (3.25)$$

$$\phi = \max(\phi_1, \phi_3) \quad (3.26)$$

$$X_a = \frac{\lambda}{2\Delta\psi} \quad (3.27)$$

$$X_r = \frac{c}{2b_w \sin \phi} \quad (3.28)$$

$$L_{pb} = \frac{k_1 \lambda h}{F_a \cos \phi} \quad (3.29)$$

$$A_{eff} = f_a A_{act} \quad (3.30)$$

$$= f_a \left(\frac{\pi}{4} L_{pb}^2 \right) \quad (3.31)$$

$$A_{eff_{min}} = \frac{4k_a k_r \lambda v_{orb} \min(R_{sl_1}, R_{sl_3}) \tan \phi}{c} \quad (3.32)$$

$$L_{synth} = \frac{2\lambda h}{L_{pb}} \quad (3.33)$$

$$R_s = \frac{L_{synth} \tan \phi}{2 \cos \phi} \quad (3.34)$$

$$= \frac{\lambda h \tan \phi}{L_{pb} \cos \phi} \quad (3.35)$$

$$f_R = \frac{f_{R_{min}} + f_{R_{max}}}{2} \quad (3.36)$$

$$= \frac{\frac{2v_{orb}}{L_{pb}} + \frac{c}{2R_s}}{2} \quad (3.37)$$

Building on the attitude maneuver and reflector diameter requirements, the power requirements process is showcased in Figure 3.6 using the equations summarized in eq. set 3.38 [139, 141]. In this process, the Radar equation is used to get the required transmitter power at times t_1 and t_3 based on achieving the given signal-to-noise ratio (SNR). The largest requirement of these extreme points (thus at time t_3 where the transmit distance is greatest) is used to set the transmitter power, then supplemented by a factor of f_{oth} to run the transmitter's support systems. The result is then rounded up into the final power requirement, $\overline{P_r}$.

$$P_{t_1} = \frac{(SNR) 8\pi k T_n b_w \lambda h^3 b_w \sin \phi_1}{L_{pb}^3 c l \sigma \cos^4 \phi_1} \quad (3.38)$$

$$P_{t_3} = \frac{(SNR) 8\pi k T_n b_w \lambda h^3 b_w \sin \phi_1}{L_{pb}^3 c l \sigma \cos^4 \phi_3} \quad (3.39)$$

$$P_r = \max(P_{t_1}, P_{t_3}) \quad (3.40)$$

$$\overline{P_r} = \text{round}(P_r) \quad (3.41)$$

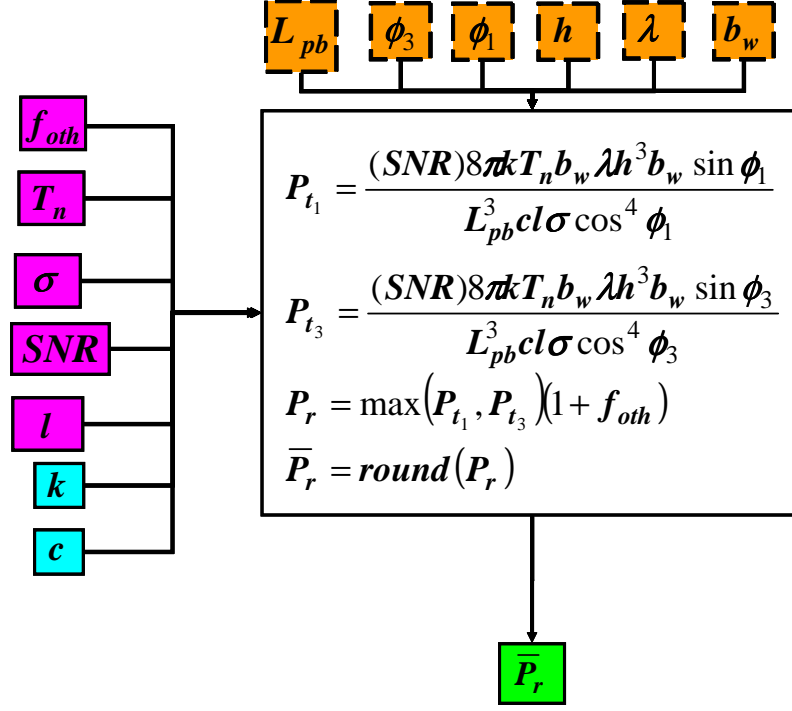


Figure 3.6: Spotlight SAR Power Calculations

Having defined the processes for the calculating the key aspects of the spotlight SAR link budget, the total spacecraft mass and inertia can be calculated. Before identifying these calculations, its useful to present a plausible implementation of a small satellite SAR system. One such concept is highlighted in Figure 3.7.

As previously implied, the final sizing process used to generate the spotlight SAR requirements is that of determining the proper reflector mass and inertia and the anticipated non-ESACS satellite mass. This process uses the assumed mechanical design dimensions reflected in Figure 3.8. The process is given in Figure 3.9 which uses the equations captured by eq. set 3.42.

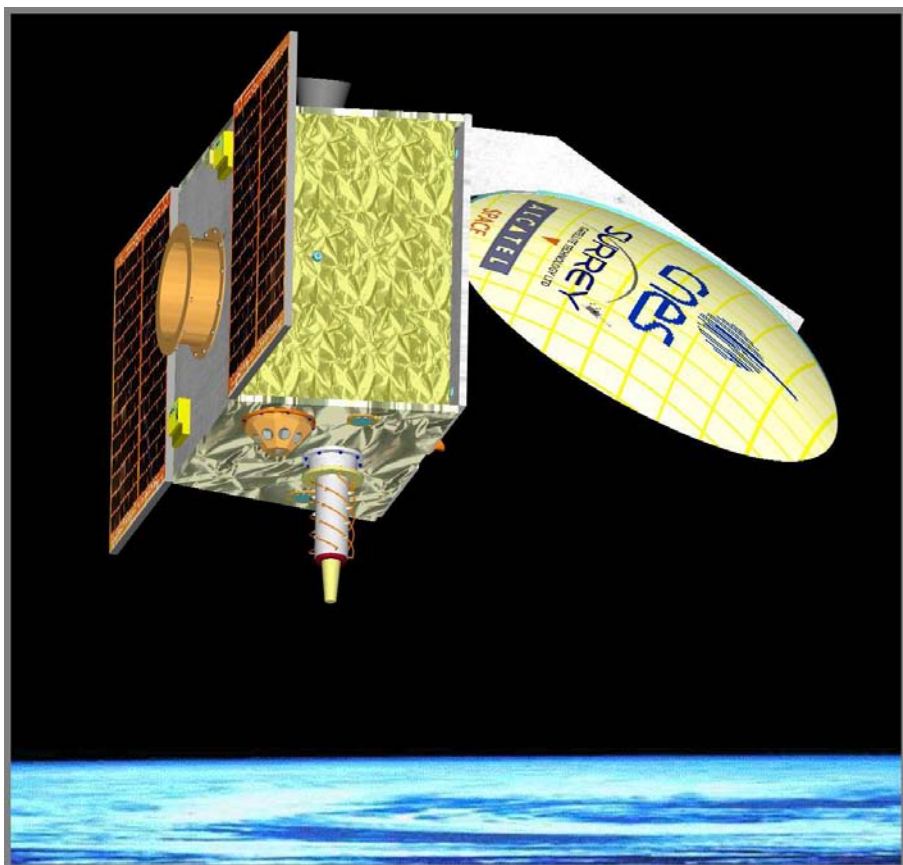


Figure 3.7: Conceptual Design of a Small Spotlight SAR Satellite

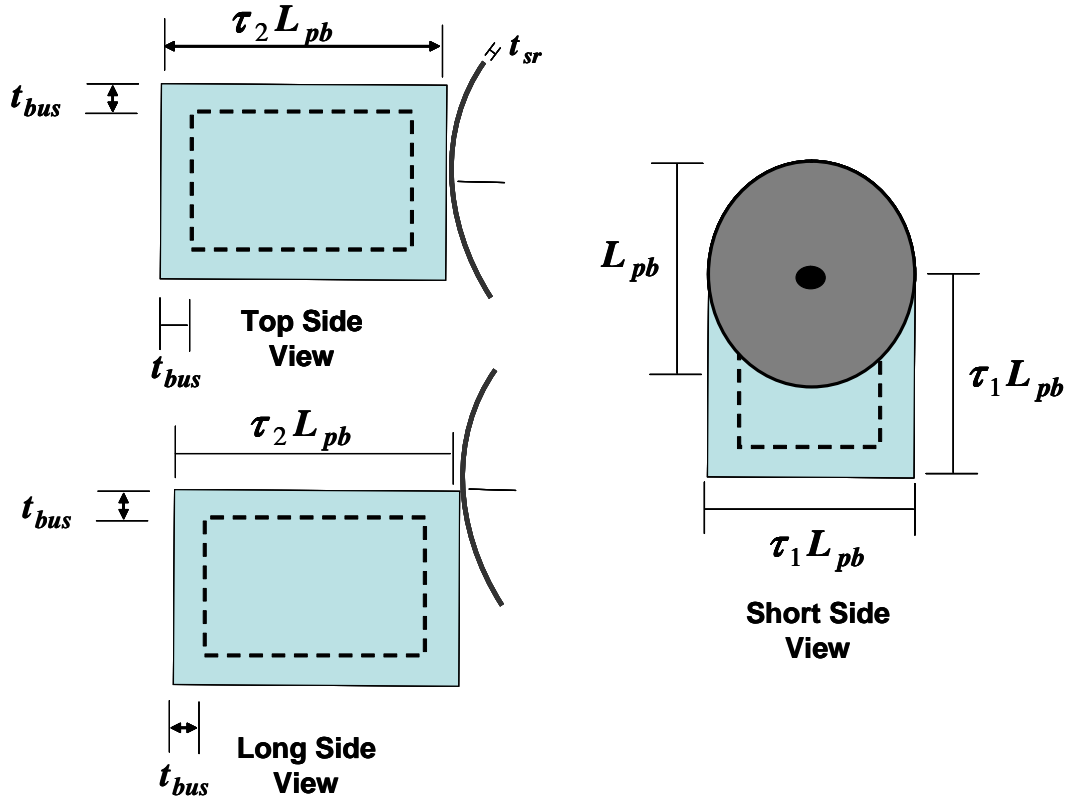


Figure 3.8: Spotlight SAR Mechanical Dimensions

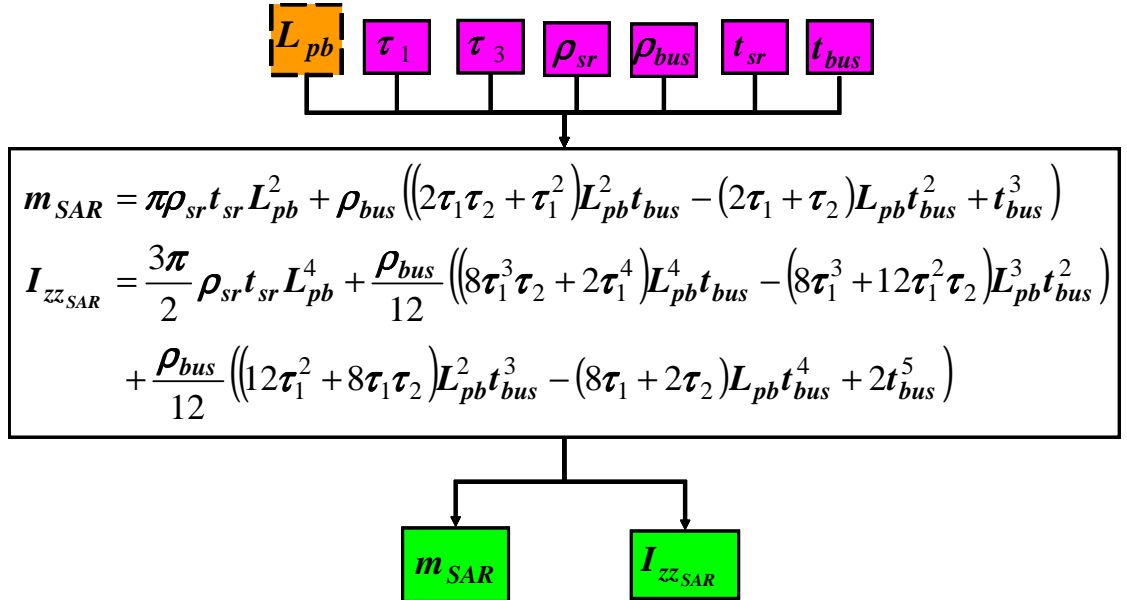


Figure 3.9: Spotlight SAR System Mass and Inertia Calculations

$$m_{SAR} = m_{sr} + m_{bus} \quad (3.42)$$

$$m_{sr} = \pi \rho_{sr} t_{sr} L_{pb}^2 \quad (3.43)$$

$$m_{bus} = \rho_{bus} \left((2\tau_1 \tau_2 + \tau_1^2) L_{pb}^2 t_{bus} - (2\tau_1 + \tau + 2) L_{pb} t_{bus}^2 + t_{bus}^3 \right) \quad (3.44)$$

$$I_{zz_{SAR}} = I'_{zz_{sr}} + I_{zz_{bus}} \quad (3.45)$$

$$I'_{zz_{sr}} = I_{zz_{sr}} + m_{sr} d_{sr}^2 \quad (3.46)$$

$$d_{sr}^2 = L_{pb}^2 \quad (3.47)$$

$$I'_{zz_{sr}} = \frac{3\pi}{2} \rho_{sr} t_{sr} L_{pb}^4 \quad (3.48)$$

$$I_{zz_{bus}} = \frac{\rho_{bus}}{12} \left((8\tau_1^3 \tau_2 + 2\tau_1^4) L_{pb}^4 t_{bus} - (8\tau_1^3 + 12\tau_1^2 \tau_2) L_{pb}^3 t_{bus}^2 \right) \quad (3.49)$$

$$+ \frac{\rho_{bus}}{12} \left((12\tau_1^2 + 8\tau_1^2 \tau_2) L_{pb}^2 t_{bus}^3 - (8\tau_1 + 2\tau_2) L_{pb} t_{bus}^4 + t_{bus}^5 \right) \quad (3.50)$$

Thus, the equations and processes for mission geometry, mass/inertia sizing, and link budgeting drive the attitude, power, and mass requirements. In addition, these processes yield the parabolic reflector diameter, spotlight SAR azimuth and range resolution, synthetic array size, ground swath, and pulse repetition frequency. By developing/summarizing these process, one can capture the driving requirements behind a spotlight SAR mission which will govern the ESACS design in the subsequent chapters of this thesis.

3.3 Synthetic Aperture Radar Requirements

Having addressed the required calculations to size a spotlight SAR system, a representative example is in order to tie the spotlight SAR requirements to the overall VSCMG-based ESACS requirements. Here, the mission collection geometry is first selected followed by assumptions about the parabolic reflector size, the link characteristics, and the spacecraft bus dimensions/materials. Then design factors/parameters are set and combined with additional spacecraft bus assumptions yielding a set of representative mission design requirements.

In terms of the collection geometry, a 450 km near circular, equatorial, retrograde orbit is chosen with a 70 s dwell time over the target. The altitude choice is a compromise between reduced link power the closer the satellite is to the surface whilst too small of an altitude reduces mission life due to atmospheric drag. The circular orbit is assumed to keep the altitude near constant for target collection. Although orbital perturbations and the Earth's oblateness preclude achieving a perfectly circular orbit (especially in the absence of an on-orbit

maneuvering propulsion system), near circular (i.e. lower eccentricity) orbits are possible. Also, a circular mission orbit reduces equation complexity in the first order mission scenario analysis accomplished here. Next, the equatorial, retrograde orbit is assumed as a worst case scenario as orbital-to-target ground distance differential is greatest. The maximum target velocity with respect to the Earth's surface is assumed at 0.25 km/s in the anti-along-track direction. Another geometric assumption is that the roll angle varies between 20 and 45 degrees while the pitch rate is controlled to keep the unrolled yaw axis perpendicular to the ground (i.e. nadir tracking). Also, the satellite is slewed about the yaw-axis to keep the spotlight on an acquired target. Each spotlight itself is assumed to have a 10 km ground swath width. In terms of the spotlight SAR transmitter link budget and parabolic reflector design, the assumed bandwidth, b_w , signal-to-noise ratio, SNR, antenna noise temperature, T_n , antenna wavelength, λ , target cross section, σ are 10 MHz, 2, 300 K, 1 cm, and 1 dB, respectively. Then, the spacecraft and SAR parabolic reflector materials and thickness are chosen as Aluminium ($2700\text{kg}/\text{m}^3$) with 0.03 m for the spacecraft bus and Graphite Epoxy composite ($1600\text{kg}/\text{m}^3$) with 0.02 m for the SAR reflector. These assumed values are then combined with a few spotlight SAR design factors to capture the mission design. These factors are k_1 , k_a , k_r , f_a , α' , f_{oth} , and l which were set to 1.2, 1.0, 1.0, 0.80, 3 dB, 10%, and 3 dB, respectively.

Using these assumptions and design factors, the resulting attitude maneuver parameters call for a 140 deg slew in 70 s. This is supplemented with a 12 s dead-band to showcase a more realistic bang-of-bang maneuver as the system will level off for a short duration before initiating the stopping torque. More about this maneuver for sizing is addressed later in the thesis. Nevertheless, in sizing the spotlight SAR system, a synthetic aperture length was found to be 16.65 km with azimuth resolution of 0.3 cm, and range resolution of 43.9 m. The pulse repetition frequency was calculated as 20.5 kHz. Then, the other primary outputs of the SAR reflector sizing process are a peak power demand of 1100 W, a major axis inertia of 120 kgm^2 , and 400 kg mass. The latter of these comes from adding the total subsystem power (e.g. for attitude control, data handling, communications, thermal control, etc.) of 100 W, which is consistent with other SSTL satellites [8, 9], to 1000 W calculated from the SAR reflector sizing process captured in Figure 3.6, which combines the Radar transmitter power at 832 W plus 10% (or 83.2 W) allocated for running the SAR support systems plus 84W for Spotlight SAR power margin. Also, the spacecraft is assumed to have a (fairly standard) bus voltage of 28 V, ESACS depth-of-discharge of 80 % and transmission efficiency of 90 %

(values often assumed in the literature, see Chapter 2). The SAR is assumed to have a duty cycle of 10 % to push technology (typical SAR values are in the neighborhood of 2 % for a small satellite such as AstroSAR [138, 145], so the 10 % value is an objective rather than a threshold). Meanwhile, the Radar antenna diameter was found as 0.54 m which is reasonable for a small satellite. The 120kgm^2 inertia value and 400kg mass are a direct result of the SAR reflector and bus materials and dimensions along with the all important parabolic reflector diameter, L_{pb} . Note that the mission assumes a launch vehicle will allow a per satellite mass limit of 450 kg yielding an overall spacecraft mass margin of 50 kg. It is also assumed as done for previous SSTL small satellite missions that the basic attitude and energy storage subsystems will be about 10 % of the total spacecraft mass [146], which means that the 450 kg requirement translates to a required attitude plus energy subsystem mass of 45 kg.

Applying these spotlight SAR design processes with the assumed values just discussed yields the requirements given in Table 3.1. These requirements drive the ESACS design described throughout the remainder of the thesis.

Table 3.1: Spotlight Synthetic Aperture Radar Requirements

Parameter	Value
Orbit Altitude, h , km	450
Depth-of-Discharge, dod , %	80
Transmission Efficiency, x_{msn} , %	90
Peak Power Demand, P_r , W	1100
Eclipse Duty Cycle, d_{ty} , %	10
Power Bus Voltage, V_{bus} , V	28
Max Single-axis inertia, $I_{T_{max}}$, kg m ²	120
Slew maneuver angle, θ_f , deg	140
Slew maneuver time, t_f , s	70
Slew maneuver dead-band, t_{off} , s	12
Satellite Total Mass, M_{sc} , kg	400
Allowable Satellite Mass, M_{ta} , kg	450
Allowable ACS plus ES Mass, M_r , kg	45

3.4 Power and Attitude Profiles

The preceding discussion focused on static performance requirements which will be translated to the ESACS system for sizing its components. However, when the ESACS is implemented, its dynamic performance is of great value to the designer as well. In that case, the reference open-loop power profile and the reference closed-loop attitude profile help drive the design of the controlled system response. Example profiles are given in Figure 5.1. Here, one can see

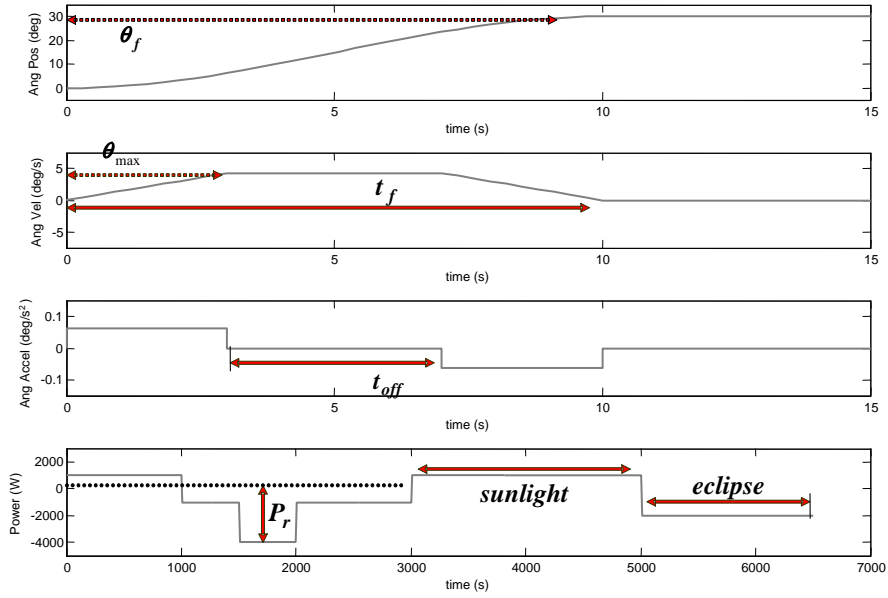


Figure 3.10: Bang-off-Bang Attitude Reference Maneuver and Power Profile

the key extremity values used for sizing the system (that is, the maneuver angle, θ_f , maneuver time, t_f , dead-band, t_{off} , and required instantaneous peak power, P_r) which will be applied in Chapter 5. However, the waveforms of the reference also drive how well the selected control laws and steering laws (defined further in Chapters 4 and 6) perform. As this will be defined in more detail later, suffice it here to mention that the spacecraft attitude angle over time can be thought of as a single-axis maneuver angle (or for a three-axis maneuver, relates to an Euler angle representation as defined later) which changes as the spacecraft travels in orbit. Profiles which transition the spacecraft from a rest attitude to another rest attitude (rest being that there is no angular velocity with respect to a sufficiently inertial reference frame)

usually exhibit a smooth s-curve whereas sinusoidal motion has the inertial attitude change over time in a sinusoid. Both approaches can be used (along with other curve shapes) to test the capabilities of the system. Each has its own advantages. In realistic system sizing, the worst-case attitude profile of the spotlight SAR system (by assumption) is driven by the ability to track a target while pitching to maintaining the unrolled yaw axis perpendicular to the ground, rolling to maintain adequate cross-track/range resolution, and yawing in the azimuth direction ahead of the satellite's ground trace at initial contact then slewing in yaw to maintain the target until losing contact to the target behind the spacecraft's ground trace. Note that the Earth's velocity further compounds the problem. Here, the limiting target-tracking case occurs when the satellite travels due west equatorially (retrograde) and the target moves due east with respect to the ground. Geometry for this scenario is included in Figure 3.1. This assumes a smooth rotation at the highest rate (2 deg/s in the case of the defined example). Note that future high power systems with rapid slewing may involve several transitions to multiple targets. At this stage, such requirements are beyond the scope of this thesis, but within the realm of logical follow-on work.

Meanwhile, the power profiles usually involve positive values during charging (i.e. when the system wheels speed up) and negative values during discharge to run the spacecraft subsystems. These negative values drop much further when the payload (in the example of this chapter, this payload is the spotlight SAR system) is operated in eclipse. One should note that in the thesis, the power profile can be thought of in terms of the required peak power P_r over time with its maximum value occurring during payload draw. That P_r along with its duty cycle, d_{ty} , drive the ESACS sizing. However, other power profiles can also be implemented to test the ESACS. In the steering law chapter (Chapter 6), these profiles have a large effect as the shape is as important as the peak values. In these cases, the same basic form of the power profile shown here are applied, but the values are for larger satellites. This consideration in that chapter allows the results to be compared to existing literature (using that literature as benchmark data), for example the results of Yoon in [109,110], Shen in [59,60], and Richie in [12,107,108].

Here it is important to note that while all these works use rectangular-shaped power profiles, the attitude profiles vary greatly. In Shen and Richie's work, the idea is that one axis of the spacecraft is kept perpendicular to the sun (i.e. an axis drawn from the spacecraft center of mass to the sun) as much as possible with the other axis pointed to a selected ground station location on the Earth even if the ground station is not in view. On the other hand,

Yoon implemented profiles set so that the quaternion representation of the attitude has four parameters that change sinusoidally over time. This latter profile works to keep the satellite rotating an even amount whereas more practical implementations involve long periods of slow rotation with a few periods of rapid slewing activity. The former profile is more like that of the spotlight SAR or TDI mission maneuvers, but Yoon's approach is better for sizing since it fully taxes the attitude system while tracking the desired power profile.

These two attitude profile approaches actually lead to one approach beyond the scope of the current thesis that is of interest in follow-on work: having a rapid slewing mission (like that used in spotlight SAR or TDI maneuvers) during payload operation, but generic scanning following the quaternion sinusoidal profile while the primary payload is off (or perhaps is kept running in a low energy mode with limited data collected for queueing a primary Radar collection). Or, perhaps there is an optimal Euler attitude/nadir tracking configuration that the spacecraft always returns to in-between data collections, making it better able to re-orient when a new ground target arises. In fact, if the system were to return to an advantageous sun-bathing mode, it would keep the solar panels perpendicular to the sun vector to maximize power generation – an important consideration for low-cost, small satellite SAR. This is as opposed to leaving the satellite in the ending inertial orientation after image collection. These considerations add further requirements to the ESACS system and will greatly test its merit in such future work.

3.5 Mission Scenarios Requirements Summary

Understanding the genesis of these mission requirements allows the designer to assess the ramifications of modifying one of these values during the design and test stages. As one can see, one change to a mission parameter through the several processes defined here could lead to several impacts in sizing the ESACS. It is imperative that the ESACS designer ensures the mission developer clearly defines the requirements as the ripple effects on the ESACS design can be great. Nevertheless, having defined and derived the static and dynamic mission requirements for ESACS, it is now necessary to develop the fundamental principles to ESACS design before optimally sizing the VSCMGs and constructing actuator steering algorithms. Then, the basic concepts can be tested in the laboratory for a system built on the mission requirements developed here.

Chapter 4

Attitude Control and Energy Storage Fundamentals

In this Chapter, the fundamentals behind the satellite attitude control subsystem (ACS) and the electrical power subsystem (EPS) including its energy storage (ES) function are presented. Concepts behind sizing these subsystems for a conventional mission are presented. In addition, these concepts are demonstrated through a numeric example by building on the requirements from Chapter 3.

4.1 Attitude Control Subsystem

The attitude control subsystem (ACS) aims to point the spacecraft in the proper rotational direction based on input from the attitude determination subsystem (ADS) which may be combined with it into a common subsystem known as the attitude determination and control subsystem (ADCS). The requirements for the ACS flow directly from the mission-level pointing requirements (e.g. “the ACS shall slew the satellite 30 degrees in 10 seconds” as stated in the defined attitude reference maneuver), but may also include derived requirements from the mission or from other subsystems’ requirements (e.g. “the ACS shall point the apogee kick motor (of the propulsion subsystem) within 0.5 degrees of its desired direction within 10 seconds of a given command”).

A typical closed loop satellite ADCS is functionally captured by the block diagram of Figure 4.1. The underlying feature of such a closed loop system is that the system uses feedback from

sensors to help correct errors between the system output and the reference input. The primary components shown in this block diagram are the attitude reference position/orientation (e.g. a commanded attitude profile or reference maneuver), the feedback attitude sensors and attitude determination algorithms which form the ADS, the attitude controller programmed to follow a vehicle control law/algorithm that acts to ensure the vehicle’s measured orientation follows the reference orientation, the actuators which take controller input signals and convert them to output physical motion, and the satellite’s governing physical response to changing spacecraft torques (disturbance plus control torque) also known as the plant. When evaluating the response of the spacecraft to different inputs, these key blocks are often modelled to differing degrees of detail including open loop models or profiles and closed loop or nested control loops within the main ADCS loop.

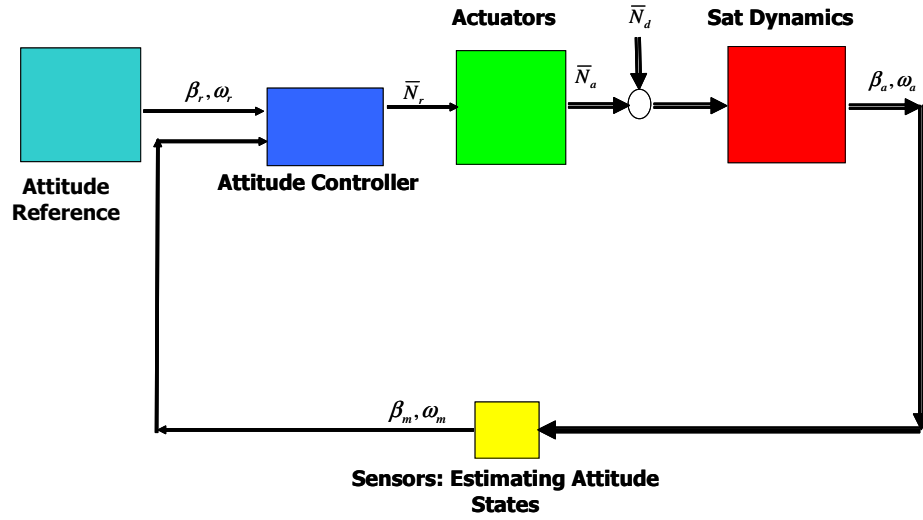


Figure 4.1: Block Diagram for Conventional Attitude Control Subsystem

As depicted in Figure 4.1, not only does the ACS need to point the spacecraft in the desired direction, but also it needs to overcome attitude disturbance torques relevant to the given orbit. These torques typically include aerodynamic drag (especially relevant in low earth orbit(LEO)), gravity gradient torque, magnetic torque from Earth’s magnetic field interacting with the spacecraft’s dipole, and solar radiation pressure torque [114]. These torques can arise cyclically, secularly, or as a combination of both.

Combined, the slewing performance, attitude maintenance, and disturbance rejection are the key elements leading to the ACS’ torque capability, sometimes referred to as the “control authority” [114]. This capability directly drives the sizing process for the selected attitude

actuators as well as dictates the dynamic control algorithms used for the spacecraft. As half of the design challenge for a small satellite ESACS relies on properly sizing and applying the attitude control actuators selected (e.g. momentum wheels or VSCMGs), determining this control authority from the given mission requirements is critical to achieving mission success, defined as achieving the derived ACS requirements. To best capture this control authority, then, the remainder of this section addresses calculating the typical disturbance torques in LEO, the process for sizing the VSCMG actuators from the mission requirements, basic dynamic attitude tracking using VSCMGs (i.e. the applicable kinematics and dynamics equations governing the necessary control algorithms), and a common challenge inherent to developing CMG control algorithms – momentum singularities incurred in a CMG configuration.

4.1.1 Disturbance Torques in Low Earth Orbit

As implied thus far, rejecting disturbance torques for a given orbit contribute to the satellite's ACS design. In the VSCMG ESACS sizing process, it is important to understand and quantify these effects from the given requirements. The four primary disturbance torques mentioned will be further discussed following the approach found on p. 366 of ref. [114].

4.1.1.1 Gravity Gradient

In earth orbit, a spacecraft has the tendency to align itself with the earth's gravitational field. The ensuing rotational twist from this tendency is known as the gravity gradient torque. As mentioned in [114], this vector quantity can be calculated as

$$\mathbf{N}_{gg} = \left(\frac{3\mu}{(R_e + h)^3} \right) (\hat{\mathbf{r}} \times (\underline{\underline{\mathbf{I}}} \cdot \hat{\mathbf{r}})) \quad (4.1)$$

where R_e is the earth's radius, h is the orbital altitude, μ is the earth's gravitational parameter, $\hat{\mathbf{r}}$ is the nadir unit vector, and $\underline{\underline{\mathbf{I}}}$ is the spacecraft inertia tensor. As further presented in [114], estimating the worst case gravity gradient torque for a spacecraft can be accomplished using the maximum and minimum principle axis inertia scalars, I_{T_x} and I_{T_n} , respectively, the maximum deviation of the spacecraft's major axis with the local vertical, θ_{gg} , and the values mentioned in eq. 4.1, to form the scalar magnitude

$$N_{gg} = \frac{3\mu}{2(R_e + h)^3} |I_{T_x} - I_{T_n}| \sin(2\theta_{gg}) \quad (4.2)$$

As one can see, the magnitude of this torque decreases cubically with orbital altitude and depends on the major-minor axis numerical spread as well as the orientation of the major axis.

4.1.1.2 Earth's Magnetic Field

Similarly to the gravity gradient torque, orbital spacecraft will often seek to align themselves in the Earth's magnetic field, \mathbf{B} , based on the spacecraft's magnetic dipole, \mathbf{D} . This, too, as presented in [114], is generically defined by a vector equation in and simplified with a scalar magnitude, this time through eqs. 4.4 and 4.3.

$$\mathbf{N}_{MT} = \mathbf{D} \times \mathbf{B} \quad (4.3)$$

$$N_{MT} = DB \quad (4.4)$$

where B is the magnitude of the field, \mathbf{B} , and D is the magnitude of the dipole \mathbf{D} .

4.1.1.3 Solar Radiation Pressure

Another disturbance torque routinely affecting satellites in LEO is that of solar radiation pressure (SRP) torque. Vector and scalar equations for SRP are given in eqs. 4.5 and 4.6

$$\mathbf{N}_{SR} = K_s (\mathbf{u}_s \cdot \mathbf{u}_n) A_s \left[(\alpha + r_d) \mathbf{u}_s + \left(2r_s + \frac{2}{3}r_d \right) \mathbf{u}_n \right] \times \mathbf{s}_c \quad (4.5)$$

where K_s is the solar pressure constant, 4.644×10^{-6} N/m², A_s is the cross-sectional area of the largest (most conservative) facet of the spacecraft, \mathbf{u}_s is a unit vector in the direction toward the sun, \mathbf{u}_n is a unit vector normal to facet area A_s , \mathbf{s}_c is a vector from the spacecraft mass center to the geometric center of area A_s , α is the surface A_s absorptivity coefficient, r_s is surface area A_s specular reflectance coefficient, and r_d is the surface area A_s diffuse reflectance coefficient. Also note that $\alpha + r_s + r_d = 1$. It is important to mention that this torque can be calculated for different spacecraft appendages and components that extend from the spacecraft and are in direct sunlight. Typically, conventional solar radiation pressure torque is largest on the solar panels. Therefore, the SRP vector equation from 4.5 is refined for the scalar version based of this torque as defined in eq. 4.6

$$N_{SP} = \frac{F_s}{c} A_s (1 + q) \cos i (c_{ps} - c_g) \quad (4.6)$$

where A_s is defined as before, F_s is the solar constant, 1367 W/m², c is the speed of light, 3×10^8 m/s, q is the reflectance factor ranging from 0 to 1.0, i is the angle of incidence of the

sun, c_{p_s} is the location of the center of pressure for facet A_s , and c_g is the center of spacecraft center of gravity. One can see from this that the center of pressure/center of gravity difference has a significant effect on the solar radiation pressure torque.

4.1.1.4 Aerodynamic Drag

Finally, Aerodynamic Drag, which acts on the surface of spacecraft quite similarly to solar radiation pressure torque, is also governed by the proximity of the satellite to the Earth's gravitational center. Defining vector and scalar equations to find the aerodynamic drag disturbance torque in eqs. 4.7 and 4.8 yields

$$\mathbf{N}_{AD} = \frac{1}{2} \rho C_d A_s v^2 (\mathbf{u}_v \times \mathbf{s}_{c_p}) \quad (4.7)$$

$$N_{AD} = \frac{1}{2} \rho C_d A_s v^2 (c_{p_a} - c_g) \quad (4.8)$$

where A_s and c_g are as before, c_{p_a} is the center of aerodynamic pressure for facet A_s , \mathbf{u}_v is a unit vector in the spacecraft velocity direction, \mathbf{s}_{c_p} is a vector from the center of spacecraft mass center to the center of pressure of facet A_s , C_d is the drag coefficient for facet A_s , ρ is the air density, and v is the spacecraft velocity magnitude. Note that the air drag is larger in the lower LEO altitudes and drops off with the atmospheric density drop off as altitude increases.

4.1.1.5 Designing the Largest Spacecraft Facet

As one can grasp from the disturbance torques presented, the area of a spacecraft side facet is an important quantity. So, before attacking a numerical disturbance torque example, it is important one determine the area of one side (or in this case, one wing) of the spacecraft. This is done by examining the solar panel design process, which drives the facet design as the primary power production source is normally solar power. The resulting solar panels can potentially fill a large area with solar cells to provide the required sunlight and storage power during orbital daylight. The chosen solar array must provide the amount of power defined in eq. 4.9

$$P_{sar} = \frac{\frac{P_{r_d}}{X_d} + \frac{P_{r_e}}{X_e}}{T_d} \quad (4.9)$$

where it assumed that the instantaneous peak power requirements of eclipse and daylight are identical and found as $P_{r_d} = P_{r_e} = d_{ty_{pl}} P_{r_{pl}} + d_{ty_{subs}} P_{r_{subs}}$, T_e and T_d are the eclipse

and daylight durations per orbit, X_d is the daylight transmission efficiency, and X_e is the round-trip transmission efficiency from daylight storage to usage in eclipse. In contrast, the solar panel power achievable is given as eq. 4.10:

$$P_{sa_a} = A_t F_s \eta_{sp} \cos i \quad (4.10)$$

where F_s and i are as defined earlier, A_t is the total area of all facets in the sunlight at one time, and η_{sp} is the solar cell conversion efficiency of the implemented solar cells. Finally, the solar array margin, P_{sa_m} , is given as

$$P_{sa_m} = P_{sa_a} - P_{sa_r} \quad (4.11)$$

where $P_{sa_m} \geq 0$ ensures that the designed solar panel system meets the given requirements. At this stage, the goal is to find the area of one facet, A_s , which for the two wing sun-tracking solar panels assumed for this design keeps the area of one facet as small as possible (due to the magnitude of instantaneous peak power of the payload, sun tracking arrays will keep costs under control without wasting 2/3 of side panel area as body-mounted panels usually do). For the wing design, then,

$$A_s = \frac{1}{2} A_t \quad (4.12)$$

Assuming the solar arrays are designed to match the requirements, thus, $P_{sa_m} = 0$, one finds that $P_{sa_a} = P_{sa_r}$. By using this fact and rearranging eqs. 4.9 and 4.10, yields the following equation for A_t

$$A_t = \frac{\left(\frac{P_{r_d}}{X_d} + \frac{P_{r_e}}{X_e} \right)}{T_d F_s \eta_{sp} \cos i} \quad (4.13)$$

Using eq. 4.12, one can find A_s from A_t , completing the desired design.

4.1.1.6 Numerical Example

Having defined several common disturbance torques for small satellite earth orbits, these definitions are best understood in light of an example. This example uses the mission requirements defined in Chapter 3 whilst adding a few more parameters necessary to evaluate the most conservative conditions. Using the parameters given in Table 4.1 as inputs and following eqs. 4.13, 4.12, 4.2, 4.4, 4.6, and 4.8, leads to the torques listed in Table 4.2. Note that the values used in Table 4.1 focus on generating and reporting the worst case (most

Table 4.1: Disturbance Torque Inputs

Parameter	Value
Daylight Payload Duty Cycle, $d_{ty_{pl}}$, %	25
Daylight Subsystem Duty Cycle, $d_{ty_{subs}}$, %	100
Eclipse Payload Duty Cycle, d_{ty} , %	25
Eclipse Subsystem Duty Cycle, d_{ty} , %	100
Payload Peak Power Demand, $P_{r_{pl}}$, W	1000
Subsystem Peak Power Demand, $P_{r_{subs}}$, W	100
Solar Cell Efficiency, η_{sp} , %	7
Round-trip Transmission Efficiency, X_e , %	60
Daylight Transmission Efficiency, X_d , %	80
Solar Incidence Angle, i , deg	0
Solar Cell Degradation, d , % per yr	5
Planned Lifetime, L_t , yrs	5
Maximum Single-axis Inertia, $I_{T_{max}}$, kg m ²	120
Minimum Single-axis Inertia, $I_{T_{min}}$, kg m ²	30
Orbit Altitude, h , km	450
Maximum Major Axis-Local Vertical Deviation, θ_{gg} , deg	45
Satellite Worst Case Magnetic Dipole, D , Am ²	10
Earth's Magnetic Field at the Poles, $M_{e_{polar}}$, tesla	7.96E15
Solar Panel Center of Pressure, c_{ps} , m	0
Aerodynamic Facet Center of Pressure, c_{ps} , m	0
Center of Gravity Projected to Largest Facet, c_g , m	0.5
Solar Array Margin, P_{sa_m} , W	0
Facet Reflectance Factor, q	1.0
Atmospheric Density at Orbital Altitude, ρ	3.61E-12
Aerodynamic Drag Coefficient of Largest Facet, c_d	2.5

Table 4.2: Disturbance Torque Outputs

Parameter	Value
Solar Array Power, $P_{sa_r} = P_{sa_a}$, W	800.82
Required Attitude Maneuver Torque, N_r , Nm	0.24661
Gravity Gradient Torque, N_{gg} , Nm	0.00017
Magnetic Field Torque, N_{mt} , Nm	0.00050
Solar Pressure Torque, N_{sp} , Nm	0.00003
Aerodynamic Drag Torque, N_{ad} , Nm	0.00071

conservative) values in the ensuing disturbances. Several of the listed values are assumed such that each torque is at its realistic maximum for the given orbit. From this, one can analyze these torques in contrast with the required torque for the given maneuver, both of which are listed in Table 4.2. An initial glance reveals that the required torque for the given maneuver is three orders of magnitude larger than the calculated disturbance torques for this design. Thus, the attitude control system will be sized more to meet this maneuver since the disturbance rejection barely affects the required sizing torque. If, however, one were to alter the requirements for the payload duty cycle in eclipse (e.g. change it from 5% to 100%), he or she would find that the magnetic and gravity gradient torques remain the same, but the torques dependent upon facet size, aerodynamic drag and solar radiation pressure, increase by more than threefold, to 7.745×10^{-5} Nm and 0.00224 Nm, respectively. The latter of these is enough to slightly modify the torque requirement stemming from the desired reference maneuver, but is still 2 orders of magnitude smaller. Therefore, the anticipated disturbance torques in the given orbit have little effect on the total required sizing torque. Hence, these effects are ignored in light of the reference maneuver. Nevertheless, due to its magnitude, designing the ACS to meet the given reference maneuver is addressed next in more depth.

4.1.2 Sizing Conventional Attitude Control Systems

Designing the system to meet the required maneuver defined in Chapter 3 involves ensuring a design margin comprised of the difference between the actual torque capability of the designed system, N_a , and the required maneuver torque, N_r , is greater than or equal to 0. The process associated with this key idea as it applies to sizing conventional momentum wheels is given in Figure 4.2. Note that the subscript b is added to the attitude margin to signify the determined system is a conventional baseline system for which the VSCMG actuators will be compared in Chapter 5. The process can be summarized by three key equations: the required torque, actuated torque, and baseline torque design margin, N_{mb} . The latter of these uses a simple equation similar to other margins defined thus far, $N_{mb} = N_a - N_r$. Then, the equation for the required torque is found from the assumed spacecraft major axis inertia, I_{T_x} , the characteristic maneuver angle, θ_f , the total maneuver time, t_f , and the slewing dead-band, t_{off} . On the other hand, the actuated torque uses the product of the wheel spin axis inertia,

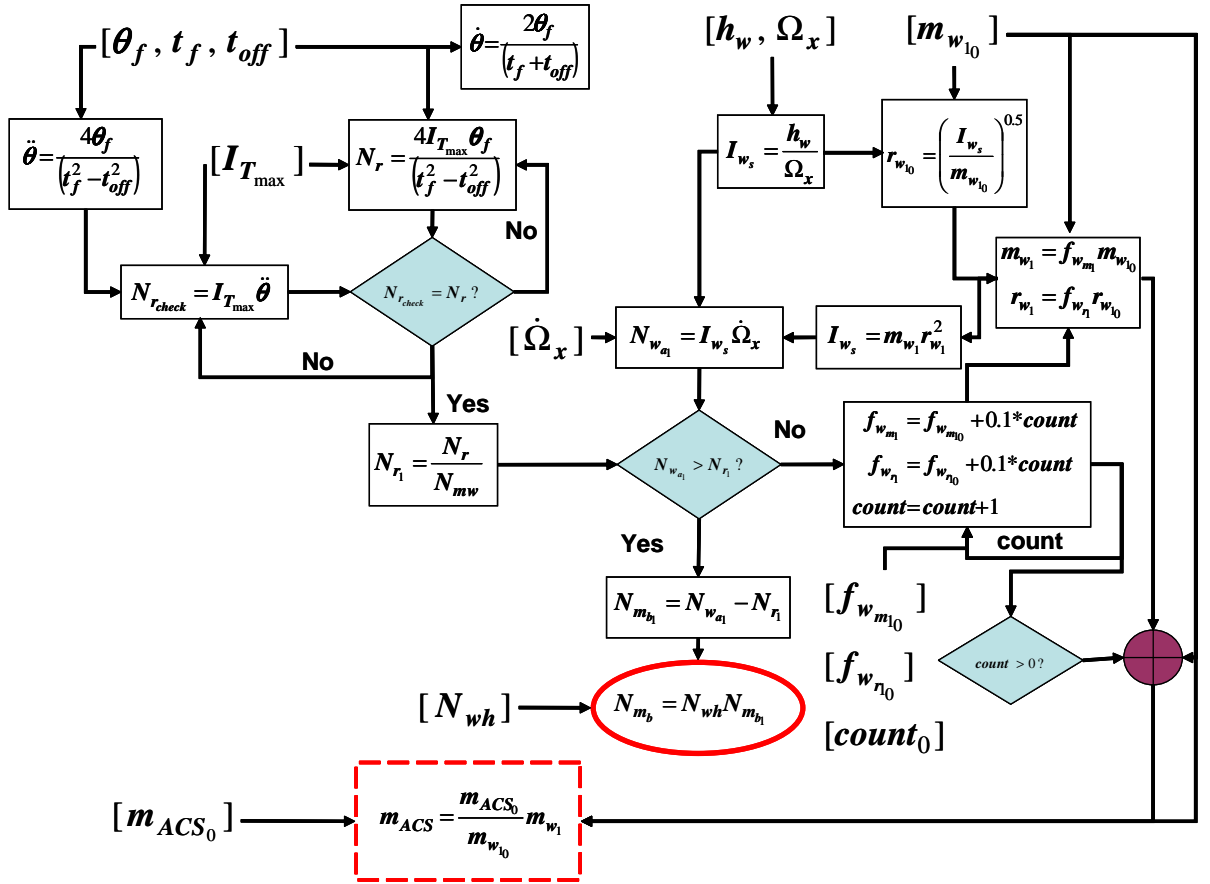


Figure 4.2: Conventional Attitude Control Subsystem Sizing Process

I_{w_s} , and the maximum wheel acceleration, $\dot{\Omega}_x$. The equations for N_r and N_a are given below

$$N_r = \frac{4I_{T_x}\theta_f}{t_f^2 - t_{off}^2} \quad (4.14)$$

$$N_a = I_{w_s}\dot{\Omega}_x \quad (4.15)$$

Note that the desired maneuver parameters, I_{T_x} , θ_f , t_f , and t_{off} come from mission requirements, while I_{w_s} is scaled from the recent Bilsat-1 mission's (part of the SSTL Disaster Monitoring Constellation) ACS mass. The acceleration capability, $\dot{\Omega}_x$, follows from studying the published SSTL micro-satellite momentum wheel data sheet included in [13]. Since the particular wheel one uses may not be well suited to meet the input requirements, steps are included in this process to adjust the inertia (and therefore wheel and ACS mass) to meet required torque. That is, negative margin is unacceptable, so in such a case, the wheel radius and mass scaling factors from the Bilsat design, $f_{w_{m_1}}$ and $f_{w_{r_1}}$, are adjusted if N_{m_b} is less than 0. After iterating mass and radius to get the design margin greater than or equal to zero, the ultimate baseline torque margin is the first feasible value for N_{m_b} using this process.

To help illustrate the idea in this sizing approach, an example is presented using the mission requirements defined in Chapter 3. The defined maneuver calls for a 140 deg slew in 70 s with a 12 s dead-band for a spacecraft with largest principle axis inertia of 120 kgm². These values lead to a required cluster torque of 0.2466 Nm, or a per wheel required torque of 0.0617 Nm.

In contrast, a maximum momentum wheel speed of 5000 RPM and maximum acceleration of 25 rad/s² are found from the actual wheel specifications. More specifically, using the given micro-satellite momentum of h_w , one can substitute the speed into the equation $h_w = I_{w_s}\Omega$ to determine the wheel has an original spin-axis inertia of $I_{w_s} = 0.0008$ kgm². The resulting actuated wheel torque for one wheel is $N_{w_{a_1}} = 0.0201$ Nm. Using these sizing results (which assume a 1 to 1 scaling from Bilsat) yields a baseline torque margin of $N_{m_b} = -0.0416$ Nm. This is an infeasible value. For this reason, the initial sizing factors for wheel radius and mass are implemented as 2.6 each. Taking the per wheel size from Bilsat of 1.21 kg with determined radius of $r_w = 0.0257$ m that equates to the given I_{w_s} , and applying this 2.6 factor equates to $r_w = 0.0669$ m, $m_w = 3.1460$ kg, and $N_{w_{a_1}} = 0.352$ Nm. This latter value gives an N_{m_b} of 1.1632 Nm. As the momentum wheel cluster contains 4 wheels, multiplying m_{w_1} by 4 yields an ACS mass of 17.238 kg. N_{m_b} is then used as basis for comparing the VSCMG cluster design in terms of torque, whilst the other baseline values are addressed in the energy storage section of this chapter.

4.1.3 Attitude Tracking Using VSCMGs

As shown in [12] and derived in Appendix D, a model encompassing the spacecraft dynamics, kinematics, required attitude reference torque, and VSCMG attitude steering is

$$\overline{\mathbf{N}}_d = \mathbf{I}_T \dot{\omega} + \tilde{\omega} \mathbf{I}_T \omega + \mathbf{B} \ddot{\delta} + \mathbf{E} \dot{\Omega} + \mathbf{D} \dot{\delta} + \mathbf{F} \Omega \quad (4.16)$$

$$\dot{\beta} = \frac{1}{2} q(\beta) \omega \quad (4.17)$$

$$\overline{\mathbf{N}}_r = \mathbf{K}(\omega - \omega_r) - k q^T(\beta) \beta_r - \tilde{\omega} \mathbf{I}_{sc} \omega \quad (4.18)$$

$$q(\beta) = \begin{bmatrix} -\beta_1 & -\beta_2 & -\beta_3 \\ \beta_0 & -\beta_3 & \beta_2 \\ \beta_3 & \beta_0 & -\beta_1 \\ -\beta_2 & \beta_1 & \beta_0 \end{bmatrix} \quad (4.19)$$

$$\overline{\mathbf{N}}_r + \overline{\mathbf{N}}_d = \mathbf{B} \ddot{\delta} + \mathbf{E} \dot{\Omega} + \mathbf{D} \dot{\delta} + \mathbf{F} \Omega \quad (4.20)$$

where $\overline{\mathbf{N}}_d$ is the inertial torque acting on the combined system of the spacecraft platform plus the VSCMGs, \mathbf{I}_T is the system inertia assuming the gimballed VSCMG inertia (from rotor dynamics) is negligible, β is the Euler parameter set $(\beta_0, \beta_1, \beta_2, \beta_3)$ representing the satellite body frame orientation with respect to the inertial frame, ω is the angular velocity of the body frame with respect to the inertial frame expressed in body frame coordinates, $\dot{\beta}$ and $\dot{\omega}$ are the body frame time derivatives of β and ω , β_r and ω_r are command reference versions of β and ω , δ is an $n \times 1$ column matrix of n -VSCMG gimbal angles, $\dot{\delta}$ and $\ddot{\delta}$ are $n \times 1$ gimbal angular velocity and angular acceleration column matrices, $\tilde{\omega}$ is a 3×3 skew-symmetric matrix using the elements of ω ; \mathbf{B} , \mathbf{D} , \mathbf{E} , \mathbf{F} are $3 \times n$ matrices transforming actuator parameters from the gimbal coordinate frame to the body frame where \mathbf{B} is a function of δ and is constant in the body frame, \mathbf{D} depends on ω , δ , and Ω , varies in the body frame, and is approximated as its wheel angular momenta component, \mathbf{E} transfers the wheel acceleration to the body frame and is dependent upon the gimbal angles, and \mathbf{F} depends on the gimbal angles and body angular velocity ω and is equivalent to the $\tilde{\omega} h$ defined in [110, 147]. \mathbf{I}_{ws_d} is a $n \times n$ diagonal matrix of VSCMG wheel spin-axis inertias. Finally, k is a positive gain scalar, \mathbf{K} is a 3×3 positive definite gain matrix, and $\overline{\mathbf{N}}_r$, which uses k and \mathbf{K} , is the required torque for stable spacecraft attitude tracking.

Noted often in the literature (e.g. [12, 75]), CMGs typically exploit torque amplification properties through gimbal rate control (i.e keeping gimbal motor torques small such that $\ddot{\delta} \approx 0$). The result is a velocity-based steering law to replace eq. 4.20 (assuming no external

torques are applied)

$$\mathbf{E}\dot{\boldsymbol{\Omega}} + \mathbf{D}\dot{\boldsymbol{\delta}} = \overline{\mathbf{N}}_r - \mathbf{F}\boldsymbol{\Omega} \quad (4.21)$$

This velocity-based steering law permits different combinations of gimbal rate and wheel acceleration (similarly torque) to achieve a desired attitude maneuver. Much more on steering VSCMGs is addressed in Chapter 6, especially the following challenge one faces in selecting a CMG-based attitude control approach.

4.1.3.1 Singularity Problem

A large advantage to using CMGs in a satellite ACS comes from the torque amplification property best described in [13], where the output torque for a CMG is much larger than its input motor gimbal motor torque for an equivalent momentum wheel design as the CMG takes advantage of fixed wheel speed momentum in generating such torque. However, a primary limitation of CMG clusters is that there are certain configurations of a CMG cluster (assuming these CMGs use a single gimbal design approach) where the commanded torque from the vehicle control law cannot be produced in at least one direction. These configurations are known as singularity states and have been well studied in the existing literature. However, the variable-speed capability of VSCMGs, on the other hand, helps neutralize this effect. This is best seen in comparing the well-known CMG saturation singularity surface (top plot of Fig. 4.3) and compared to the VSCMG saturation singularity surface (bottom plot of Fig. 4.3). Notice that the singular regions (voids) of the CMG momentum envelope are filled in the case of VSCMGs since the VSCMGs change mode to act as momentum wheels near singularity.

4.2 Power Subsystem

As stated in [114], “the (electrical) power subsystem generates power, conditions and regulates it, stores it for periods of peak demand or eclipse operation, and distributes it throughout the spacecraft.” Consistent with intuition, the energy storage (ES) function of this EPS is to store the energy generated by the primary power source, typically solar panels. In fact, a solar array design was presented already in the chapter in subsection 4.1.1.5. From this, there are two typical approaches used to connect the primary power supply, the secondary (energy storage) supply, and the spacecraft plus payload power loads. The first of these is called “Direct Energy Transfer,” or DET, where these components are directly connected.

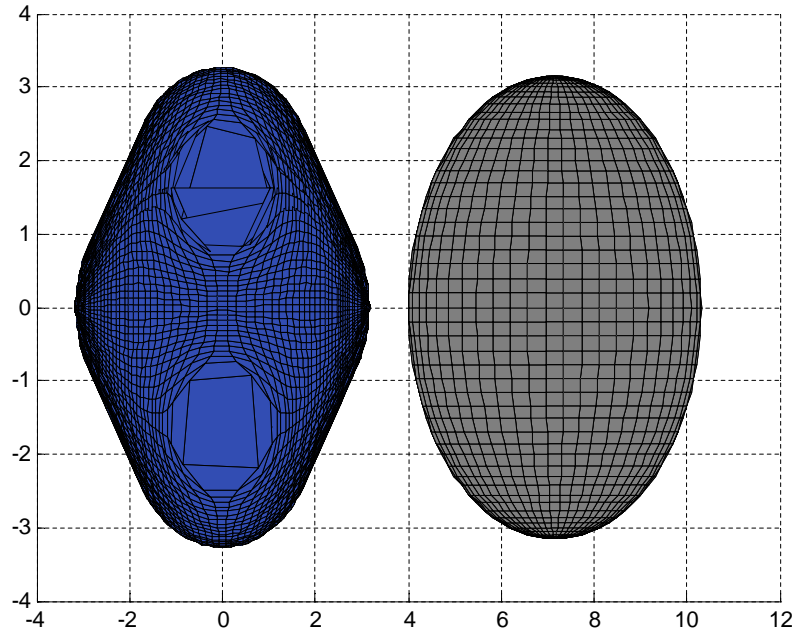


Figure 4.3: Pyramid Cluster CMG and VSCMG Momentum Envelopes

An example of a DET circuit is illustrated in Figure 4.4(a). Although the DET is an effective way to move the precious commodity power, spacecraft design teams continually strive to conserve as much power as possible through effective power bus design. The second method of power configuration, embodying the conservation effort, is the Peak Power Tracker (PPT) strategy in which an active power management system regulates the flow of power between the primary source, the storage portion, and the loads. This architecture is depicted in Figure 4.4(b). A drawback of the PPT approach that counters the gain in efficiency is that the power management system adds complexity to the design. The “smart” electronics of the PPT power management system can also add monetary cost and performance risks to this subsystem’s success. For this reason, the DET approach is implemented here for development with the idea that a future, more complex PPT can be implemented to further garner as much power in the circuit as possible.

As addressed already in this thesis, most contemporary spacecraft use secondary battery systems to fulfill the ES role for storing excess energy created by solar panels. The ES sizing process and an example for employing such an ES during the eclipse period is the topic investigated next. This ES system is driven by two primary requirements, the required instantaneous peak power during eclipse, P_r , and the required battery capacity during eclipse,

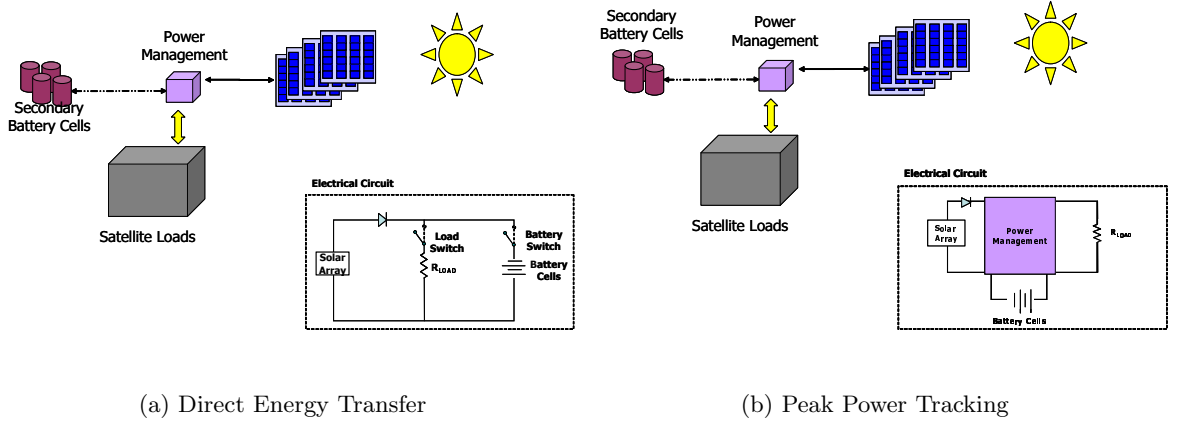


Figure 4.4: Electrical Power Architectures

C_r . These requirements govern the selected battery system, which yields, then, the available battery power and capacity of the ES, P_a and C_a . As one might expect, the idea is to ensure the available quantities are larger than the required ones. This leads to the power and capacity design margins, P_m and C_m . The idea is to ensure these margins are greater than or equal to 0, otherwise the requirements will not be achieved with the implemented system. Figure 4.5 illustrates the conventional process to size a secondary battery ES based on the design margin concept. As done for the attitude margin, N_{m_b} , the b subscript is added to the margins defined here to identify these baseline values. In addition, one will notice Figure 4.5 contains a third baseline design margin – the mass margin, M_{m_b} , found from sizing both the ACS and ES. In contrast to the other margins, though, it is found by subtracting the actual value from the requirement since the requirement is an allowable maximum value, thus the difference will be positive if there's any margin for growth in the design.

Nevertheless, the process shown here (in 4.5) results in the comparison values of C_{m_b} , P_{m_b} , and M_{m_b} that one finds from sizing the requisite batteries and supplementing this idea with the momentum wheel mass addressed earlier. The equations governing this process are given

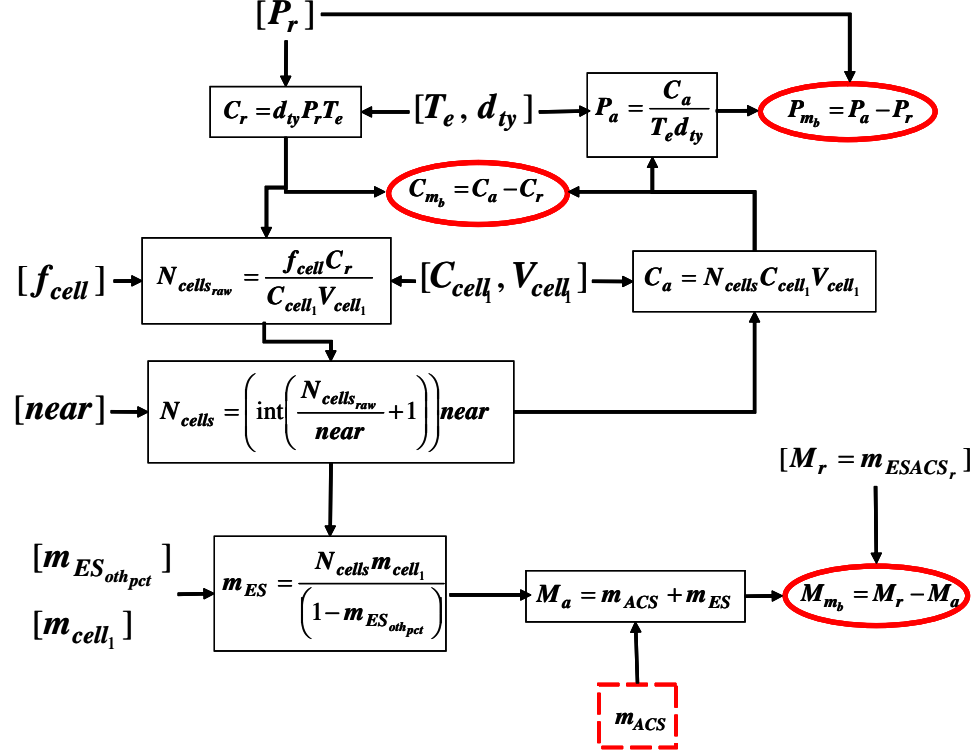


Figure 4.5: Conventional Energy Storage Subsystem Sizing Process

as

$$C_r = d_{ty} P_r T_e \quad (4.22)$$

$$N_{cells_{raw}} = \frac{f_{cell} C_r}{C_{cell_1} V_{cell_1}} \quad (4.23)$$

$$N_{cells} = \left(\frac{N_{cells_{raw}}}{near} + 1 \right) near \quad (4.24)$$

$$C_a = N_{cells} C_{cell_1} V_{cell_1} \quad (4.25)$$

$$P_a = \frac{C_a}{T_e d_{ty}} \quad (4.26)$$

$$M_a = \left(\frac{N_{cells} m_{cell}}{m_{ES_{oth_{pct}}}} \right) + m_{ACS} \quad (4.27)$$

$$(4.28)$$

where f_{cell} is a safety factor in the number of cells required, m_{cell} is the mass of a cell, V_{cell_1} and C_{cell_1} are the voltage and capacity of a single cell, $N_{cells_{raw}}$ is the initially calculated need for cells, whilst N_{cells} is the proper value rounded to $near$. T_e , d_{ty} , and P_r have already

been defined in this document. Thus, all four baseline margins are found as

$$P_{m_b} = P_a - P_r \quad (4.29)$$

$$C_{m_b} = C_a - C_r \quad (4.30)$$

$$M_{m_b} = M_r - M_a \quad (4.31)$$

$$N_{m_b} = N_a - N_r \quad (4.32)$$

Continuing the example established in an earlier section on baseline torque margin, the other three baselines can be found similarly if one assumes f_{cell} is 1.5 (50% additional mass to sustain errors), V_{cell_1} is 1.2 V, C_{cell_1} is 4 Ahr, d_{ty} is taken to be 10%, T_e is found from the orbit as 0.6 hr, P_r is 1100 W, the nearest rounding number is 1 cell, $m_{cell} = 0.16$ kg, depth of discharge is 80%, and short-trip, direct discharge transmission efficiency is taken as 90%. The resulting design, then, follows, calling for 21 cells with $C_{m_b} = 34.95$ Whr and $P_{m_b} = 583.8$ W. This yields an ES mass of 5.89 kg comprised of 3.36 kg in cells and 2.53 kg in other supporting mass. All told, the baseline ES plus ACS systems contribute a total mass of 23.13 kg yielding a mass margin (assuming $M_r = 45$ kg) of $M_{m_b} = 21.87$ kg. In short, the baseline margins for this example are

$$P_{m_b} = 583.8 \quad (4.33)$$

$$C_{m_b} = 34.95 \quad (4.34)$$

$$M_{m_b} = 21.87 \quad (4.35)$$

$$N_{m_b} = 0.2466 \quad (4.36)$$

As mentioned, these values will serve as comparison values for the designed VSCMG-based ESACS.

4.3 Flywheel Energy Storage

Besides demonstrating the principles behind secondary battery design, flywheel battery operating principles also require some development here. These principles follow from the previous work addressed in [107] and tie the kinetic energy of flywheels to the power stored in then drained from these wheels.

First, one defines the kinetic energy, T_j of the j th wheel as

$$T_{Wj} = \frac{1}{2} \omega_{Wj}^T \mathbf{I}_{Wj} \omega_{Wj} \quad (4.37)$$

where ω_{Wj} represents the angular velocity of the wheels with respect to the gimbal structure written in \mathcal{G}_j components. This can be re-written as:

$$\omega_{Wj} = \begin{bmatrix} \Omega_j \\ 0 \\ 0 \end{bmatrix} \quad (4.38)$$

Next, note that for n actuators, the total energy is just the sum of each of the individual actuator energies

$$T_W = \sum_{j=1}^n T_{Wj} \quad (4.39)$$

Then, taking the first derivative of the energy yields the power generated by the wheels. Recall that P_r is the required power to store/drain in the wheels, while P_w is the actual power contained in the wheels. Since $\mathbf{V} = \Omega^T \mathbf{I}_{ws_d}$, then $P_w = \mathbf{V} \dot{\Omega}$, thus

$$P_w = \mathbf{V} \dot{\Omega} = \Omega^T \mathbf{I}_{W_{sd}} \dot{\Omega} \quad (4.40)$$

Now, notice that P_w for this dynamic equation (4.40) is equivalent to the actuated power for the sized system, P_a when the wheel speed, Ω , and wheel acceleration, $\dot{\Omega}$ are at maximum values. Also note that the P_r used in sizing the system is merely the maximum allowable $P_r(t)$ per these dynamic flywheel equations.

4.4 Summary of Fundamentals

Having laid the groundwork in developing the fundamental attitude control and energy storage principles, one can now understand the optimal sizing process, the steering law algorithms and simulations, and hardware implementations presented in the chapters that follow. This foundational knowledge will help one see the relevance of the advancements made in the thesis.

Chapter 5

Small Satellite ESACS Sizing/Optimization

A novel optimal sizing algorithm is developed in this chapter based on the applicable design margins of this system including the attitude torque, peak power, energy capacity, and sub-system mass margins. The algorithm uses a performance index crafted from these margins which also employs the margins of a baseline comparison system. This allows comparison of new technology performance to an existing system in order to identify the advantages and disadvantages of such new technology. The process shown generates point designs which are then compared via a design scoring process. An additional topic covered is that of realistic usable energy capacity and how using it yields a more practical system capable of meeting the desired requirements albeit with reduced mass savings benefits from theoretical levels. This factor, although presented in the early 1970s, is often overlooked in the related literature on flywheel batteries for energy storage.

5.1 Optimization Problem

5.1.1 Process Inputs

The VSCMG-based ESACS physical principles and optimal sizing process described next rely on reference profiles for attitude and satellite energy storage/power as depicted in Fig. 5.1. The top three plots show the desired angular acceleration, angular velocity, and angular position of a spacecraft doing a bang-off-bang single axis maneuver (e.g. roll, pitch, or more

generally, a maneuver about the Euler axis), where the starting and stopping torque portions are separated with a dead-band coasting period, denoted as t_{off} , and the bottom plot shows a flywheel “battery” power profile where positive values represent power added to the energy storage system for charging whereas negative values represent power to be drained from it to supply other subsystems (e.g. during eclipse periods). These profiles set two of the key requirements for the ESACS design.

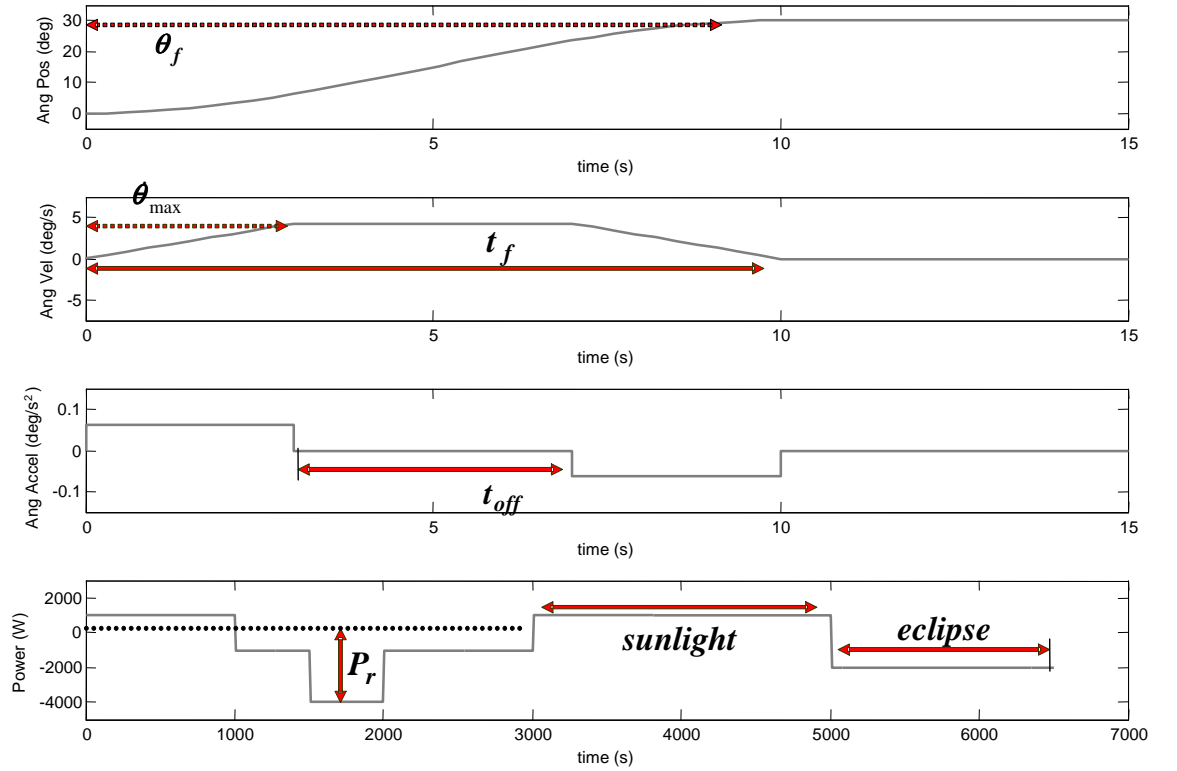


Figure 5.1: Bang-off-Bang Attitude Reference Maneuver and Power Profile

5.1.2 Optimal Sizing Theory

To achieve success, the ESACS engineer needs subsystem design margins (i.e. the differences between the actual design and its associated requirement) that are at or above 0, namely the instantaneous peak power, energy storage capacity, and torque design margins, P_m , C_m , and

N_m , which drive the designs of the two most prominent ESACS components, the power and attitude control subsystems, and the mass margin, M_m , due to its importance to cost-effective satellite designs. These margins are defined as

$$N_m = N_a - N_r \quad (5.1)$$

$$P_m = P_a - P_r = N_{vc}P_{a1} - P_r \quad (5.2)$$

$$C_m = C_a - C_r = N_{vc}C_{a1} - C_r \quad (5.3)$$

$$M_m = M_r - M_a = M_r - N_{vc}M_{a1_i} \quad (5.4)$$

where in the case of N_m , P_m , and C_m , logically require the actual value to be greater than its requirement to ensure the requirement is met. On the other hand, M_m involves a given budget (i.e. requirement), M_r , in which the actual mass, M_a , must be less than or equal to M_r . Also, in the case of using a VSCMG cluster for ESACS, the number of actuators, N_{vc} , is important to capturing the actual storage capacity and peak power—more identical flywheels means more storage capacity and more instantaneous peak power are available—and for obvious reasons, the actual mass of the system. Next, P_r and M_r are directly given by mission requirements, however, N_r is found from the desired maneuver (assumed to be the bang-off-bang maneuver mentioned earlier) as

$$N_r = \frac{4I_{T_{max}}\theta_f}{(t_f^2 - t_{off}^2)} \quad (5.5)$$

and the required storage capacity is found from P_r and other mission requirements such as eclipse duration, eclipse duty cycle, flywheel “battery” depth-of-discharge, and transmission efficiency as defined in [114]

$$C_r = \frac{d_{ty}T_eP_r}{dodx_{msn}} \quad (5.6)$$

Knowing the requirements, the actual values are computed next in order to find the design margins. First the cluster peak torque, N_a , discussed in [148], relies on the torque efficiency of the cluster, the configuration (assumed to be a pyramid configuration as will be addressed later), wheel spin axis inertia (since it is the largest inertia for each VSCMG), the minimum wheel speed (N_a must be producible at all wheel speeds in each VSCMG’s envelope, where the wheels only spin in one direction from minimum speed to maximum speed), and the maximum gimbal rate, in other words,

$$N_a = \chi I_{ws}\Omega_{min}\dot{\delta}(2 + 2\cos\beta) \quad (5.7)$$

Second, the actual power comes from differentiating the wheel spin-axis kinetic energy, $0.5I_{ws}\Omega^2$ for each VSCMG, using the maximum power (wheels spinning at maximum speed) but subtracting the unusable power (power produced below the minimum wheel speed)

$$P_{a_1} = I_{w_s} (\Omega_{max} - \Omega_{min}) \dot{\Omega} \quad (5.8)$$

Similarly, the storage capacity in the wheels was best defined by Varatharajoo in [78]

$$C_{a_1} = k_s \sigma_\theta \pi l_{rot} (r_o^2 - r_i^2) \left(1 - \left(\frac{\Omega_{min}}{\Omega_{max}} \right)^2 \right) / 3600 \quad (5.9)$$

Finally, the actual ESACS mass follows from the design approach used, but can typically be described as a sum of the incorporated components. Three different examples of this mass computation are given later in this paper, but each defines $I_{w_s} = 0.5\pi\rho_{rot}l_{rot}(r_o^4 - r_i^4)$. Furthermore, Eqs. 5.1, 5.2, and 5.3 ensure the actual values are greater than or equal to the required values when the design margins are non-negative. A feasible and practical design is thus defined as one in which the design margins are non-negative and the relevant constraints are met. Only feasible designs are considered.

Next, six variables drive the design margins and are thus interrelated: Ω_{max} , Ω_{min} , l_{rot} , $\dot{\Omega}$, $\dot{\delta}$, and σ_θ/ρ_{rot} . Selecting these decision variables, via an optimal sizing algorithm is addressed next. Furthermore, these parameters are constrained in that Ω_{max} , Ω_{min} , l_{rot} , $\dot{\Omega}$, $\dot{\delta}$, σ_θ/ρ_{rot} plus N_m , P_m , C_m , and M_m must be non-negative for design feasibility. Added to this, Ω_{max} is structurally limited by the flywheel rotor strength, Ω_{min} is limited in ensuring enough torque and power is produced by the flywheel, and the disparity between the maximum and minimum allowable wheel speeds is limited to ensure proper energy is stored. Thus, these constraints drive the feasible selection of these six ESACS design variables.

5.1.3 Optimization Logic

Designing effective ESACS VSCMGs centers on selecting the best decision variable combination that optimizes a suitable performance index to meet mission requirements subject to the aforementioned constraints. Since an underlying aim in this task is to produce a system that outperforms the baseline MW ACS plus NiCd ES, three different candidate performance indices, J_a , J_b , and J_c , were crafted to capture the relationship of the ESACS design compared to the baseline. First, J_a is defined as the weighted ratio of the four VSCMG design margins to their baseline counterparts

$$J_a = \frac{\gamma_{a_1} C_m \gamma_{a_2} P_m \gamma_{a_3} N_m \gamma_{a_4} M_{m_i}}{C_{m_b} P_{m_b} N_{m_b} M_{m_b}} = \frac{N_{vc}^3 \gamma_{a_1} \gamma_{a_2} \gamma_{a_3} \gamma_{a_4} C_{m_1} P_{m_1} N_{m_1} M_{m_{i1}}}{C_{m_b} P_{m_b} N_{m_b} M_{m_b}} \quad (5.10)$$

where the index $i = 1, 2$, or 3 relates to the candidate alternative in consideration (i.e. #1, #2, or #3) and its differently calculated mass. The capacity and power margins are calculated using equations applicable to a single VSCMG and then multiplied by N_{vc} as is the mass margin, but the torque margin (as are the baseline margins) is calculated for the entire VSCMG suite. This has been included in finding J . Regardless, J_b is based on summing the square of the design margins as in

$$J_b = \frac{1}{4} \left[\gamma_{b1} \left(\frac{N_{vc} C_{m1}}{C_{mb}} \right)^2 + \gamma_{b2} \left(\frac{N_{vc} P_{m1}}{P_{mb}} \right)^2 + \gamma_{b3} \left(\frac{N_m}{N_{mb}} \right)^2 + \gamma_{b4} \left(\frac{N_{vc} M_{m1}}{M_{mb}} \right)^2 \right] \quad (5.11)$$

and, for J_c , an experimental error-approach is taken in regards to the difference between each design margin and its baseline, as in

$$J_c = \frac{1}{4} \left[\gamma_{c1} \left(\frac{N_{vc} C_{m1} - C_{mb}}{C_{mb}} \right) + \gamma_{c2} \left(\frac{N_{vc} P_{m1} - P_{mb}}{P_{mb}} \right) + \gamma_{c3} \left(\frac{N_m - N_{mb}}{N_{mb}} \right) + \gamma_{c4} \left(\frac{N_{vc} M_{m1} - M_{mb}}{M_{mb}} \right) \right] \quad (5.12)$$

Furthermore, for the best ESACS to baseline ratio one needs to maximize J_i , or equivalently, minimize $J = -J_i$. Incorporating the constraints, one can cast the problem as a standard Nonlinear Programming Problem (NLP) using $J = -J_a$ (or similarly, J_b or J_c):

Minimize

$$J = -\frac{N_{vc}^3 C_{m1} P_{m1} N_m M_{m1}}{C_{mb} P_{mb} N_{mb} M_{mb}}, i = 1, 2, 3 \quad (5.13)$$

Subject to

$$C_{m1}, P_{m1}, N_m, M_{m1} \geq 0 \quad i = 1, 2, 3 \quad (5.14)$$

$$\Omega_{max}, \Omega_{min}, l_{rot}, \dot{\Omega} \geq 0 \quad (5.15)$$

$$(\Omega_{max}^2 - \Omega_{min}^2) l_{rot} \geq \frac{4T_e P_r}{N_{vc} \pi \rho_{rot} (r_o^4 - r_i^4)} \quad (5.16)$$

$$\Omega_{max} \leq \Omega_{struct} \quad (5.17)$$

$$l_{rot} \leq l_{real} \quad (5.18)$$

$$\dot{\Omega} \leq \dot{\Omega}_{real} \quad (5.19)$$

$$J \leq -1.0 \quad (5.20)$$

where Ω_{struct} follows from applying the radial force equilibrium equations defined by Danfelt et. al. and addressed in Varatharajoo [78, 149] for a typical, anisotropic (orthotropic), single-layer rotor. Captured directly from [78, 149], the governing stress equations for a constant

speed flywheel are

$$\sigma_r = \alpha_1 \frac{E_r (\lambda + \nu_{\theta r})}{(1 - \nu_{\theta r} \nu_{r\theta})} r^{\lambda-1} + \alpha_2 \frac{E_r (\nu_{\theta r} - \lambda)}{(1 - \nu_{\theta r} \nu_{r\theta})} r^{-\lambda-1} - \frac{(3 + \nu_{\theta r}) \rho \Omega^2}{9E_r - E_\theta} r^2 \quad (5.21)$$

$$\sigma_\theta = \alpha_1 \frac{E_\theta (1 + \lambda \nu_{r\theta})}{(1 - \nu_{\theta r} \nu_{r\theta})} r^{\lambda-1} + \alpha_2 \frac{E_\theta (1 - \lambda \nu_{r\theta})}{(1 - \nu_{\theta r} \nu_{r\theta})} r^{-\lambda-1} - \frac{(1 + 3\nu_{r\theta}) E_\theta \rho \Omega^2}{9E_r - E_\theta} r^2 \quad (5.22)$$

The integration constants, α_1 , α_2 , are found by applying radial stress boundary conditions (i.e. $\sigma_r = 0$ at $r = r_o$ and $\sigma_r = -t_{sp}\rho_{sp}\Omega^2 r_i^2$ at $r = r_i$). Substituting these two values in Eqs. 5.21 and 5.22, one can calculate the stress distribution in the wheel for a given wheel speed, or conversely, use the maximum allowable rotor stress to define the maximum allowable wheel speed. The latter of these techniques yields Ω_{struct} . The stress distribution can be viewed graphically in Fig. 5.2 which directly follows from [149] and [78]. In these plots, the allowable stress (tensile and compressive) values are superimposed upon the stress distribution plots for determining the maximum allowable structural wheel speed.

Next, the NLP from Eqs. 5.13 and 5.14 is solved using a reduced-order gradient method based on crafting a Hamiltonian from the performance index supplemented by a linear combination of the constraints. As applied here, this approach was implemented using the author's Microsoft Excel Solver-based sizing tool. Functionality of this iterative process is shown in Fig. 5.3. The process involves defining mission and actuator parameters; selecting design inputs based on engineering judgement such as design alternative number, optimization type (maximize, minimize, or set to a specific value), and optimization parameter (performance index J or mass M_m); running the optimizer software tool; and interpreting the decision variable outputs for different combinations of σ_θ/ρ_{rot} (i.e. rotor material parameters). On a basic level, the optimizer software performs the standard parametric design optimization through systematically perturbing the system's parameters in order to find the best performance index value, but it also uses an iterative reduced order gradient algorithm designed to reduce the number of computations required for multiple-decision variable problems with hundreds of decision variables as well as robust error checking code to trap user input errors. Here, the optimizer function generates a single point design (i.e. a specific combination of decision variables) for the given process inputs, another software function generates different variable input combinations such that the entire process produces multiple feasible point designs through several individual optimization iterations in batch mode. The resulting collection of design points is then reviewed, scored, and evaluated in selecting a design. This is further illustrated with a practical example in the next section.

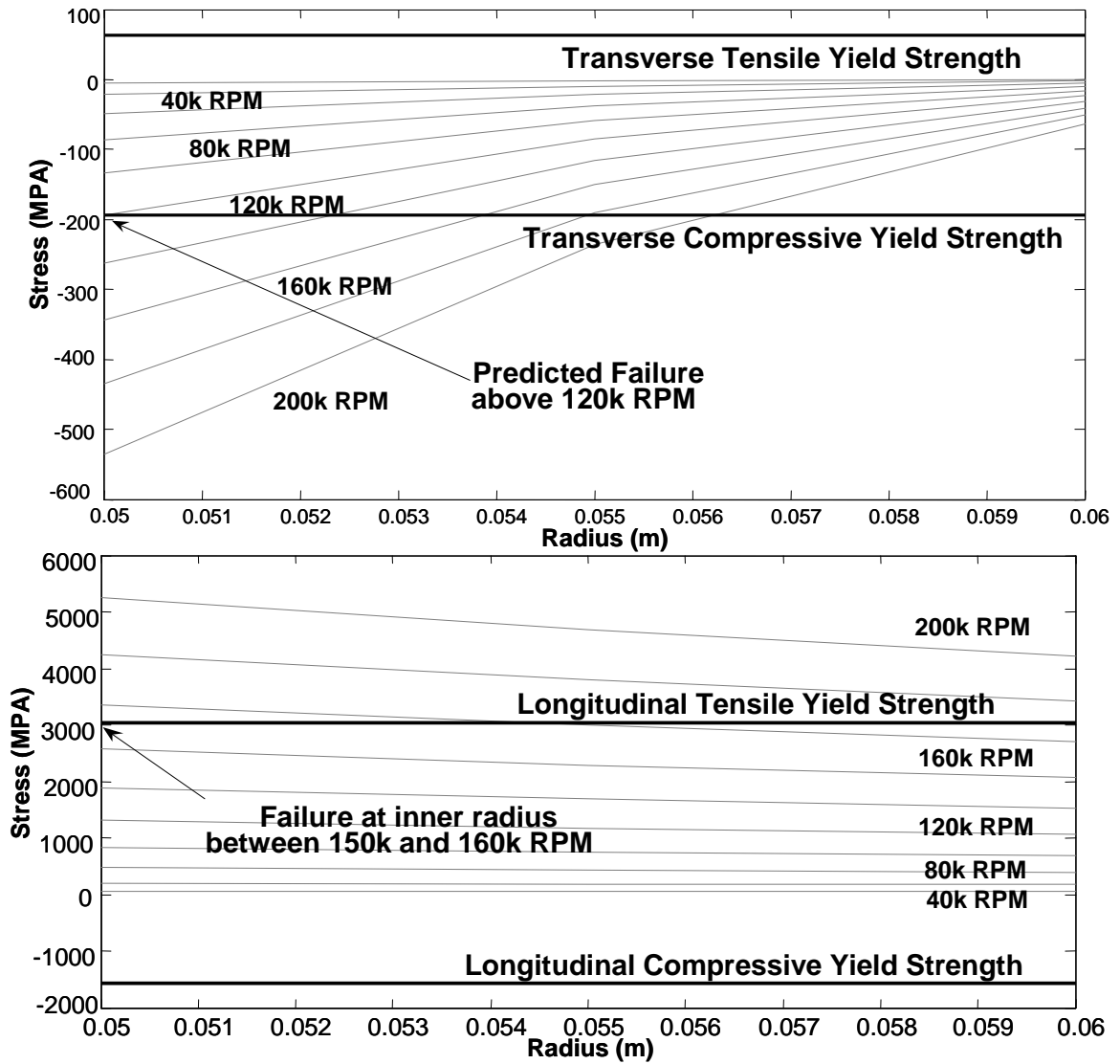


Figure 5.2: T1000G Carbon Fiber Radial and Tangential Stress Distributions

5.2 Trade Studies

5.2.1 Assumptions

Before examining the results from this example, it's important to identify some assumptions made. First, although it has not been included here, rotor containment to prevent personnel and/or systems damage in the event of catastrophic wheel failure is very important, but the larger the containment method used, the greater the mass impact. It is expected that system designers consider this fact when designing a VSCMG-based ESACS for any satellite class. Second, there are several different schemes for initial system start-up once the satellite is deployed. This study has not ventured to explore all of these, but awareness of this issue is

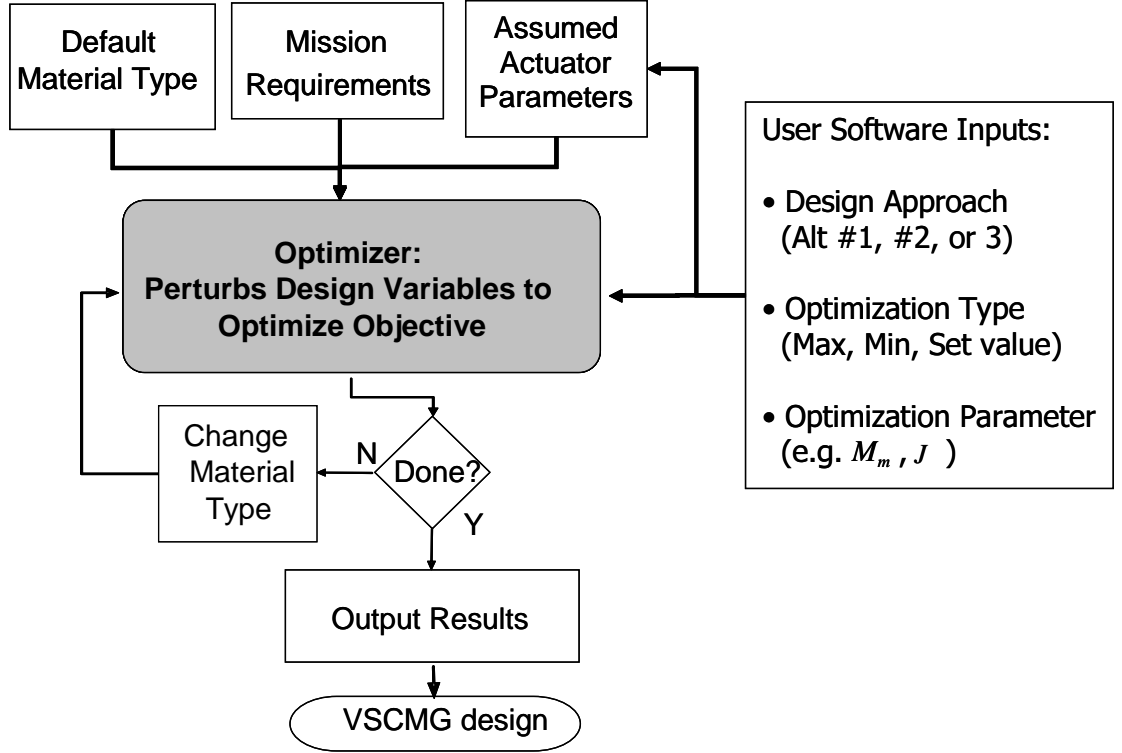


Figure 5.3: Basic Optimal Sizing Process

paramount to future on-orbit success. Plausible methods could include flywheel “battery” trickle charging; solar panel to super capacitor to VSCMG ESACS charging; or employment of a small primary battery to handle the power load until the VSCMGs are adequately charged to commence on-orbit operation. Third, due to its built-in redundancy and prevalence in the existing literature [13, 66, 74, 147], it’s assumed a pyramid cluster of VSCMGs is to be used in ESACS. This configuration permits all four gimbals to fail while maintaining the ability to recover three-axes of attitude control using the remaining wheels in MW mode and still keeps enough redundancy for energy storage. However, it is recognized that there are several different plausible cluster configurations [147]. The key effect is that a different configuration will change the N_{vc} used as well as change the geometry-based $2 + 2 \cos \beta$ term in the N_a equation. Fourth, this technology only applies for missions with simultaneous high precision pointing and high peak power requirements. If either requirement is eliminated, this approach loses its utility. Fifth, the volume is constrained in the sense that outer and inner flywheel rotor radii are fixed where the rotor length can vary between point designs up to a realistic limit. Finally, the presented arguments focus on this technology’s role in fulfilling the entire energy storage mission for a satellite, however, an equally plausible alternative is to

employ VSCMG ESACS on missions wherein a high-power, high-agility payload only needs the high-power properties of the ESACS during some operations, but the satellite does not need them all the time to run satellite support subsystems. Thus, a contemporary satellite ES can supply eclipse subsystem power using conventional batteries but run the payload at the high-power level with energy from the VSCMG ESACS.

5.2.2 Technology Trades

In order to apply the optimal sizing process to the given mission requirements, we next identify a few competing candidate design approach alternatives based on the trade tree of key technologies found in Fig. 5.4. For the purposes of this paper, this rather wide trade space has been narrowed down to three design alternatives by practical pruning of the trade tree. These designs are Alternative #1 which uses a cluster of mechanically-levitated, gimballed flywheels, based on a conventional design approach like that shown in [17]; Alternative #2 which uses an open motor/generator with a magnetically-levitated, mechanically-gimballed flywheel; and Alternative #3 which uses a magnetically-levitated, mechanically-gimballed flywheel with embedded electromagnets in the rotor for motor/generator functionality like Varatharajoo's non-gimballed flywheel shown in [78]. Next, these alternative definitions lead to three different mass (M_a) calculations by summing the appropriate sub-components:

$$M_{a1_1} = m_{rot}(l_{rot}) + m_{oth}(l_{rot}) + m_{kii_{scaled}} + m_{dc_{scaled}} \quad (5.23)$$

$$M_{a1_2} = m_{rot}(l_{rot}) + m_{oth}(l_{rot}) + m_{mb}(l_{rot}) + 2m_{m_2}(l_{rot}) \quad (5.24)$$

$$M_{a1_3} = m_{rot}(l_{rot}) + m_{oth}(l_{rot}) + m_{mb}(l_{rot})m_{m_3}(l_{rot}, \Omega_{max}) \quad (5.25)$$

Directly impacting one of the four key design margins, the functions have an important role in the optimal sizing process, thus the better one can define them ahead of time, the more accurate the results.

5.2.3 Sizing Results

Several iterations of the sizing process were run with different variations in the decision variables generating more than 5000 point designs. Selected results reflecting trends in these point designs are shown next. We note here that there are two prominent strategies in completing a design sizing comparison of this nature, sizing for optimal (minimum) mass at a performance equivalent to the baseline system (where "performance" in this sense refers to

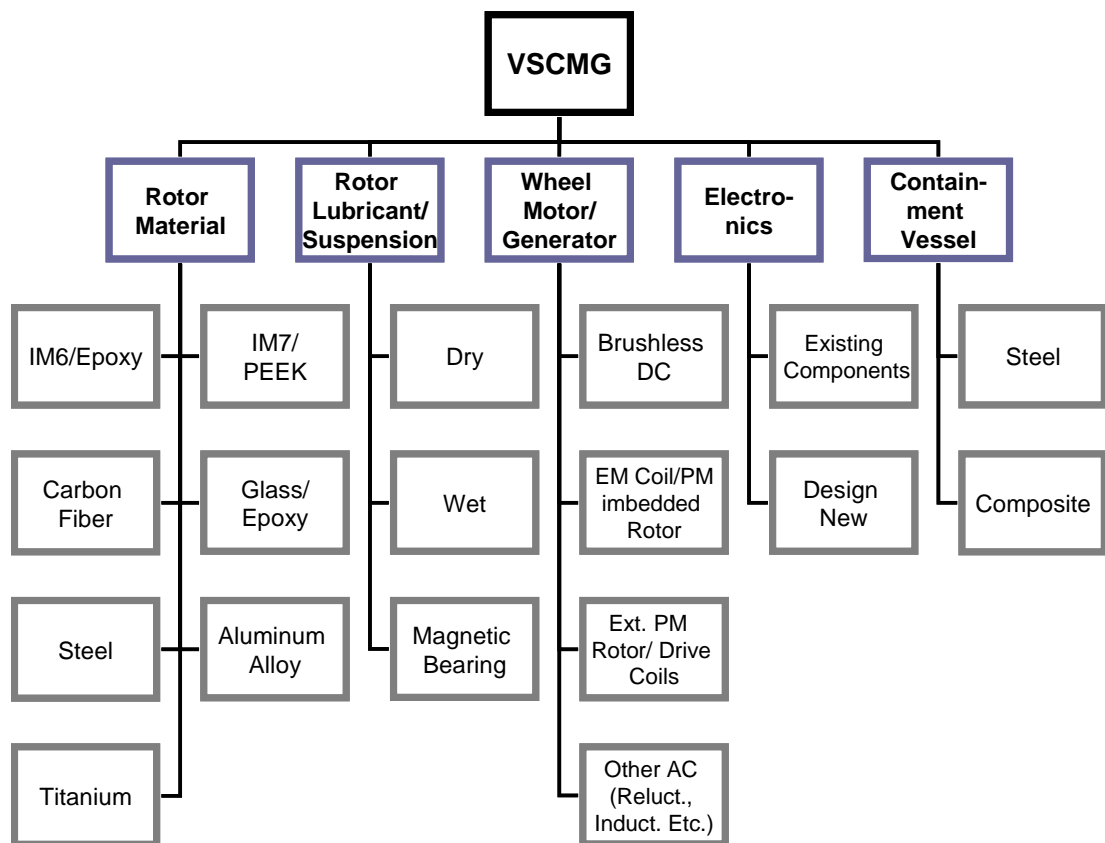


Figure 5.4: Key Variable-Speed CMG Technologies

the non-mass margins, i.e. N_m , P_m , and C_m), or sizing for optimal (maximum) performance at a mass equivalent to the baseline (i.e. $M_m = M_{mb}$). The former of these often arises when the designer strives to do a similar mission to the baseline but at less mass, while the latter arises when the designer attempts to extend the system's capability with the same mass as the old system. Nevertheless, both cases add equality constraints to the NLP.

The first trend investigated is that of different rotor materials. In Fig. 5.5, the material types have been plotted in terms of wheel acceleration and gimbal rate versus optimal J_c and mass savings. As one can see, the composite materials outperform conventional ones due to more favorable strength to density ratios, σ_θ/ρ_{rot} . Logically, the material with the greatest, σ_θ/ρ_{rot} , T1000G Carbon Fiber, yields the greatest mass savings.

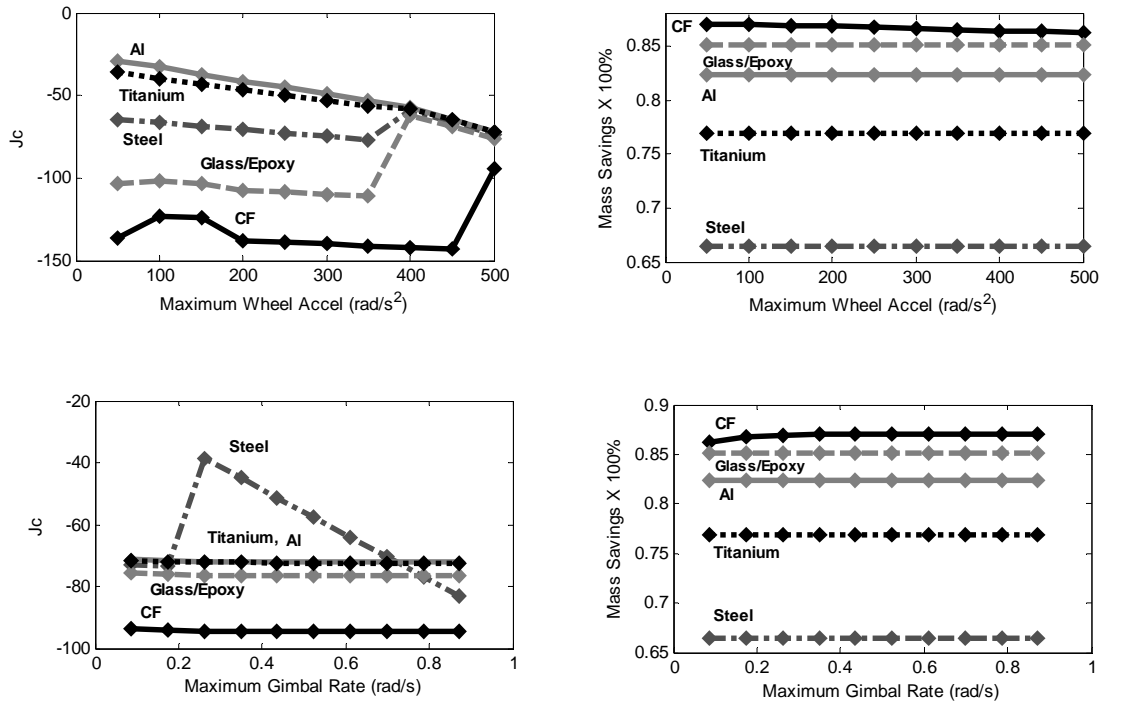


Figure 5.5: Optimal Performance/Optimal Mass Results for Selected Rotor materials

The next trend considered is that of performance index from the choices presented earlier. Fig. 5.6 demonstrates these performance index trends in terms of rotor length. The plots on the left side show the optimal performance indices for different maximum gimbal rate values whereas those on the right show the performance indices at optimal mass for different maximum wheel acceleration values. Notice that better performance is more negative in value. In both cases, a higher value maximum gimbal rate or maximum wheel acceleration

means a better (more negative) performance index, whether using J_a , J_b , or J_c . Also notice that there is a sizable shift in J at a rotor length of approximately 0.035 m in the optimal mass cases. This isolates a good rotor length for which to focus one's design. It should also be noted that each curve is comprised of a finite number of design points (10 for each of the cases presented in this report), thus a point on a curve can be thought of as a specific optimized design. Furthermore, J_c yields the best comparison to the baseline. Recall that J_c is defined by the percentage difference between the current design and the baseline where a better point design is a negative value and a better baseline is a positive value. These values, for the case of direct comparisons (as are done in the optimal mass savings case), when multiplied by -100 % give the percent improvement over the baseline. Both figures show a clear transition from positive (better baseline) to negative (better point design) as the rotor length is increased. On the other hand, similar information is harder to glean from the J_b and J_a plots where the performance indices become more negative as rotor length increases, but a percentage improvement as well as the transition from a better baseline to better point design is harder to decipher. Due to its comparative advantages over J_a and J_b , performance index J_c will be used for further plots.

Another very interesting trend is shown in Fig. 5.7 where mass savings for Alternative #3 is plotted against rotor length. This result illustrates that decreased rotor length is strongly related to improved mass savings.

Next, trends in the decision variables under various conditions are examined. Fig. 5.8 shows trends in wheel speed as compared to the other decision variables and Fig. 5.9 highlights other relationships between the decision variables. One can see from the wheel speed plots that in design for optimal J , maximum gimbal rate has little to no effect on the wheel speed limits, whereas maximum wheel acceleration has a profound effect on the result. In the latter case, the maximum wheel speed of Alternative #3 is significantly less than the others. As for Mass Savings (MS), a similar wheel speed trend occurs with increased $\dot{\Omega}$ where one will notice that very high maximum wheel speeds are required for lower $\dot{\Omega}$ (i.e. those less than about 100 rad/s^2). However, higher maximum gimbal rates counter-intuitively increase the required maximum wheel speed – but this comes from trying to constrain the non-mass margin design margins (i.e. for equivalent performance) and improve mass savings as much as possible. Also in the optimal mass savings plots, one can see a large decrease in maximum wheel speed at a rotor length near 0.035 m . Since rotor length affects all of the design margins, this is clearly a rotor length where the margins best match. Continuing on to Fig. 5.9, one can see

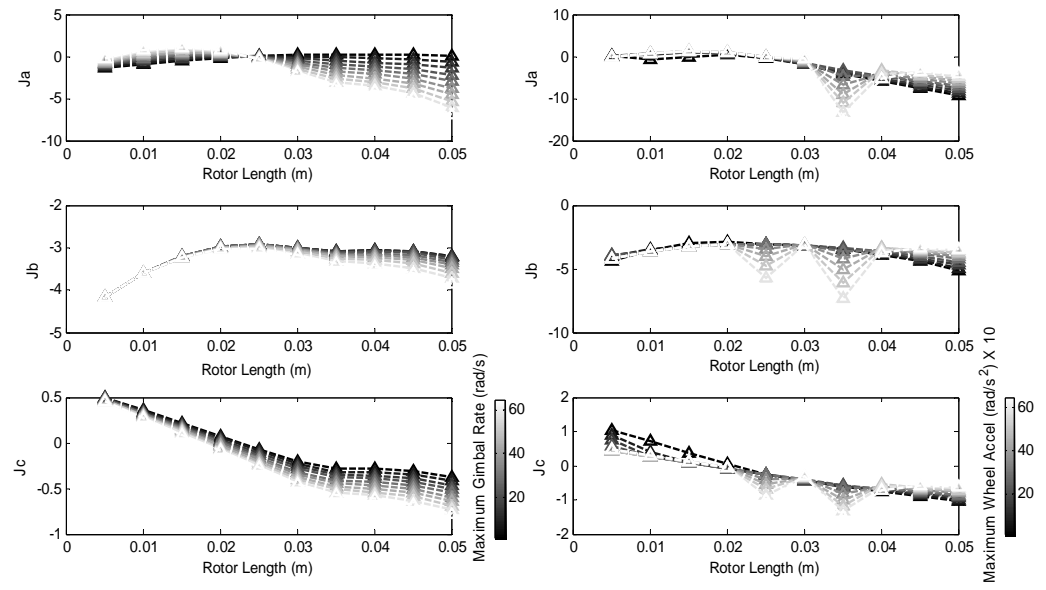


Figure 5.6: Rotor Length versus Performance Indices J_a , J_b , and J_c for Three Alternatives at Optimal Performance and Optimal Mass

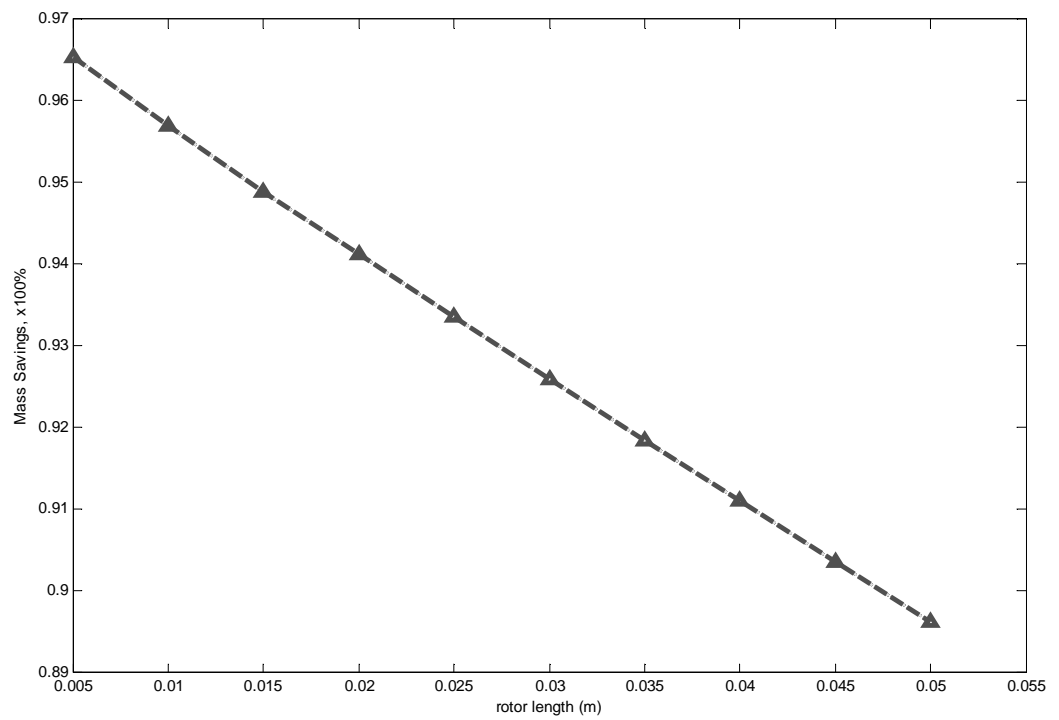


Figure 5.7: Rotor Length Versus Optimal Mass Savings

the trends in increasing maximum gimbal rate which decreases the required maximum wheel acceleration as well as the rotor length for optimal mass savings. This plot directly illustrates the benefit of torque amplification—increasing the maximum gimbal rate enables decreasing the maximum wheel acceleration in producing equivalent torque while keeping $N_m = N_{m_b}$, $C_m = C_{m_b}$, and $P_m = P_{m_b}$. This change, then accounts for the slight decrease in mass savings with increased maximum gimbal rate (similarly maximum wheel acceleration) as the rotor length is also increasing, however this trend (which is for Alternative #1) is inverted for optimal J using Alternative #3 (the bottom plot). However, since Alternative #3 allows for changes in wheel speed and rotor length when determining motor/generator mass, a key difference in the two parts of Fig. 5.9 besides optimal MS vice optimal J is that the $\dot{\Omega}$ curves actually intersect.

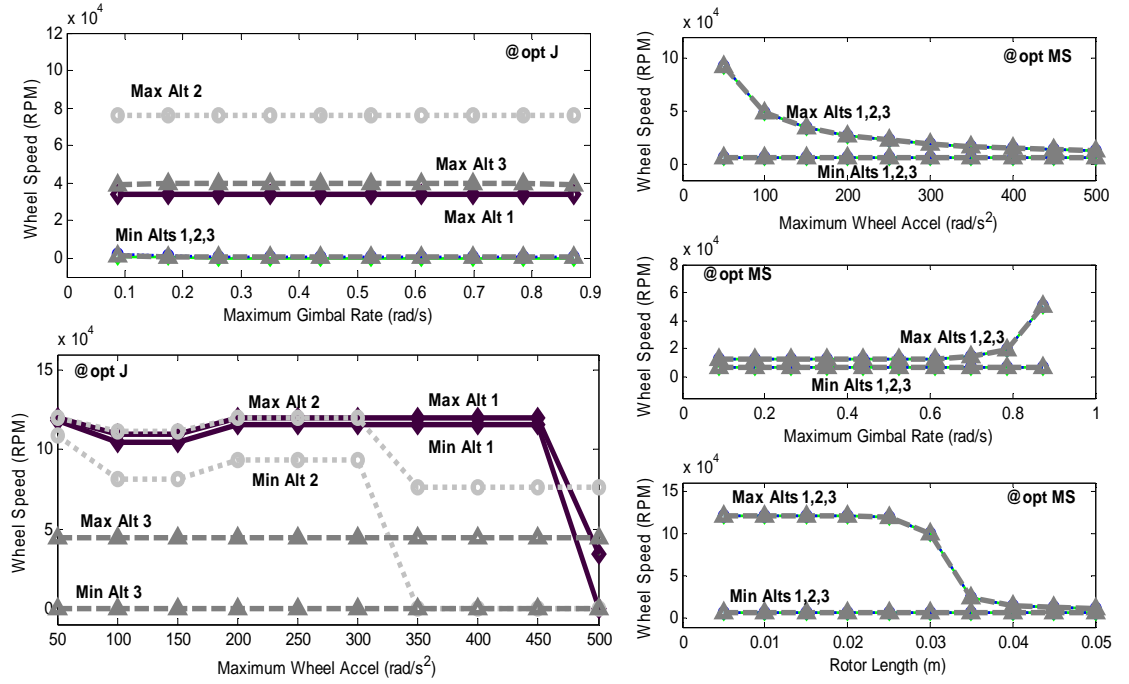


Figure 5.8: Maximum and Minimum Wheel Speed Comparisons with Other Decision Variables for Three Alternatives at Optimal Performance (two plots at left) and Optimal Mass (three plots at right)

Next, Fig. 5.10 shows the relationship between maximum wheel acceleration and rotor length, the energy density, E_d , and the power density, P_d at optimal MS and optimal J . In the case of optimal mass savings, as rotor length increases, energy density increases, until the critical 0.035 m point, then it decreases with increases in rotor length. This is directly correlated to

the dominance of the equality-constrained capacity margin (set equal to the baseline capacity margin) until the critical rotor length after which the mass dominates the energy density calculation (which is simply the actual capacity divided by the subsystem mass). One can also see the main difference in the three technologies at optimal MS in terms of Ω_{max} versus E_d and P_d , with Alternative #3 showing a significant advantage over the other two technologies. At optimal J, one can see that higher maximum wheel accelerations yield higher energy and power densities. In fact, Alternative #1 substantially increases in power and energy density after 450 rad/s^2 .

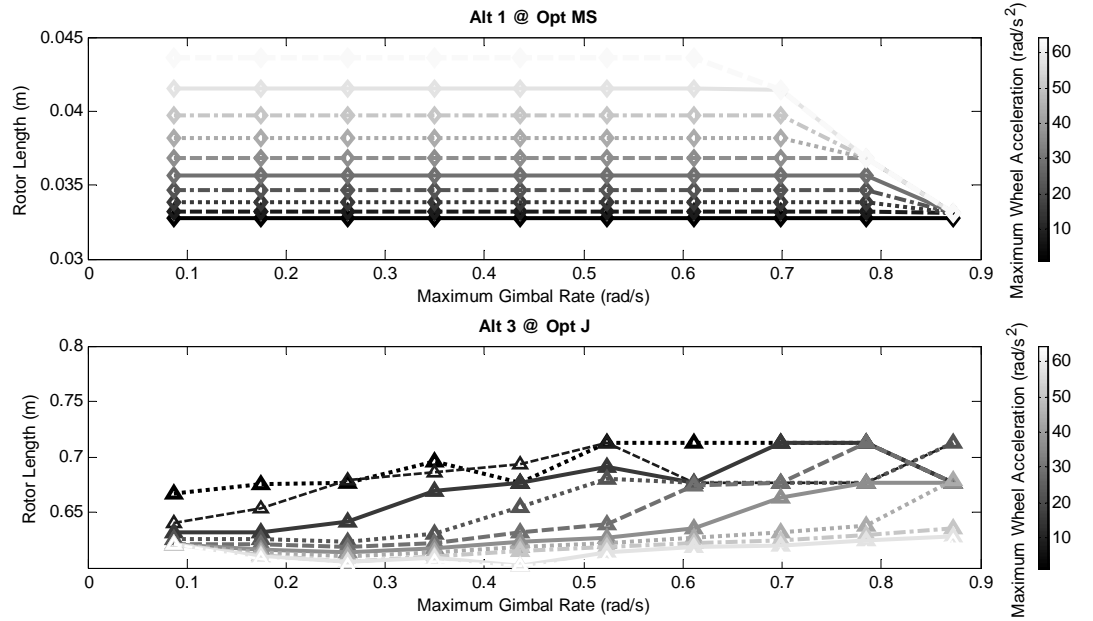


Figure 5.9: Maximum Gimbal Rate versus Rotor Length Comparisons by Maximum Wheel Acceleration for Alternatives #1 and #3 at Optimal Mass Savings

5.2.4 Benefits & Scored Designs

The benefits of this approach are significant mass savings, longer lifetime, increased slewing agility, robust singularity avoidance, and improved power density as compared to the baseline. First, faster slewing agility comes from the torque amplification advantage of the actuators'

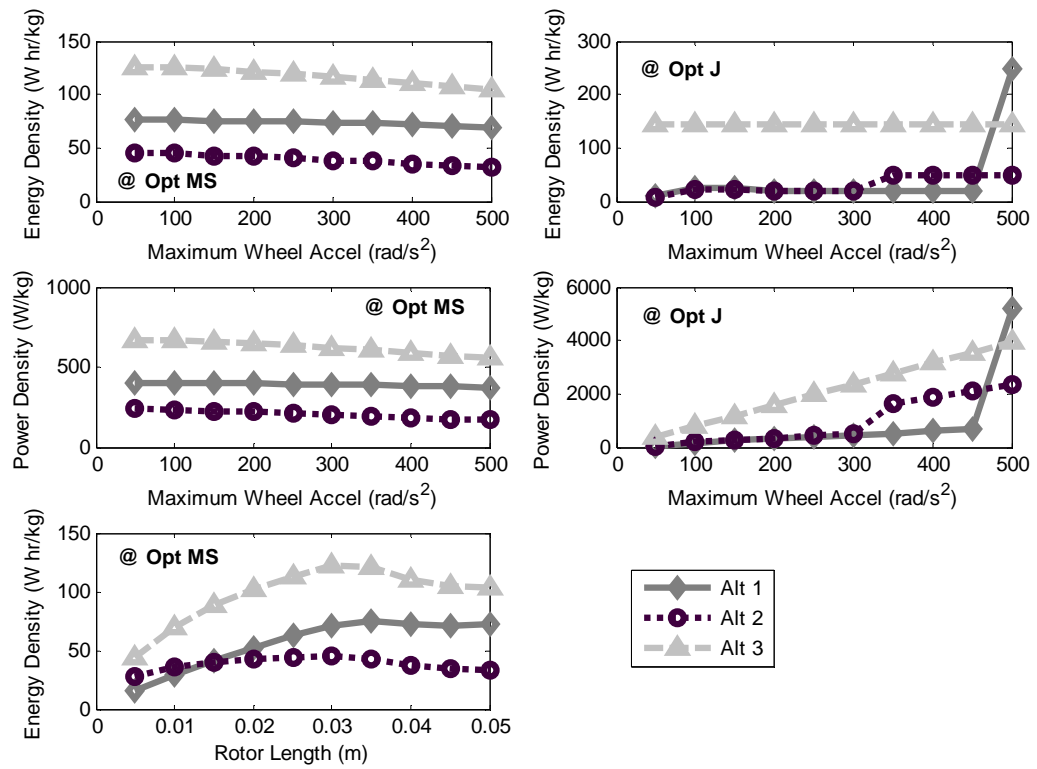


Figure 5.10: Selected Decision Variables Versus Energy and Power Density at Optimal Mass and Optimal Performance for All Three Alternatives

CMG mode as alluded to earlier. Second, mass savings, measured in terms of percent difference between the ESACS subsystem mass and the NiCd secondary battery energy storage system plus the MW portion of the attitude control system. Note that forecasted ESACS mass improvements have been listed anywhere from 5-15% up to 40-50% and beyond in the literature [150,151], however the key difference comes from measuring mass savings in terms of direct mass change in the overall spacecraft mass (of which the energy storage plus attitude control subsystems comprise about 10-20% of the total mass) or in terms of the actual subsystem mass percent difference (often well over 50% from combining subsystems). This mass advantage, reflected in the mass comparison before and after combining the systems into a consolidated ESACS using the method defined here as shown in Fig. 5.11, is one of the primary advantages of implementing this type of system. Third, robust singularity avoidance

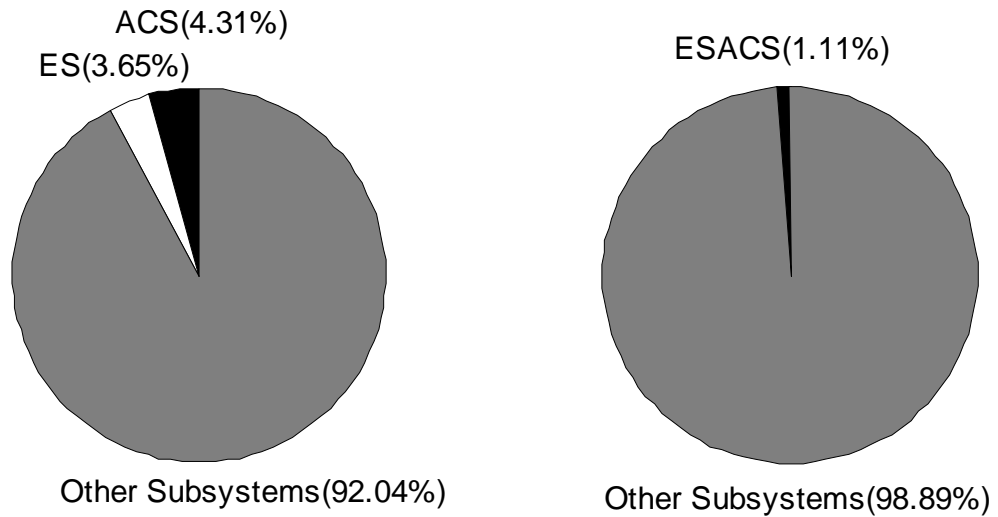


Figure 5.11: Spacecraft Mass Breakdown Before and After Combining Subsystems

is reflected in the well-known CMG saturation singularity surface as mapped on top of the VSCMG saturation singularity surface in Fig 5.12). Notice that the singular regions (voids) of the CMG momentum envelope are filled in the case of VSCMGs since the VSCMGs change mode to act as momentum wheels near singularity. Fourth, longer lifetime stems from assuming the best implementation of the VSCMG design comes from magnetic-levitation. When enabled, this magnetic-levitation permits higher depths of discharge for the flywheel “batteries” as compared to conventional batteries and will return to essentially the same amount of stored energy when topped up after draining them as opposed to conventional batteries which wear out after far fewer cycles. The lifetime argument is best illustrated in Fig. 5.13,

which shows the theoretical position of the flywheel batteries in relation to common secondary battery depths-of-discharge (dod) versus lifetime. The flywheel depth-of-discharge has been shown to be limited by the failure time of other on-board subsystems (e.g. solar panels) with an assumed lifetime of 15 years in Low Earth Orbit. The actual flywheel curve could be much further out in terms of cycles depending upon the performance of the magnetic bearings. As an aside, when reliability details of the ESACS actuator components are known, these reliability factors (which optionally can be thought of as a function of decision variables such as maximum/minimum wheel speed, maximum wheel acceleration, etc.) can be used to calculate the lifetime of the system and refine its position in Fig. 5.13. An example of this would be to calculate the wheel motor/generator's mean time-to-failure as a function of wheel speed, then determine it's lifetime in terms of cycles or orbits. This, then, permits refining the VSCMGs place in this chart. In terms of the study shown here, this was actually done for the system used, but it was determined the lifetime of the first non-ESACS subsystem to fail was less than the motor/generator's lifetime.

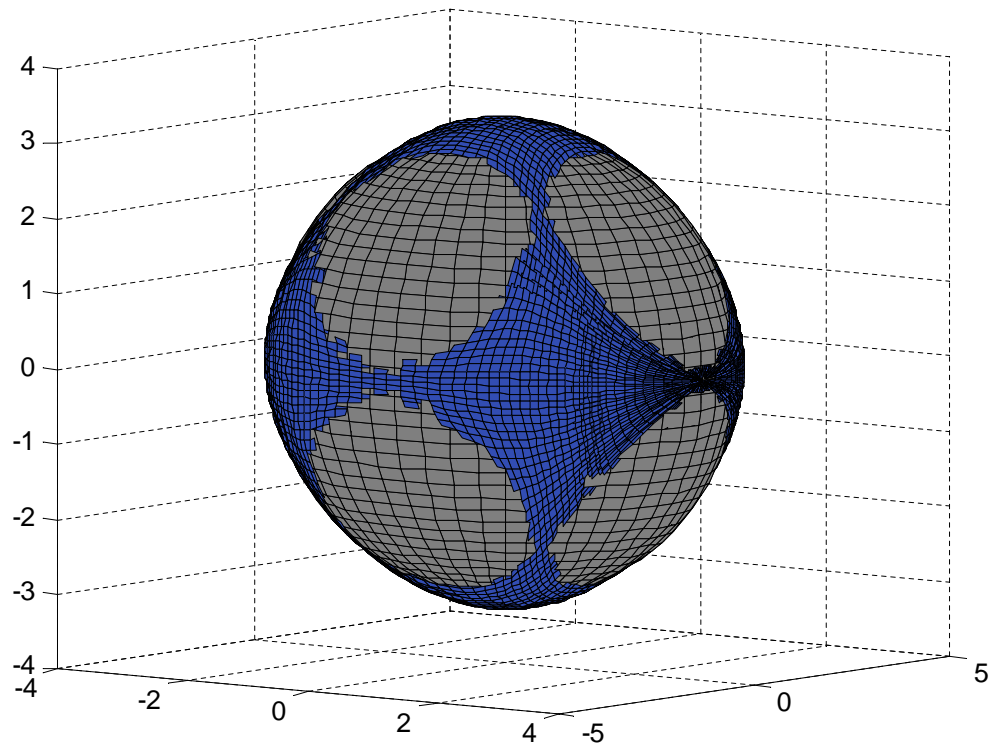


Figure 5.12: Pyramid Cluster CMG and Superimposed VSCMG Momentum Envelopes

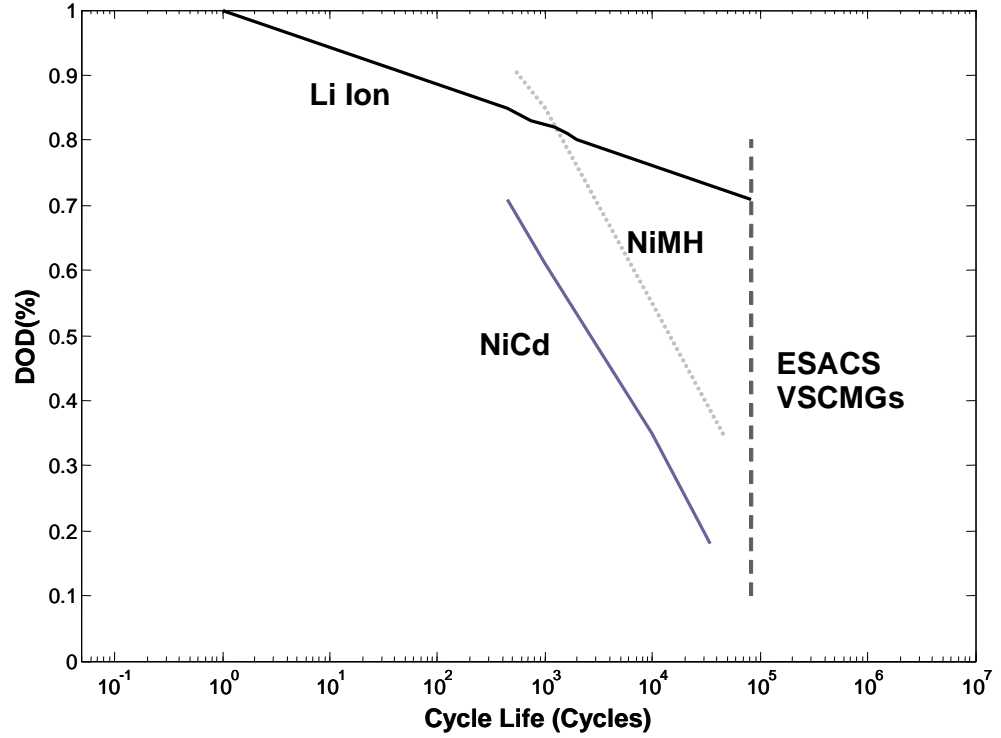


Figure 5.13: Depth-of-Discharge Versus Lifetime

The final and perhaps biggest advantage of using an ESACS is reflected in the Ragone plot of Fig. 5.14, which shows energy density versus power density for the flywheels and the typical secondary batteries, both of which have been adjusted by mass of the entire energy storage system vice a single battery (as is typically computed). This plot illustrates that even though battery technology is improving (such as Lithium-ion) in terms of energy density, flywheels are excellent performers in terms of power density. This is important for small satellites since its primary bus can be designed to handle low peak power requirements using standard secondary batteries and then be supplemented with a VSCMG-based ESACS for high slewing capability and enjoy the vast improvement in peak power due to the flywheel power density advantage (reflected in the Ragone plot). This is ideal for missions such as earth imaging and spotlight synthetic aperture RADAR which have these aggressive peak power and agility requirements. In such a case, a VSCMG system would be an ideal fit combined with a standard small satellite bus. From the dual-objective sizing process described earlier (i.e. design for maximum mass savings and design for equivalent mass), a table of scored designs was crafted weighting the dual objectives equally. An important note is that the weights can be adjusted based on the designer's preference within the scoring function similar to the design margin weights in the performance index. The scoring function, T , is given for T_a

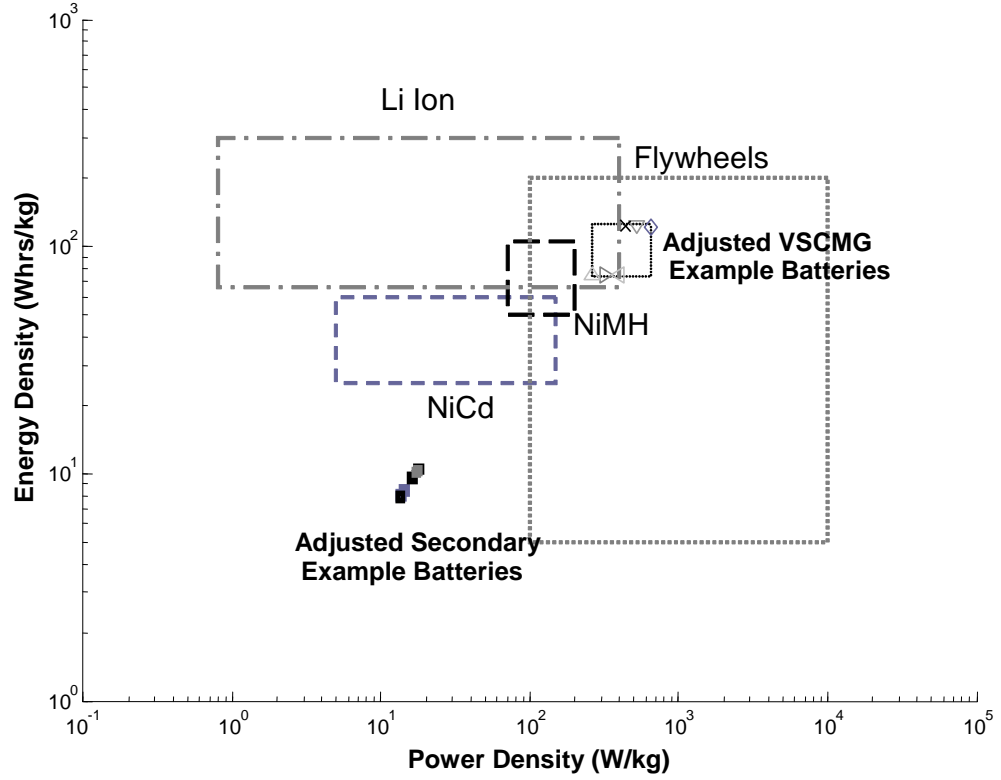


Figure 5.14: Adjusted Technology Ragone Plot, Energy Density Versus Power Density

in Eq. 5.26 which uses J_a (or alternately, T_b and T_c which use J_b and J_c , respectively), the weights, w_i , already mentioned, and normalization factors, f_i , for equivalent comparisons:

$$\begin{aligned}
 T_a = & \omega_1 f_1 t_{life} + \omega_2 f_2 E_{dMS} + \omega_3 f_3 E_{dJa} + \omega_4 f_4 P_{dMS} + \omega_5 f_5 P_{dJa} + \omega_6 (1 - f_6 \Omega_{maxMS}) \\
 & + \omega_7 (1 - f_7 \Omega_{maxJa}) + \omega_8 (1 - f_8 \Omega_{maxMS}) + \omega_9 (1 - f_9 \Omega_{maxJa}) + \omega_{10} (1 - f_{10} l_{rotMS}) \\
 & + \omega_{11} (1 - f_{11} l_{rotJa}) + \omega_{12} (1 - f_{12} \dot{\delta}_{MS}) + \omega_{13} (1 - f_{13} \dot{\delta}_{Ja}) + \omega_{14} (1 - f_{14} \dot{\Omega}_{MS}) \\
 & + \omega_{15} (1 - f_{15} \dot{\Omega}_{Ja}) + \omega_{16} f_{16} MS_{MS} + \omega_{17} f_{17} J_{aJa}
 \end{aligned} \tag{5.26}$$

Note that this scoring function sums the effects of the benefits (the first five terms), the decision variables (the next 10 terms), the optimization objective (the next two terms), and the technology readiness (the last term). Furthermore, the decision variable quantities are penalized in the scoring function in order to keep the values as small as permissible (i.e. easier to implement in hardware) given the constraints. Also, the normalization factors are the maximum possible values of each parameter (e.g. (i) the upper bound on a decision variable or (ii) the largest value in the table of point design parameters).

For the purpose of sizing a system to meet the given requirements, several point designs were generated with the different objectives (i.e. optimal mass savings and optimal performance)

and scored, weighting the benefits, decision variables, optimization objectives, and technology readiness on an equivalent basis (and the individual terms equally within these groups). In practice, these weights should be tailored to the needs of the designer. Nevertheless, some of the key design points and associated scores are shown below in Tables 5.1, 5.2, and 5.3, relating to results from designing for optimal performance, optimal mass, and a hybrid between the two, respectively, assuming a carbon fiber rotor-based design. Also, the design points were generated using a design-of-experiments, full factorial test matrix approach wherein variation of each decision variable was controlled (either fixed or free) to isolate the relationships between decision variables, benefits, and performance. Only a sample of these variation types (all of which use a carbon fiber rotor and permit l_{rot} and Ω_{max} to freely vary) are shown in the tables where the types are defined to be I: $\dot{\Omega}$ fixed at upper boundary, $\dot{\delta}$ free to vary, II: $\dot{\Omega}$ free to vary, $\dot{\delta}$ fixed at upper boundary, III: $\dot{\Omega}$ free to vary, $\dot{\delta}$ fixed at lower boundary, IV: $\dot{\Omega}$ fixed to intermediate boundary, $\dot{\delta}$ fixed at upper boundary, V: $\dot{\Omega}$ fixed to intermediate boundary, $\dot{\delta}$ fixed at high intermediate boundary, VI: $\dot{\Omega}$ fixed to intermediate boundary, $\dot{\delta}$ free to vary, VII: $\dot{\Omega}$ free to vary, $\dot{\delta}$ fixed at high intermediate boundary, VIII: $\dot{\Omega}$ fixed at upper boundary, $\dot{\delta}$ fixed at upper boundary

Table 5.1: Selected Optimal J Results

Alt	J_c	Ω_{min}	Ω_{max}	l_{rot}	$\dot{\delta}$	$\dot{\Omega}$	E_d	P_d	Score	Rank	Variation
1	-94.6	50	34030	0.825	50	500	249	5220	0.452	1(Tie)	I
1	-94.6	50	34030	0.825	50	500	249	5220	0.452	1(Tie)	II
3	-78.5	990	38900	0.632	5	500	191	4460	0.392	15	III
3	-78.8	830	39100	0.624	50	500	189	4450	0.392	16	II
2	-35.4	230	76200	0.164	50	500	50	2330	0.224	108	I

Table 5.4 summarizes the key parameters for the selected near-term, mid-term, and long-term designs from applying this method. The chosen design concept uses a carbon fiber rotor 0.035 m long that is mechanically levitated in the near term and magnetically levitated in the long term with wheel speed envelope of 6510-50600 RPM, maximum gimbal rate of 50 deg/s, near- and mid-term maximum wheel acceleration of 96 rad/s², and long-term maximum wheel acceleration of 500 rad/s², resulting in an energy density of 76 W hr/kg and power density of 404 W/kg in the near-term evolving to 103 W hr/kg and 665 W/kg in the long-term.

Table 5.2: Selected Optimal MS Results

Alt	MS_c	Ω_{min}	Ω_{max}	l_{rot}	$\dot{\delta}$	$\dot{\Omega}$	E_d	P_d	Score	Rank	Variation
3	92.1%	6510	48950	0.0332	50	100	124	665	0.314	1	IV
3	92.1%	6510	48900	0.0332	45	100	124	665	0.314	3	V
3	92.1%	6510	50600	0.0332	50	96	125	665	0.314	12	II
1	87.0%	6510	48900	0.0332	50	100	76	403	0.280	105	VI
2	78.0%	6510	48950	0.0332	50	100	45	238	0.247	241	IV

Table 5.3: Selected Composite Results using Opt MS Parameters

Alt	J_c	MS_c	$\Omega_{min} - \Omega_{max}$	l_{rot}	$\dot{\delta}$	$\dot{\Omega}$	E_d	P_d	Score	Rk	Variation
3	-78.8	92.1%	6510-50600	0.033	50	96	125	665	0.772	1	II
3	-78.0	91.6%	6510-19200	0.037	45	301	116	622	0.757	2	VII
3	-78.8	92.1%	6510-15000	0.033	50	500	103	665	0.745	3	VIII
1	-94.6	87.0%	6510-50600	0.033	50	96	76	403	0.731	16	II
2	-35.4	78.0%	6510-50600	0.033	50	96	45	238	0.537	129	II

Table 5.4: Summary of Selected Designs Using Presented Sizing Algorithm

Parameter	Value	Value	Value
Timing	Near-term	Medium-term	Long-term
Alternative	1	3	3
Overall Rank	16	1	3
Minimum Wheel Speed, Ω_{Min} , RPM	6510	6510	6510
Maximum Wheel Speed, Ω_{Max} , RPM	50600	50600	15000
Rotor length, l_{rot} , m	0.0332	0.0332	0.0332
Maximum Gimbal Rate, $\dot{\delta}$, deg/s	50	50	50
Maximum Wheel Acceleration, $\dot{\Omega}$, rad/s^2	96	96	500
Energy Density, E_d , Whr/kg	76	125	103
Power Density, P_d , W/kg	404	665	665

5.3 Maximum Structural versus Usable Capacity Effects on Rotor Design

Either design approach (optimal mass savings or optimal performance) involves further constraining the basic optimal sizing problem (i.e. adding more constraint equations to the NLP). For the case of optimal mass savings, the problem is further constrained by the keeping the (non mass-margin) performance equivalent such that $P_m = P_{m_b}$, $C_m = C_{m_b}$, and $N_m = N_{m_b}$, permitting a controlled implementation in which only M_m changes through decision variable (Ω_x , Ω_n , $\dot{\Omega}$, $\dot{\delta}$, and l_r) selection. Interestingly, these constraints force an analytic solution to the problem for designs where the mass depends only on one decision variable (e.g. l_r), which can then be used to validate the results. The basic idea is to substitute the baseline margin values into equations 5.1, 5.2, and 5.3. Setting $C_{m_1} = C_{m_b}/N_{vc}$, $P_{m_1} = P_{m_b}/N_{vc}$, and $N_m = N_{m_b}$, and defining constant values c_1 , c_2 , and c_3 , one finds

$$c_{1_x} = l_r \left(\frac{\Omega_x^2 - \Omega_n^2}{\Omega_x^2} \right) = \frac{3600 (C_{m_b} + C_r)}{N_{vc} \sigma_\theta k_s \pi (r_o^2 - r_i^2)} \quad (5.27)$$

$$c_{1_u} = l_r (\Omega_x^2 - \Omega_n^2) = \frac{7200 (C_{m_b} + C_r)}{N_{vc} \pi \rho_r (r_o^4 - r_i^4)} \quad (5.28)$$

$$c_2 = l_r (\Omega_x - \Omega_n) \dot{\Omega}_x = \frac{2 (P_{m_b} + P_r)}{N_{vc} \pi \rho_r (r_o^4 - r_i^4)} \quad (5.29)$$

$$c_3 = l_r \Omega_n \dot{\delta}_x = \frac{2 (N_{m_b} + N_r)}{\pi \rho_r (r_o^4 - r_i^4) \chi |\vec{v}|_{tc}} \quad (5.30)$$

This equation set illustrates the direct dependency of l_r on the remaining decision variables when ESACS to baseline performance is equal. In contrast, for the equivalent mass problem, one needs to further constrain the basic NLP through equating $M_m = M_{m_b}$, but in that case, there is more design freedom to choose results and an analytic solution isn't as easy to find. If, for example, a constraint is added, such as $N_m = N_{m_b}$, which is realistic in the case of the satellite customer that only desires equivalent torque and equivalent mass with increased energy storage and/or peak power demand to operate an experiment, a similar set of analytic equations can be found. However, we only examine the equivalent performance case here and draw conclusions about its impact on the design. The results are next illustrated in a mass savings sizing example.

5.4 Numerical Example and Results

We now size the small satellite ESACS for the spotlight Synthetic Aperture RADAR (SAR) example investigated in [14] as summarized by table 5.5. This type of mission requires agile slewing simultaneously with high instantaneous peak power demand. Table 5.5 reflects realistic requirements for such a system. Notice the agile slew maneuver parameters, θ_f , t_f , and t_{off} and high peak power demand, P_r delivering mission payload power for 10% of the eclipse period. As in [14], the outer and inner rotor radii are fixed while the rotor length is permitted to vary.

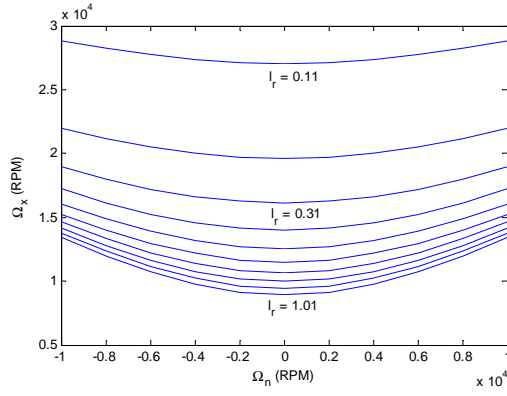
Before analyzing different feasible design points, it's instructive to investigate the parametric effects of decision variable changes. A sample of these trends is included as Figures 5.15(a) through 5.15(d). Figures 5.15(a) and 5.15(b) show loci of minimum versus maximum wheel speed design points for different rotor lengths. The difference between these plots is that the factor c_1 is reduced by three magnitudes in Fig. 5.15(b), resulting in a sharper vertex pointing to a specific minimum wheel speed. Fig. 5.15(c) shows $\dot{\delta}_x$ asymptotically changes with Ω_n when holding $P_m = P_{m_b}$. In contrast, Fig 5.15(d) shows the maximum wheel acceleration has a smaller effect on the minimum wheel speed for similar conditions. Figure 5.15(e) shows a very interesting trend in rotor length versus maximum wheel speed for different minimum wheel speeds as minor increases in rotor length greatly decrease the required maximum wheel speed to maintain the baseline performance. The reduced speeds lead to extended lifetime and reduced control complexity. Prior to finding the longest rotor one can find for his or her new VSCMG-based ESACS, it's imperative to understand that this increased rotor length

Table 5.5: Space RADAR Requirements and Assumptions

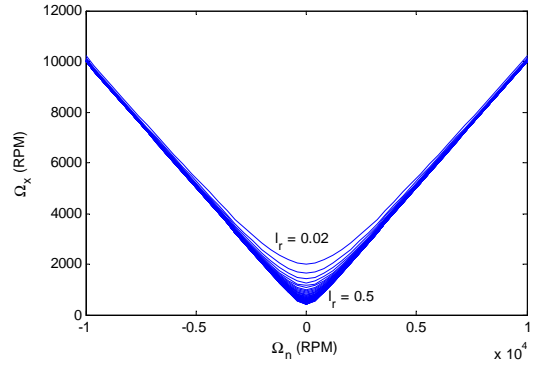
Parameter	Value
Orbit Altitude, h , km	450
Depth-of-Discharge, dod , %	80
Transmission Efficiency, x_{msn} , %	90
Peak Power Demand, P_r , W	1100
Eclipse Duty Cycle, d_{ty} , %	10
Power Bus Voltage, V_{bus} , V	28
Max Single-axis inertia, $I_{T_{max}}$, kg m ²	120
Slew maneuver angle, θ_f , deg	140
Slew maneuver time, t_f , s	70
Slew maneuver dead-band, t_{off} , s	12
Satellite Total Mass, M_{sc} , kg	400
Allowable Satellite Mass, M_{ta} , kg	450
Allowable ACS plus ES Mass, M_r , kg	45
Allowable Outer Rotor Radius, r_o , m	0.1016
Allowable Inner Rotor Radius, r_i , m	0.0500

will eventually lead to a reduced mass savings which may still reside in the desired realm.

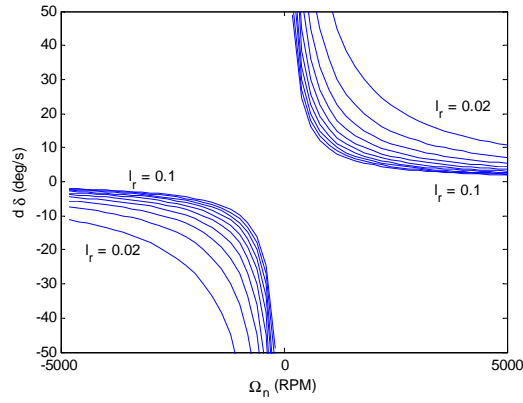
Using the given mission requirements, subsystem point designs were found three different ways for the maximum mass savings problem with fixed minimum and maximum wheel speeds and wheel acceleration, gimbal rate, and rotor length. The first two approaches use the available capacity equation presented in [14] while the third approach applies the usable capacity concept defined here. The designs were determined in the following order: first, an optimization with fixed rotor length was done, then, an optimization was done by changing the available capacity equation to the method from [14], and finally, a separate optimization was done for the old design. This approach yielded three distinctly different point designs that are illustrated in Figure 5.15(f) and summarized in Table 5.6. In this plot, one can see the two lines represent available capacity for multiple point designs by rotor length, C_{a_x} representing the old method and C_{a_u} representing the new one, labelled I, II, and III. Notice that the two point designs from the old method are shown as points I and II on the top line and fall on the same continuum if one were to use the C_{a_x} value for C_a . In contrast, the second line shows the practical C_{a_u} values for C_a and contains point III. One can also see that III is directly below I since both have the same rotor length. Thus, Figure 5.16 highlights the similarities and differences between the showcased design points based on usable and maximum structural available capacity.



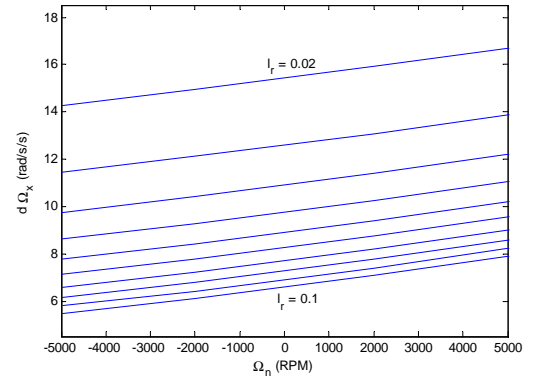
(a) Min versus Max Wheel Speed by Rotor Length



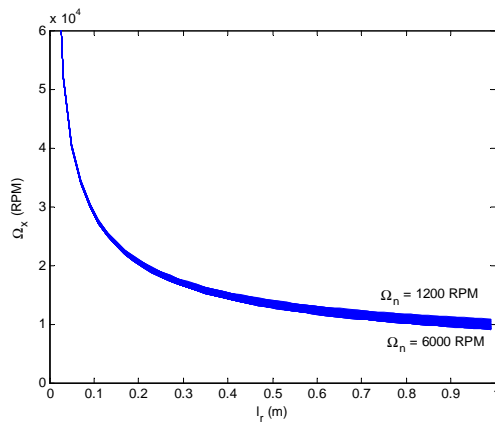
(b) Magnified Min versus Max Wheel Speed by Rotor Length



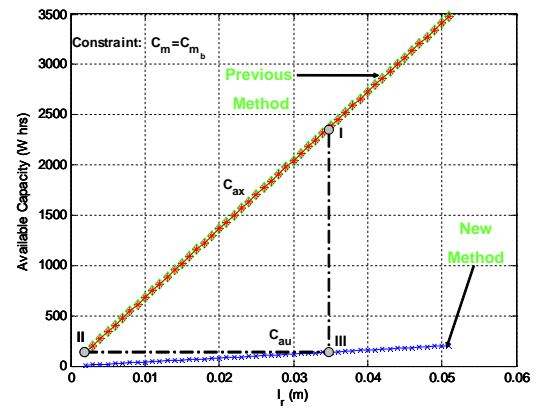
(c) Min Wheel Speed versus Gimbal Rate by Rotor Length



(d) Wheel Acceleration versus Gimbal Rate by Rotor Length



(e) Rotor Length v. Max Speed



(f) Rotor Length v. Available Capacity

Figure 5.15: VSCMG-based ESACS Figures

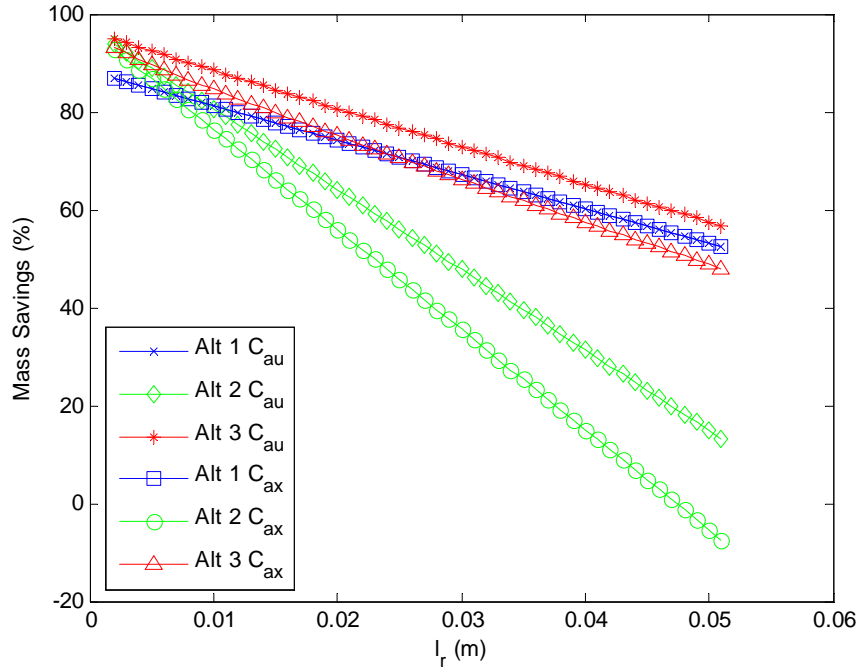


Figure 5.16: Capacity Impact on Mass Savings

The culmination of this effort yields the mass savings versus rotor length for different design alternatives as reflected in Figure 5.16. Here one can see two curves for three candidate design alternatives explained in ref. [14] where one curve is lower than the other. The lower one corresponds to the more accurate C_{au} calculation while the higher one reflects a $C_a = C_{ax}$ approach. The direct impact is a 20 - 30 % decrease in mass savings using the more realistic C_{au} for a given set of requirements. Even with this change, the NLP framework for casting this design problem and its constraints continues to be a viable method for comparing and contrasting a conventional momentum wheel plus secondary battery approach with a VSCMG-based ESACS.

5.5 Gimbal Motor Sizing

Due to its torque amplification property, the gimbal motor is the quintessential component in a single-gimbal, Variable Speed Control Moment Gyroscope (VSCMG) system. The gimbal motor gives the VSCMG, especially for a small satellite Energy Storage and Attitude Control System (ESACS), its fundamental advantages over other attitude control actuators such as momentum wheels, magnetorquers, and gas-jet thrusters. Thus, properly selecting this

Table 5.6: Point Design Comparison

Parameter	Pt 1 C_{a_x} by C_m	Pt 2 C_{a_x} by l_r	Pt 3 C_{a_u}
Baseline Power Margin, P_{m_b} , Whr	1225.31	1225.31	1225.31
Baseline Torque Margin, N_{m_b} , Nm	1.1632	1.1632	1.1632
Baseline Mass Margin, M_{m_b} , kg	19.62	19.62	19.62
Baseline Capacity Margin, C_{m_b} , Whr	47.74	47.74	47.74
Minimum Wheel Speed, Ω_n , RPM	6510	6510	6510
Maximum Wheel Speed, Ω_x , RPM	48416	48416	48416
Maximum Wheel Accel, $\dot{\Omega}_x$, rad/s ²	13.35	228.92	13.35
Maximum Gimbal Rate, $\dot{\delta}_x$, deg/s	4.73	81.11	4.73
Rotor Length, l_r , m	0.035	0.002	0.035
Inst. Peak Power Margin, 1-VSCMG, P_m , W	306.33	306.33	306.33
Torque Margin, 4-VSCMGs N_m , Nm	1.1632	1.1632	1.1632
Alt. #1 Mass Margin, 1-VSCMG, $M_{m_{11}}$, kg	8.9432	10.4158	8.9432
Alt. #2 Mass Margin, 1-VSCMG, $M_{m_{12}}$, kg	7.4148	10.8479	7.4148
Alt. #3 Mass Margin, 1-VSCMG, $M_{m_{13}}$, kg	9.2833	10.8198	9.2833
Capacity Margin, 1-VSCMG C_m , Whr	574.101	11.936	11.936
Available Capacity, $C_a = C_{a_x}$ or C_{a_u} , Whr	2387.86	139.200	139.200
Mass Optimization Constant c_{1_x}	3.4367 $E - 2$	2.0034 $E - 3$	3.4367 $E - 2$
Mass Optimization Constant c_{1_u}	8.8348 $E + 5$	5.1502 $E + 4$	8.8348 $E + 5$
Mass Optimization Constant c_2	1.9691 $E + 0$	1.9691 $E + 0$	1.9691 $E + 0$
Mass Optimization Constant c_3	2.0497 $E + 3$	2.0497 $E + 3$	2.0497 $E + 3$
Alt. #1 Mass Savings, MS_1 , %	63.64	86.85	63.64
Alt. #2 Mass Savings, MS_2 , %	39.55	93.66	39.55
Alt. #3 Mass Savings, MS_3 , %	69.00	93.22	69.00

critical component is paramount to its success, especially in applications requiring high wheel speeds, such as combined energy storage and attitude control.

Reference [148] describes the process for sizing gimbal motors for satellite CMGs. Figure 5.17 captures the logic flow in this process. As one can see, sizing depends upon the gimbal axis inertia of the actuator (assumed as a rigid body for now), the gimbal rate defined in the optimal sizing process just described with added safety margin, the maximum wheel angular momentum, spacecraft ACS bandwidth, and the maximum required body rate for the defined attitude reference maneuver computed from the slew requirements. These factors combine to permit the designer to select a gimbal motor (assumed to be a Brushless DC (BLDC) motor here). Examples of applying this approach are given in [148].

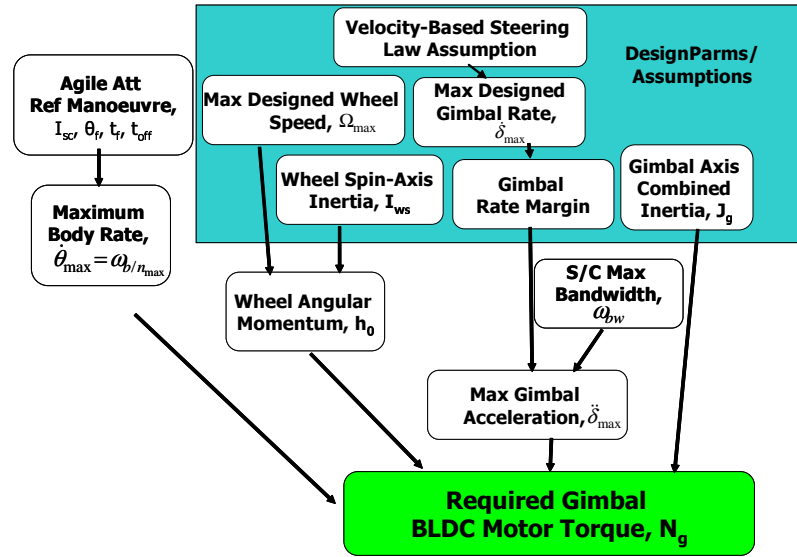


Figure 5.17: Gimbal Motor Sizing Process

5.6 Summary

First, a compact and novel optimal sizing algorithm for a small satellite combined energy storage and attitude control subsystem (ESACS) has been developed and applied to a practical synthetic aperture RADAR mission to compare and contrast technology design alternatives, trade key system/decision variable parameters, and showcase several benefits. Merging the subsystems eliminates redundant secondary battery mass while incorporating advanced technologies such as composite flywheel rotors and magnetic levitation allows higher sustained

rotor speeds and further decreases subsystem and total spacecraft mass. Flywheel energy density advantages are on par with improvements in new secondary battery technologies while increased flywheel power densities over mature and burgeoning secondary batteries follows from the ability to rapidly discharge the energy in the flywheel at much faster rates. Employing magnetically-levitated flywheels also permits longer subsystem lifetime through more charge/drain cycles at higher depths-of-discharge than secondary batteries. The employed redundant VSCMG pyramid configuration with flywheel speed variability permits transition to momentum wheel mode to pass through singularities while predominantly using the CMG mode for its torque amplification advantages. Increased slewing agility is a well-documented direct consequence of employing this CMG mode.

In the new sizing/optimization method, a performance index is used to identify trends in decision variables and pinpoint the optimum rotor length for different technology alternatives. Three candidate performance indices were presented and compared leading to selection of the best of these, which uses an experimental error approach, since it best isolates the transition from conventional to VSCMG-based ESACS design utility.

The sizing/optimization algorithm has shown some important design trends for an ESACS besides the subsystem/spacecraft mass savings. Increasing the gimbal rates of the VSCMGs at an optimal mass reduces the required flywheel acceleration therefore enhancing CMG torque amplification and reducing the problem of flywheel lifetime due to very high wheel speeds. Analysis of the performance index shows that at an optimal mass the maximum flywheel acceleration corresponds to an optimal rotor length, which is used to select the optimal ESACS design. When further analyzed for flywheel acceleration against flywheel speed, the data shows that the embedded motor magnetic bearing technology alternative is superior to other technologies but critical flywheel acceleration points were determined in which other motor technologies can have similar performance values. Additional analysis highlights the benefit of using carbon fiber flywheel rotors—the best performance with maximum mass savings. This fact was also used to qualitatively validate the developed algorithm.

The sizing algorithm was further refined for usable available energy capacity. The modified algorithm was applied to a practical mission to compare and contrast the effects of this refinement. The key resulting impact is that the rotor length must be increased to meet capacity requirements, thereby reducing the amount of mass savings enjoyed by the design. Sensitivity to rotor length is heightened in that the rotor outer and inner radii are assumed fixed for the given small satellite design, thus the rotor length is the primary source for

increasing wheel inertia. Plots highlighting the decision variable trends from this usable available capacity change were presented and illustrate the system performance impact. From these plots and based on the assumption that system performance must remain constant, one can see that increasing maximum wheel speed actually increases the required minimum wheel speed when rotor length is held constant, the maximum wheel speed corresponding to zero minimum wheel speed increases as rotor length increase, this direct relationship in maximum-minimum wheel speed becomes more pronounced as the constant c_1 is decreased, maximum wheel acceleration increases with minimum wheel speed increase and rotor length increases, maximum gimbal rate decreases with minimum wheel speed increase when rotor length increases actually increasing maximum gimbal rate, and maximum wheel speed falls quite rapidly if rotor length is increased thereby forming a key decision variable trade in terms of maximum wheel speed for mass savings.

It was also shown that the optimal mass curve for maximum structural available capacity, a straight line for a given design, forms a boundary for the usable available capacity curve. However, the latter curve is a more appropriate quantity for an achievable design as it focuses on the energy capacity actually convertible to power based on motor/generator peak wheel speed capability. This also relates directly to a more realistic, decreased yet still significant mass savings as compared to the baseline design method.

By using this design approach with more realistic usable available capacity equation, one can best optimally size a VSCMG-based ESACS for optimal mass, quickly identify its utility compared to a contemporary system, and pinpoint the key system parameters required to make the design a reality. The leads to a more mass efficient, lighter yet highly effective subsystem design at less mass.

Chapter 6

Steering Laws

This chapter investigates the ESACS VSCMG steering laws mentioned in Chapter 4. These laws fall into two primary categories: simultaneous and one-way coupled. The simultaneous steering laws are the only ones described in the existing literature whereas the one-way coupled laws employ a new approach proposed here. The former of these applies when the ESACS is permitted to command the wheel and gimbal motors at the same time while the latter is a more immediately practical method in which the wheel motors are controlled independently of the gimbal motors. The practicality arises when an EPS incorporates flywheel batteries directly into its energy topology via a passive circuit. In such a case, the wheel changes momentum automatically during energy storage and drain which imparts a disturbance torque on the spacecraft's attitude. Depending upon the relative magnitude of the wheel accelerations and wheel spin-axis inertias of the VSCMGs this disturbance torque can have a significant impact on tracking the desired attitude. It must be rejected by the gimbals since the wheels are controlled via an isolated electrical circuit. Thus, the gimbals are not only used for attitude maneuvers but also rejecting wheel disturbance torques from changing speeds.

Investigating these steering law categories, the chapter begins by presenting the literary context of simultaneous steering for attitude and power tracking with VSCMGs first defined in [12, 133]. Then, the mathematical theory behind this approach is presented. Next, a method for separating gimbal rate and wheel speed VSCMG steering in the practical one-way coupled method is theoretically developed. Following this, two small satellite numerical examples, one a simultaneous steering law comparison and the other a one-way coupled steering law comparison are given along with their resulting performance. Then, these results

are analyzed and discussed.

A refined version of the ACS block diagram presented in Chapter 4 is shown in Fig. 6.1 Here, one can see that the steering laws are a key function within the overall ACS block

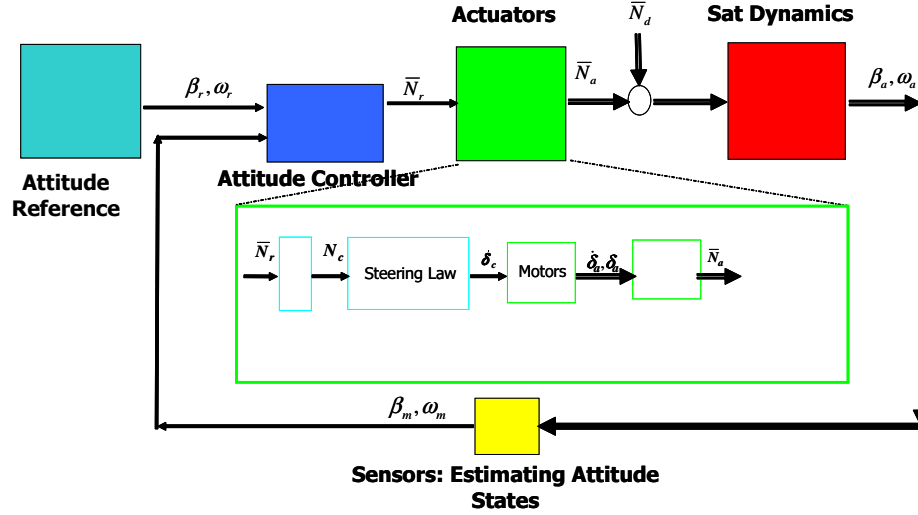


Figure 6.1: Attitude Control Block ed Diagram with CMG Steering Architecture Inset

architecture and serve an important role: ensure the VSCMG actuators are employed as best possible to meet the given power and attitude tracking requirements.

6.1 Literary Background

The literary history behind CMGs, VSCMGs, and flywheel energy storage for satellites is summarized in Chapter 2. Key related contributions were made in [1, 17, 58, 62, 64, 66, 68, 73, 76]. The CMG work enabled Ford and Hall's efforts, who were the first to investigate the generic nonlinear equations of motion for momentum exchange devices (i.e. Reaction Wheels, Momentum Wheels, and CMGs) [72, 73]. Thus generalising the theory for these devices led directly to the work by Schaub, Junkins, and Vadali, which detailed, for the first time, the nonlinear dynamics behind single-gimbal VSCMGs and inherent singularity avoidance properties these actuators provide [74–77]. Flywheel Energy Storage (FES) results engendered the gyrostat investigation in ref. [58] and simultaneous control design for an ESACS subcategory, an Integrated Power and Attitude Control System (IPACS), using four redundant, non counter-rotating, momentum wheels in ref. [59]. In parallel to these efforts, Hall gave an excellent literature review for this problem in ref. [19]. Another excellent resource

capturing the evolution of flywheel technology for satellites is captured in [21].

Building on Shen et. al.'s work, Richie et. al. [12] showed simultaneous momentum wheel and gimbal control through a CMG-like steering law method were possible by employing the new momentum exchange device theoretical generalization known as the VSCMG, conceptualized by the combined efforts of Ford and Hall [72,73] and Schaub et. al. [76]. The VSCMG development was predicated on the detailed CMG theory offered by Jacot and Liska [64], Marguilles and Aubrun [65], Oh and Vadali [66], Wie [147], and several others [67–69]. Following Richie et. al.'s work, Yoon and Tsiotras identified a wheel speed equalization technique for reducing the risk that one VSCMG reaches saturation, effectively increasing a VSCMG-suite's utility [109,110]. Other related work involves Roithmayr's VSCMG-gyrostad generalization to gimballed, counter-rotating wheels including satellite to actuator damping torque [150] with direct application to systems with a mixture of counter-rotating MWs and standard CMGs.

Advancing this VSCMG work for ESACS, ref. [14] optimally sizes the actuator components for a realistic small satellite mission. The results from this development identified maxima for the operation of these actuators, however the related steering laws required further advancement. Such steering law advancement followed with the efforts of refs. [152,153], which studied the effects of adapting the CMG-based Generalized Singularity Robust (GSR) steering law from [154,155] for the combined attitude and power tracking case using CMG/MW weighting matrices which when misordered, force singularity. The impact of crossing these weighting matrices is demonstrated further in this paper, but follows from how the singularity condition is calculated and implemented.

As one can see, much has been studied in the recent past on combined attitude and power tracking. However, all of this work has focused on simultaneously commanding the wheel accelerations and gimbal rates whereas there appears to be no mention of a more practical case – accommodating independent control of the wheels and gimbals. This case is practically relevant as existing designs permit the plug-and-play of the wheels into the electrical power topology as flywheel batteries. Then, the torques generated through changing wheel speeds as flywheel batteries need to be handled by attitude control steering – a task which only has command authority over the gimbals through the gimbal rates [12]. Therefore, there is a void in the archived literature on treatment of ESACS which control the VSCMG motors independently. This void is fulfilled later in this chapter, but first further development of simultaneous tracking is in order.

6.2 Vehicle Controllers

There are two main vehicle attitude controllers which are relevant to the given problem. The first of these is the Lyapunov controller presented in [12, 107, 108] which involves driving the inertial angular position and angular velocity errors to zero based on desired performance gains. The second controller is the variable-limiter proportional-plus-integral-plus-derivative (VLPID) controller presented by Wie et. al. in [154, 156]. Both of these controllers were applied to the present attitude and power tracking cases for comparing and contrasting the effectiveness of the ESACS approach. However, since the Lyapunov controller used is essentially a PD controller and the VLPID controller contains the PD terms plus additional terms, the VLPID is more general than the Lyapunov controller. Thus, the VLPID controller is the preferred vehicle controller of choice. Regardless, each of these controllers is mathematically summarized next.

6.2.1 Lyapunov

The equation for the Lyapunov controller was presented in eq. 4.18 of Chapter 4. Repeating it here for clarity yields

$$\overline{\mathbf{N}}_r = \mathbf{K}(\boldsymbol{\omega} - \boldsymbol{\omega}_r) - kq^T(\beta)\beta_r - \tilde{\boldsymbol{\omega}}\mathbf{I}_{sc}\boldsymbol{\omega} \quad (6.1)$$

Notice that the key information of this controller is the current vehicle angular position and angular velocity. As shown in [12, 107, 108] and Appendix D, this controller stably tracks the desired attitude position and attitude rates of the system. Although developed from a Lyapunov based stability analysis approach, this controller is also often termed a PD controller since it has a proportional gain related to the position error and a derivative (rate) gain multiplied by the rate error. However, it does lack direct accommodation of actuator and vehicle saturation limits. In contrast, these items are included in the Variable Limiter Proportional-Plus-Integral-Plus-Derivative (VLPID) controller highlighted next.

6.2.2 Variable-Limiter PID

The VLPID was originally developed by Wie et. al. in [156] and further applied in [154, 155]. Due to its integral term, it allows for more accurate steady state control whilst still driving the present vehicle position to the desired position. An added bonus, though, is the inclusion

of actuator and vehicle saturation limits. This controller permits one to not only include the desired damping ratio (which affects percent overshoot) and settling time, but also command torque limits based on actuator capabilities, momentum saturation terms (which is driven by the maximum wheel speed), gimbal rate saturation limits, and optionally, if applying the results from [157], gimbal angle limits. Thus, not only are performance settings included along with Lyapunov-like asymptotic stability, but practical saturations limits are inherent as well. A summary of the equations governing this controller are given in equations 6.2 through 6.6

$$\overline{\mathbf{N}}_r = -\mathbf{I}_T \left(2k \underset{L_i}{sat} \left(\mathbf{e} + \frac{1}{T} \int \mathbf{e} \right) + c(\boldsymbol{\omega} - \boldsymbol{\omega}_r) \right) \quad (6.2)$$

$$L_i = \frac{c}{2k} \min \left(\sqrt{4a_i |e_i|}, |\omega_i|_{max} \right) \quad (6.3)$$

$$\mathbf{D}^\# = \mathbf{D}^T [\mathbf{D}\mathbf{D}^T + \alpha\mathbf{G}]^{-1} \quad (6.4)$$

$$\mathbf{u} = -\overline{\mathbf{N}}_r - \mathbf{F}\boldsymbol{\Omega} \quad (6.5)$$

$$\dot{\delta}_c = \underset{\delta_{max}}{sat} \left(\mathbf{D}^\# \mathbf{u} \right) \quad (6.6)$$

where i varies from 1 to 3 for the general 3-dimensional motion case, sat_{L_i} implies that when the term in question is saturated, it cuts off at the absolute value of L_i , $sat_{\delta_{max}}$ saturates the term to the absolute value of δ_{max} , a_i is the maximum permissible vehicle acceleration in the i_{th} direction, e_i is the angular position error limit, $\omega_{i_{max}}$ is the maximum permissible vehicle velocity in the i_{th} direction, and c, k, T are derivative, proportional, and integral inverse controller gains. The other parameters follow as before.

6.3 Simultaneous Steering

As shown in refs. [12, 109, 133], one can store (drain) energy by increasing (decreasing) the VSCMG wheel speeds in combinations that still permit the desired net torque for attitude tracking. The mechanics of this process is developed next.

From eqs. 4.40 and 4.21, one can define the set

$$\begin{bmatrix} \mathbf{E} & \mathbf{D} \\ \mathbf{V} & \mathbf{0}_n \end{bmatrix} \mathbf{u} = \begin{bmatrix} \mathbf{Q} \\ \mathbf{S} \end{bmatrix} \mathbf{u} = \begin{bmatrix} N_c \\ P_c \end{bmatrix} \quad (6.7)$$

where $\mathbf{u} = [\dot{\boldsymbol{\Omega}}^T \ \dot{\boldsymbol{\delta}}^T]^T$, $N_c = \overline{\mathbf{N}}_r - \mathbf{F}\boldsymbol{\Omega}$, $P_c = P_r(t)$, $\mathbf{Q} = [\mathbf{E} \ \mathbf{D}]$, \mathbf{O}_n is a $1 \times n$ matrix of zeros, and $\mathbf{S} = [\mathbf{V} \ \mathbf{0}_n]$. Eq. 6.7 enables simultaneously tracking an attitude reference and a

power profile provided the quantity $\mathbf{S}(I_n - \mathbf{Q}\mathbf{Q})$ is not $[0 \dots 0_n]^T$ as mentioned in [110]. From this, the fundamental VSCMG attitude steering problem is ensuring

$$\mathbf{Q}u_c = \mathbf{Q} \begin{bmatrix} \dot{\Omega} \\ \dot{\delta} \end{bmatrix}_c = N_c \quad (6.8)$$

which yields a general VSCMG steering law

$$\begin{bmatrix} \dot{\Omega} \\ \dot{\delta} \end{bmatrix}_c = \mathbf{Q}^\dagger N_c \quad (6.9)$$

where \mathbf{Q}^\dagger is some generalized inverse of \mathbf{Q} such as

$$\mathbf{Q}^\dagger = W_1 \mathbf{Q}^T (\mathbf{Q} W_1 \mathbf{Q}^T)^{-1} \quad (6.10)$$

in which W_1 is a weighting matrix for prioritizing the two VSCMG modes: Momentum Wheel (MW) mode and CMG mode. As defined in [12, 74, 107] and others, $W_1 = [W_s W_g]$ with the wheel weights as W_s and the gimbal weights W_g . Interestingly, the method in [109] (and further investigated in [153]), sets the W_g term based on the singularity condition of \mathbf{D} whereas the method contained in [74] and [12] applies the weighting to the wheel term, W_s . The difference in the two approaches will be presented later in a numerical example.

6.4 One-way Coupled Steering

Despite the advantages of simultaneous VSCMG steering for ESACS, originally defined for IPACS in [133], [107], [12], and [108], a more practical near-term implementation for most satellite programs is to physically separate the ES function from the ACS function of the VSCMGs. In this approach, the attitude torques produced by the energy storage system's wheel acceleration adjustments are accommodated in the ACS through gimbal control. In this case, it is assumed that wheel speed measurements for the VSCMGs are available as inputs to the ACS steering law, but command of these wheel speeds (i.e. wheel accelerations) is strictly governed by the EPS electrical circuit (e.g. using a DET or PPT approach). This change in scheme engenders a modification of the simultaneous steering equations presented earlier. Furthermore, for the benefit gained in permitting the EPS to have exclusive wheel control, a drawback is incurred in that automatic singularity avoidance via the MW-mode of the VSCMGs now is changed to requiring a logical CMG-type singularity avoidance law to steer through these singularities. However, in the latter case, much literature (as discussed

much already) exists addressing the topic of conventional singularity avoidance and can be applied here. The primary difference is that the potential singular directions change in time as the momentum envelope size and shape changes with changing wheel speeds. Nevertheless, the idea of separating the systems is further investigated mathematically in the remainder of section 6.4, then tested via numerical simulation in section 6.4, and analyzed in section 6.4.4.

The simultaneous attitude and power tracking steering equation set given in eq. 6.7, which follows from eqs. 4.16 and 4.37 of Chapter 4, is comprised of an attitude part (its top row) and a power part (the bottom row). The attitude part was presented as eq. 4.21 and is typically used for classical, fixed rotor speed, single-gimbal CMGs. The fixed speed means that $\mathbf{E}\dot{\boldsymbol{\Omega}}$ is zero and the resulting steering law is

$$\dot{\delta}_c = \mathbf{D}^\dagger (\overline{\mathbf{N}}_r - \boldsymbol{\omega} \times \mathbf{h}) = \mathbf{D}^\dagger (\overline{\mathbf{N}}_r - \mathbf{F}\boldsymbol{\Omega}) \quad (6.11)$$

where \mathbf{D}^\dagger is the applicable pseudo-inverse steering logic for several different methods, including null motion, preferred gimbal angles, singularity robust steering logic, etc. contained in the literature surveyed in Chapter 2. Meanwhile, the energy storage part was presented in eq. 4.40 and contains an individual solution of

$$\dot{\boldsymbol{\Omega}}_c = \mathbf{V}^\dagger \mathbf{P}_c \quad (6.12)$$

Together, eqs. 6.11 and 6.12 differ by a factor of $\mathbf{E}\dot{\boldsymbol{\Omega}}$ in the solution to eq. 6.7, which seeks to find the control vector at the current time step, $u_c = [\dot{\boldsymbol{\Omega}}_c^T \ \dot{\delta}_c^T]^T$ using the wheel speed measurements from the previous time step, $\boldsymbol{\Omega}$. In fact, eq. 6.7 describes a one-way coupled system. That is, its attitude part is coupled in the control terms, $\boldsymbol{\Omega}_c$ and $\dot{\delta}_c$, whilst the power equation is independent of $\dot{\delta}_c$. Thus, a practical limitation of the simultaneous steering approach is that it requires the wheel speed and gimbal rate control be driven from the same controller with synchronized commanding of $\dot{\boldsymbol{\Omega}}_c$ and $\dot{\delta}_c$. However, to be effective, the electrical power subsystem, critical to typical spacecraft, must have direct control of the battery state-of-charge at all times. For flywheel batteries, this means direct command of the wheel speed. Unless a paradigm shift in spacecraft EPS architecture is instantiated in which the EPS and ACS are completely integrated into one system at the initial design stage, near-term ESACS implementations will require that the EPS control $\dot{\boldsymbol{\Omega}}$ through its battery charge control system. This is usually done one of two ways, via Direct Energy Transfer (DET) or via Peak Power Tracking [114]. The DET control of $\dot{\boldsymbol{\Omega}}$ is an integral aspect of the demonstrated ESACS in chapters 7 and 8. Nevertheless, from an ACS perspective, one can

accommodate the loss of wheel controllability in the gimbal rate steering law by estimating the wheel acceleration in addition to the wheel velocity provided these values are observable in the wheel motor/generator telemetry. Put another way, if the EPS is viewed as independently controlling the power part of eq. 6.7, then the top part can be rearranged as

$$D\dot{\delta} = \overline{N_r} - F\Omega - E\dot{\Omega} \quad (6.13)$$

At this point, the shift in thinking changes to the ACS using the EPS inputs (which drive the $E\dot{\Omega}$ term) as a disturbance torque that is accommodated in the steering through this $E\dot{\Omega}$ term. To differentiate VSCMG actuator states that have been measured on the previous time step, a bar is added to the Ω and $\dot{\Omega}$, thus eq. 6.13 becomes

$$D\dot{\delta} = \overline{N_r} - F\overline{\Omega} - E\overline{\dot{\Omega}} \quad (6.14)$$

Summarizing the refined steering equations yields

$$\begin{bmatrix} 0_n & D \\ V & 0_n \end{bmatrix} u = \begin{bmatrix} \overline{N_r} - F\overline{\Omega} - E\overline{\dot{\Omega}} \\ P_c \end{bmatrix} \quad (6.15)$$

This equation set represents contemporary systems implementing ESACS with flywheel batteries in the electronics loop wherein power is affected by changing $\dot{\Omega}$ and the ensuing attitude disturbance is accommodated in the $E\overline{\dot{\Omega}}$ term of the gimbal rate steering law. Furthermore, future systems that aim to completely integrate ACS and EPS by driving $u_c = [\dot{\Omega}_c^T \ \dot{\delta}_c^T]^T$ together can use eq. set 6.15 as an evolutionary stepping stone toward eq. set 6.7.

The primary limitation of eq. set 6.15 is that the simultaneous control conducive to VSCMG singularity avoidance through the momentum wheel mode is sacrificed. Also, eq. set 6.15 implies accurate estimates of $\overline{\dot{\Omega}}$ given that estimates of $\overline{\Omega}$ are already a feature of practical CMG systems as part of \mathbf{h} in the $\omega \times \mathbf{h}$, or $F\overline{\Omega}$, term.

Numeric Examples

The following two examples apply the concepts presented above. The first uses three simultaneous steering laws for a small satellite system with parameters proportionally similar to the examples found in previous work by Richie et. al. [12], Yoon and Tsiotras [109,110], and Richie, Asghar, and Lappas [153]. Then, the second example uses the same small satellite parameters for two candidate one-way coupled system steering laws.

Table 6.1: Cases

No.	Description
1a	Simultaneous Steering Law, Inverse Weighting, Lower Initial Wheel Speeds
1b	Simultaneous Steering Law, Inverse Weighting, Higher Initial Wheel Speeds
1c	Simultaneous Steering Law, Logical Weighting, Higher Initial Wheel Speeds
2a	One-Way Coupled Steering Law, $\dot{\delta}_c = \overline{N}_r - \mathbf{F}\Omega$
2b	One-way Coupled Steering Law, $\dot{\delta}_c = \overline{N}_r - \mathbf{F}\Omega - \mathbf{E}\dot{\Omega}$

The power profile used here assumes the subsystems are run at 100% eclipse duty cycle with the payload run at 10% eclipse duty cycle. Another important item to mention is that both examples do not treat wheel or gimbal motor friction (for mechanical bearings) or eddy current losses (for magnetic bearings). Such treatment is beyond the scope of the key steering law objective: implement steering laws for a VSCMG ESACS to advance and validate practical control strategies.

Each of the two examples has been broken down into a set of cases, yielding the five cases listed in Table 6.1. The three cases for the simultaneous steering example are listed as cases 1a, 1b, and 1c, whereas those for the one-way coupled steering example are in cases 2a and 2b. Cases 1a and 1b swap the wheel and gimbal weighting terms from the work done in [12] and differ in wheel speed initial conditions. The goal of this swap was originally addressed by Yoon and Tsiotras in [110] as a method to investigate the worst case singularity avoidance environment of VSCMGs for an ESACs. On the other hand, case 1c uses the same weighting approach included in [12] and employs the higher set of initial wheel speeds matching that of case 1b. Next, cases 2a and 2b use one-way coupled steering laws, the primary difference being the inclusion of the wheel torque disturbance term, $\mathbf{E}\dot{\Omega}$, in case 2b. As alluded to earlier in this chapter, the primary assumption for cases 2a and 2b are that the wheels and gimbals are commanded independently, but the gimbal control will have wheel speed measurements and (for the more practical case 2b) wheel acceleration estimates. Note that several other cases were run using various settings, but these five cases are most representative of the advantages and disadvantages in the steering law approaches. Parameters for the two examples are given in Table 6.2.

Table 6.2: Simulation Parameters

Symbol	Value
N_{vc}	4
θ , deg	54.75
$\omega(0)$, rad/s	[0 0 0]
$\beta(0)$	[-0.5 0.5 -0.5 0.5]
$\delta(0)$, rad	$[\frac{\pi}{4} -\frac{\pi}{4} -\frac{\pi}{4} \frac{\pi}{4}]$
$\dot{\delta}(0)$, rad/s	[0 0 0 0]
$\Omega(0)_{smaller}$, rpm	[11000 9625 8250 7150]
$\Omega(0)_{larger}$, rpm	[20000 17500 15000 13000]
I_{W_j} , kgm ²	diag{0.009946, 0.005, 0.005}
I_{G_j} , kgm ²	diag{0.001, 0.001, 0.001}
I_{sc} , kgm ²	$\begin{bmatrix} 120 & -5 & -3 \\ -5 & 100 & 1.5 \\ -3 & 1.5 & 100 \end{bmatrix}$
K_{nom}, k_{nom}	diag{0.1, 0.1, 0.1}, 0.01
K_{big}, k_{big}	diag{5.5, 5.5, 5.5}, 9.54
$\mu, \mu_2, W_{2_{j0}}, W_{g_{j0}}$	1, 1000, 0.1, 0.1
$W_{1_{A/B}}$	$[W_{s_0} W_g]$
W_{1_C}	$[W_g W_{s_0}]$

6.4.1 Simultaneous Steering Law Example

The next set of plots captures the dynamic responses of the system based on the simultaneous steering law parameter approaches. It begins with vehicle angular position and velocity tracking results, then shows singularity index and power tracking performance, and closes out with actuator (wheel and gimbal) performance responses.

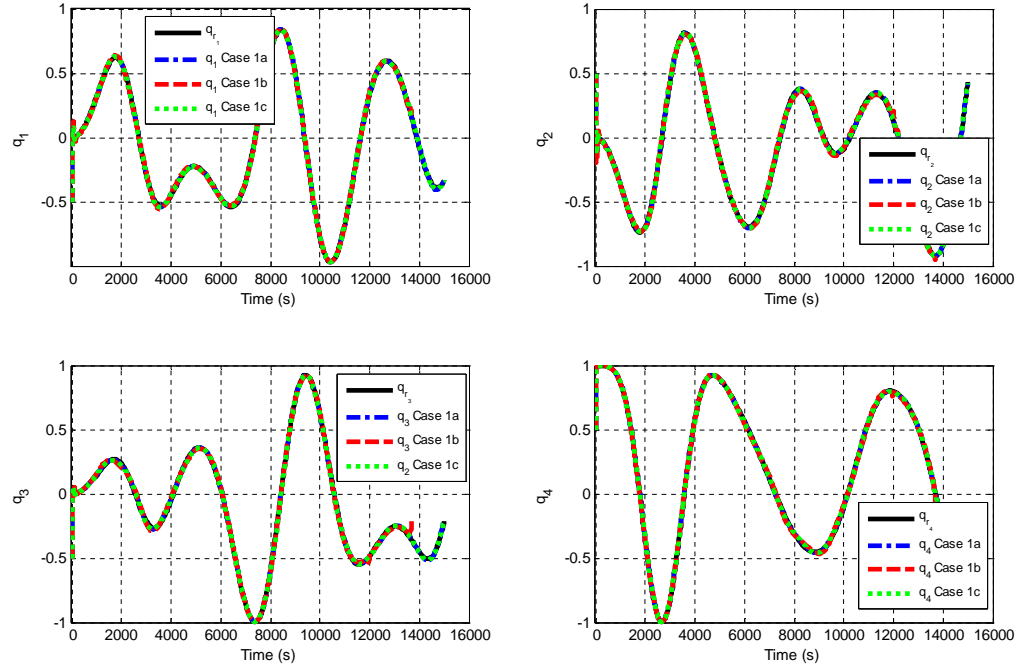


Figure 6.2: Example 1 Angular Position

6.4.2 One-way Coupled Steering Law Example

The second set of plots presents similar results to those from the previous example. The key difference is that only two steering cases (2a and 2b) are compared in the plots rather than 3 cases. Nevertheless, these results are presented beginning with vehicle angular position and angular velocity tracking followed by singularity index and power tracking performance then finishing with actuator performance responses. As before, the actuators include wheel speed and gimbal angle histories. Analysis of these results and those from the previous example are given in the ensuing section.

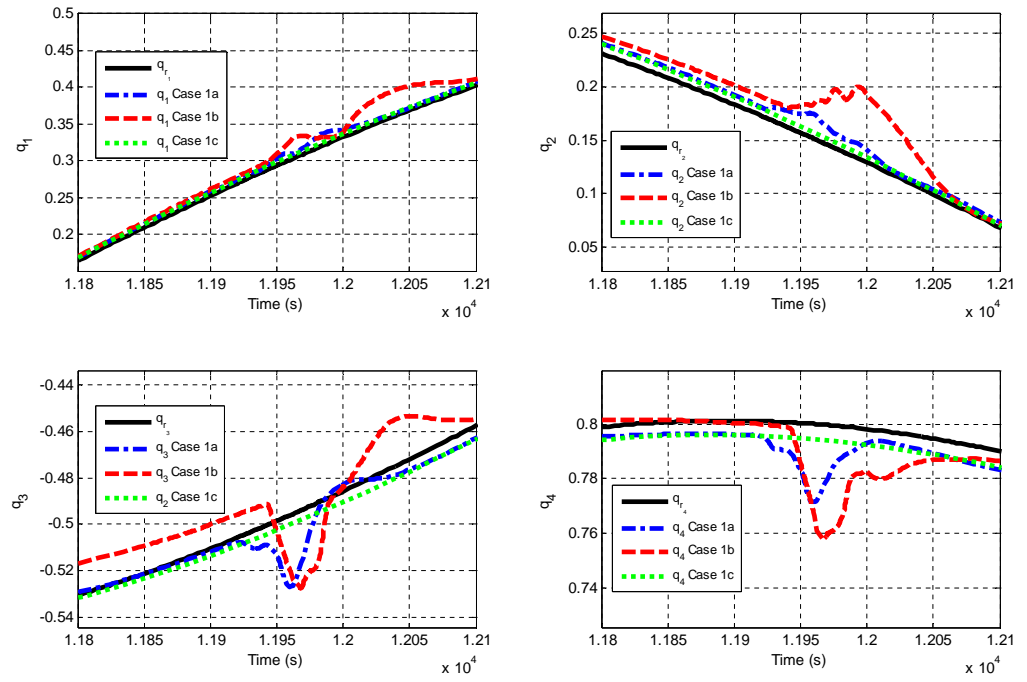


Figure 6.3: Example 1 Angular Position, Zoomed

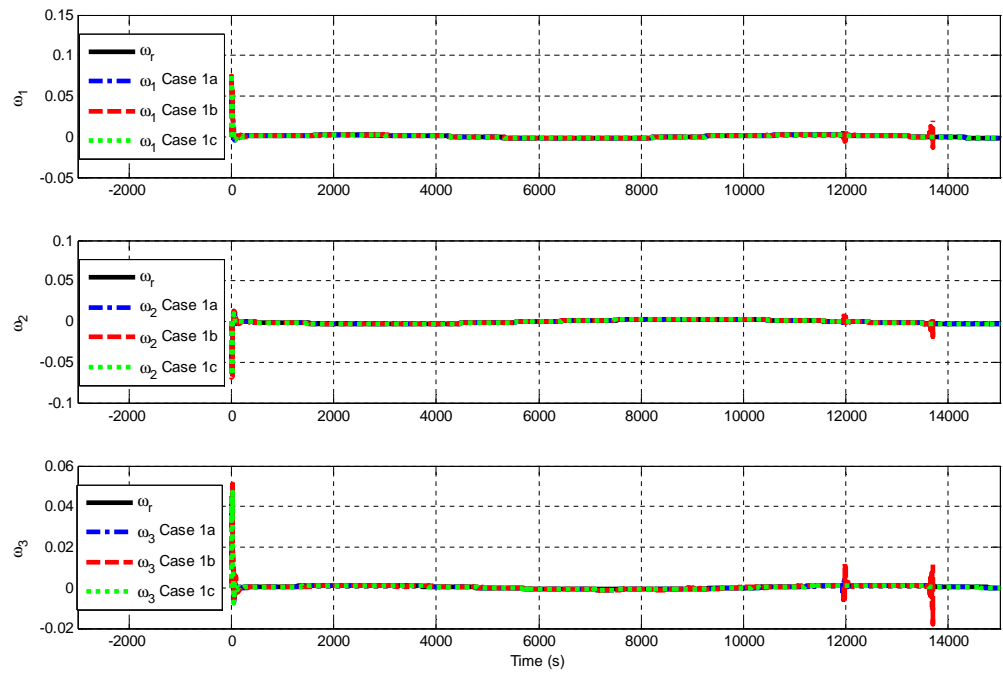


Figure 6.4: Example 1 Angular Velocity

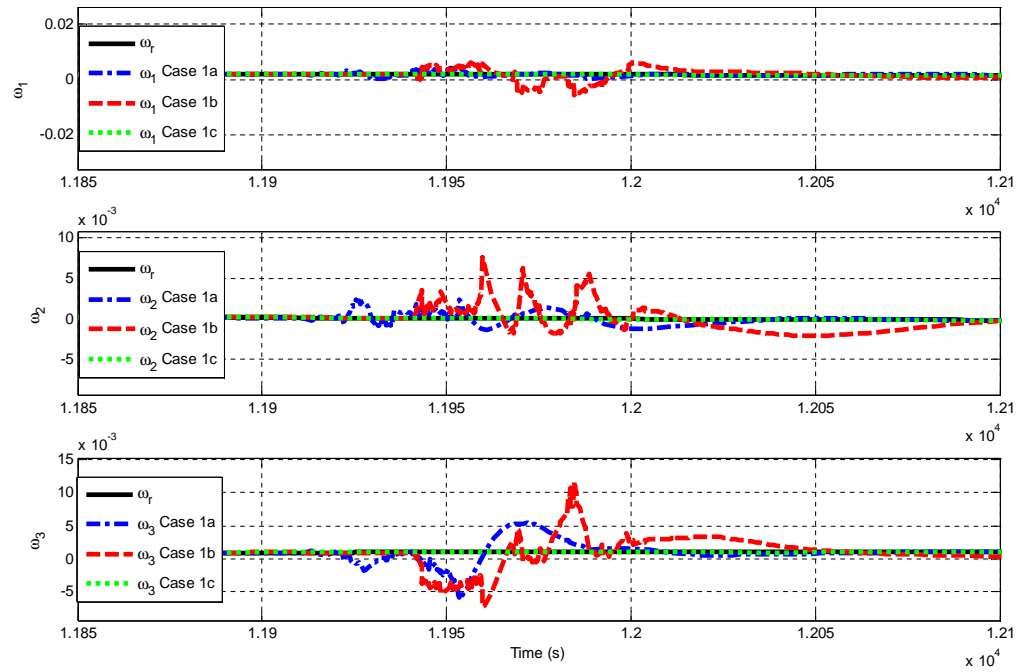


Figure 6.5: Example 1 Angular Velocity, Zoomed

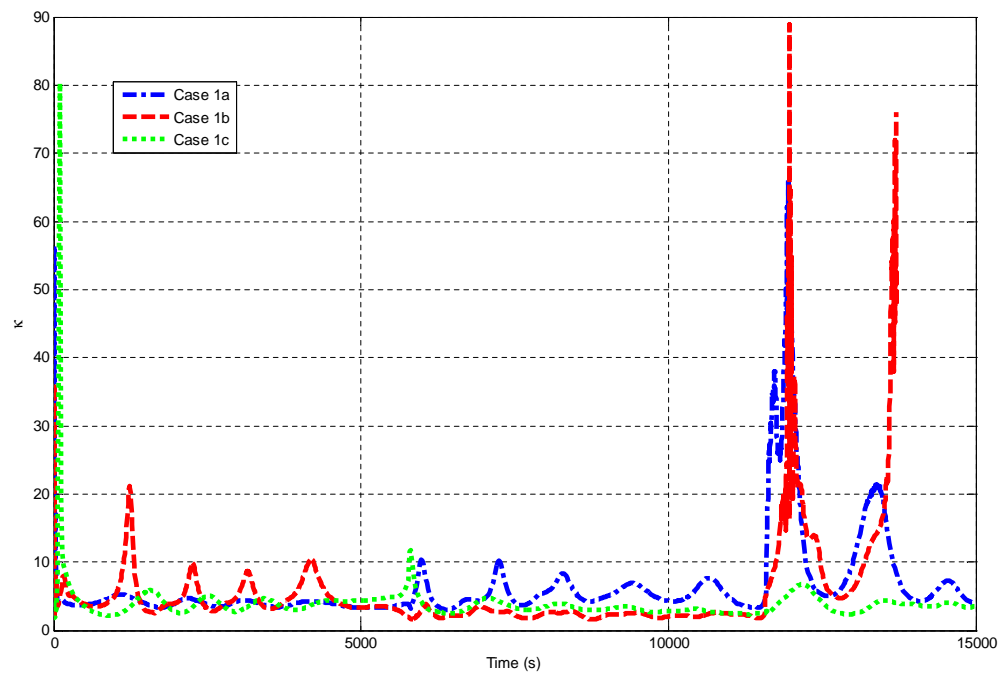


Figure 6.6: Example 1 Singularity Index

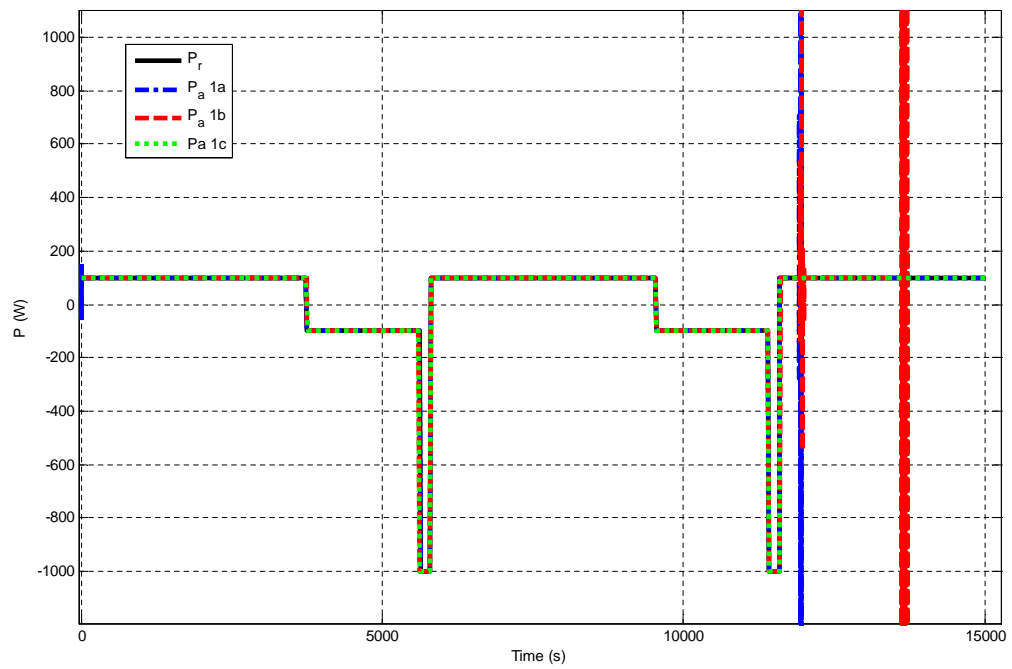


Figure 6.7: Example 1 Power Plot

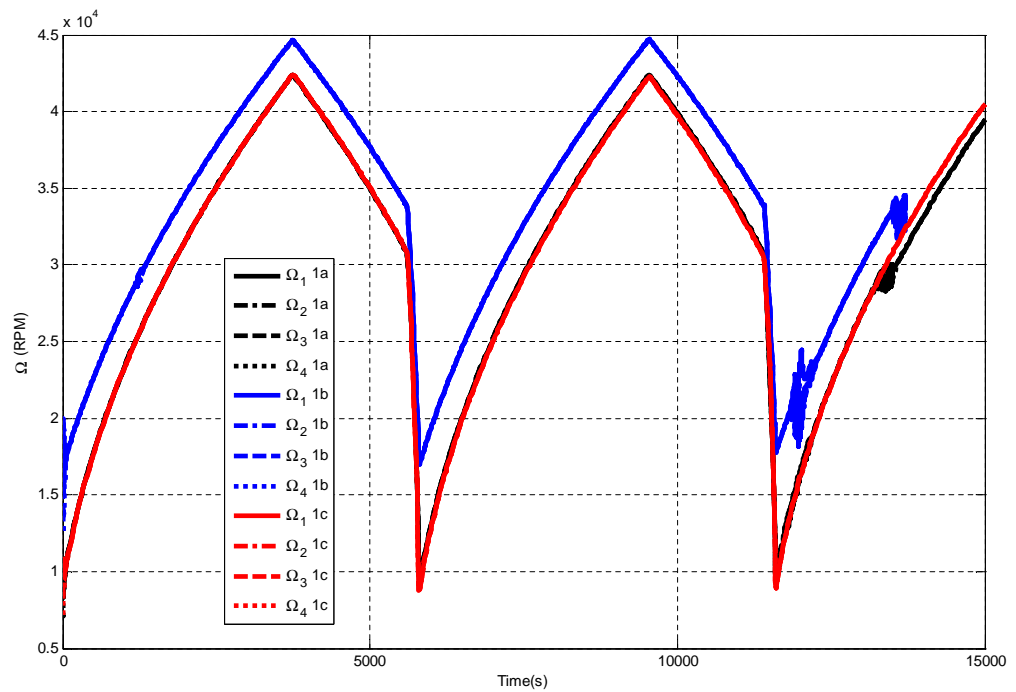


Figure 6.8: Example 1 Wheel Speed

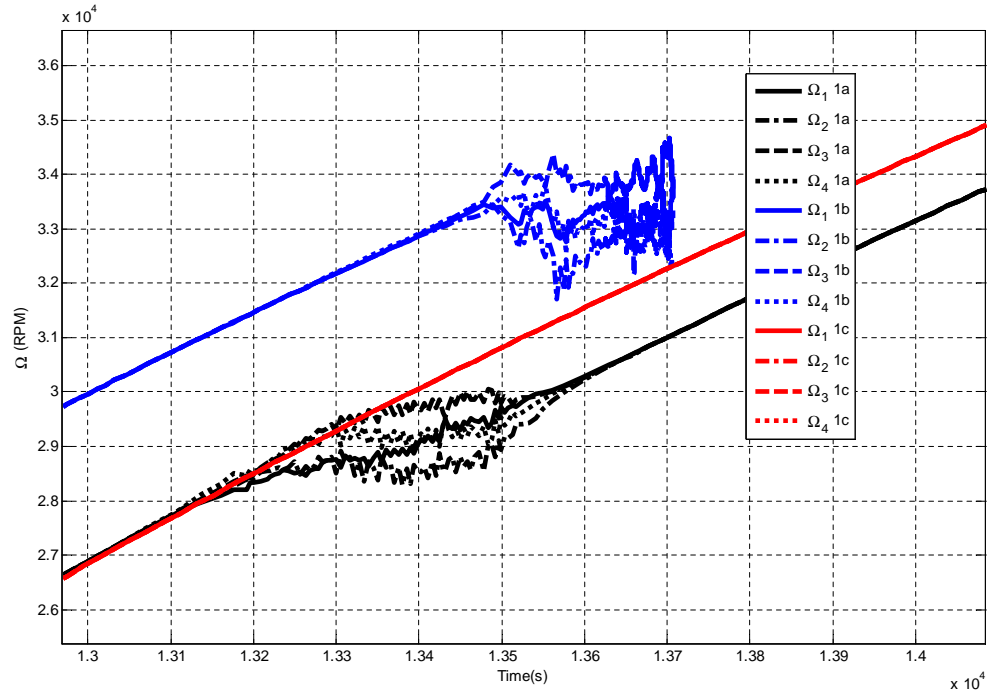


Figure 6.9: Example 1 Wheel Speed, Zoomed

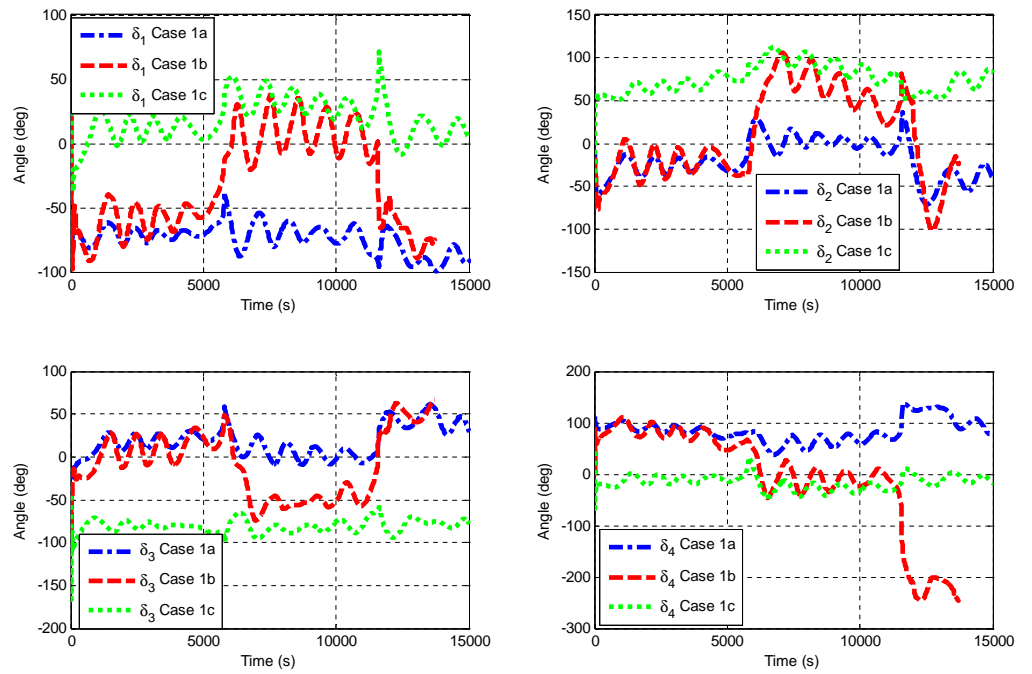


Figure 6.10: Example 1 Gimbal Angle

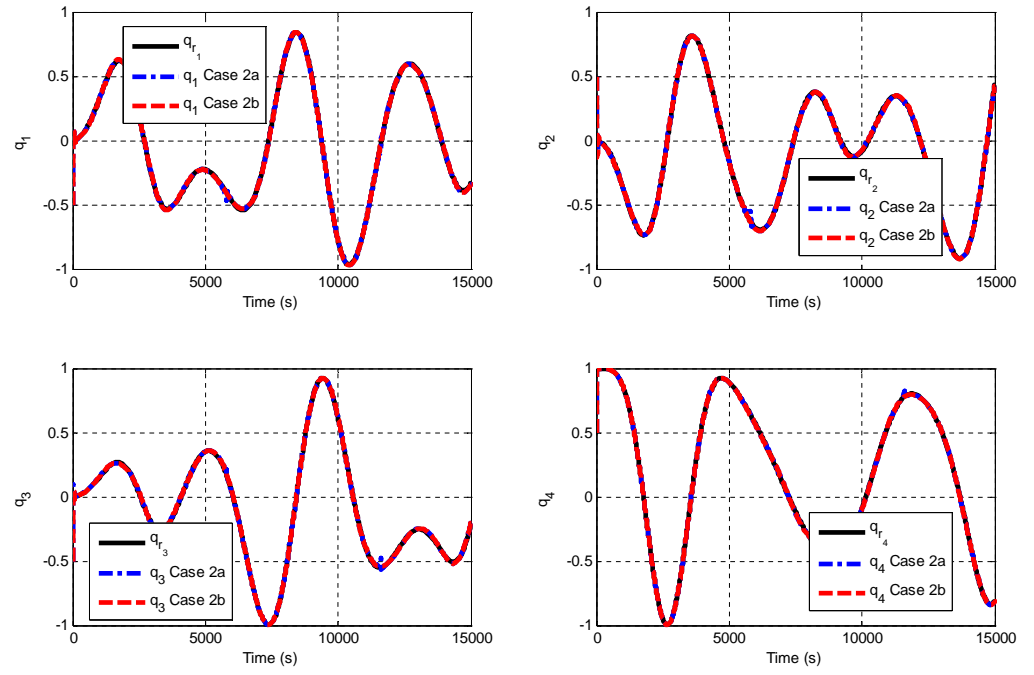


Figure 6.11: Example 2 Angular Position

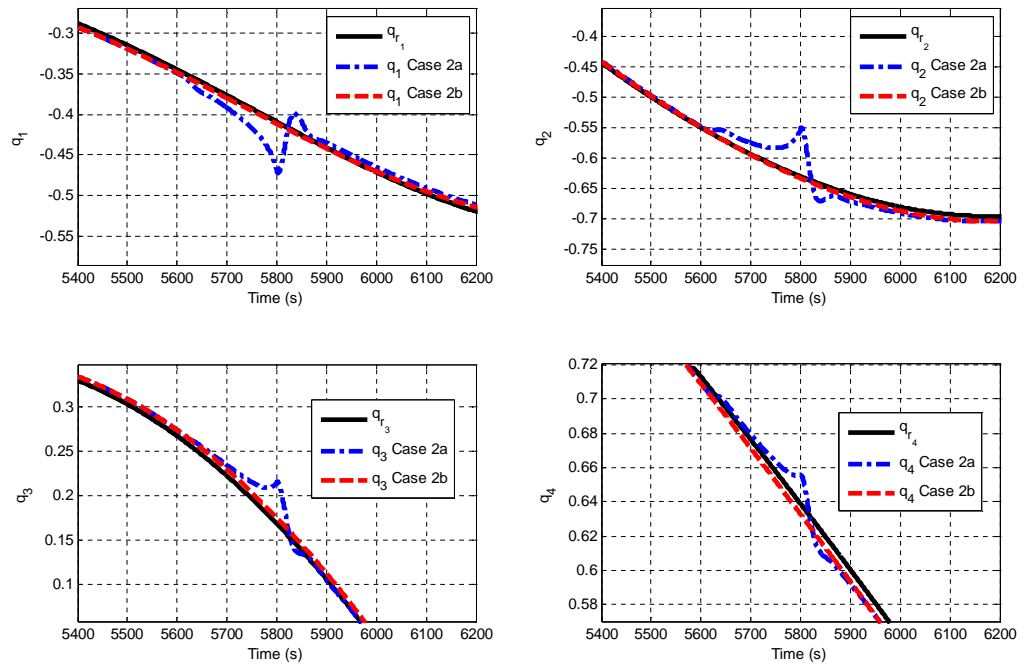


Figure 6.12: Example 2 Angular Position, Zoomed In

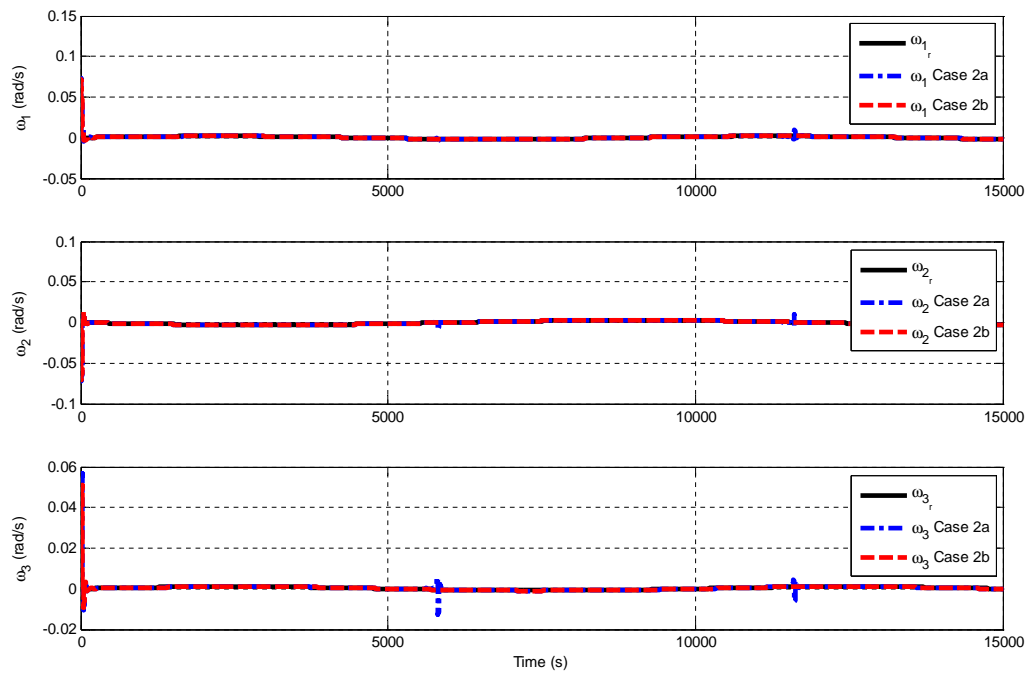


Figure 6.13: Example 2 Angular Velocity

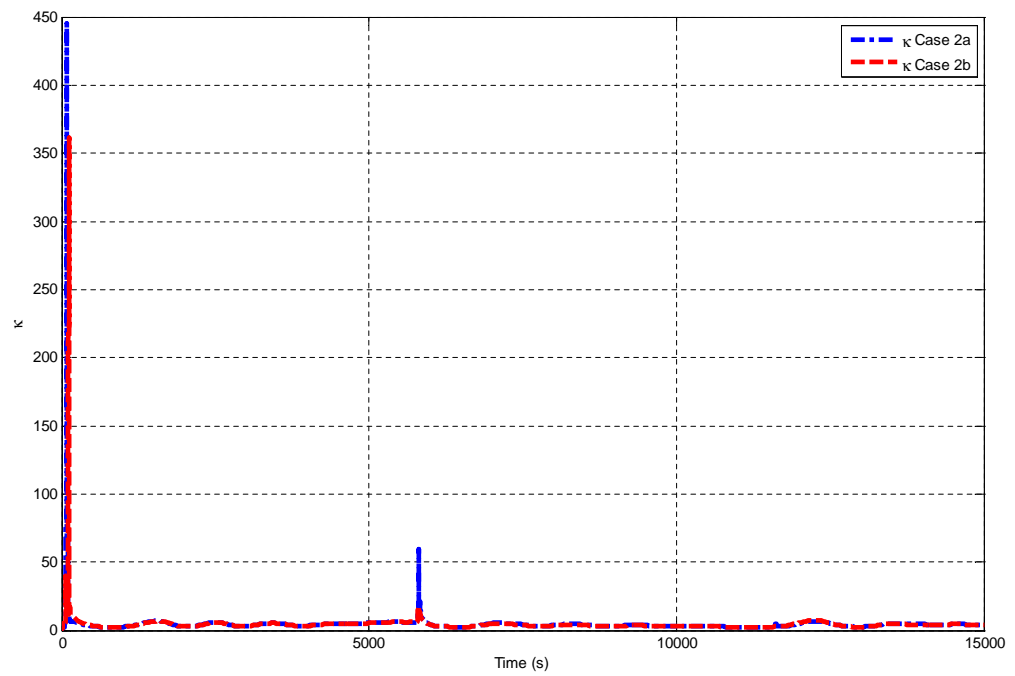


Figure 6.14: Example 2 Singularity Condition

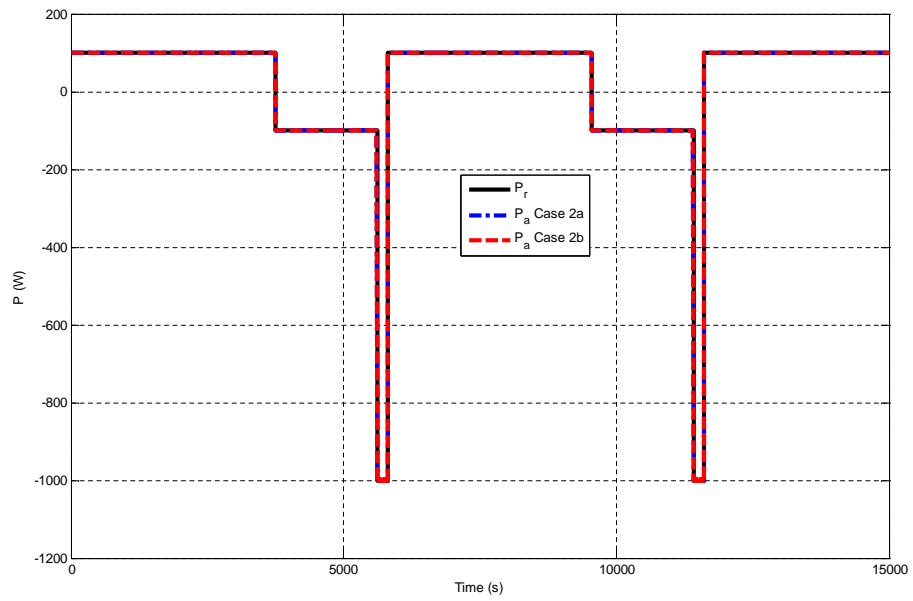


Figure 6.15: Example 2 Power

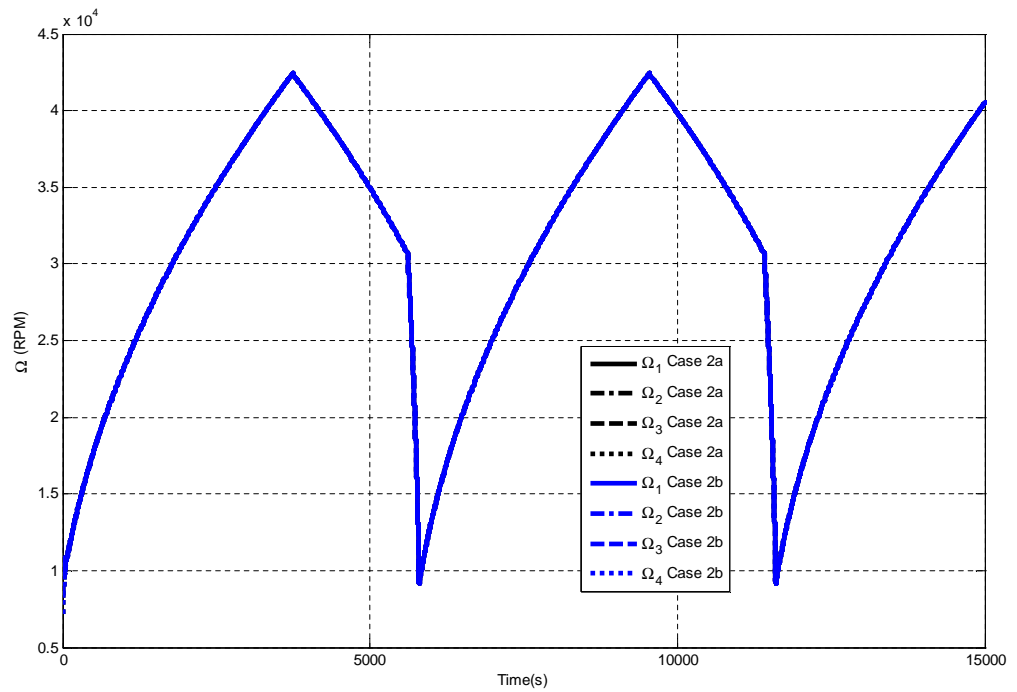


Figure 6.16: Example 2 Wheel Speed

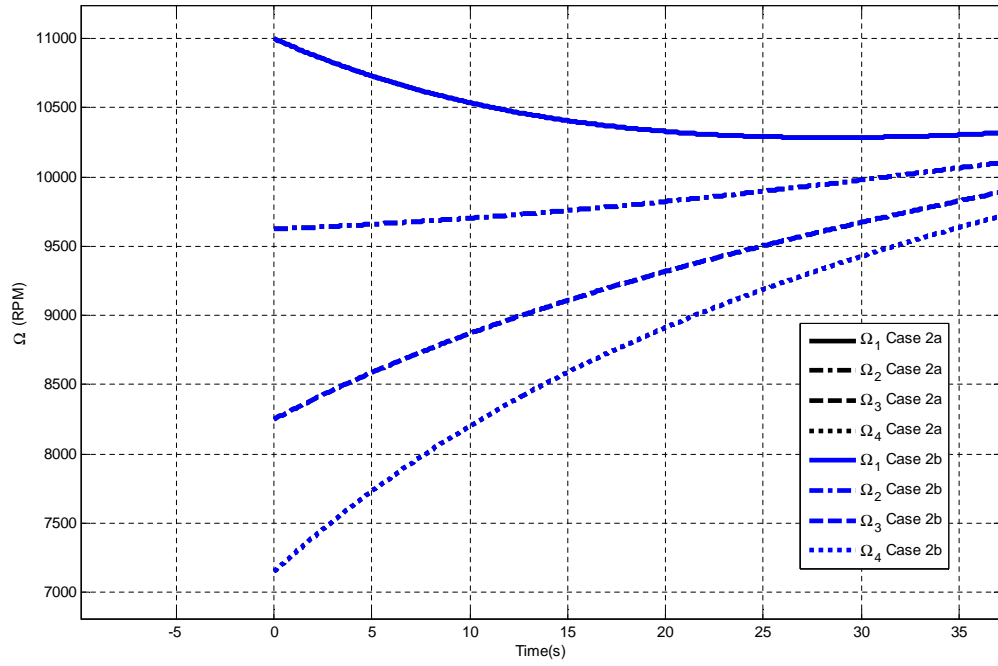


Figure 6.17: Example 2 Wheel Speed (Zoomed)

Discussion of Results

6.4.3 Simultaneous Steering Example

Analysis of the first example results for cases 1a, 1b, and 1c begins with the vehicle angular position as reflected in Figures 6.2 and 6.3. From Fig. 6.2, one can tell that each quaternion maintains a relatively close track (in a macroscopic sense) after the first 100-200 s when the desired attitude is acquired. However, this is somewhat misleading as the zoomed in version of Fig. 6.2 paints a more accurate picture. Here one can see that case 1b has the most error of the three (when compared to the reference) for all four quaternions. It appears from this analysis that increasing the initial wheel speed condition also imparts a little more instability in the track as slight changes in wheel momentum have a larger effect. This makes sense – if the wheel speeds are higher (thus the wheels have more momentum) and the same acceleration is required to maintain a track as with lower speeds, small errors in the acceleration will have greater attitude impact in the higher momentum case. Meanwhile, case 1c appears to have a smoother response overall, but this response is a little slower at tracking the reference than the other results but does not have the same oscillatory error.

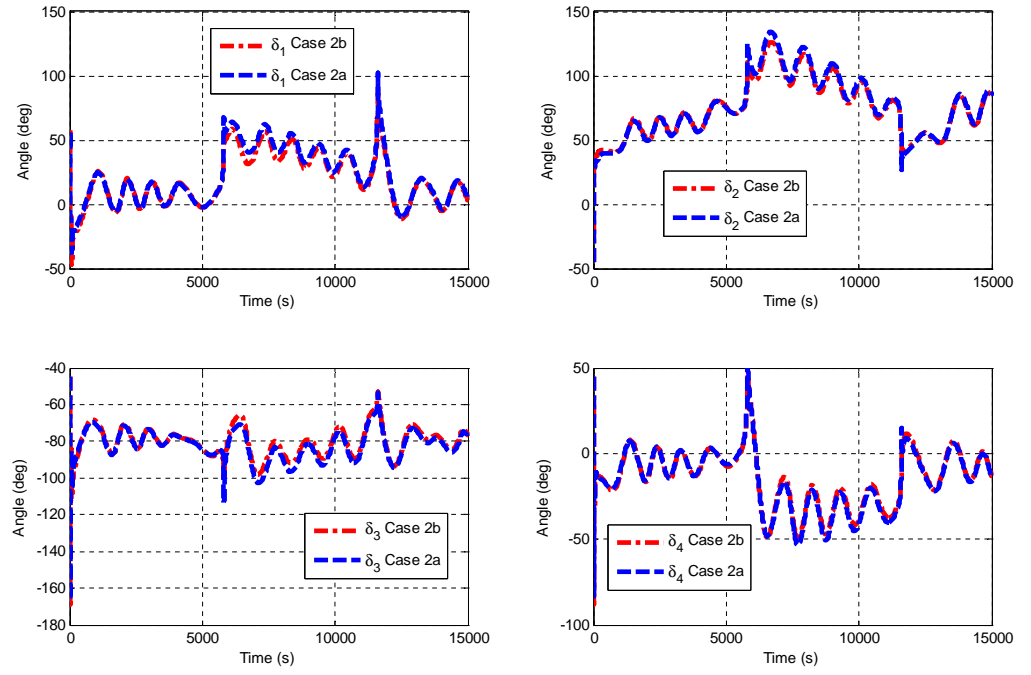


Figure 6.18: Example 2 Gimbal Angle

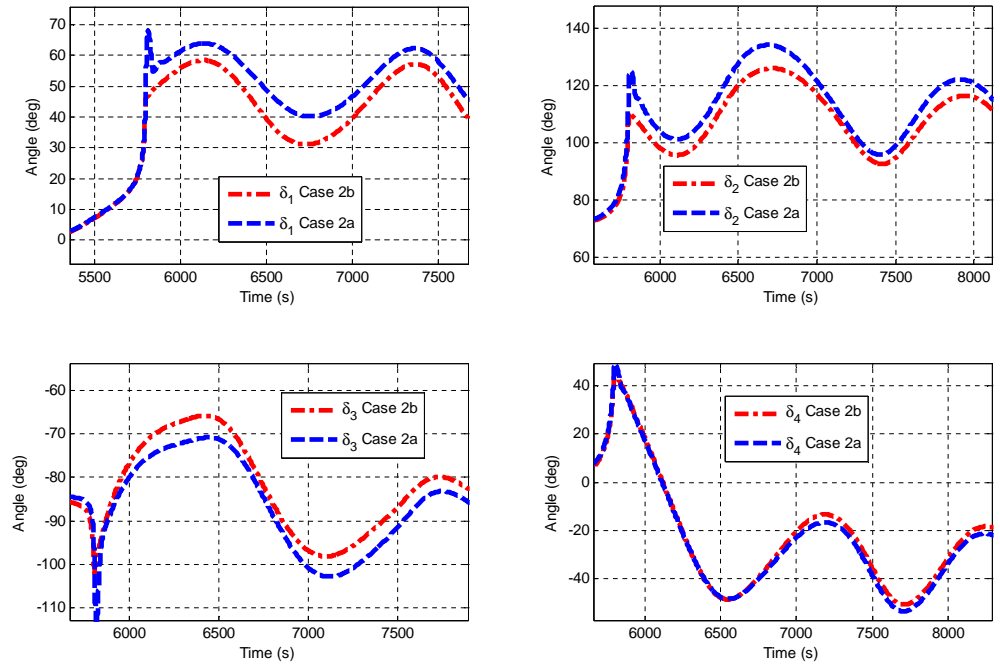


Figure 6.19: Example 2 Gimbal Angle (Zoomed)

Similarly for angular velocity, one can see in Figure 6.4 that after the first few hundred seconds, the tracks match in velocity until near the end of the plot when at least one track appears to have error. Zooming into this track as done in Figure 6.5, it becomes clearer that case 1b has significant error, case 1a has some error, and case 1c has small error in relation to the reference.

Another vehicle result is that of the power plot shown in Figure 6.7. This plot shows fairly clearly that case 1b's power performance has very large error between 11500 to 12000 s. It allows one to contrast the three steering laws during the transition. It should be noted here that this scenario assumes the satellite has an orbital period around 5600 to 5700 s which relates to this transition. Thus, Figure 6.7 shows two orbital cycles and the errant zone is in the second payload duty transition.

Next, once one understands the impact these steering laws have on the vehicle's performance (both in terms of power and attitude), one can delve deeper into the ESACS VSCMG actuator performance that results in this vehicle performance. One interesting plot that illustrates the direct correlation between the actuators and the vehicle is captured in Figure 6.6. Figure 6.6 shows that the biggest actuator singularities coincide with the power profile transitions. Note that the singularity index is a measure of VSCMG configuration singularity in which no-torque can be produced in at least one direction through use of the CMG mode. In such a case, the wheels are called on to change speeds, effectively operating as momentum wheels, to transition the singularity. As one can infer, much depends on having available wheel output power (torque and speed). In fact, the wheel momentum is a key contributor to CMG-mode torque production. Thus, the correlation between singularity and payload peak power operation in eclipse makes sense as such peak power draw limits the amount of momentum available to the CMG-mode and thereby aggravating the singularity from a CMG-mode standpoint. However, one should note that the singularity plots only show that the CMG-mode is drained, overall performance of the actuators during a maneuver is best captured by gimbal angle and wheel speed plots.

Related to this, the gimbal angle history is illustrated in Figure 6.10. Here one can see that the higher initial wheel speeds correspond to a set of gimbal angles with more separation whilst the lower initial wheel speed case corresponds to reduced gimbal angle separation. Also, a weak correlation between the singularity index and tendency for the gimbal angle paths to change direction is evident in the gimbal angle history.

Figure 6.8 and its zoomed version, Figure 6.9, illustrate the wheel performance during this

Table 6.3: Simultaneous Steering Tracking Error Comparison

Steering Law	Max q_e element (Unit-less)	Max P_e (W)
1a	0.0443	3.0856e3
1b	0.1753	4.3239e4
1c	0.0157	2.2737e-13

small satellite maneuver. All three steering laws, of course, use a wheel speed equalization scheme as defined by Yoon and Tsiotras in [109]. In Figure 6.9, one can see the wheel sets for the different steering laws acquiring the average speed amongst them. Having all sets equalize helps contrast the steering laws. Meanwhile, the wheel performance illustrated in Figure 6.8 shows that case 1b has the most jitter/separations (thus error) as compared to the other methods while case 1c is the smoothest. This is a direct result of using the proper weighting matrix mentioned previously.

Finally, comparing the largest attitude quaternion and power tracking error magnitudes of the simultaneous steering laws helps one contrast these laws. The Case 1a, 1b, and 1c curves in Figures 6.20 and 6.21 capture this comparison, while Table 6.3 summarizes the peak values in this result. As one can see, the largest error quaternion magnitude arises in case 1b as does the largest power tracking error. However, the order of magnitude of the largest quaternion error is similar for cases 1b and 1c but one order of magnitude less for 1a. This points to the fact that the error magnitude seems to grow with initial wheel angular velocity. Another key observation one can make is that the duration of larger tracking error is affected by both using the proper weighting matrix and keeping the initial wheel speeds lower. Furthermore, in terms of power error, the 16 orders of magnitude between cases 1b and 1c point to the accuracy of the simultaneous steering law using the best weighting method. Thus, from analyzing the tracking errors, it is evident that keeping the wheel speeds lower and using the proper wheel/gimbal weighting matrix yields the best response in terms of controlling tracking errors.

6.4.4 One-Way Coupled Steering Example

Next, investigation of the one-way coupled steering law example yields interesting results as well. These results are captured in figures 6.11, 6.12, 6.13, and 6.15 for the vehicle attitude and power response and figures 6.14, 6.16, 6.17, 6.18, and 6.19 for the actuators response which highlight the set 2 cases, 2a and 2b.

First, the vehicles' angular position and velocity are reflected in Figures 6.11, 6.12, and 6.13. Similar to case set 1, the macro view of tracking the attitude over two orbits seems fairly benign. However, the view in Figure 6.12 pinpoints the performance of these laws during a taxing part of the maneuver. In fact, as one can see, this error lasts more than 100 s. This can be detrimental to a highly sensitive imaging camera or space RADAR mission in that the wrong ground point may be imaged. The angular velocity plot further confirms this result (i.e. in Figure 6.13).

In contrast, Figure 6.15 shows the power tracking results which are very close to the reference for both of the laws. This follows from the fact that the power in the one-way coupled implementation only interacts with the wheels. The wheel motion imparts attitude disturbances. This means that the power tracks first by changing the wheel speeds then the attitude uses this result to react but does not control such wheel response. Thus, both steering laws have very similar power responses with little error.

Next, the singularity index plot shown in Figure 6.14 shows a relatively tame singularity condition plot with some growth at the end of the second orbit. Here one can see that the gimbals stay outside of challenging singularities for most of the maneuver. Correlated to this, the gimbal angle response shown in Figure 6.18 and its zoomed version in Figure 6.19 reflect a fairly benign response—the angles do not vary as happened in the previous example. However, the zoomed version in Figure 6.19 shows that the gimbal angle histories for 2a and 2b split. After initially separating, these gimbal histories have an identical trend due to identical gimbal rate command histories.

Meanwhile, one can see the transitory nature of wheel speeds in Figure 6.16 as the average wheel speed grows to 43000 RPM and decays back to 9000 RPM at the end of eclipse for each orbit. Notice that this figure appears to contain one distinct line as the four wheel speeds for 2a and the four for 2b each follow the average speed, which is identical for each case since the power profile is exactly the same. This plot along with the power plots serve to validate the results. In addition, Figs. 6.17 shows the zoomed view of wheel speed, starting with initial wheel speed equalization.

Next, as done in the previous case set, the associated tracking errors for this small satellite maneuver employing the two one-way coupled system steering laws are captured in Table 6.4 and Figures 6.20 and 6.21. From this table and the plots, one can see that the peak power tracking errors are on the same order as the best simultaneous steering law power error (i.e. in case 1c presented earlier), are identical, and are very small. This falls out of

Table 6.4: One-way Coupled Tracking Error Comparison

Steering Law	Max q_e element (Unit-less)	Max P_e (W)
2a	0.1001	4.5475e-013
2b	0.0171	4.5475e-013

the fact that the steering laws in this case set (in opposition to the laws in case set 1) only use the wheel speed and acceleration measurement but do not command them. Thus, the true contrast in the laws of cases 2a and 2b arise in the quaternion errors. Here, one can see that the peak quaternion magnitude is one order of magnitude worse in case 2a. Also, as mentioned earlier, the attitude tracking error lasts more than 100 s in which the case 2a attitude error is well outside of the case 2b error. This stems from the fact that the steering law in case 2b uses information about the wheel acceleration whereas the case 2a law does not. As shown here, this information is important and should be included in the steering law. For this reason, in the case of one-way coupled implementation of ESACS VSCMGs, steering law 2b, $\dot{\delta}_c = \bar{N}_r - \mathbf{F}\Omega - \mathbf{E}\dot{\Omega}$, is a better suited steering law as compared to steering law 2a. Plus, the additional wheel disturbance torque term, $\mathbf{E}\dot{\Omega}$, has a significant impact upon the result when peak wheel accelerations are high and wheel spin axis inertia is low as in the small satellite example shown here.

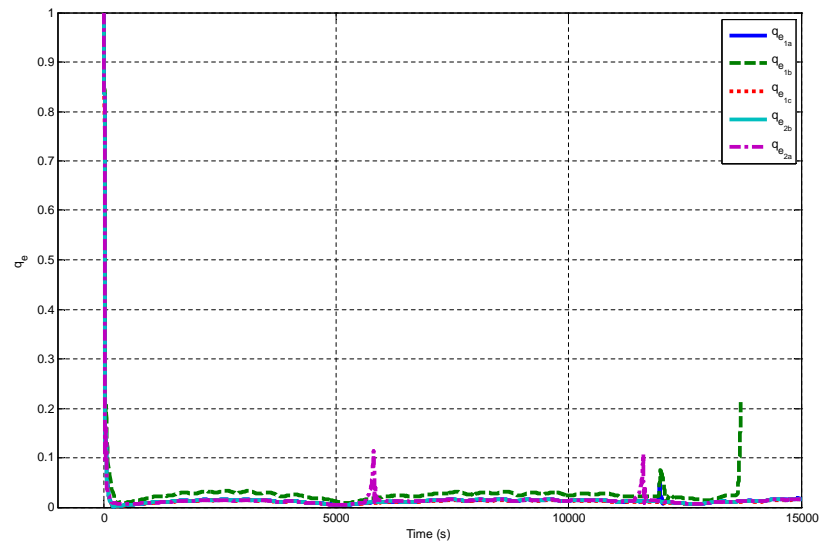


Figure 6.20: Quaternion Error Max Magnitude

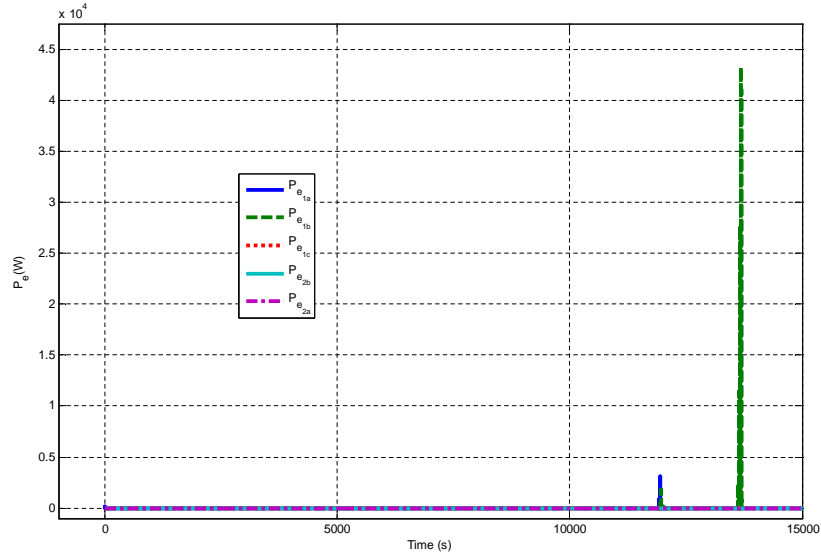


Figure 6.21: Power Tracking Error Magnitude

6.5 Summary

In this chapter, a novel gimbal steering law was derived to address the practical case when automatic control of the wheels by the electrical power subsystem's electrical circuit topology is conducted independently of the gimbal motors, thus generating the potential for disturbance torques on the spacecraft.

These disturbance torques must be accommodated in the attitude steering of the actuators which is accomplished by this steering law. This law serves as a linchpin in evolving conventional independent attitude and power subsystems for spacecraft into the simultaneous control envisioned in previous work contained in the literature, building on the author's previous work.

For the benefit gained in power subsystem exclusive wheel control, a drawback is incurred in that automatic singularity avoidance via the momentum-wheel mode of the VSCMGs now is changed to requiring a logical CMG-type singularity law to steer through singularities. However, much literature on CMG singularity avoidance exists in the literature and can be applied here, but an interesting consequence of this new law is that the potential singular directions change in time as the momentum envelope size and shape changes with changing wheel speeds.

Chapter 7

ESACS Hardware Design

7.1 Requirements Summary

Early in Chapter 5, Small Satellite ESACS Sizing/Optimization, a notional VSCMG design was determined that met the mission requirements from Chapter 3, Mission Scenarios. The initial version of this design was modified to accommodate adjustments in rotor length due to usable available capacity concerns. The ensuing updated design parameters serve as a starting point for the design and build of the first VSCMG prototype hardware and are summarized next.

Table 7.1: Summary of Usable Design Requirements

Parameter	Value
Minimum Wheel Speed, Ω_n , RPM	6150
Maximum Wheel Speed, Ω_x , RPM	46100
Rotor length, l_r , m	0.035
Wheel Spin Axis Inertia, I_{ws} , kgm^2	0.009926
Maximum Gimbal Rate, $\dot{\delta}$, deg/s	5
Maximum Wheel Acceleration, $\dot{\Omega}$, rad/s^2	10.13
Energy Density, E_d^* , Whr/kg	8.38
Minimum Power Density, P_d^* , W/kg	22.5
Maximum Power Density, P_d^* , W/kg	168.6

* Assumes 80% conversion efficiency, 4 VSCMG cluster, and 9.23 kg cluster mass

Several hurdles were overcome in the procurement and development of the first VSCMG prototype, dubbed the Revision A (Rev A) model. The first and foremost of these is that commercial-off-the-shelf technology (COTS) only permitted BLDC motors that were either

high power (e.g. 250W-400W shaft output power) with reduced maximum speed (e.g. 5000-11500 RPM) or were high speed (e.g. 40000-46000 RPM) at reduced power (e.g. 40-50W). As one may infer from these practical values, even the maximum COTS capabilities do not meet the original mission requirements defined in Chapter 3. When faced with this implementation challenge, one has a few options: have a custom built system without leveraging key COTS technology but also substantially increasing the cost; use COTS technologies and accept a compromise in performance; or implement a mixture of the first two options. It was decided in this development to use a mixture of options, employing a custom design/build of the Carbon Fibre rotor system and basic mechanical integration structure, but procuring a COTS gimbal motor, COTS wheel motor-generator, and COTS gimbal and wheel motor drive electronics. These drive units interface to very basic electronics built in-house at SSC based on simple resistor-diode components with Integrated Circuit (IC) chips for current sensing. Details about these COTS and custom components will be discussed throughout the remainder of this chapter.

Returning to the motor torque-speed dilemma, the COTS implementation was chosen to include both the high-speed, low-torque motor and the low-speed, high-torque motor, with the thought that the former would help demonstrate the energy storage capacity and test the mechanical design, forming the primary focus of the research, while the latter would help demonstrate the power capability of the technology. However, as often happens in practical work, the Rev A design (which included mechanical interfaces to both, very different motor types) actually over-loaded the high-speed, low-torque motor's internal ball bearings. This problem damaged the initial version and necessitated a mechanical re-design. Therefore, the re-design and implementation of this motor was moved to the Rev B build whilst Rev A was deemed to only include the low-speed, high-torque motor. Anticipated ESACS VSCMG performance parameters using these two motor versions are given in Tables 7.3(a) and 7.3(b).

One may notice that the gimbal rate in Rev B is significantly different than that of Rev A. This reflects the second hurdle faced in component procurement. Due to an initial error in calculating the required gearing, an excessive gear ratio was chosen for the Rev A design. This gearing is fixed in Rev B, greatly increasing the system torque performance.

Besides the wheel and gimbal motor difficulties, other issues in procurement involved practical limits in drive electronics (e.g. 50V maximum potential along with 5A continuous current limit for the wheel motor's servo-amplifier), Aluminium containment and support structures

Table 7.2: Prototype Parameters

Parameter	Value
Minimum Wheel Speed, Ω_n , RPM	2000
Maximum Wheel Speed, Ω_x , RPM	9000
Rotor length, l_r , m	0.035
Wheel Spin Axis Inertia, I_{ws} , kgm^2	0.009946
Maximum Gimbal Rate, $\dot{\delta}$, deg/s	10
Maximum Wheel Acceleration, $\dot{\Omega}$, rad/s^2	100
Energy Density, E_d^* , Whr/kg	0.14
Max Power Density, P_d^* , W/kg	36.7
Min Power Density, P_d^* , W/kg	8.0

* Assumes 80% conversion efficiency and a single VSCMG mass of 5.0 kg.

(a) Rev A Parameters

Parameter	Value
Minimum Wheel Speed, Ω_M , RPM	6510
Maximum Wheel Speed, Ω_M , RPM	46000
Rotor length, l_r , m	0.035
Maximum Gimbal Rate, $\dot{\delta}$, deg/s	50
Maximum Wheel Acceleration, $\dot{\Omega}$, rad/s^2	10
Energy Density, E_d^* , $W\ hr/kg$	5.4
Maximum Power Density, P_d^* , W/kg	1095.1
Minimum Power Density, P_d^* , W/kg	154.7

* Assumes 80% conversion efficiency and a single VSCMG mass of 3.5 kg.

(b) Rev B Parameters

leading to extra mass than necessary for flight, and much longer lead times in getting hardware ordered as well as receiving the mechanical system. Despite these barriers to development of the Rev A prototype, the Rev A system was successfully implemented as is demonstrated in Chapter 8.

The remainder of the current chapter details the key elements of the VSCMG design for Rev A, mentions changes for Rev B, and then addresses the proposed design for Rev C. It is divided into sections on wheel motor/generator, wheel gimbal motor, mechanical, electrical, cluster, and follow-on flight model design.

7.2 Wheel Motor/Generator Design

As mentioned in the previous section, contemporary COTS brushless DC motors either produce high shaft power and moderate maximum speed or high maximum speed with moderate shaft power. Therefore, in order to fully exercise the design, both types of BLDC motors were procured. The motors were chosen from Maxon Motors, a company with a track record for building effective motors for space, including 11 motors for the 1997 Mars Pathfinder mission, 39 of the 43 electric motors used on each of the 2005 Mars Spirit and Opportunity Rovers, and several motors for the Phoenix-Mars mission slated to land on Mars in May 2008 [158–160]. The goal in selection for the high speed motor was to match the optimal sizing design specifications from Chapter 5 as closely as possible with COTS components. Thus, an EC-16, 40W motor was selected with a nominal voltage of 24 V. This motor operates at this voltage up to 41000 RPM and was deemed sufficient for the task. Note that specifications from two years of data are summarized with other wheel motor candidates in Table 7.4(a). Also, a photograph of this motor is included in Figure 7.1(b).

Building on the fact the maximum wheel speed required of the VSCMG design as listed in Table 7.1 is 46100 RPM and not 41000 RPM as is achievable by the EC-16, the EC-22, 50W, model number 199154 motor, with parameters as captured in Table 7.4(a), is a better candidate than the EC-16 for this mission. Furthermore, this increase in maximum permissible speed increases the maximum storage capacity by the square of the speed. In addition, the mechanical shaft output power of the EC-22 is 10W more than the EC-16 value, so the EC-22 can deliver more instantaneous peak power as well. Due to this improved performance, the EC-22 is selected for future versions of the SSC ESACS VSCMG. Since the EC-16 motor has already been included in the Rev B build, the EC-22 change will be made

in Rev C.

In contrast with the EC-16 and EC-22 which operate at high speeds, the moderate speed plus high torque (i.e. shaft power) motor selected was Maxon's EC-45, 250 W version. The EC-45 was selected since it was the highest power EC motor available at the time, but that has recently changed with the advent of the EC-60, 400W motor. This motor can produce up to 2.25 Nm of torque, but such production relies upon electronics built to handle higher current than the other motors mentioned. As in the case of the EC-16, the key parameters of the EC-45 are listed in Table 7.4(a) while an image of this motor is shown in Figure 7.1(a).

The sheer contrast in size of the EC-16 and EC-45 actually imparted a dual requirement on the initial VSCMG mechanical design for Rev A. That is, the mechanical interface to the Carbon Fibre rotor had to be made to accommodate this size difference. This design will be further described later in this chapter.



(a) Large Motor: Maxon EC45, 250W



(b) Small Motor: Maxon EC16, 40W

Figure 7.1: Candidate Motors for the Rev A Design

Table 7.3: Relevant Motor Data

Parameter	EC-45	EC-45	EC-16	EC-16	EC-22	EC-22	EC-22
Catalog Year	2006	2005	2006	2005	2007	2005	2005
Model Number	136207	136207	232241	232241	167130	167130	199154
Output Power, W	250	250	40	40	50	50	50
No-load Speed, RPM	5250	5300	41400	41400	38700	38800	46700
Max Perm. Speed, RPM	12000	12000	50000	50000	50000	50000	50000
Voltage, V	24	24	24	24	32	32	32
No-load Current, A	0.435	0.435	0.222	0.222	0.327	0.304	0.218
Torque Constant, NM/A	0.0433	0.0433	0.0055	0.0055	0.00785	0.0079	0.0065
Speed Constant, RPM/V	221	220	1740	1736	1220	1216	1464
Speed/Torq Grad, RPM/Nm	2190	2400	226000	237000	56200	56000	81000
Resistance, Ohm	0.43	0.46	0.716	0.75	0.363	0.36	0.36
Stall Torque, Nm	2.420	2.250	0.184	0.176	0.692	0.693	0.575
Max Efficiency, %	84	83	85	84.3	88	89	90
Motor Shaft Inertia, gcm^2	209	209	1.27	1.27	4.20	4.2	3.1
Max Radial Load, N	180	180	10	10	16	16	16
Max Dynamic Axial Load, N	20	20	3	3	4	4	4

(a) Key Wheel/Generator Parameters

Parameter	EC-16max	+ GP-22C Rev A	+ GP-22C Rev B
Gear Ratio	N/A	4592:1	950:1
Max Allowable Speed	20000	8000	8000
Desired Post-Gearing Speed, RPM	N/A	8.333	8.333
Required Pre-Gearing Speed, RPM	N/A	38267	7083

(b) Key Gimbal Motor Parameters

7.3 Gimbal Motor Design

Gimbal motor selection was briefly alluded to at the outset of this chapter. Also procured from Maxon, the Rev A gimbal motor contains gearing in the form of the GP-22C planetary gearhead, a magnetic resonance encoder known as the MR-128, and a brushless DC motor, the EC-16max, 8W motor. Specifications for each of these components is summarized in Table 7.4(b), while a photograph of the Rev A gimbal motor is given in 7.2.

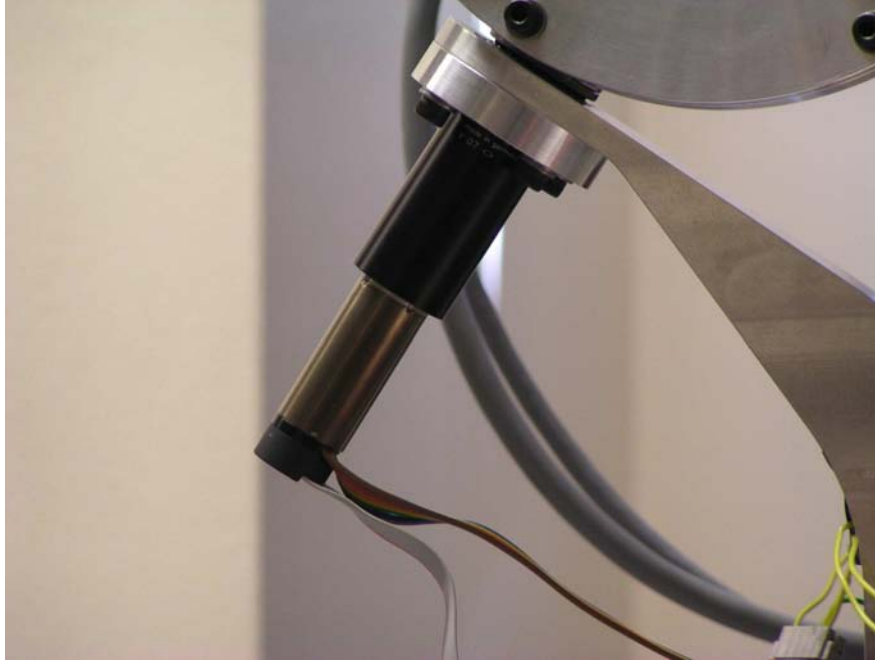


Figure 7.2: Rev A Gimbal Motor, Gearing, and Encoder

As alluded to in the introduction to this chapter, an error made in selection of the Rev A motor has been fixed for Rev B. First, one should note that the original required gimbal rate was 50 deg/s as it was selected prior to the ESACS re-sizing resulting from incorporating usable energy storage capacity effects presented in Chapter 5. Nevertheless, this error had two plausible root causes, either the wrong gimbal motor data (i.e. EC-16 versus the EC-16 max) or the wrong gimbal rate (i.e. 50 deg/s equals 0.872 rad/s equals 8.333 RPM, and the initial sizing may have used 0.872 RPM in the gearhead data) was used for selecting the particular GP-22C gearhead. From this knowledge, the gear ratio was then recalculated/reselected. Noting that although specification sheets state the EC-16max can reach an 11900 RPM no-load speed at 24 V with a maximum up to 20000 RPM, the GP-22C gearhead is limited to 8000 RPM. Thus, the ratio 8000:8.333 yields a required Rev B gear ratio of 960:1 (the Rev

A value is 4592:1). A gear ratio less than 960:1 will ensure 8.333 RPM is reachable with a motor's un-gear'd speed not exceeding 8000 RPM. Here, one should note that the Rev A ratio of 4592:1 drove a selection of a gimbal gearhead shaft interface of 2.5 mm shaft diameter. To retain the same dimensionality of the VSCMG assembly, a 2.5 mm shaft diameter is also selected for Rev B. From the GP-22C data in Table 7.4(b), a gear ratio less than 960:1 and 2.5 mm corresponds to a gear ratio of 850:1. From this, one can see that $8000/850$ corresponds to 9.411 RPM or 56.5 deg/s. This means that the 850:1 gear ratio for the GP-22C as attached to the EC-16max motor is a feasible selection for the Rev B gimbal motor with margin as the gimbal rate requirement has changed from 50 deg/s to 5 deg/s. From this, the 850:1 gearing will be used in Rev B. In short, with a gear ratio of 850:1, the maximum flexibility in performance can be tested to see if improved attitude performance with reduced motor wear results.

7.4 Mechanical Design

The mechanical design of the VSCMG system has two goals. First, it provides the primary structural backbone for connecting the VSCMG subcomponents. Second, it seeks to construct a structurally sound Carbon Fibre rotor and interface that enables achieving the mass savings benefits mentioned earlier. Both of these goals have driven the VSCMG mechanical design, documentation of which is captured in a collection of assembly and as-built drawings. Note that several of these 2-D drawings are contained in Appendix C. However, the key components of these drawings are captured in Figures 7.3, which shows the full configuration of VSCMG components, and 7.4, which illustrates the components of the wheel assembly.

As one can see, the structure consists of a gimbal support bracket, wheel assembly, and containment bowl. The support structure fulfills the first goal in providing the connecting structure to the other assemblies. The containment bowl, depicted in both Figs. 7.3 and 7.4, serves to muffle the blast if the high speed Carbon Fibre composite undergoes catastrophic failure. This structure needs strength to contain such a blast and is therefore made of a metal, Aluminium, in the prototype. However, to enjoy increased mass savings, future versions of this component should be built of Kevlar to make it rugged yet light.

Next, the wheel assembly, depicted in Figure 7.4, consists of the rotor assembly, the containment bowl, and the motor assembly. The rotor assembly includes a center mount, a two-part hub, and the Carbon Fibre ring while the motor assembly includes the motor/generator, the

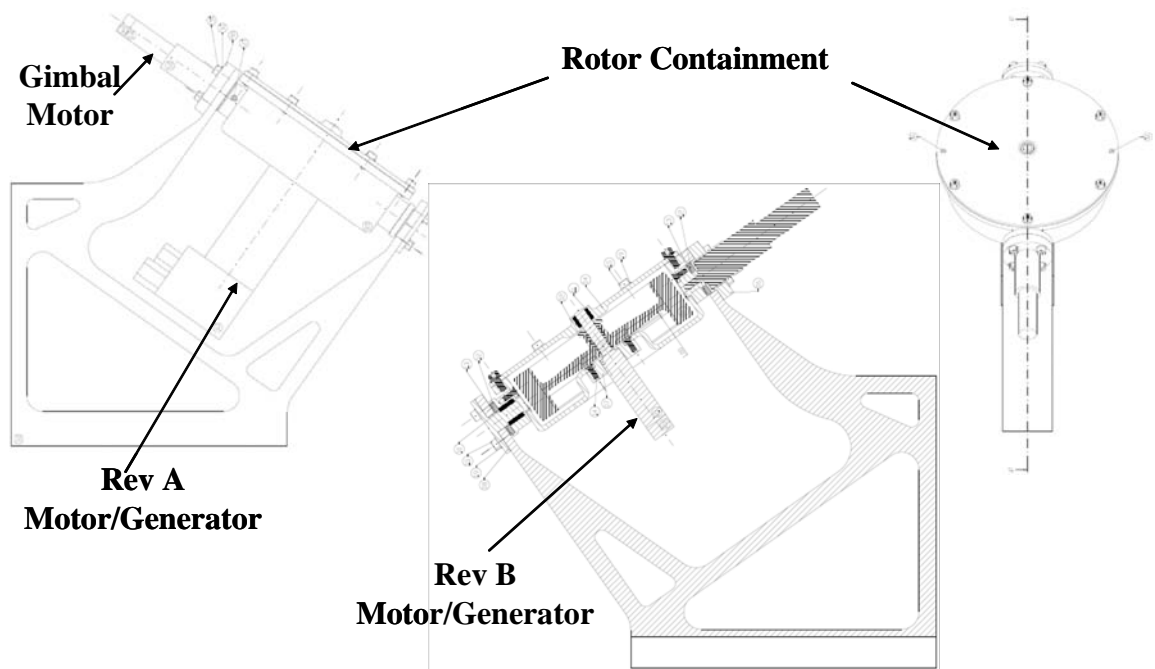


Figure 7.3: VSCMG Assembly Design

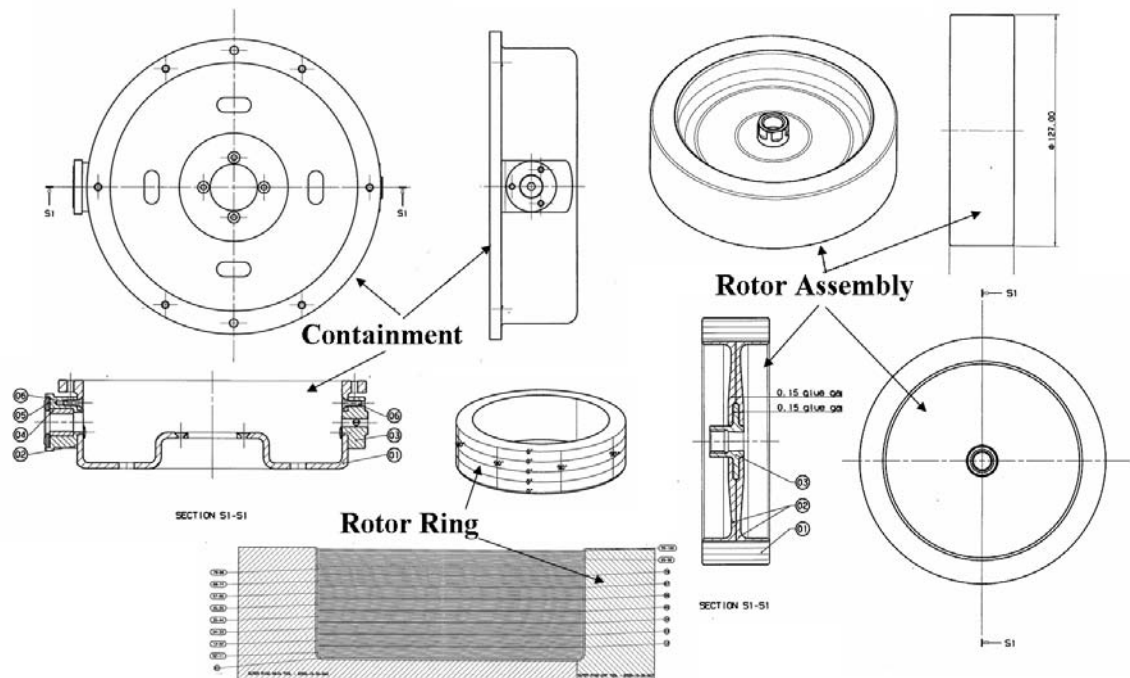


Figure 7.4: Wheel Assembly and Components

wheel motor interface, and locking nut which keeps the rotor attached to the motor. The containment bowl mentioned previously, then provides the structure that links the wheel assembly to the support structure and gimbal assemblies. Fulfilling the second goal addressed earlier, a key contributor to the wheel assembly is the Carbon Fibre rotor that provides the low mass, high strength inertia necessary to sustain high speed operation and deliver adequate energy. This Carbon Fibre rotor, made of uni-directional fibres in the hollow ring outside of a multi-directional Carbon Fibre hub made in two pieces, is comprised of several plies or layers. These plies are depicted in Figure 7.4.

As earlier implied, the gimbal assembly bracket, made of Aluminium in the prototype to reduce initial development costs, provides structure to connect the gimbal motor to the wheel assembly and containment in such a fashion as to permit commanded rotation of the wheel assembly about the gimbal axis. It also provides mechanical primary structure to support the full VSCMG set of components and is an integral part of the whole system.

Combining these assemblies together, Figure 7.5 illustrates the integrated mechanical design of Rev A VSCMG system through the Rev A CAD model (Figure 7.5(a)) and the as-built prototype (Figure 7.1(b)). From the CAD model, one can see the Rev A components mentioned thus far in a single VSCMG unit, including the containment bowl, the Carbon Fibre rotor within the containment bowl, the wheel EC-45 motor/generator, the gimbal EC-16max motor, and the support structure. These components interact to provide adequate rotor speed and inertia for ensuring the proper energy storage/drain and attitude torquing are delivered to the spacecraft. In addition, the Rev A prototype photograph shows the VSCMG system with the containment bowl lid removed and the EC-45 motor on the right prior to its installation. Also, a clear view of the Carbon Fibre rotor is captured in this image. One can see that the actual build of the VSCMG closely matches the design set forth in the CAD model. Although the design calls for a cluster of VSCMG assemblies, a single VSCMG can provide the full functionality of an ESACS but on a reduced scale.

7.5 Electrical Design

In order to make the mechanical system just illustrated work effectively, the electrical system must provide the current and voltage necessary to make each component operate. The electrical system for the VSCMG system consists of the wheel motor/generator servo-amplifier and its associated interface provided by the SSC Flywheel Energy Storage (FES) board in

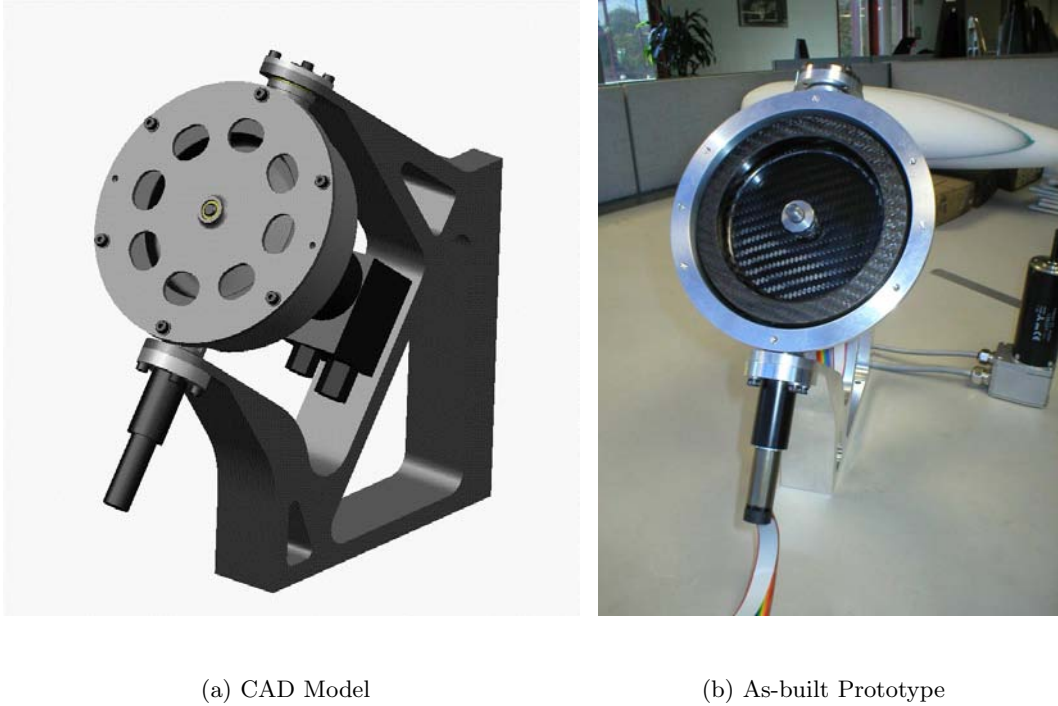
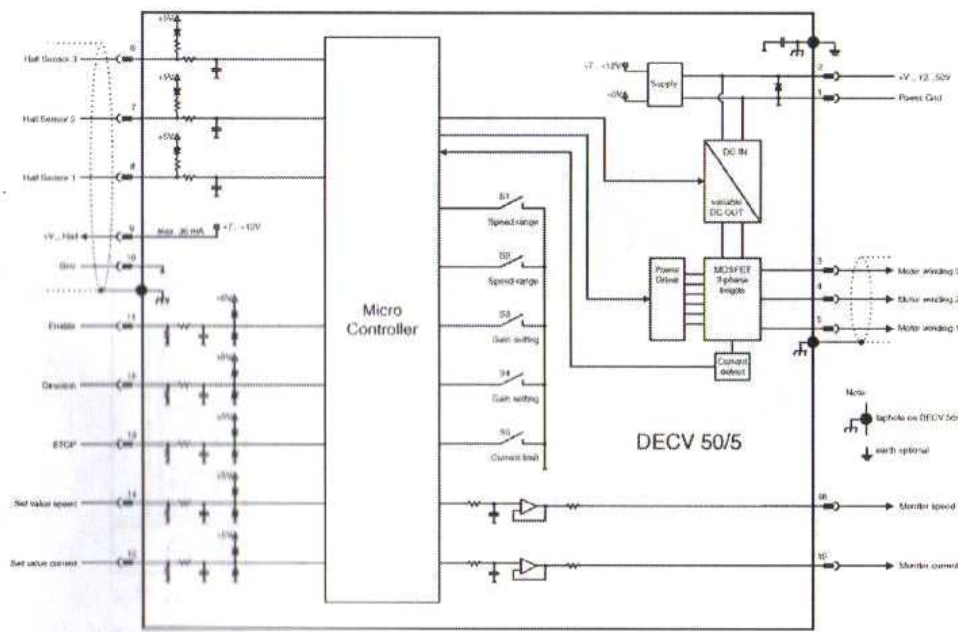


Figure 7.5: Rev A Design

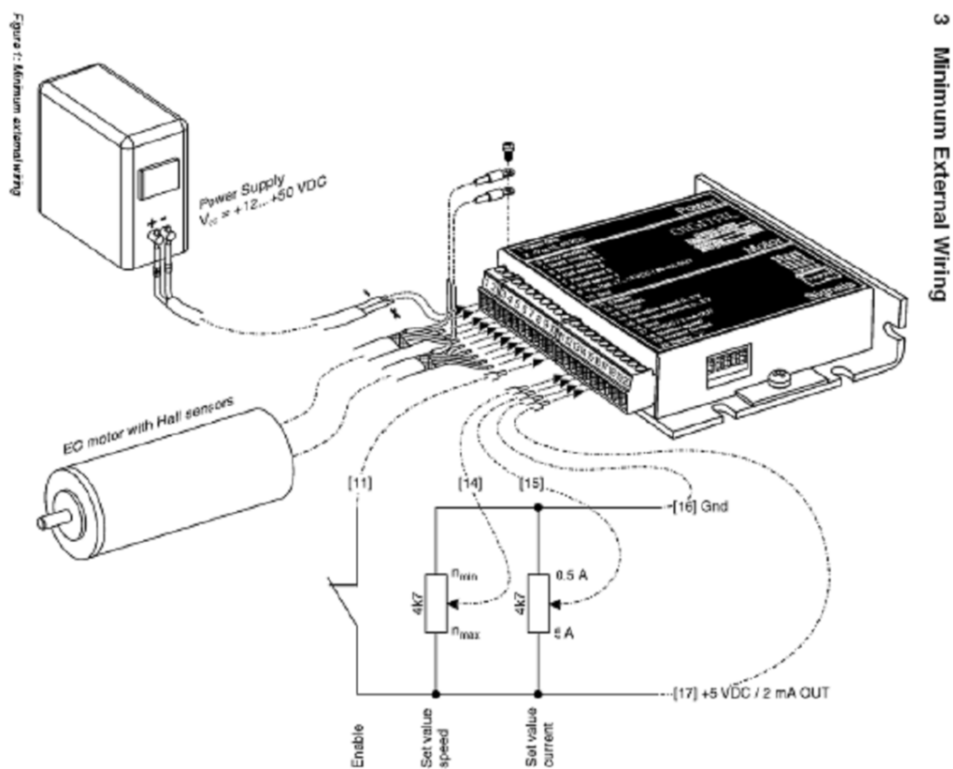
addition to the gimbal motor servo-amplifier and its associated connection circuit board with optional magnetic resonance encoder circuit. Note that the rest of the support electronics is delivered to the wheel and gimbal electronics via the satellite electrical power system as described in Chapter 8.

As both the wheel and gimbal motors require a servo-amplifier to drive them, the servo-amplifier was chosen to ensure a match between both boards. The governing requirement was that the system needed not only to be able to sustain fast speeds (to at least 50000 RPM) of Brushless DC Motors potentially without an encoder, but also permit external speed and current control. The most obvious servo-amplifier alternatives for the EC-16 and EC-16max were the DES 50/5 and DECV 50/5. As it turns out, the DES 50/5 will not operate without an encoder, so the DECV 50/5 was chosen of the two. One should note that the schematic layout for this servo-amplifier is given in Figure 7.6(a) and its minimum wiring interface is given in Figure 7.6(b)

Next, the interface electronics for the gimbal motor connections to the gimbal DECV 50/5 servo-amplifier are included in the minimum wiring diagram of Figure 7.6(b). Note that stop/enable, direction, and un-gearred gimbal motor speed inputs to the DECV are designed to be automatically controlled by the satellite data command system, an example of which



(a) DECV Schematic



(b) DECV Minimum Wiring Requirements

Figure 7.6: Wheel and Gimbal DECV 50/5 Servo-Amplifier

is described in Chapter 8.

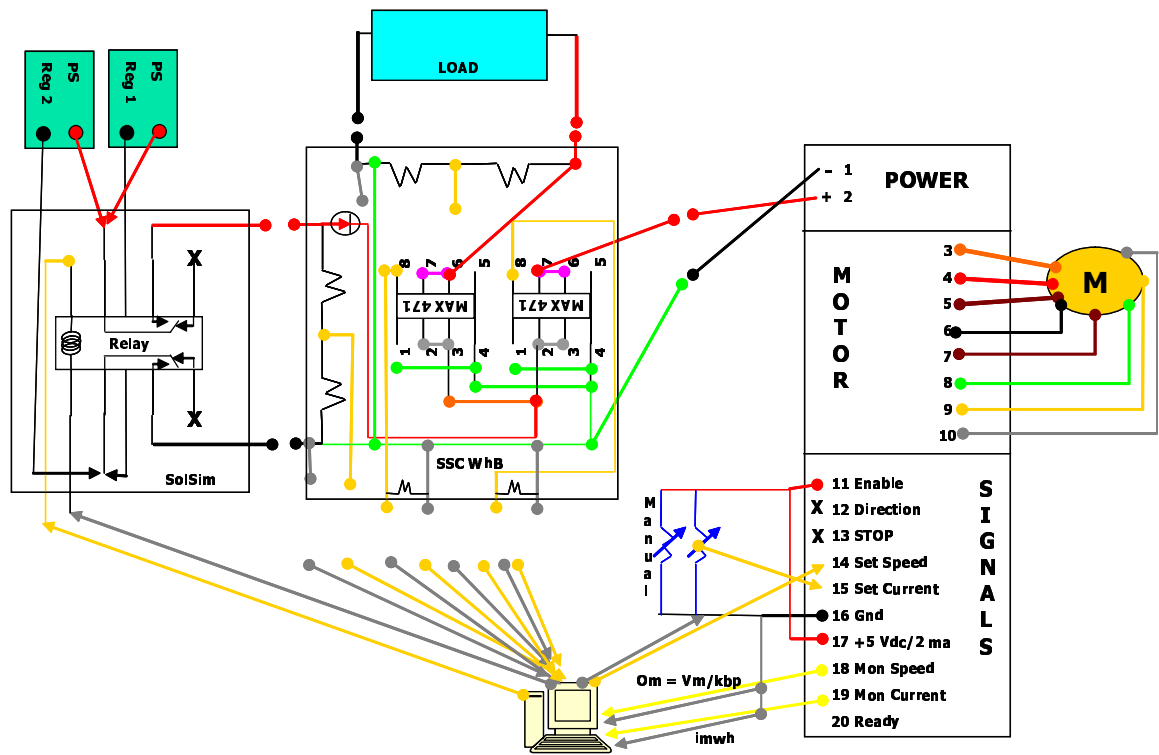
Finally, perhaps the most important electrical development for the VSCMG ESACS prototype is shown in the schematic of Figure 7.7(a). This schematic contains two circuits, one for providing the minimum electronics and the other for interfacing the wheel, electronic load, and power source while simultaneously linking important measurements to the telemetry system. Although direction command is not relevant here as the wheel rotor spins in one defined direction, command of the wheel motor speed is permitted in a manual mode, or more desirably, automatically commanded through a computer interface. The latter option is used in the validation tests of Chapter 8. One should note here that the load and supply voltages are measured by voltage dividers with load and supply current are measured with bi-directional current sensors. Envisioned future work will explore adding a third set of these measurements for the motor electrical input to the DECV as well.

In summary, the electronics of the single VSCMG actuator is primarily provided by the combination of two DECV 50/5 servo-amplifiers, one each for the gimbal and wheel motors, with a basic circuit connected to the gimbal driver and a two-part circuit board for the wheel driver. One of these circuits drives the servo-amplifier's motor control and the other regulates power flow between the wheel, motor, and driven electronic load.

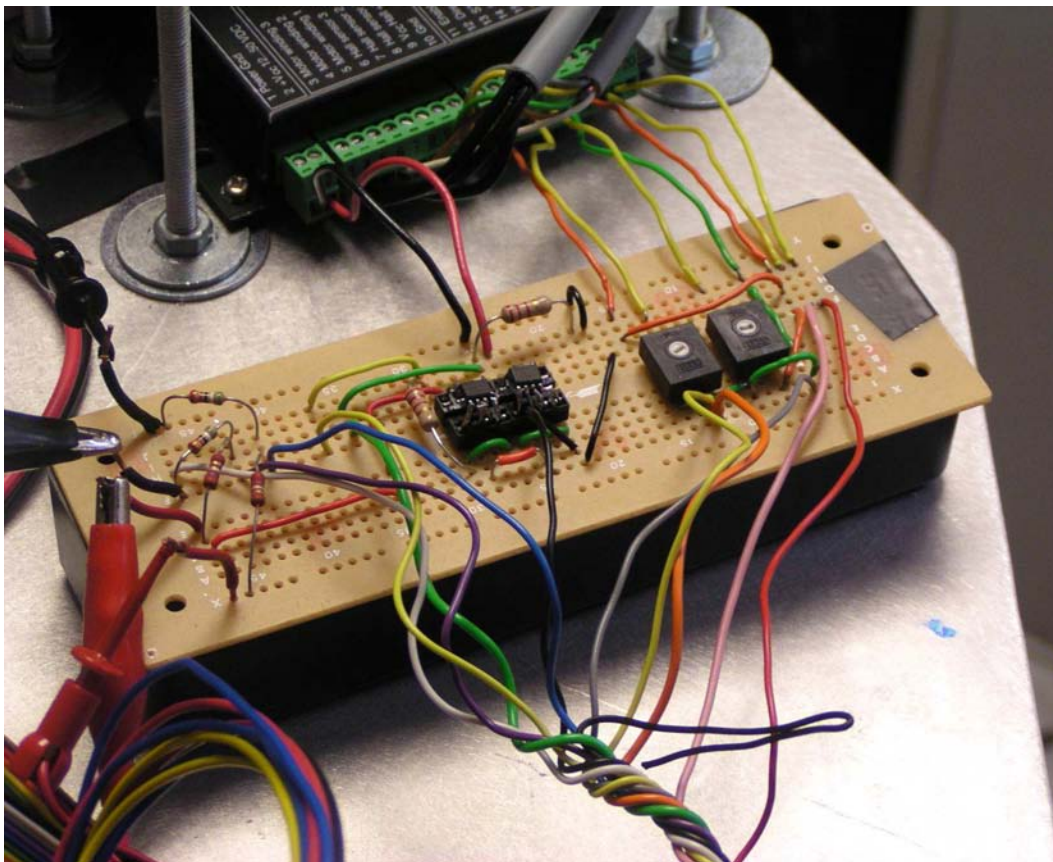
7.6 Cluster Design

Building on the wheel motor/generator, gimbal motor, mechanical structure, and electrical circuit designs of the single VSCMG prototype presented in the previous sections, it is now possible to address the anticipated design for a cluster of VSCMGs. At this point, the standard CMG pyramid is the design of choice due to its inherent redundancies, but a strong case may be made for other configurations, including using three VSCMGs aligned along the vehicle's roll, pitch, and yaw axes. The benefit of the pyramid cluster is that if there are failures in achieving the desired wheel changes but the system can still maintain an acceptable fixed speed, redundant CMG control is still possible (assuming one can sustain the loss of the FES capability). Or, if the gimbal motors fail, the full cluster can be operated as four momentum wheels and retain both attitude and power control while losing the torque efficiency tendered by gimbaling.

The Rev A design using the Large Motor for this configuration is depicted in Figure 7.8(a) whereas the Rev B design is shown in Figure 7.8(b). The illustrated, inter-locking cluster



(a) Board Design



(b) Board Photo

Figure 7.7: SSC FES Board

design approach permits gradual development of the system as one actuator can be built and tested, followed by one or more actuators added and tested individually, culminating in the new group this creates tested together. For example, one can transition from a one VSCMG cluster to a three VSCMG cluster by testing one VSCMG by itself, then two more individually, and then adding these two to the cluster quite easily through the inter-locking architecture. Then, the full three actuator cluster can be tested while awaiting development of a fourth VSCMG. Also, if follow-on versions are made, these components can be tested with the previous versions as long as VSCMG matching is not a requirement. This concept should prove useful in the laboratory build-up of a VSCMG ESACS cluster when evolving from the Rev A prototype to the Rev B build to the final Rev C design. The idea is to use the Rev A prototype in a cluster with the Rev B build when demonstrating a pair or even 3 VSCMGs (i.e. if 2 Rev B models are made). Note that a key trade investigation this may engender is exploring what happens when a member of the VSCMG cluster has different wheel speed and torque capabilities than the other VSCMGs. In other words, investigating the precautions and operational envelopes of a mixed set. Regardless, the pyramid cluster connection approach shown in Figure 7.8 should prove quite beneficial for future builds.



(a) Rev A VSCMG Cluster Design



(b) Rev B VSCMG Cluster Design

Figure 7.8: VSCMG Cluster Images

7.7 Proposed Design Changes for a Possible Flight Design

Having illustrated the key elements of the Rev A design as well as the anticipated changes for Rev B, it is now important to identify the concepts necessary for the anticipated Rev C flight

model. First, the Aluminium support structure should be replaced with multi-directional Carbon Fibre composite. This will save mass and also increase strength. Additionally, the Aluminium containment bowl should be replaced with Kevlar composite. This will also increase strength while reducing mass. These changes should cut 2 to 3 kg off the current 5 kg design and will make the system more competitive for flight.

Second, an additional current sensor plus voltage divider pair should be added to the SSC FES system or its follow-on replacement. This will help monitor the efficiency of the motor/generator drive electronics as the motor's electrical input during charge and export during discharge can be directly compared to the mechanical state during charge and discharge.

Third, an additional improvement to the drive electronics is desired through developing a full servo-amplifier plus energy storage board in-house. Notionally this would take advantage of increased/controllable discharge current while potentially integrating with SSTL's existing momentum wheel drive electronics. As shown in Lee's thesis (Ref. [161]) on BLDC generator drives, actively controlling a BLDC's windings during discharge can increase power production up to 30 %.

Another improvement to the electronics should be the use of manufactured Printed Circuit Boards with components populated by machine within the motor/generator drive board. This will help make the system lighter, more rugged, more reliable, and cleaner. This system should also contain a manual switch capability for easy switching between manual and automatic modes for flywheel operation. This can be accomplished, perhaps, with a rocker switch or a set of DIP switches.

Another recommended improvement is that the mechanical bearings in the wheel motor/generator and along the wheel shaft be replaced with magnetic bearings to reduce high speed vibration. Also, such bearings will better stabilize the system and much further reduce the friction. Depending upon the degree of power efficiency enjoyed by these bearings, such reduced friction may permit keeping the maximum wheel speed lower while keeping the wheel near its freewheel speed in eclipse.

If the previous improvement is not possible, a motor with decreased bearing friction should at least be used as the motor/generator. This action would permit a longer lifetime where the goal is a motor that can discharge throughout eclipse. Another motor change recommended is the use of the Maxon EC-22 discussed earlier for its 6000 RPM increase in speed over the EC-16 max from Rev A and Rev B.

Finally, the system should be tested in a thermal/vacuum chamber for potential outgassing of the composite materials, thermal heating in the motor, and other space environment limitations on its operation. Such ground testing allows the spacecraft developer to glean and resolve these affects during ground operations rather than have the system suffer in orbit.

7.8 Summary

This chapter has investigated the design and development of an initial prototype for a VSCMG-based ESACS as well as future prototype developments leading to a flight model (Rev C). Several issues have been raised in this process and key future improvements to the mechanical and electrical components identified. Having defined and presented the development of this prototype, it is now possible to use this prototype to validate key concepts as is investigated in Chapter 8.

Chapter 8

Practical Experimentation

This chapter describes the practical experimentation of the Rev A combined ESACS VSCMG prototype detailed in Chapter 7 and is organized into sections on testing goals and requirements, integrated ESACS testing, experimental results, discussion of experimental results, and proof of research novelty. The latter of these is the culmination of the research effort as it bridges the theoretical sizing developments identified in Chapter 5, the hardware design from Chapter 7, and the experimental results of this chapter.

8.1 Test Goals and Requirements

The first step in initiating a subsystem test regime is to identify the test goals and requirements. This helps focus the effort in detailing performance and these goals and requirements serve as a yardstick to which the experimental results are measured. Following this idea, the primary goal for the integrated test program is to demonstrate that an Energy Storage and Attitude Control Subsystem (ESACS) can slew a spacecraft while storing and draining energy, preferably employing COTS components. Fulfilling this goal is akin to answering the question “Does it work?” More specifically, the current work aims to demonstrate that one VSCMG actuator can achieve this goal. Next, the secondary experimentation goal is to identify the performance of a single-actuator system. It seeks to answer the question “How well does the system work?” Details related to this goal are to identify the available capacity (energy density), power density, energy/power efficiency, and flywheel battery depth-of-discharge for the given VSCMG ESACS mass. Note here that these details all relate to the ES performance of the ESACS. Due to its experimental complexity, assessing the detailed attitude torque per-

formance of the system is planned for future research, but notional attitude slewing results are desired to fulfill the primary goal. Finally, the tertiary goal is to identify imperfections and generalizations in the initial theory as well as key areas for further investigation in continuation of this research program. Fulfilling this goal involves identifying possible sources of experimentation error which may significantly contribute to these perceived imperfections. The error sources also help illustrate hurdles encountered during the present work which may be resolved as experimental methods evolve. Thus, the research goals can be summarized as verifying that the design approach works, validating the resulting system against its requirements, and accruing lessons learned from prototype testing for improved performance in future builds.

In order to achieve the validation goals mentioned in the previous section, the objective requirements of such testing must be understood. These are best summarized in the following requirements matrices (Tables 8.2(a), 8.2(b), 8.3(a), and 8.3(b)) extended from Tables 7.1 in Chapter 7 and 3.1 in Chapter 3. These tables show the mapping between the initial mission requirements, the derived VSCMG-based ESACS design requirements to meet these mission requirements, the anticipated basic performance specifications for the Rev A prototype system, and the more complete Rev B specifications. One may notice that the desired design calls for a pyramid of VSCMGs with wheels that can reach 46100 RPM with a 0.035 m length, 0.0099 kg m² spin inertia, and 5 deg/s gimbal rate to yield 168.6 W/kg power density, 8.23 W hr/kg energy density, 60 % round-trip transmission-efficiency, and a 140 deg maneuver in 70 s with a 12 s dead-band. To achieve such capability, the aim is for Rev A to yield 9000 RPM in maximum wheel speed, 10 deg/s in gimbal rate, 36.7 W/kg in power density, and 0.14 W hr/kg in energy density for a 20 deg maneuver in 10 s and Rev B to yield 46100 RPM in maximum wheel speed, 50 deg/s in gimbal rate, 1095.1 W/kg in power density, and 5.4 W hr/kg in energy density for a 140 deg maneuver in 70 s with a 12 s dead-band. The key idea here is that the Rev A system demonstrates a core set of ESACS design goals while the rest are satisfied in Rev B. Eventually, a magnetic-bearing design will be added to the VSCMG ESACS for long-term, on-orbit performance, but many VSCMG ESACS lessons can be learned in Rev A and Rev B. Thus, the requirements and goals identified here set the stage for the Rev A prototype testing investigated here and also build toward future tests.

Table 8.1: Mission and Design Requirements

Parameter	Value
Orbit Altitude, h , km	450
Depth-of-Discharge, dod , %	80
Transmission Efficiency, x_{msn} , %	90
Peak Power Demand, P_r , W	1100
Eclipse Duty Cycle, d_{ty} , %	10
Power Bus Voltage, V_{bus} , V	28
Max Single-axis inertia, $I_{T_{max}}$, kg m ²	120
Slew maneuver angle, θ_f , deg	140
Slew maneuver time, t_f , s	70
Slew maneuver dead-band, t_{off} , s	12
Satellite Total Mass, M_{sc} , kg	400
Allowable Satellite Mass, M_{ta} , kg	450
Allowable ACS plus ES Mass, M_r , kg	45

(a) Mission Requirements

Parameter	Value
Minimum Wheel Speed, Ω_n , RPM	6510
Maximum Wheel Speed, Ω_x , RPM	46100
Rotor length, l_r , m	0.035
Wheel Spin-axis Inertia, I_{ws} , kgm ²	0.0099
Maximum Gimbal Rate, $\dot{\delta}$, deg/s	5
Maximum Wheel Acceleration, $\dot{\Omega}$, rad/s ²	10.13
Round-trip Efficiency, X_e , %	60
Transmission Efficiency, X_{msn} , %	90
Depth-of-Discharge, dod , %	80
Energy Density, E_d , Whr/kg*	8.23
Minimum Power Density, P_d , W/kg*	22.5
Maximum Power Density, P_d , W/kg*	168.6
Maneuver Angle, θ_f , deg	140.0
Maneuver Time, t_f , s	70.0
Maneuver Dead-band, t_{off} , s	12.0

* Assume 9.23kg cluster mass and 80% energy conversion efficiency.

(b) Design Requirements

Table 8.2: Rev A and Rev B Requirements

Parameter	Value
Minimum Wheel Speed, Ω_n , <i>RPM</i>	2000
Maximum Wheel Speed, Ω_x , <i>RPM</i>	9000
Rotor length, l_r , <i>m</i>	0.035
Wheel Spin-axis Inertia, I_{ws} , <i>kgm²</i>	0.0099
Maximum Gimbal Rate, $\dot{\delta}$, <i>deg/s</i>	10
Maximum Wheel Acceleration, $\dot{\Omega}$, <i>rad/s²</i>	100
Round-trip Efficiency, X_e , %	60
Transmission Efficiency, X_{msn} , %	90
Depth-of-Discharge, <i>dod</i> , %	80
Energy Density, E_d , <i>Whr/kg*</i>	0.14
Minimum Power Density, P_d , <i>W/kg*</i>	8.0
Maximum Power Density, P_d , <i>W/kg*</i>	36.7
Maneuver Angle, θ_f , <i>deg</i>	20.0
Maneuver Time, t_f , <i>s</i>	10.0
Maneuver Dead-band, t_{off} , <i>s</i>	0.0

* Assume 5*kg* single unit mass and 80% energy conversion efficiency.

(a) Rev A Requirements

Parameter	Value
Minimum Wheel Speed, Ω_n , <i>RPM</i>	6510
Maximum Wheel Speed, Ω_x , <i>RPM</i>	46100
Rotor length, l_r , <i>m</i>	0.035
Wheel Spin-axis Inertia, I_{ws} , <i>kgm²</i>	0.0099
Maximum Gimbal Rate, $\dot{\delta}$, <i>deg/s</i>	50
Maximum Wheel Acceleration, $\dot{\Omega}$, <i>rad/s²</i>	10
Round-trip Efficiency, X_e , %	60
Transmission Efficiency, X_{msn} , %	90
Depth-of-Discharge, <i>dod</i> , %	80
Energy Density, E_d , <i>Whr/kg*</i>	5.4
Minimum Power Density, P_d , <i>W/kg*</i>	154.7
Maximum Power Density, P_d , <i>W/kg*</i>	1095.1
Maneuver Angle, θ_f , <i>deg</i>	140.0
Maneuver Time, t_f , <i>s</i>	70.0
Maneuver Dead-band, t_{off} , <i>s</i>	12.0

* Assume 3.5*kg* single unit mass and 80% energy conversion efficiency.

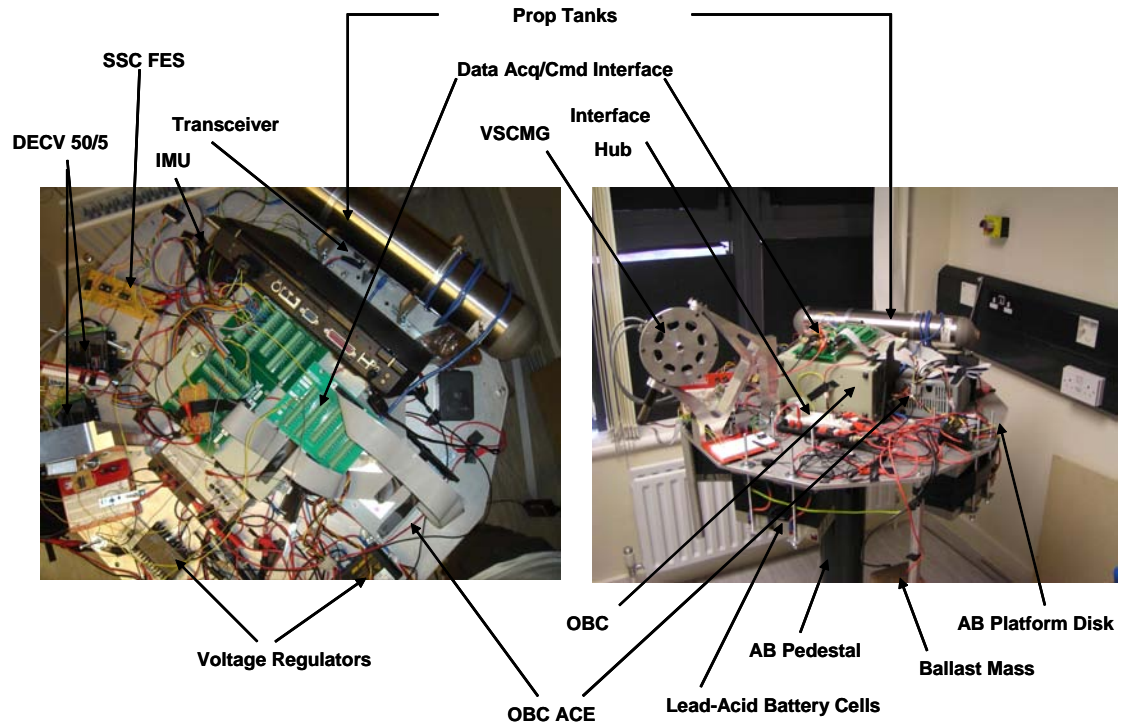
(b) Rev B Requirements

8.2 Integrated Testing

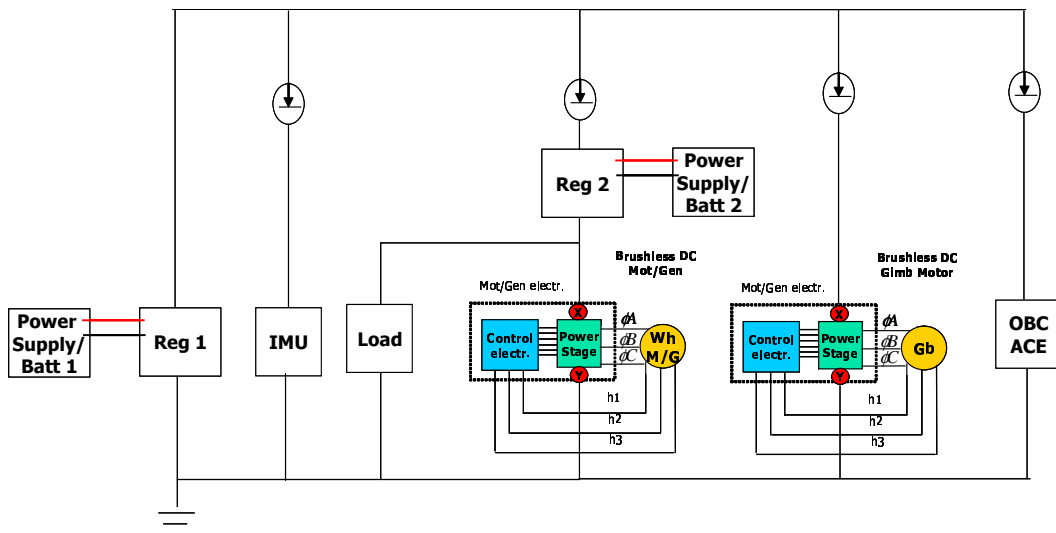
Integrated testing of the Rev A prototype seeks to satisfy the Rev A performance requirements spelled out in Table 8.3(a) and was accomplished using the spherical, air-bearing test article shown in Figure 8.2(a). This test article consists of an Aluminium platform built around a smooth, hemispherical ball that sits in a cushion of air generated through a structural pedestal. By using this central, air-bearing concept, the structure floats, simulating the free-fall of Earth orbit. This allows fairly realistic tests of three-dimensional attitude actuators on the ground. Note that the electrical design of this test article for demonstrating the benefits of the ESACS is captured in Figure 8.2(b). Here one can see that the system uses two power supplies (regulated at 24 V each) to feed the on-board computer power supply (ACE), two DECV servo-amplifiers attached to the wheel and gimbal motors, the attitude determination Inertial Measurement Unit (IMU), and the electronic load, all of which are protected by high current diodes. Sunlight is simulated via lead-acid batteries through the voltage regulators which are shutoff via the SolarSim, a 5V relay tied to the command circuitry. Additional details on this test article's configuration and performance are included in Appendix C as well as presented conceptually in [162].

Several test procedures govern the test regimen conducted during developmental and integrated testing of the ESACS. A flowchart of the inter-connectivity of these tests is given in Appendix C. The critical tests captured therein include wheel rotor balancing, SSC FES voltage and current sensor calibration, and IMU calibration. One cannot over-emphasize the importance of these tests. First, rotor balancing is paramount for ESACS. An unbalanced rotor can produce several undesirable modes on the structure such as hammering (static unbalance) and wobbling (dynamic unbalance) which can wear down motor bearings, fatigue the spinning rotor, yield in-accurate data, and render the ESACS useless. Since this issue is driven primarily by rotor build imperfection vice rotor support bearings, such effects can be present even in magnetically-supported VSCMG rotors. Nevertheless, details of the rotor balancing process used for space flight hardware by SSTL and applied to the Rev A prototype are included in Appendix C, including the test equipment, initial test day configuration, balance machine calibration, and mass addition iteration. Also addressed are practical errors one can make in interpreting balancing requirements depending upon whether one uses industry vernacular or international standard to define performance. Second, calibration of the measurement sensors is critical to successful prototype testing. This proves especially

Figure 8.1: Air Bearing Test Article



(a) Test Article Configuration



(b) Test Article Electronics

difficult when the calibration curve is assumed linear but one needs calibration values in the nonlinear region. These concepts are elaborated in Appendix C. Third, similar calibration issues for the IMU used in air-bearing attitude determination are presented in Appendix C. This later topic contributes to the experimental error found in initial attitude torque testing and will be further tested by others in follow-on research.

8.3 Experimental Results

Several test configurations and trial runs were completed in testing the power and attitude control performance of the Rev A prototype, including three different wheel speeds (5000, 7000, and 9000 RPM), two different gimbal rates (5.88 deg/s and 9.80 deg/s), and 3 different load conditions (no-load, low power (small) load, and higher power (big) load) with 15 different runs covering the two extreme combinations of factors. The Test Matrix in Appendix C gives further details of these runs. Nevertheless, results of these tests which helped validate the performance for the Rev A system follow, setting the stage for further development of this technology. One should note that the emphasis of the current research lies in validating the fact that energy can be stored and drained while changing vehicle attitude with one actuator. Future results will address higher power electronic loads and isolate the attitude performance for a full cluster. However, this research effort will build on the groundwork set forth in the experiments described.

The test results that follow can be divided into the categories of wheel speed, power storage/drain, and attitude slewing. These results are those from direct measurement of the test article during combined attitude and power operations. Figure 8.2 shows the wheel speed time history for a typical run with the largest electronic load (40 W) in the loop. One can also see in this plot the results of a model built from first principles used to match the data. This model helped determine the values for key parameters such as true line resistances and additional voltage losses (e.g. Pulse Width Modulation (PWM) capped at 95% of the maximum voltage). One should note here that this model can also be compared to the curve fitting results from analyzing the raw motor data. This becomes important in Figures 8.2 and 8.3 which show the model compared to the raw experimental data (Fig 8.2) as well as the model compared to polynomial fits of the raw data (Fig 8.3) for the key system aspects, motor, supply, and electronic load power histories. These figures are centered on reflecting the third load cycle, chosen to avoid additional losses by beginning and ending wave forms.

The final topic mentioned above is that of attitude slewing. Preliminary results follow in Figures 8.4(a) and 8.4(b), which show the Euler Axis vector components and rotation angle histories during full load and no-load operation. Analysis of the raw data depicted here is further described in Appendix C and leads to the results discussion in the next section.

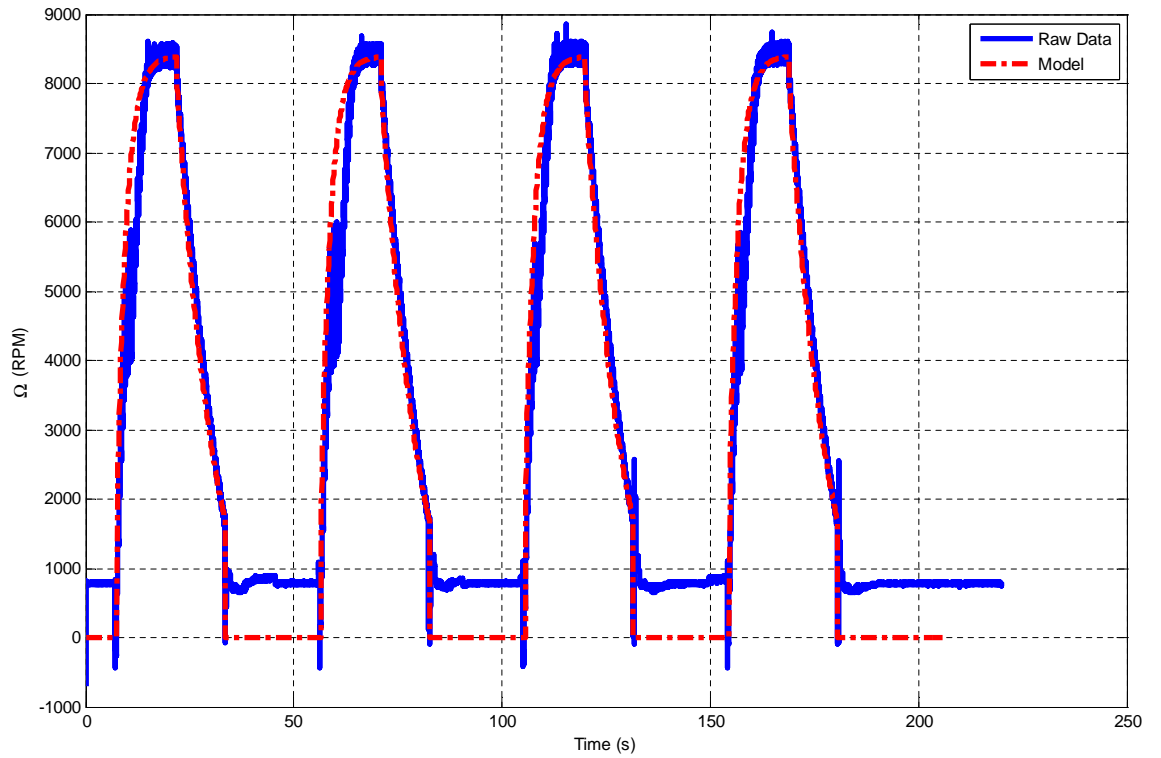
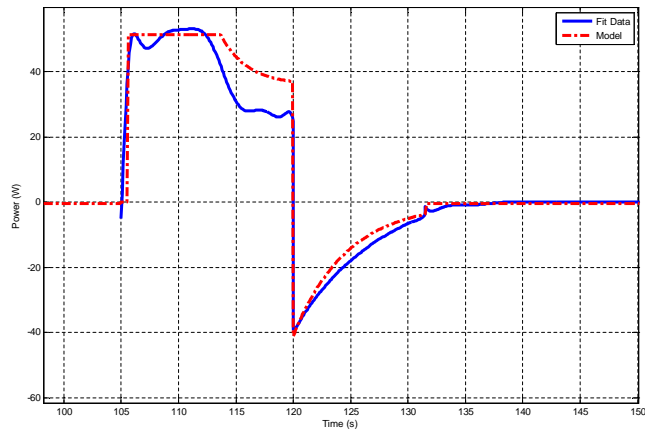


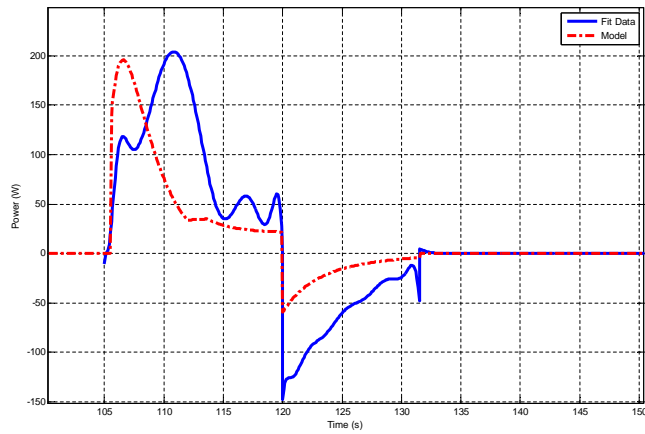
Figure 8.2: Wheel Speed Performance

8.4 Discussion of Results

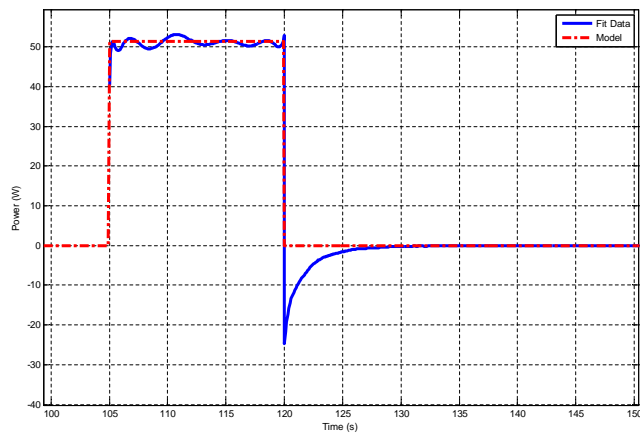
Having captured the results of the Rev A prototype experiments conducted for this thesis, it is now possible to analyze and discuss these results then draw key conclusions. As mentioned earlier, the results shown in Section 8.3 were processed using equations in Appendices C and B and analyzed. The output of these equations is summarized in Table 8.3. This table includes the reduced desired requirements values (reduced by limiting the wheel speed – necessary to glean as much value from COTS experiments as possible), theoretical values obtainable with a magnetically-levitated system that still contains iron loss (additional values



(a) Net Load Power Data Fit Versus Model

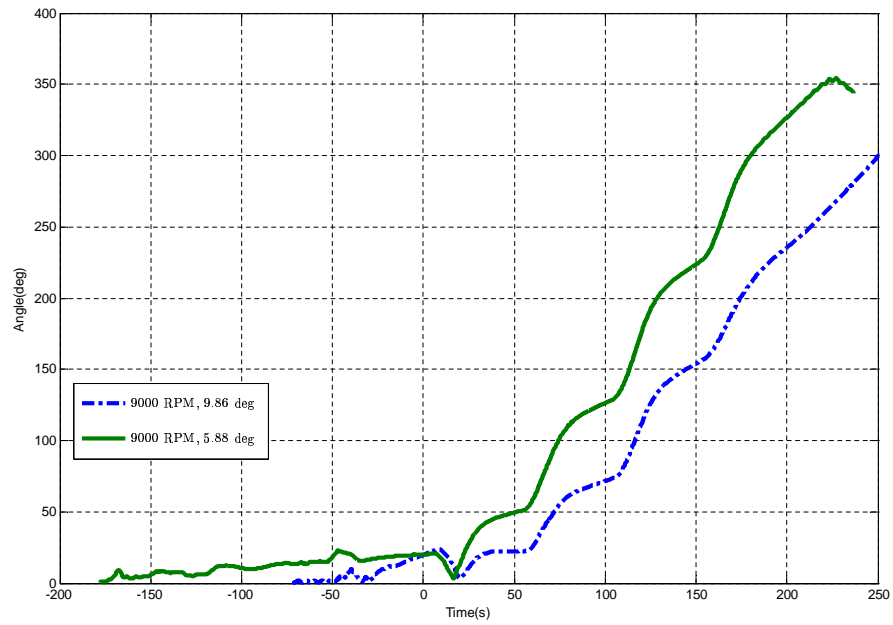


(b) Net Motor Power Data Fit Versus Model

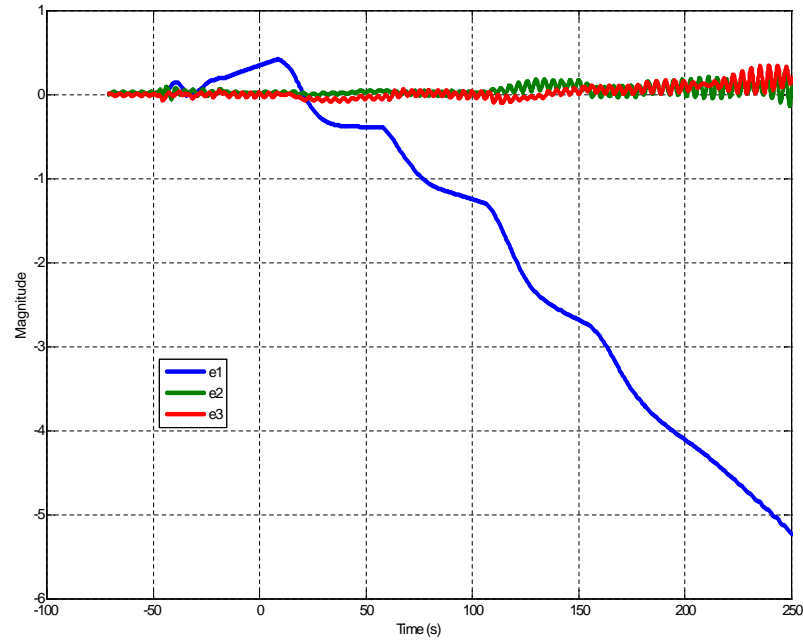


(c) Net Supply Power Data Fit Versus Model

Figure 8.3: Net Power History



(a) Euler Rotation Angle History



(b) Euler Angle History

Figure 8.4: Attitude Data Histories

without iron loss are described in the Table 8.3 note), theoretical mechanical bearing results, experimentally measured/data fit values, and the resulting Experimental Error for the fully-loaded problem. In a first-of-its-kind experiment of this type, 10-20% experimental error is

Table 8.3: Experimental Error

Parameter	Reqts	Mag B	Mech B	Exper	% Error
Min Wheel Speed, Ω_n , RPM	2000	1676	1676	1616	3.58
Max Wheel Speed, Ω_x , RPM	9000	8582 [§]	8380	8420	0.48
Max Gimbal Rate, δ_x , rad/s	10	10	10	9.86	1.40
Direct Transmission Efficiency, x_{msn} , %	90	83.16	83.18	57.52	30.85
Round-Trip Transmission Efficiency, x_e , %	60	64.25	64.18	57.01	11.17
Depth-of-Discharge, dod , %	80	80.02 [§]	79.99	84.11	5.15
Vehicle Slew Rate, $\dot{\theta}$, deg	2	2	2	3 [‡]	N/A [‡]
Energy Density, E_d , whr/kg	0.140	0.024 [§]	0.024	0.028	15.36
Max Power Density, P_{dx} , w/kg	36.7	20.10 [§]	20.06	19.47	2.94
Min Power Density, P_{dn} , w/kg	8.0	1.86 [§]	1.86	2.06	10.90

[§] These values assume eddy current loss replaces mechanical bearing friction loss and the system has full iron losses, which should actually decrease dramatically with a magnetic-levitation system. If iron losses are eliminated, for the same charge and discharge periods, Ω_x , DoD , E_d , P_{dx} , and P_{dn} become 130040 RPM, 98.71 %, 35.2 Wh/kg, 4380 W, and 3183 W, respectively.

[‡] This preliminary value is not conclusive and only listed here to demonstrate fulfillment of the primary objective. Further detailed performance testing will be accomplished in follow-on research.

to be expected, but much more than that requires explanation. From this, one can see that the minimum, maximum wheel speeds, maximum gimbal rate, round-trip transmission efficiency, depth-of-discharge, energy density, and maximum, minimum power density all have realistic experimental error values. Also notice that the attitude performance is preliminary and only included for completeness. Finally, one major reason the Direct Transmission Efficiency is the motor efficiency drops significantly with wheel speed decrease. Thus the transmission efficiency also drops as the speed decreases. Additional reasons for these errors as well as those listed in Table 8.3 are addressed next.

These errors can be attributed to several sources as identified in Table 8.4 and allocated to the measured parameters in Table 8.5. These sources include brushless DC motor bearing friction, operating the wheel motor/generator primarily outside its efficient speed range, lack of testing the maximum possible resistive electronic load that operates for a minimal time

frame, inaccuracies in equations adopted from the literature, inaccurate calibration of the Maxon Motor current, presence of aerodynamic drag from the ambient air surrounding the test article, test article mass center determination, IMU calibration and time synchronization, extra slew performance obtained during wheel motor spin-up/spin-down since the wheel rotor acts as a reaction wheel and starts slewing the test article prior to and during gimbaling, and extra design margin added to the gimbal performance calculations manifested in slewing. These sources of error will be discussed next along with the parameters impacted by each.

First, in the case of operating the wheel motor/generator primarily outside its efficient speed range, the candidate wheel brushless DC motor/generator data reflects $> 80\%$ efficiency when operating near the normal operating speed for a given voltage, however this value drops quite rapidly when below the stall speed. As it turns out, most of the wheel speed profiles follow that shown in Figure 8.2 and rely on ramping up for charge directly followed by ramping down for discharge to avoid losing energy to bearing friction during the freewheel phase. This, however, means that the motor is operating inefficiently during the ramp up until exceeding the stall speed and during the ramp down after dropping past the stall speed. Since much time is spent in this inefficient regime, the efficiency of the power conversion is directly impacted.

Second, it was found during the data analysis phase that the VSCMG was not tested with the maximum load possible. The approach used in testing was to try to run a light bulb with adequate power to keep it on for several seconds. However, higher power (i.e. with reduced resistance) loads are possible as the motor energy can drain much faster than displayed here. This is necessary to determine where the limit of capability occurs in terms of current and voltage of the load in conjunction with maximum speed and current of the VSCMG's wheel/motor. This factor contributes significantly to calculating the peak energy and power densities as these values have been limited by the electronic load employed.

Third, most of the equations crafted in the literature for the terms investigated in this thesis use wheel speed in the calculations vice using the actual power conversion values. This yields more optimistic results than necessary for a practical ESACS implementation.

Next, the calibration of the wheel motor/generator's motor current is not clearly defined in the motor operating manual or data sheets. This makes the current measurement for a laboratory experiment suspect. The resulting impact is uncertainty in the power conversion parameters (transmission efficiency, power density, and energy density).

Another impact which affects all the values is that of aerodynamic drag/windage loss on the VSCMG rotor via testing the system in ambient air conditions. However, much of this loss comes in limiting the efficiency of the wheel motor/generator, which has rolled bearing friction, windage, and copper loss into the bearing friction value associated with the starting current listed in the motor data. Although the preliminary attitude slewing results will be

Table 8.4: List of Most Likely Error Sources

Id No.	Error Source
A	Bearing Friction
B	Motor Run Outside Efficient Regime
C	Did Not Test Maximum Possible Load
D	Calculation Based on Actual Power, Not Wheel Speed
E	Motor Current Calibration
F	Aerodynamic Drag
G	Test Article Center of Mass Determination
H	IMU Calibration and Time Synchronization
I	Extra Slew Performance from Motor Spin-up/Spin-down (MW Mode)

Table 8.5: Error Allocation Table

Parameter	Error Sources
Direct Transmission Efficiency, x_{msn} , %	D, B, E, A, F
Energy Density, E_d , (Whr)/kg	C, B, D, E, A, F
Max, Min Power Density, P_{dx} , W/kg	C, B, D, E, A, F
Vehicle Slew Rate, $\dot{\theta}$, deg/s	G, H, F, I

refined and presented in follow-on work, several error sources render this initial performance as inconclusive. First, the air-bearing test article mass center was found via trial and error. Next, the IMU data bias calculation/calibration and time synchronization process was imprecise. Third, extra slewing performance (i.e. performance in the momentum wheel mode outside of the sized CMG mode) was attained when the wheel was spun up and down as these regions dominated the test regime. The gimbal was demonstrated with changing speeds, but there were periods when the gimbal was not actuated that the wheel changed speeds. In contrast, for the full actuator set (i.e. the full pyramid), this should not be a problem as unwanted wheel disturbance torque generated during spin-up and down can be rejected via the gimbals in a matched pyramid.

Next, although brushless DC motors are well known to reduce high friction inherent in commutation brushes, these COTS motors still have contact points through the ball bearings supporting the mechanical shaft. This contact causes friction and heating that reduces the

performance of the motor. To illustrate the effects of this problem, Figure 8.5 compares the discharge mode of a system that is mechanically suspended by ball bearings with iron losses, one that has magnetic bearing eddy currents with iron losses, and one that only has magnetic bearing eddy currents and no iron losses. This illustration assumes the power to the wheel motor is cutoff and the wheel is allowed to freewheel in the presence of drag, i.e. ball bearing friction for the mechanical case or eddy current drag for the magnetic case. Note that the eddy current analysis follows from the work by Wilson et. al. in [132] and was scaled by wheel spin axis inertia for EC motor ball bearing friction. This result shows the stark contrast in time it takes the system to slow down. Also depicted here is the laboratory data (with and without the electronic load) superimposed onto the different bearing models. An interesting result seen here is that the reduction of iron (joules heating) losses in the magnetic-bearing system have a more profound impact than the eddy current replacement of friction heating.

Carrying this idea further, Figures 8.6(a) and 8.6(b) further illustrate the no-iron loss case. In Figure 8.6(a), a full cycle that only tops out below 9000 RPM is shown for direct comparison to the mechanical results depicted earlier. As one can see, the discharge period is several hundred seconds as opposed to tens of seconds. Then, Figure 8.6(b) demonstrates what happens if similar time cycles for charge and discharge period are used – the wheel speed grows due to the rapid acceleration periods. This figure also depicts the nominal iron losses cases (mechanical and magnetic bearing) to contrast with the no iron-loss magnetic bearing case.

Finally, mitigation for these experimental error sources are summarized in Table 8.6 and discussed next. First, incorporating miniature magnetic bearings within the motor and in support of the wheel shaft external to the motor will unlock the benefits of an ESACS as the system can run much longer and more effectively during eclipse as captured in Figures 8.5, 8.6(a), and 8.6(b). Second, properly selecting the operating minimum and maximum wheel speeds will ensure the motor efficiency enjoyed by cost effective brushless DC motors is transferred to power conversion efficiency. Next, testing higher resistive loads will better identify the limits of power conversion performance for an ESACS using COTS technology. In addition, continued calculation of the power values using the actual power amounts moved through the system will ensure accurate power performance as is required if flying a VSCMG-based ESACS onboard a conventional small satellite. Fifth, building an SSC in-house brushless DC servoamplifier will afford better control over the motor current measurement process as these devices will be calibrated in the circuit to the level those in the

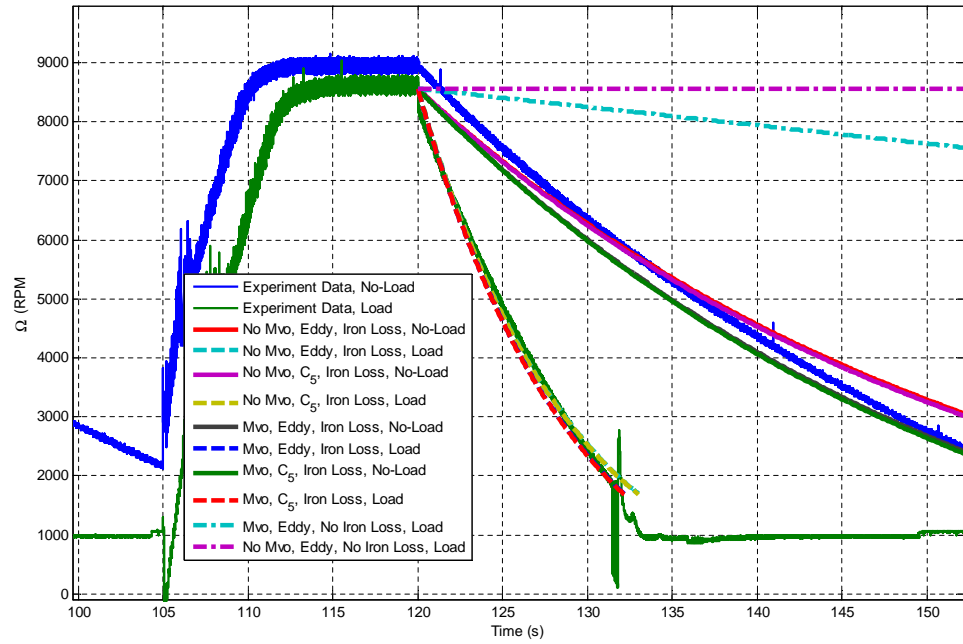
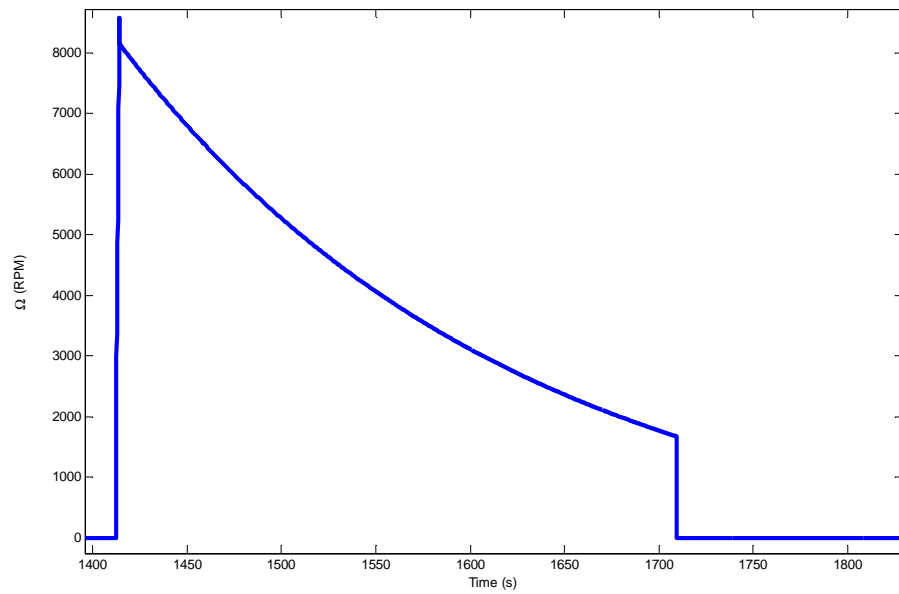
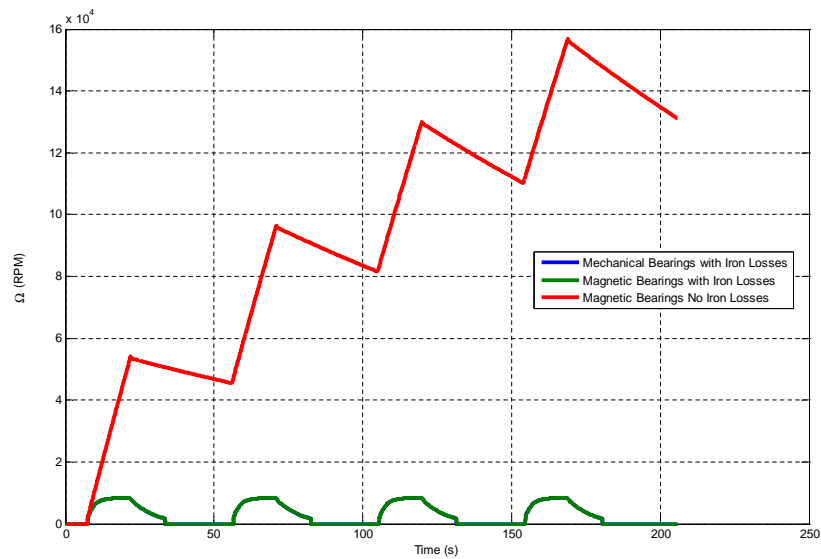


Figure 8.5: Mechanical/Magnetic Bearing Discharge Comparison

SSC FES board were calibrated. Next, the next generation VSCMG prototype should be tested in a vacuum chamber. This will help eliminate the effects of the rotor due to aerodynamic drag. By products of such testing will also prove advantageous as out-gassing of system components (e.g. the Carbon Fibre rotor) and brushless DC Motor thermal heating can be adequately studied and addressed for space flight. In terms of improving the attitude performance, one should isolate the attitude performance of the VSCMG system (alone and in a cluster), slewing of a single-axis air-bearing test article should be accomplished to isolate this performance. Of particular importance to this testing will be the ability to keep the test article locked in orientation until the motor speed levels out at efficient performance. This helps not only for motor efficiency, but also for eliminating the momentum wheel mode from VSCMG performance which is ideally characterized by its CMG mode capability. Next, one should use a more precise method to balance the test article such that the mass center is along the air-bearing pedestal axis/center of rotation. Finally, one should better leverage the vendor's built-in calibration and timing methods to help improve the accuracy of the attitude data. This will be much more important for follow-on work as the focus of testing will shift to in-depth attitude performance testing while reconfirming that the power storage and drain functions work. As one can see, for the several key error sources identified here, there



(a) 9k Magnetic Levitation Cycle



(b) 150k Magnetic Levitation Cycle

Figure 8.6: Mechanical-/Magnetic Bearing Cycles

is a direct chain for mitigating these errors and improving the accuracy of the performance calculations initiated by the work conducted here.

Table 8.6: Proposed Error Mitigation Methods

Id	Mitigation Method
A	Incorporate Miniature Magnetic Bearings in Motor/Wheel Support Shaft Drivelines
B	In Rev B, Set Minimum Operating Speed Closer to Nominal Operating Speed
C	In Rev B, Test Higher Resistive Loads with Shorter Operating Times
D	Use Actual Power-based Calcs, Compare to Wheel Speed-based Calcs
E	Craft In-house Brushless DC Motor Servo-amplifier With Calibrated Sensors
F	Test Rev B VSCMG in Vacuum Chamber
G	Exonerate then Employ IMU Built-in Calibration Function
H	Isolate VSCMG Slewing on Single Axis Air-bearing Test Article
I	Employ Precise Test Article Mass Center Determination Process

8.5 Integrated Testing Summary/Proof of System Novelty

From these tests, it has been shown that one can store and drain power in a VSCMG flywheel while simultaneously slewing this craft using conventional, widely available COTS components with reduced performance. This has fulfilled the primary testing goal mentioned at the outset of this chapter. Furthermore, these experiments have showed the initial performance of a small satellite ESACS based on employing COTS components with reduced performance, thereby fulfilling the secondary testing goal. In this process, several key error sources have been identified and mitigation techniques proposed leading to lessons learned during the process. Some of these lessons learned are the fact that ESACS performance calculations based on moving actual power is much more accurate than those based purely on wheel speed performance, the necessity to operate the motor in its efficient range, the effect of bearing friction on energy and power density results, and the critical importance of motor three-phase current calibration. The fact that imperfections in previous calculation approaches and other measurement errors have been identified satisfies the tertiary goal of the experimentation program. Therefore, as one can see, the key goals of the identified test program have been satisfied, identifying several areas of improvement, but ultimately exonerating the basic functionality of a VSCMG-based ESACS. In addition, there are several benefits including high, better measurable depth-of-discharge (at least 84% demonstrated here with inefficient COTS components), comparable to/better round-trip conversion efficiency (55-60% with mechanical bearings, potentially much higher with magnetic bearings), and reduced rotor mass through Carbon Fibre composite rotor use than a conventional momentum wheel plus NiCd secondary

battery system. In short, the first known, hardware-in-the-loop experimental demonstration of a variable-speed control moment gyroscopes for a small spacecraft scale energy storage and attitude control subsystem was effectively employed with a low-cost prototype crafted from current off-the-shelf technology. Follow-on work will implement the lessons identified here to further characterize and evolve the design of an ESACS for small satellite space missions while simultaneously harnessing benefits associated with a VSCMG-based ESACS, including agile slewing with robust singularity avoidance, subsystem mass savings, increased lifetime, and high power density. This opens the door for missions previously reserved for large satellites, such as precision imaging and space RADAR.

Chapter 9

Conclusion

9.1 Summary of Results

This thesis documented the first ever designed, built, and tested combined energy storage and attitude control subsystem for small satellites. This system used a low-cost, COTS-based variable-speed control moment gyroscope actuator to achieve its goals. Herein, a hardware sizing algorithm, actuator steering laws, and experimental prototype were developed. The critical outcomes of such developments is summarized next.

First, a compact and novel optimal sizing algorithm for a small satellite combined energy storage and attitude control subsystem (ESACS) has been developed and applied to a practical synthetic aperture RADAR mission to compare and contrast technology design alternatives, trade key system/decision variable parameters, and showcase several benefits. Merging the subsystems eliminates redundant secondary battery mass while incorporating advanced technologies such as composite flywheel rotors and magnetic levitation allows higher sustained rotor speeds and further decreases subsystem and total spacecraft mass. Flywheel energy density advantages are on par with improvements in new secondary battery technologies while increased flywheel power densities over mature and burgeoning secondary batteries follows from the ability to rapidly discharge the energy in the flywheel at much faster rates. Employing magnetically-levitated flywheels also permits longer subsystem lifetime through more charge/drain cycles at higher depths-of-discharge than secondary batteries. The employed redundant VSCMG pyramid configuration with flywheel speed variability permits transition to momentum wheel mode to pass through singularities while predominantly using the CMG mode for its torque amplification advantages. Increased slewing agility is a well-documented

direct consequence of employing this CMG mode.

In the new sizing/optimization method, a performance index is used to identify trends in decision variables and pinpoint the optimum rotor length for different technology alternatives. Three candidate performance indices were presented and compared leading to selection of the best of these, which uses an experimental error approach, since it best isolates the transition from conventional to VSCMG-based ESACS design utility.

The sizing/optimization algorithm has shown some important design trends for an ESACS besides the subsystem/spacecraft mass savings. Increasing the gimbal rates of the VSCMGs at an optimal mass reduces the required flywheel acceleration therefore enhancing CMG torque amplification and reducing the problem of flywheel lifetime due to very high wheel speeds. Analysis of the performance index shows that at an optimal mass the maximum flywheel acceleration corresponds to an optimal rotor length, which is used to select the optimal ESACS design. When further analyzed for flywheel acceleration against flywheel speed, the data shows that the embedded motor magnetic bearing technology alternative is superior to other technologies but critical flywheel acceleration points were determined in which other motor technologies can have similar performance values. Additional analysis highlights the benefit of using carbon fiber flywheel rotors—the best performance with maximum mass savings. This fact was also used to qualitatively validate the developed algorithm.

The sizing algorithm was further refined for usable available energy capacity. The modified algorithm was applied to a practical mission to compare and contrast the effects of this refinement. The key resulting impact is that the rotor length must be increased to meet capacity requirements, thereby reducing the amount of mass savings enjoyed by the design. Sensitivity to rotor length is heightened in that the rotor outer and inner radii are assumed fixed for the given small satellite design, thus the rotor length is the primary source for increasing wheel inertia. Plots highlighting the decision variable trends from this usable available capacity change were presented and illustrate the system performance impact. From these plots and based on the assumption that system performance must remain constant, one can see that increasing maximum wheel speed actually increases the required minimum wheel speed when rotor length is held constant, the maximum wheel speed corresponding to zero minimum wheel speed increases as rotor length increase, this direct relationship in maximum-minimum wheel speed becomes more pronounced as the constant c_1 is decreased, maximum wheel acceleration increases with minimum wheel speed increase and rotor length increases, maximum gimbal rate decreases with minimum wheel speed increase when rotor

length increases actually increasing maximum gimbal rate, and maximum wheel speed falls quite rapidly if rotor length is increased thereby forming a key decision variable trade in terms of maximum wheel speed for mass savings.

It was also shown that the optimal mass curve for maximum structural available capacity, a straight line for a given design, forms a boundary for the usable available capacity curve. However, the latter curve is a more appropriate quantity for an achievable design as it focuses on the energy capacity actually convertible to power based on motor/generator peak wheel speed capability. This also relates directly to a more realistic, decreased yet still significant mass savings as compared to the baseline design method.

By using this design approach with more realistic usable available capacity equation, one can best optimally size a VSCMG-based ESACS for optimal mass, quickly identify its utility compared to a contemporary system, and pinpoint the key system parameters required to make the design a reality. This leads to a more mass efficient, lighter yet highly effective subsystem design at less mass.

Next, a novel ESACS gimbal steering law was derived to permit independent gimbal and wheel control of the VSCMGs with continued singularity avoidance, a situation that allows direct incorporation of an ESACS into the existing electrical energy storage topology of conventional, small satellite energy storage (ES) subsystems. This law rejects the disturbances generated during independent ES wheel control which can be significant provided the power is stored and drained rapidly demanding high wheel deceleration/acceleration. Meanwhile, the separation of control renders simultaneous control law singularity avoidance through coordinated wheel torquing and gimbaling impossible. Instead, singularity avoidance is attained through employing conventional gimbal singularity avoidance steering algorithms (e.g. the gimbal singularity condition method) on top of the new, independent gimbal control mentioned above. Nevertheless, as it permits directly interfacing this small satellite ESACS into a conventional satellite, this novel gimbal steering law is more immediately practical than the simultaneous steering laws that exist in the literature.

Finally, a prototype designed and built from applying the sizing algorithm to current hardware technology was tested on a three-axis air-bearing structure, thereby yielding the first known three-axis, small spacecraft scale, ground demonstration of ESACS using VSCMGs. The prototype used the first known miniature Carbon Fibre rotor for a VSCMG, a commercial-off-the-shelf four quadrant servo-amplifier for charging and draining energy, and a simple interface electronics module to control the flow of energy from the primary source to the

wheel motor/generator and load. This energy transfer electronics topology used the standard Direct-Energy-Transfer (DET) architecture that serves as a simple yet effective means to regulate power on a satellite. However, the key difference with a conventional DET configuration is that secondary battery functionality is replaced with the flywheel batteries fulfilled by the VSCMG wheels.

As shown in the presented experimental results, even whilst running at conservative maximum speeds (i.e. on the order of 10000 RPM), the system yields round-trip efficiencies consistent with conventional secondary batteries (50-60%) as well as very favourable depths of discharge (80+%) while simultaneously permitting the satellite to be rotated in three dimensions via gimbaling. Furthermore, in the test regime, the energy and power densities demonstrated were consistent with the limited maximum speed and limited resistance tests shown in the test results.

Also addressed in the laboratory demonstration of this technology were key sources of experimental error, including wind resistance through testing in air (aerodynamic friction), operation of the wheel at moderate maximum speeds thus forcing operation in the less energy-efficient regime for the motor, and limited resistance testing for the spacecraft load. Follow-on work to this thesis will address limiting all of these error sources with testing the prototype in a vacuum chamber, reduced gear ratio (thus reduced time delay) with a battery of gimbal motor tests, high speed motor (with reduced torque) testing, and several different load resistances.

Through these experiments, it was shown the VSCMG-based ESACS concept works on commercial-off-the-shelf (COTS) hardware and illustrates benefits consistent with the theory as scaled for the prototype. Future work will build on the findings presented here with the ultimate goal to be a full pyramid, high-speed rotor test ready for spaceflight. This will achieve the goal of reducing the mass it takes for a small spacecraft to achieve missions previously reserved for larger satellites, especially those requiring high peak power with satellite agility at reduced mass and cost.

9.2 Contribution to the Current State-of-the-Art

In short, this thesis makes the following contributions to the current state-of-the-art:

- A novel algorithm for optimally sizing a small satellite energy storage and attitude con-

trol system was crafted for a system employing COTS-based VCSMGs. This algorithm permits comparing design alternatives to a baseline system using key subsystem design margins in a performance index to generate point designs that are separated with a scoring algorithm based on these margins and key benefits parameters. It was specifically applied to a spotlight-synthetic aperture RADAR mission which requires high instantaneous peak power with pointing agility, yielding an effective design to advance current technology.

- A practical VSCMG steering law was generated and simulated for the conventional application of independent, automatic flywheel motor/generator battery and attitude gimbal motor control. It permits immediate implementation on conventional systems through replacing conventional secondary batteries with plug in flywheel battery units in a direct energy transfer configuration. Alternatively, this system can be added in series to conventional secondary batteries to supplement the peak power for high power missions such as synthetic aperture RADAR and precision imaging.
- A low-cost prototype using current off-the-shelf technology was effectively employed in a hardware-in-the-loop, experiment demonstration of the concepts investigated in the thesis. This is the first known demonstration of variable-speed control moment gyroscopes for a small spacecraft scale energy storage and attitude control subsystem.

9.3 Summary of Publications

The following publications were generated from the work contained herein. These include three peer-reviewed conference papers and a peer-reviewed journal article in a top-ranked, world-renowned spacecraft technology publication. The works are:

- Richie, D., Lappas, V., and Palmer, P., “Sizing/Optimization of a Small Satellite Energy Storage and Attitude Control System,” *AIAA Journal of Spacecraft and Rockets*, Vol. 44, No. 4, 2007, pp. 940-952.
- Richie, D. and Lappas, V., “Saving Mass in Optimally Sizing A Small Satellite Energy Storage and Attitude Control System,” paper no. 07-177, AAS Spaceflight Mechanics Meeting, Sedona, Az, February 2007, 17 pgs.

- Richie, D., Lappas, V., and Asghar S., “Combined Singularity Avoidance for Variable Speed Control Moment Gyroscope Clusters,” paper no. 07-181, AAS Spaceflight Mechanics Meeting, Sedona, Az, February 2007, 12 pgs.
- Richie, D., Lappas, V., and Asghar, S., “Constrained Singularity Avoidance Using VSCMGs for Combined Attitude and Power Tracking”, *10th the European Control Conference*, Kos Island, Greece, July 2007, 7 pgs.

9.4 Proposed Future Work

The work initiated by this thesis has several promising avenues for future development and employment in the space industry. The areas range from optimal sizing of the hardware to steering law development to practical experimentation of the developed system.

First, in terms of development of the sizing algorithm, it is recommend that bearing friction and eddy current losses are added to the actual power and actual capacity equations within the framework of the present algorithm. As shown by Wilson et. al. in [132], the magnetic bearing eddy current losses over the length of the eclipse duration can decrease the capacity of the system up to 30 %. The result is even higher for mechanical bearing friction losses. In addition, these losses should also be modelled in the attitude calculations. For that case, the impact affects both the baseline and the proposed system.

Another addition to the sizing algorithm should be the addition of containment mass in the subsystem mass calculation. This mass can add up to 30 % increase in mass of the system, but construction of Kevlar or another composite will make it much lighter than the Rev A prototype containment made of Aluminium. One should note, though, that this Aluminium containment calculation was not included in the sizing example presented in the thesis.

Also, there are other applications where the structure of the sizing algorithm can prove useful. One such area involves the trade-offs between mass, power, and volume in a Twin CMG cluster for small satellites. Plus, such an algorithm can help in sizing double gimbal CMGs for similar small satellite missions. In each case, the logical baseline for comparison can be either the standard momentum wheel configuration or a four in a pyramid cluster configuration. In such investigation, one should study the impact/appropriateness of scaling the mini-CMG component mass from [13] vice a more complex approach. Regardless, the algorithm will help best size these systems to meet the desired requirements.

The impact of flexible modes can be accommodated in the torque margin equation as well. These flexible modes associated with wheel and gimbal shaft lengths can have an impact especially as when scaling VSCMGs for larger missions. Investigating this area should reveal trades in keeping the same modes while employing stronger gimbal motors versus decreasing length/strengthening the shafts to eliminate the effects of these modes.

Second, the steering law developed here can be investigated in terms of the sliding singularity space resulting from changing wheel momentum but without wheel control by the gimbal motor. Methods such as null motion, preferred gimbal angles, and gimbal acceleration-based steering provide ripe areas for evolving such an algorithm for small satellite use. In addition, testing this algorithm on differing cluster shapes and sizes (e.g. twin-CMGs, four VSCMGs in a pyramid, and three VSCMGs along primary satellite axes) will also unveil interesting results and applications associated with a VSCMG-based ESACS.

Third, there are many practical hardware and experimentation developments anticipated for the future since only brief initial results have been demonstrated here. First, building on the lessons learned and proposed error source mitigation methods from testing the Rev A prototype, Rev B will permit implementation of a less powerful, but faster motor, with speeds up to 45000 RPM as compared to the 9500 RPM of Rev A. This equates to higher energy and power density capability as the energy conversion will be more efficient if the wheel is operated more often in the efficient regime. Also, the Rev B design adds faster gimbaling (75 deg/s vice 10 deg/s in Rev A) which should also impart less time delay in generating torque. Here, one should note that gimbaling tests will be more effective at capturing performance limits when the VSCMG is operated as a CMG (i.e. at fixed rotor speed) vice employing its momentum wheel mode. Another improvement anticipated with Rev B implementation is the application of a full cluster of VSCMGs which will help in demonstrating the advancements in attitude control/torquing as the full cluster will provide the necessary opposing torques to yields precision three-dimensional maneuvers.

Further practical work anticipated for Rev B includes improved, robust electronics along with more resistive load options. More resistance settings for the load means one can better characterize the instantaneous peak power limits of the system. Another electrical addition helping to make the testing more realistic for spacecraft is using a solar panel with a halogen light source to simulate the sun rather than a laboratory power supply. This will make the results easier to envision for orbital use even though the power generation should be the same. One can even investigate the effects of shadowing solar cells on wheel operation and

energy storage usage. Also, adding a current sensor and voltage divider to the motor power line on the SSC FES board for more accurate calibration and building/procuring a custom motor/generator servo-amplifier are important electrical improvements for follow-on efforts.

Next, several repetitions (at least 6) of each combination of wheel speed and gimbal rate should be completed to build statistical relevance of power-focused, attitude-focused, and combined tests. Continued use of more accurate energy conversion equations is necessary. Then, the VSCMG should be tested in a vacuum chamber to analyze motor thermal heating and rotor out-gassing properties, better forecasting on-orbit conditions. Another improvement to testing is to incorporate the IMU data directly to XPC target and eliminating the bias processing method done here.

One long term practical improvement promises to be the addition of magnetic levitation to the wheel motor/generator drive-line. The advantages of such an advancement were discussed in the thesis and include longer lifetime, longer sustained operation in eclipse, and more efficient power conversion. Despite the losses imparted by eddy currents associated with magnetic bearings, the absence of friction torque loss vastly improves the resulting system performance. Another drawback is the power required to maintain operation of the magnetic bearings, but this effect added to the eddy current loss should prove to still be a substantial improvement over mechanical friction loss of motor/generator ball bearings.

Still another test regime for the future should be to test a Carbon Fibre rotor to failure via a burst-test in a controlled chamber. The idea here is to see how benign the failure mode of the fiber is in its unidirectional carbon elements. This test can go a long way to breed confidence in the satellite user of this technology.

All these areas make the future of this research existing yet useful. Such work should further expand the present state-of-the-art in using variable-speed control moment gyroscopes for combined energy storage and attitude control.

9.5 Proof of Novelty

The work presented here illustrates the optimal design strategy, practical actuator steering algorithm, and hardware test performance of the world's first small satellite ESACS and thereby fills the gaps in current state-of-the-art identified in Chapter 2. It is also the first ESACS using variable-speed control moment gyroscopes crafted from low-cost, COTS compo-

nents. Before the research began, no sizing algorithms for VSCMGs used in an ESACS were known to exist. The present work has generated such an algorithm which permits comparing and contrasting technologies and scoring point designs based on the designer's preferences using key design margins necessary for effective power and attitude control systems. This algorithm has been developed and refined through extensive peer review and is now a standard which future practical CMG-actuator developments can apply.

Next, the existing steering laws for a VSCMG-based ESACS involve simultaneous control of the wheel and gimbal motors. However, conventional applications require that the wheels be controlled automatically in an electrical circuit resident in the Electrical Power Subsystem (EPS). The novel steering law developed here meets this need with the trade coming in giving up automatic singularity avoidance through momentum wheel mode. Instead, to avoid singularities, the law built here summons advancements made in CMG singularity avoidance that has a rich-literary base dating back over 25 years, using the existing VLPID-focused GSR.

Lastly, before the work started, no actual VSCMGs using Carbon Fibre rotors existed for small satellite combined energy storage and attitude control systems. This left a void in practical arguments for using this technology as no one had demonstrated its merits in a small spacecraft context. However, the work shown here gives the first insight into employing such a system, which is even possible using conventional motor/generator technology despite its limitations in mechanical motor shaft bearings. Even though such limitations exist, the initial experimental data shows the scalable benefits in depth-of-discharge and round-trip power efficiency with plausible results in terms of power and energy density. The latter two of these will grow when faster wheels with reduced friction are evolved.

From this, one can see that the work undertaken here is novel and useful. It clearly makes a positive contribution to the current state-of-the-art. Future applications will grow from the advancements made here. In a nutshell, this technology has substantial benefits relevant to attacking complex space missions with low cost, COTS-based small satellites.

Bibliography

- [1] Roes, J. B., “An Electro-Mechanical Energy Storage System for Space Application,” *Progress in Astronautics and Rocketry*, Vol. 3, 1961, pp. 613–622.
- [2] Notti, J., Schmill, W., Klein, W., and Cormack, A., I., “Integrated Power/Attitude Control System (IPACS) Study: Volume II–Conceptual Designs,” Tech. Rep. NASA CR-2384, Rockwell International Space Division, Downey, CA, 1974.
- [3] Rodriguez, G. E., Studer, P. A., and Baer, D. A., “Assessment of Flywheel Energy Storage of Spacecraft Power Systems,” Tech. Rep. NASA TM-85061, NASA Goddard Space Flight Center, Greenbelt, MD, 1983.
- [4] Oglevie, R. E. and Eisenhaure, D. B., “Advanced Integrated Power and Attitude Control System (IPACS) Technology,” Tech. Rep. NASA Technical Report CR-3912, Rockwell International Space Station Systems Division, Downey, CA, November 1985.
- [5] Stickel, H., “Space Qualification Testing of the TELDIX Magnetic Bearing Wheel MWX,” *Proceedings of the 1st International Workshop on Spacecraft Attitude and Orbit Control Systems*, 1997, pp. 221–228.
- [6] Hebner, R., B. J. and Walls, A., “Flywheel Batteries Come Around Again,” *IEEE Spectrum*, April 2002, pp. 46–51.
- [7] Wilson, B., “Power System Design of a Spacecraft Simulator Using Energy Storage Flywheels,” Power Point Presentation, April 18 2005, Aerospace Corporation, Space Power Workshop.
- [8] Ward, J., Jason, S., and Sweeting, M., “Microsatellite Constellation for Disaster Monitoring,” *Proceedings of the 13th Annual AIAA/USU Conference on Small Satellites*, Logan, Utah, 1999.

-
- [9] Bradford, A., Gomes, L., and Sweeting, M., "BILSAT-1: A Low-Cost, Agile, Earth Observation Microsatellite for Turkey," *Proceedings of the 53rd International Astronautical Congress*, Houston, Texas, October 2002.
- [10] Van Der Zel, V., Blewett, M., Clark, C., and Hamill, D., "Three Generations of DC Power Systems for Experimental Small Satellites," *Proceedings of the Applied Power Electronics Conference*, Vol. 2, San Jose, CA, March 1996, pp. 664–670.
- [11] Ward, J. and Sweeting, M., "First In-Orbit Results from the UOSAT-12 Minisatellite," *Proceedings of the 13th Annual AIAA/USU Conference on Small Satellites*, Logan, Utah, 1999.
- [12] Richie, D., Tsiotras, P., and Fausz, J., "Simultaneous Attitude Control and Energy Storage using VSCMGs: Theory and Simulation," *Proceedings of the American Control Conference*, American Automatic Control Council, New York, 2001, pp. 3973–3979.
- [13] Lappas, V., *A Control Moment Gyro (CMG) Based Attitude Control System (ACS) For Agile Small Satellites*, Ph.D. Dissertation, School of Electronics and Physical Sciences, University of Surrey, Guildford, United Kingdom, October 2002.
- [14] Richie, D., Lappas, V., and Palmer, P., "Sizing/Optimization of a Small Satellite Energy Storage and Attitude Control System," *AIAA Journal of Spacecraft and Rockets*, Vol. 44, No. 4, 2007, pp. 940–952.
- [15] Scharfe, M., Meinzer, K., and Zimmermann, R., "Development of a Magnetic-Bearing Momentum Wheel for the AMSAT Phase 3-D Small Satellite," *Proceedings for the International Symposium on Small Satellites*, Annecy, France, 1996, website: www.amsat.org/amsat/sats/phase3d/wheels/.
- [16] AMSAT, "AMSAT P3-D Launch Campaign Kourou," website: <http://www.amsat-dl.org/launch/part5.htm>, 2000, Last Accessed May 31, 2005.
- [17] Lappas, V., Steyn, W., and Underwood, C., "Design and Testing of a Control Moment Gyroscope Cluster for Small Satellites," *Journal of Spacecraft and Rockets*, Vol. 41, No. 6, pp. 1–11, preprint.
- [18] Lee, E., "Microsatellite Combined Attitude/Energy Systems," *IEEE A & E Systems Magazine*, April 2004, pp. 27–32.

-
- [19] Hall, C., "Integrated Spacecraft Power and Attitude Control Systems Using Flywheels," Report AFIT/ENY/TR-000, the Air Force Institute of Technology, Dayton, OH, 2000.
- [20] Babuska, V., Beatty, S., Debunk, B., and Fausz, J., "A Review of Technology Developments in Flywheel Attitude Control and Energy Transmission Systems," *Proceedings of the IEEE Aerospace Conference*, Vol. 4, 2004, pp. 2784–2800.
- [21] Fausz, J., Wilson, B., Hall, C., Richie, D., and Lappas, V., "A Review of Technology Developments in Flywheel Attitude Control and Energy Storage Systems," *AIAA Journal of Guidance, Control, and Dynamics*, submitted for publication, May 2007, pp. 1–31.
- [22] Clerk, R., "The Utilization of Flywheel Energy," *Trans. SAE*, Vol. 72, 1964, pp. 508–543.
- [23] Morganthaler, G. and Bonk, S., "Composite Flywheel Stress Analysis and Materials Study," *Advances in Structural Composites D-5*, Vol. 12, October 10-12 1967, SAMPE Science of Advanced Materials and Process Engineering.
- [24] Rabenhorst, D., "Primary Energy Storage and the Super Flywheel," Tech. Memo. TG 1081, Johns Hopkins University, September 1969.
- [25] Adams, L., "Application of isotenoid flywheels to spacecraft energy and angular momentum storage," NASA Tech. Report NASA CR-1971, Astro Research Corporation, Santa Barbara, CA, 1972.
- [26] Notti, J., Cormack, A., and Klein, W., "Integrated Power/Attitude Control System (IPACS)," *Journal of Spacecraft and Rockets*, Vol. 12, No. 8, 1975, pp. 485–491.
- [27] Henrikson, C., Lyman, J., and Studer, P., "Magnetically Suspended Momentum Wheels for Spacecraft Stabilization," *Proceedings of the 12th AIAA Aerospace Sciences Meeting*, Washington, DC, January 30- February 1 1974, AIAA Paper No. 74-128.
- [28] Kirk, J. A., "Flywheel Energy Storage Part I: Basic Concepts," *International Journal of Mechanical Sciences*, Vol. 19, No. 4, 1976, pp. 223–231.
- [29] Notti, J., "Integrated Power/Attitude Control System (IPACS) Study; Vol 1 - Feasibility Studies," NASA Report CR 2383, NASA, April 1974.

-
- [30] Anderson, W. and Keckler, C., "Integrated Power/Attitude Control System (IPACS) for Space Application," *Proceedings of the 5th IFAC Symposium on Automatic Control in Space*, 1973.
- [31] Cormack III, A., "Three Axis Flywheel Energy and Control Systems," Tech. Rep. NASA TN-73-G&C-8, North American Rockwell Corp., 1973.
- [32] Keckler, C. R. and Jacobs, K. L., "A Spacecraft Integrated Power/Attitude Control System,," *9th Intersociety Energy Conversion Engineering Conference*, 1974.
- [33] Will, R., Keckler, C., and Jacobs, K., "Description and Simulation of an Integrated Power and Attitude Control System Concept for Space-Vehicle Application," Tech. Rep. NASA TN-D-7459, NASA, 1974.
- [34] Kirk, J. A. and Studer, P., "Flywheel Energy Storage Part II: Magnetically Suspended Superflywheel," *International Journal of Mechanical Science*, Vol. 19, No. 4, 1976, pp. 233–245.
- [35] Cormack, A. and Notti, J., "Design Report for the Rotating Assembly for an Integrated Power/Attitude Control System," NASA Report CR-172317, NASA, NASA LaRC, September 1974.
- [36] Keckler, C., "Integrated Power/Attitude Control System (IPACS)," *Proceedings of the Integrated Flywheel Technology Workshop*, NASA GSFC, Greenbelt, MD, 1983 1983, pp. 5–22.
- [37] Olszewski, M. and O’Kain, D., "Advances in Flywheel Technology for Space Power Applications," *Proceedings of the 21st Intersociety Energy Conversion Engineering Conference*, Vol. 3, 1986, pp. 1823–1828.
- [38] Olmsted, D. R., "Feasibility of Flywheel Energy Storage in Spacecraft Applications," *Proceedings of the 20th Intersociety Energy Conversion Engineering Conference*, Vol. 2, 1985, pp. 444–448.
- [39] Studer, P. A. and Rodriguez, G. E., "High Speed Reaction Wheels for Satellite Attitude Control and Energy Storage," *Proceedings of the 20th Intersociety Energy Conversion Engineering Conference*, Vol. 2, 1985, pp. 349–352.

-
- [40] Olszewski, M., "Development of Regenerable Energy Storage for Space Multimegawatt Applications," *Proceedings of the 21st Intersociety Energy Conversion Engineering Conference*, Vol. 3, 1986, pp. 1838–1841.
- [41] Tassel, K. V. and Simon, W., "Inertial Energy Storage for Advanced Space Station Applications," *Proceedings of the 20th Intersociety Energy Conversion Engineering Conference*, Vol. 2, 1985, pp. 337–342.
- [42] Eisenhaure, D., Downer, J., Bliamptis, T., and Hendrie, S., "A Combined Attitude, Reference and Energy Storage System for Satellite Applications," *Proceedings of the 22nd Aerospace Sciences Meeting*, Reno, NV, January 9-12 1984, paper no. AIAA 84-0565.
- [43] Eisenhaure, D., Ogleview, R., and Keckler, C., "Energy and Momentum Management of the Space Station Using Magnetically Suspended Composite Rotors," *Proceedings of the 20th Energy Conversion Engineering Conference*, Vol. 1, 1985, pp. 197–203.
- [44] Ogleview, R., "Wheel Configuration for Combined Energy Storage and Attitude Control Systmes," *Proceedings of the Guidance, Navigation, and Control Conference*, Snowmass, CO, August 19-21 1985, pp. 788–798, paper no. AIAA 1985-1989.
- [45] O'Dea, S., Burdick, P., Downer, J., Eisenhaure, D., and Larkin, L., "Design and Development of a High Efficiency Effector for the Control of Attitude and Power in Space Systems," *Proceedings of the 20th Intersociety Energy Conversion Engineering Conference*, Vol. 2, 1985, pp. 353–360.
- [46] Davis, D. and Csomor, A., "The New Age of High Performance Kinetic Energy Storage Systems," *Proceedings of the 15th Intersociety Energy Conversion Engineering Conference*, Vol. 2, 1980, pp. 1507–1512.
- [47] Flatley, T., "Tetrahedron Array of Reaction Wheels for Attitude Control and Energy Storage," *Proceedings of the 20th Intersociety Energy Conversion Engineering Conference*, Vol. 2, 1985, pp. 2353–2360.
- [48] Gross, S., "Study of Flwheel Energy Storage for Space Stations," Tech. Rep. NASA CR-171780, Boeing Aerospace Co., Seattle, WA, 1984.

-
- [49] Oglevie, R. E. and Eisenhaure, D. B., “Integrated Power and Attitude Control System (IPACS) Technology,” *Proceedings of the 21st Intersociety Energy Conversion Engineering Conference*, Vol. 3, 1986, pp. 1834–1837.
- [50] Marcoux, “High Energy Density Rechargeable Battery for Satellite Applications,” Tech. Rep. AFWAL-TR-83-2055, Hughes Aircraft Co., 1983.
- [51] Christopher, D. and Beach, R., “Flywheel Technology Development Program for Aerospace Applications,” *IEEE Aerospace and Electronic Systems Magazine*, Vol. 13, No. 6, June 1998, pp. 9–14.
- [52] website www.afstrinity.com/company/cmp_how.html, 2005, last accessed 10 April 2005.
- [53] Kefauver, K., Walsh, G., Hromada, L., Kirk, J., and Zmood, R., “A 50 WH Open Core High-speed Flywheel,” *Proceedings of the 1999 Intersociety Energy Conversion Engineering Conference*, 1999.
- [54] “History,” website: www.hybridcars.com/history.html, 2005, last accessed May 31, 2005.
- [55] “Ragone Plot, Comparisons,” website: www.mpoweruk.com/alternatives.htm#ragone, 2005, last accessed April 28, 2005.
- [56] Decker, D., Spector, V., and Pieronek, T., “An Overview of Flywheel Technology for Space Applications,” *Proceedings of the Space Technology and Applications International Forum, Part 1*, January 1997, pp. 257–261.
- [57] Santo, G., Gill, S., Kotas, J., and Paschall, R., “Feasibility of Flywheel Energy Storage Systems for Applications in Future Space Missions,” Tech. Rep. NASA-CR-195422, NASA LaRC, January 1995.
- [58] Hall, C., “High-Speed Flywheels for Integrated Energy Storage and Attitude Control,” *Proceedings of the American Control Conference*, Vol. 3, June 4-6 1997, pp. 1894–1898, Albuquerque, NM.
- [59] Tsiotras, P., Shen, H., and Hall, C., “Satellite Attitude Control and Power Tracking with Energy/Momentum Wheels,” *AIAA Journal of Guidance, Control, and Dynamics*, Vol. 24, No. 1, 2001, pp. 23–34.

-
- [60] Shen, H. and Tsiotras, P., "Satellite Attitude Control and Power Tracking with Momentum Wheels," *Proceedings of the AAS/AIAA Astrodynamics Specialist Conference*, Girdwood, AK, Aug. 16-19 1999, AAS Paper 99-317.
- [61] Hall, C., Tsiotras, P., and Shen, H., "Tracking Rigid Body Motion Using Thrusters and Reaction Wheels," *Proceedings of the AIAA/AAS Astrodynamics Specialists Conference*, Boston, MA, August 10-12 1998, AIAA Paper 98-4471.
- [62] White, J. and Hansen, Q., "Study of a Satellite Attitude Control System Using Integrating Gyros as Torque Sources," Tech. Rep. NASA Technical Report TN D-1073, September 1961.
- [63] Lappas, V., Steyn, W., and Underwood, C., "Attitude Control for Small Satellites Using Control Moment Gyros," *Proceedings of the 52nd International Astronautics Federation Conference*, Toulouse, France, 2001.
- [64] Jacot, A. D. and Liska, D., "Control Moment Gyros in Attitude Control," *Journal of Spacecraft and Rockets*, Vol. 3, No. 9, 1966, pp. 1313–1320.
- [65] Margulies, G. and Aubrun, J., "Geometric Theory of Single-Gimbal Control Moment Gyro Systems," *Journal of the Astronautical Sciences*, Vol. 26, No. 2, 1978, pp. 159–191.
- [66] Oh, H. and Vadali, S., "Feedback Control and Steering Laws for Spacecraft Using Single Gimbal Control Moment Gyros," *Journal of the Astronautical Sciences*, Vol. 39, No. 2, 1991, pp. 183–203.
- [67] Bedrossian, N., Paradiso, J., Bergmann, E., and Rowell, D., "Redundant Single Gimbal Control Moment Gyroscope Singularity Analysis," *AIAA Journal of Guidance, Control, and Dynamics*, Vol. 13, No. 6, 1990, pp. 1096–1101.
- [68] Bedrossian, N., Paradiso, J., Bergmann, E., and Rowell, D., "Steering Law Design for Redundant Single Gimbal Control Moment Gyroscopes," *AIAA Journal of Guidance, Control, and Dynamics*, Vol. 13, No. 6, 1990, pp. 1083–1089.
- [69] Paradiso, J., "Global Steering of Single Gimballed Control Moment Gyroscopes Using a Directed Search," *AIAA Journal of Guidance, Control, and Dynamics*, Vol. 15, No. 5, 1992, pp. 1236–1244.

-
- [70] Vadali, S., Oh, H., and Walker, S., “Preferred Gimbal Angles for Single Gimbal Control Moment Gyros,” *AIAA Journal of Guidance, Control, and Dynamics*, Vol. 13, No. 6, 1990, pp. 1090–1095.
- [71] Kraft, R., “CMG Singularity Avoidance in Attitude Control of Flexible Spacecraft,” *Proceedings of the American Control Conference*, San Francisco, CA, June 2-4 1993, pp. 56–58.
- [72] Ford, K. A., *Reorientations of Flexible Spacecraft Using Momentum Exchange Devices*, Ph.D. Dissertation, Air Force Institute of Technology, Wright-Patterson AFB, Ohio, September 1997.
- [73] Ford, K. A. and Hall, C. D., “Singular Direction Avoidance Steering for Control-Moment Gyros,” *AIAA Journal of Guidance, Control, and Dynamics*, Vol. 23, No. 4, 2000, pp. 648–656.
- [74] Schaub, H., *Novel Coordinates For Nonlinear Multibody Motion with Applications to Spacecraft Dynamics and Control*, Ph.D. Dissertation, Texas A and M University, Arlington, TX, May 1998.
- [75] Schaub, H., Vadali, S. R., and Junkins, J. L., “Feedback Control Law for Variable Speed Control Moment Gyros,” *Proceedings of the AAS Spaceflight Mechanics Conference*, Monterey, CA, February 1998, pp. 581–600, paper No. 98-140.
- [76] Schaub, H., Vadali, S. R., and Junkins, J. L., “Feedback Control Law for Variable Speed Control Moment Gyros,” *Journal of the Astronautical Sciences*, Vol. 46, No. 3, 1998, pp. 307–28.
- [77] Schaub, H. and Junkins, J. L., “Singularity Avoidance Using Null Motion and Variable-Speed Control Moment Gyros,” *AIAA Journal of Guidance, Control, and Dynamics*, Vol. 23, No. 1, 2000, pp. 11–16.
- [78] Varatharajoo, R., *Synergisms for Spacecraft Attitude Control System*, Ph.D. Thesis, Dresden Technical University, Aachen, DE, June 2003, Shaker Verlag.
- [79] Scharfe, M., Roschke, T., Bindl, E., Blonski, D., and Seiler, R., “The Challenges of Miniaturisation for A Magnetic Bearing Wheel,” *Proceedings of the 9th European Space Mechanisms and Tribology Symposium (ESMATS)*, Liege, Belgium, September 19-21 2001.

-
- [80] Scharfe, M., Roschke, T., Bindl, E., and Blonski, D., “Design and Development of a Compact Magnetic Bearing Momentum Wheel for Micro and Small Satellites,” *Proceedings of the 15th Annual Utah State University Conference on Small Satellites*, Logan, Utah, 2001, pp. 1–9.
- [81] “Email exchange with Michael Scharfe, primary researcher for magnetically levited flywheel momentum wheels flown on AMSAT-D,” .
- [82] Varatharajoo, R. and Fasoulas, S., “Methodology for the Development of Combined Energy and Attitude Control Systems for Satellites,” *Aerospace Sciences and Technology* 6, Vol. 6, No. 4, 2002, pp. 303–311.
- [83] Varatharajoo, R. and Fasoulas, S., “The Combined Energy and Attitude Control System for Small Satellites – Earth Observation Missions,” *Acta Astronautica*, Vol. 56, 2005, pp. 251–259.
- [84] Lee, E., “A Micro HTS Renewable Energy/Attitude Control System for Micro/Nano Satellites,” *IEEE Transactions on Applied Superconductivity*, Vol. 13, No. 2, 2003, pp. 2263–2266.
- [85] Lee, E., “A Micro Power Supply for Space Micro-Electromechanical Systems Using a High-Temperature Superconductor-Magnet Bearing,” *Proceedings of the IEEE NANO-2001 Nanoelectromechanical Systems (NEMS)*, October 30 2001, pp. 477–482.
- [86] Lee, E., Yu, J., and Wilson, T., “High-temperature superconductor-magnet momentum wheel for micro satellite,” *Proceedings of the 2001 IEEE Aerospace Conference*, Vol. 5, Big Sky, MT, pp. 2463–2468.
- [87] Lee, E., “A Micro High-Temperature Superconductor-Magnet Flywheels with Dual Function of Energy Storage and Attitude Control,” *Proceedings of the 37th Intersociety Energy Conversion Engineering Conference*, July 19-31 2002, pp. 151–152.
- [88] Lee, E., Ma, K., Wilson, T., , and Chu, W., “Superconductor-Magnet Bearings with Inherent Stability and Velocity-Dependent Drag Torque,” *Proceedings of the 1999 IEEE/ASME International Conference on Advanced Intelligent Mechatronics*, Atlanta, GA, September 19-23 1999, pp. 806–811.

-
- [89] Lee, E., Ma, K., Wilson, T., and Chu, W., "Characterization of Superconducting Bearings for Lunar Telescopes," *IEEE Transactions on Applied Superconductivity*, Vol. 9, No. 2, June 1999, pp. 911–915.
- [90] Lee, E., "A High-Temperature Superconductor - Magnet Energy Storage and Attitude Control System for Space MEMS," *Proceedings of the 2002 IEEE Aerospace Conference*, Vol. 5, 2002, pp. 2365–2371.
- [91] Wilson, T., "A High-Temperature Superconductor Energy-Momentum Control System for Small Satellites," *IEEE Transactions on Applied Superconductivity*, Vol. 13, No. 2, 2003, pp. 2287–2290.
- [92] Anand, D., Kirk, J., Zmood, R., Pang, D., and Lashley, C., "Final Prototype of Magnetically Suspended Flywheel Energy Storage System," *Proceedings of the 26th International Energy Conversion Engineering Conference*, Vol. 4, Boston, MA, August 4-9 1991, pp. 203–208.
- [93] Hanselman, D., *Brushless Permanent Magnet Motor Design*, The Writers' Collective, Cranston, Rhode Island, 2nd ed., 2003.
- [94] "A Novel, Low-Cost, High-Performance Single-Phase Adjustable-Speed Motor Using PM Brush-less DC Machine," *2003 International Future Energy Challenge*, edited by A. Emadi and A. Villagomez, March 2003, Topic: b() Single-Phase Adjustable-Speed Motor, Final Project Report.
- [95] Chan, C., Chau, K., Jiang, J., Xia, W., Zhu, M., and Zhang, R., "Novel Permanent Magnet Motor Drives for Electric Vehicles," *IEEE Transactions on Industrial Electronics*, Vol. 43, No. 2, 1996, pp. 331–339.
- [96] Ellis, G., "Advances in Brushless DC Motor Technology, Control, and Manufacture," *Proceedings of the 1996 PCIM-Europe*, 1996.
- [97] "Producing Wound Components," 2004, website: www.ee.surrey.ac.uk/Workshop/advice/coils/index.html, instructive technical note, Last Accessed November 25, 2004.
- [98] Kascak, P., Dever, T., and Jansen, R., "Magnetic Circuit Model of PM Motor-Generator to Predict Radial Forces," *Proceedings of the 1st AIAA International Energy Conversion Engineering Conference*, August 17-21 2003, AIAA paper no. 2003-6068.

-
- [99] Nola, F., “Motor/Generator and Electronic Control Considerations for Energy Storage Flywheels,” report NASA-CP-2346, NASA Marshall Space Flight Center, Huntsville, AL.
- [100] “DC Drives Overview,” 2005.
- [101] *Chapter 2: Actuators*, 2005, website: ee.polyu.edu.hk/staff/eencheun/WebSubject2/chapter2.htm, Last Accessed January 13, 2005.
- [102] Atwar, S. and Craig, K., “Magnetic Coupling Between DC Tachometer and Motor and Its Effect on Motion Control,” *Proceedings of the 7th Mechatronics Forum International Conference*, September 6-8 2000.
- [103] Jones, D., “Brushless DC Motor Operation at High Speeds as Affected by the Core Losses,” website: www.repp.org/discussion/ev/200201/msg00923.html, 1988, last accessed December 23, 2004.
- [104] Elgerd, O., *Basic Electric Power Engineering*, Addison-Wesley Publishing Company, Reading, Massachusetts.
- [105] Michaelis, T., “Integrated Power and Attitude Control System (IPACS),” *Proceedings of the 12th Annual Utah State University Conference on Small Satellites*, Logan, Utah, 1998, pp. 1–6.
- [106] Hofmann, H. and Bakis, C., “Flywheel Technology Development for Small Satellite Applications,” Research Report NASA Grant NAG3-2598, The Pennsylvania State University, University Park, PA, February 14 2004.
- [107] Richie, D., *Simultaneous Attitude Control and Energy Storage Using VSCMGs: Theory and Simulation*, M.S. Thesis, Dept. of Aerospace Engineering, Georgia Institute of Technology, Atlanta, GA, May 2001.
- [108] Richie, D., Tsiotras, P., and Fausz, J., “Variable Speed Control Moment Gyroscope Workbench: A New Simulation Tool for Tomorrow’s Spacecraft,” *Proceedings of the 20th Digital Avionics Systems Conference*, Daytona Beach, FL, October 14-18 2001, pp. (8.A.3)1–12.
- [109] Yoon, H. and Tsiotras, P., “Spacecraft Adaptive Attitude and Power Tracking with Variable Speed Control Moment Gyroscopes,” *AIAA Journal of Guidance, Control, and Dynamics*, Vol. 25, No. 6, 2002, pp. 1081–1090.

-
- [110] Yoon, H. and Tsiotras, P., “Singularity Analysis of Variable Speed Control Moment Gyros,” *AIAA Journal of Guidance, Control, and Dynamics*, Vol. 27, No. 3, 2004, pp. 374–386.
- [111] Roithmayr, C., Karlgaard, C., Kumar, R., Seywald, H., and Bose, D., “Dynamics and Control of Attitude, Power, and Momentum for a Spacecraft Using Flywheels and Control Moment Gyroscopes,” Technical Report NASA TP-2003-212178, NASA, April 2003.
- [112] Kane, T. and Levinson, D., “Approximate Solution of Differential Equations Governing the Orientation of a Rigid Body in a Reference Frame,” *Journal of Applied Mechanics*, Vol. 54, 1987, pp. 232–234.
- [113] Underwood, C., “Class Notes from Satellite Design course,” Surrey Space Center, University of Surrey, Spring 2005, Guildford, United Kingdom.
- [114] Larson, W. and Wertz, J., *Space Mission Analysis and Design*, Kluwer Academic Publishers, Boston, 3rd ed., 2003, pp. 241–297.
- [115] Bryson, A. and Ho, Y., *Applied Optimal Control: Optimization, Estimation, and Control*, Hemisphere Publishing Corporation, revised printing ed., 1975.
- [116] Winston, W., *Operations Research: Applications and Algorithms*, Duxbury Press, Belmont, CA, 3rd ed., 1994.
- [117] Flystra, D., Lasdon, L., Watson, J., and Waren, A., “Design and Use of the Microsoft Excel Solver,” *Interfaces*, Vol. 28, No. 5, pp. 29–55, Institute for Operations Research and the Management Sciences.
- [118] “Solver Uses Generalized Reduced Gradient Algorithm,” website: support.microsoft.com, 2005, last accessed January 31, 2005.
- [119] Nenov, I. and Flystra, D., “Interval Methods for Accelerated Global Search in the Microsoft Excel Solver,” *Reliable Computing*, Vol. 9, 2003, pp. 143–159.
- [120] Lasdon, L., Waren, A., Jain, A., and Ratner, M., “Design and Testing of a Generalized Reduced Gradient Code for Nonlinear Programming,” *ACM Transactions on Mathematical Software*, Vol. 4, No. 1, March 1978, pp. 34–50.

-
- [121] Smith, S. and Lasdon, L., "Solving Large Sparse Nonlinear Programs Using GRG," *ORSA Journal of Computing*, Vol. 4, No. 1, 1992, pp. 2–5, Winter.
- [122] Berghen, F., *CONDOR: A Constrained, Nonlinear, Derivative-free Parallel Optimizer for Continuous, High Computing Load, Noisy Objective Functions*, Ph.D. Dissertation, Universite Libre de Bruxelles, 2004.
- [123] Palazzolo, A., Kenny, A., and Lei, S., e. a., "Flywheel Magnetic Suspension Developments," *Proceedings of the 37th Intersociety Energy Conversion Engineering Conference*, July 28-August 2 2002, NASA paper TM 2002-211886.
- [124] Kenny, B., Jansen, R., Kascak, P., Dever, T., and Santiago, W., "Demonstration of Single Axis Combined Attitude Control and Energy Storage Using Two Flywheels," *Proceedings of the 2004 IEEE Aerospace Conference*, Vol. 4, August 2004.
- [125] Kenny, B., Kascak, P., Jansen, R., and Dever, T., "A Flywheel Energy Storage System Demonstration for Space Applications," *Proceedings of the International Electric Machines and Drives Conference*, Madison, WI, June 1-4 2003, NASA TM 2003-212346.
- [126] Kascak, P., Jansen, R., Kenny, B., and Dever, T., "Single Axis Attitude Control and DC Bus Regulation with Two Flywheels," NASA TM NASA TM 2002-211812, NASA, August 2002.
- [127] Kenny, B., Kascak, P., Jansen, R., Dever, T., and Santiago, W., "Control of a High Speed Flywheel System for Energy Storage in Space Applications," NASA TM NASA TM 2004-213356, NASA, November 2004.
- [128] Kenny, B. and Kascak, P., "DC Bus Regulation With a Flywheel Energy Storage System," NASA TM NASA TM 2002-211897, NASA, January 2003.
- [129] McLallin, K., "AFRL/NASA Flywheel Program Overview," *Flywheel Workshop*, August 2003.
- [130] Christofer, D. and Fausz, J., "Overview of the AFRL/NASA Flywheel Program," *NASA/USAF Aerospace Flywheel Workshop*, October 1998.
- [131] "Discussions with Ray Beach, NASA, on NASA's flywheel energy storage goals and recent accomplishments, including magnetically levitated flywheels and small satellite aims, primarily concentrating on high-speed momentum wheels and less on CMGs," Telephone Conversation, March 2005.

-
- [132] Wilson, B., Babuska, V., Potter, C., and Fausz, J., "Power System Design for a Spacecraft Simulator Using Energy Storage Flywheels," *Proceedings of the 3rd International Energy Conversion Engineering Conference*, San Francisco, CA, August 15-18 2005, pp. 1–13, Preprint.
- [133] Fausz, J. and Richie, D., "Flywheel Simultaneous Attitude Control and Energy Storage using VSCMGs," *IEEE International Conference on Control Applications*, September 25-27 2000, pp. 991–995, Anchorage, AK.
- [134] Steyn, W. and Hashida, Y., "In-orbit Attitude and Orbit Control Commissioning of UOSAT-12," *Proceedings of the 4th ESA International Conference on Spacecraft Guidance, Navigation, and Control Systems*, ESTEC Noordwijk, The Netherlands, October 18-21 1999.
- [135] Underwood, C., Steyn, W., and Lappas, V., "SNAP-1 ADCS Results and Achievements," Powerpoint Presentation.
- [136] Lappas, V., Ooisthuizen, P., Madle, P., Cowie, L., Yuksel, G., and Fertin, D., "Design, Analysis, and In-orbit Performance of the BilSAT-1 Microsatellite Twin Control Moment Gyroscope Experimental Cluster," *AIAA Guidance, Navigation, and Control Conference and Exhibit*, Providence, Rhode Island, August 16-19 2004, pp. 1–34, AIAA-2004-5246.
- [137] QinetiQ, "Topsat," website: www.qinetiq.com/home/commercial/space/topsat.html, 2007, Last Accessed Date January 20, 2008.
- [138] "Feedback on PhD Thesis from Dr. Stuart Eves, Surrey Satellite Technology, Ltd., Guildford, UK," Email Exchange, December 2007.
- [139] Sullivan, R., *Radar Handbook*, chap. 17: "Synthetic Aperture Radar", McGraw-Hill Publishing Company, New York, NY, 3rd ed., January 2008, pp. 17.1–17.37.
- [140] Raney, R. K., *Radar Handbook*, chap. 18: "Space-Based Remote Sensing Radars", McGraw-Hill Publishing Company, New York, NY, 3rd ed., January 2008, pp. 18.1–18.70.
- [141] Elachi, C., *Introduction to The Physics and Techniques of Remote Sensing*, John Wiley and Sons, New York, NY, 1987.

-
- [142] Song, Y., *Motion Compensation of Spotlight SAR Images in the Presence of Unknown Translational Target Motion*, M.S. Thesis, Department of Electrical and Computer Engineering, Queen's University, Kingston, Ontario, Canada, March 1998.
- [143] Wertz, J., editor, *Spacecraft Attitude Determination and Control*, Kluwer Academic Publishers, Boston, 2002.
- [144] Schroeder, R., S. H. and Zeller, K., "Performance Analysis of Spaceborne SAR Systems," *Aerospace Science and Technology*, Vol. 6, No. 6, October 2002, pp. 451–457, Elsevier Publishing.
- [145] "Discussions on Space RADAR mission options with Stuart Eves, PhD, Surrey Satellite Technology, Ltd., Guildford, UK," Interview, December 2004.
- [146] "Discussions on BILSAT-1 and Spreadsheet of BILSAT-1 mass budget with Egemen Imre, PhD student, Surrey Space Center, University of Surrey, Guildford, UK," .
- [147] Wie, B., *Space Vehicle Dynamics and Control*, American Institute of Aeronautics and Astronautics, Inc., Reston, VA, 1998, AIAA Education series, pp. 435-445.
- [148] Lappas, V. and Wie, B., "CMG Sizing for Minisatellites," Technical Note 2, Surrey Space Centre, University of Surrey, Guildford, United Kingdom, 2004, Prepared for the European Space Agency.
- [149] Danfelt, E., Hewes, S., and Chou, T., "Optimization of Composite Flywheel Design," *International Journal of Mechanical Sciences*, Vol. 19, No. 2, 1977, pp. 69–78.
- [150] Roithmayr, C., Karlgaard, C., Kumar, R., and Bose, D., "Integrated Power and Attitude Control with Spacecraft Flywheels and Control Moment Gyroscopes," *AIAA Journal of Guidance, Control, and Dynamics*, Vol. 27, No. 5, 2004, pp. 859–873.
- [151] Radzykewycz, D., Fausz, J., and James, W., "Energy Storage Technology Development at the Air Force Research Laboratory Space Vehicles Directorate," *Proceedings of the 1999 Space Technology Conference and Exposition*, September 28-30 1999, pp. 1–5, Albuquerque, NM.
- [152] Lappas, V., Asghar, S., Richie, D., and Palmer, P., "Combined Singularity Avoidance Using Variable Speed Control Moment Gyroscope Clusters," *Proceedings of the AAS Spaceflight Mechanics Conference*, January 2007, AAS 07-181.

-
- [153] Richie, D., Lappas, V., and Ashgar, S., “Constrained Singularity Avoidance Using VSCMGs for Combined Attitude and Power Tracking,” *Proceedings of the European Control Conference*, Kos Island, Greece, July 2007.
- [154] Wie, B., Heiberg, C., and Bailey, D., “Singularity Robust Steering Logic for Redundant Single-Gimbal Control Moment Gyros,” *AIAA Journal of Guidance, Control, and Dynamics*, Vol. 24, No. 5, 2001, pp. 865–872.
- [155] Wie, B., Bailey, D., and Heiberg, C., “Rapid Multitarget Acquisition and Pointing Control of Agile Spacecraft,” *AIAA Journal of Guidance, Control, and Dynamics*, Vol. 25, No. 1, 2002, pp. 96–104.
- [156] Heiberg, C., Bailey, D., and Wie, B., “Precision Spacecraft Pointing Using Single Gimbal Control Moment Gyroscopes with Disturbance,” *AIAA Journal of Guidance, Control, and Dynamics*, Vol. 23, No. 1, 2000, pp. 77–85.
- [157] Lappas, V. and Wie, B., “CMG Steering Logic with Gimbal Angle Constraints,” *Proceedings of the AIAA Guidance, Navigation, and Control Conference*, Keystone, CO, August 2006.
- [158] Brooks, R., “Maxon Motors Make Mars Mission Mobile,” website: www.marsnews.com/archives/2004/07/10/maxon-motors-make-mars-mission-mobile.html, July 2004, last accessed January 13, 2008.
- [159] “Discussions with Urs Kafader and Peter King, Maxon Motor, on EC motor thermal issues in space,” emailed conversation.
- [160] “Mission Phoenix the new journey to Mars,” website: www.maxonmotor.com/media_releases/MissionPhoenixthenewjourneytoMars.html, 2008, last accessed January 12, 2008.
- [161] Lee, H., *Advanced Control for Power Density Maximization of the Brushless DC Generator*, Ph.D. Dissertation, Texas A&M University, Electrical Engineering, December 2003.
- [162] Prassinis, G., *Design of a Ground Based Simulator for the Controls of Spacecraft*, M.Sc. Thesis, School of Electronics and Physical Sciences, University of Surrey, Guildford, United Kingdom, August 2004.

-
- [163] Cruise, A., Bowles, J., Patrick, T., and Goodall, C., *Principles of Space Instrument Design*, Cambridge Aerospace Series 9, Cambridge University Press, Cambridge, United Kingdom, 1998.
- [164] Branch, N. G. S. C. M. E., “Outgassing Data for Selecting Spacecraft Materials Online,” website: <http://outgassing.nasa.gov>, October 26 2007, last accessed March 18, 2007.
- [165] Dixon, J., Rink, R., and Sather, S., “Digital ASIC/PLD Development Handbook for Space Systems,” Technical Report TOR-2006 (3904)-1, The Aerospace Corporation, El Segundo, CA, 19 May 2006, Prepared for Space and Missiles Systems Center, Air Force Space Command.
- [166] Stemme, O. and Wolf, P., “Principles and Properties of Highly Dynamic DC Miniature Motors,” Tech report, Maxon Motors, Sachsen, Switzerland, November 1994, 2nd Edition.
- [167] Kefadar, U., “Thermal Heating of Electrically Commutated (EC) Motors in Space Vacuum,” Email Conversation.
- [168] Yuksel, G., “BILTEN Research Satellite Flight and Engineering Model Wheel Balancing Test Report,” Tech. Rep. 7011602-B131-RP00-S03-R01, Satellite Technologies Development Group, Biltensat Project, May 8 2003, Scientific and Technical Research Council of Turkey.
- [169] for Standardization (ISO), I. O., “Mechanical Vibration - Balance Quality Requirements of Rigid Motors - Part I: Determination of Permissible Residual Unbalance,” ISO 1940, International Organization for Standardization (ISO), 1986.
- [170] Curtiss, D., Mongeau, P., and Puterbaugh, R., “Advanced Composite Flywheel Structural Design for a Pulsed Disk Alternator,” *IEEE Transactions on Magnetics*, Vol. 31, No. 1, 1995, pp. 26–31.
- [171] Genta, G., *Kinetic Energy Storage: Theory and Practice of Advanced Flywheel Systems*, Butterworth & Co. Publishers Ltd., London, 1985.
- [172] “Thick Walled Cylinders,” website: www.courses.washington.edu/me354a, 2005, last accessed November 2, 2005.

Appendix A

Impact of the Space Environment

The near vacuum of space, whether operating in Low Earth Orbit (LEO), Geosynchronous Earth Orbit (GEO), or interstellar space, has a profound impact on the performance of a spacecraft and its subsystems. The most significant effects from this near vacuum include material outgassing, single event effects (SEE) including single event upsets (SEU) that trigger digital electronics bit flips and other failures, material erosion and thermal heating of rotating surfaces that contact one another, and cold welding of both poorly insulated materials and those that change states due to outgassing. Since ESACS is intended to eventually operate in the space environment, this appendix addresses these significant effects as well as some additional assumptions about the ESACS in development, concentrating primarily on outgassing materials, bearing lubrication, single event upsets, and thermal heating as well as other underlying assumptions. Since direct follow-on research will advance the fruits of this effort, this appendix mostly identifies concentration areas for evolving the design to a flight qualified system but it does not present results from such development – such work is beyond the scope of this thesis and is left for future accomplishment.

A.1 Outgassing of Materials

As presented in [163], the space vacuum can cause materials to release gasses (called outgassing) which can contaminate sensitive surface such as optics and electronics and/or degrade the material itself. These contaminates can also be polymerized by UV radiation and change properties. Clearly these consequences are not advantageous to the survivability and performance of space subsystems. Therefore it is important for the space system designer

to understand two things on this topic. First, one must know which materials exhibit this detrimental behaviour and attempt where possible to select materials that don't exhibit these characteristics. On the positive side, this outgassing behaviour greatly decreases with time in the vacuum, thus the early exposure time is the most critical. Secondly, the designer must be aware of active methods he or she can select to inhibit the impact of such outgassing tendencies. Based on these two ideas, the following discussion will identify key materials for the Rev A, Rev B, and Rev C designs which require outgassing analysis and then will identify approaches to limit outgassing effects.

Table A.1 identifies the key materials encompassing the Rev A, Rev B, and Rev C designs. Note that specifics of several of these materials are unknown as such materials are proprietary (e.g. Maxon Motor EC motor materials) or have not been developed for the future (e.g. fasteners for the Kevlar containment bowl and Carbon Fibre for the support structure, both of which will replace Aluminium constructs to significantly save more mass). Nevertheless, when these materials are unknown, the materials are assumed to be identical to materials already contained on the list (e.g. PCB components, copper wire, stainless steel, ceramic gears, Kevlar containment, PTFE lubricant, etc). This helps yield a representative list of materials to predict the outgassing response of the system. Also included in Table A.1 are two columns from historical NASA data on materials [164]. The first of these is the Total Mass Loss, TML, of the material, captured after 24 hours at 0.13 MPa (10^{-6} Torr) and 125°C in terms of a percentage [163, 164]. A rough correlation of this measurement is that 0.1% TML equates to 0.1 microgram per cm^2 of mass loss. The other column is for CVCM, Collected Volatile Condensable Material, which is collected material on a plate adjacent to the material mounted on a second plate, at 25°C . Rules of thumb from NASA and ESA in terms of such measurements are that a material should have less than 1.0% TML and less than 0.1% CVCM in order to be adequate [163]. Meeting the CVCM requirement is more critical than the TML requirement, but both factors help an engineer get a rough idea of how the material will perform in the near vacuum of space. A key assumption made in developing Table A.1 is that metals such as steel, stainless steel, and Titanium have little to no outgassing performance unless such materials contain epoxies, adhesives, laminates, greases, lubricants, paints, films, or other coatings. These non-metal materials are the typical sources of outgassing on-orbit since metal-to-metal contact normally results in cold-welding of materials or in the case of rotating parts, friction wear out of the metal surface. As opposed to structural strength and stiffness which often relies on key features

Table A.1: ESACS Materials

Material	Use	Rev	TML	CVCM	Remarks
Carbon Fibre	Wheel Rotor	A, B, C	0.13 %	0.00 %	T300 vice T1000G
Kevlar 120	Future Containment	B, C	1.33 %	0.00 %	May Use Variant
Alum 7075	Containment/Spt Struct	A	0.00 %	0.00 %	Assumed as Metal
Duroid 5813	Bearing Cage, Dry Lube	A, B, C	0.08 %	0.00 %	Eroding Film
PCB	Electronics	A, B, C	0.09 %	0.01 %	RF41 PTFE
Al2O3 Ceramic	Motor Gears/Mechanism	A, B, C	0.78 %	0.08 %	Ceramics Vary
ZrO2 Ceramic	Motor Gears/Mechanisms	A, B, C	Unavail	Unavail	Ceramics Vary
NdFeB	Motor Magnets	A, B, C	Unavail	Unavail	Req. Conformal Coat
Braycote 601	Gear Lubricant/Coating	B, C	0.35 %	0.04 %	Low Vapor Grease
Braycote 602	Gear Lubricant/Coating	B, C	0.15 %	0.06 %	Low Vapor Grease
Anodized Al	Coated Aluminium	B, C	0.75 %	0.02 %	Surface Protection
Copper Wire	Wiring/Insulation	A, B, C	0.03 %	0.01 %	Electr. Insulation
Loctite 648	Struct Adhesive	A	5.96 %	0.01 %	Lab Testing Only
3M EA-9323	Rotor Epoxy/Adhesive	A, B, C	0.86 %	0.00 %	May Change for B,C

of metal materials, it's the non-metal surface coatings and constructs that predominantly trigger outgassing. This assumption should be further addressed in follow-on research to this thesis.

Next, it is recommended that a full thermal vacuum test is performed with the ESACS Rev A, Rev B, and Rev C models in a thermal vacuum chamber to measure outgassing. Also, to combat such effects, a thermal bake-out of the ESACS at 70°C for several days is recommended [163]. In addition, all electronics should undergo conformal coating in order to isolate components. Furthermore, before and after such vacuum testing is accomplished, full space qualification testing (random vibration, acoustic shock, etc.) should be accomplished on the systems to gauge performance and the impact of potential outgassing. The initial test will set a baseline for performance while the final test will help assess the impact of outgassing.

From this, one can see that materials of concern for the Rev A, Rev B, and Rev C designs are Kevlar 120, Loctite 648, NdFeB, and ZrO2. Although Kevlar 120 and Loctite 648 have larger Total Mass Loss than the 1.0% guideline, the TML and CVCM are unavailable for the Neodymium magnets (NdFeB) and ceramic Zirconium (ZrO2). In these latter cases, the Maxon motors containing these materials should be tested in a vacuum. If the total mass loss is excessive, then these items should undergo conformal coating at the factory prior to delivery. As for Loctite 648, this is an optional component that still has adequate CVCM despite the high TML. The employment of this material should be vacuum chamber tested and replaced in or eliminated from the ESACS design if the results are unfavourable. Finally,

the Kevlar 120 TML exceeds the limit only moderately but has 0.00% CVCM, making it plausible for the space environment. Meanwhile, the Kevlar employed for the post Rev A containment bowl may be of a different variety and should be tested in the vacuum chamber to gauge its actual outgassing properties.

A.2 Need for Bearing Lubrication

In order to limit wear and tear on rotating surfaces, mechanical bearings and associated lubrication have had essential use terrestrially for a long time. The challenge with such items on orbit is that lubricants, adhesives, and other non-metal materials outgas as explained earlier. Added to this, without these lubricants and bearings, cold welding of metal-to-metal contacting surfaces that are not rotating can ensue, rendering such metal components ineffective. Conventional bearings for motors often take the form of rotational ball bearings using film or oil-based liquid lubricants. A challenge for such items in space is that these materials deplete rapidly (similar to classic liquid propellants) in addition to the potential for outgassing. An alternative which can increase rotating ball bearing lifetime is the use of dry lubricants [163]. These items are also finite but typically have much longer lifetimes than liquid lubricants. An increasingly popular approach discussed in [163] is to use a depleting axial containment washer (often comprised of the polymer PTFE/glass/Molybdenum Disulfide (MoS_2)/glass known as Duroid 5813) on ball bearings to lubricate these bearings. As the balls rotate, the material erodes (much like the erosion of ablative material used for re-entering spacecraft heat shields), which produces a lubricating film. As noted in [163], PTFE has favourable outgassing properties in relation to the previous outgassing discussion in sec. A.1.

In contrast to mechanical lubricants, as addressed in Chapter 2, magnetic bearings provide excellent alternatives with great advantages. These bearings take much longer to wear out and remain effective as long as power is available. The key disadvantages already addressed in the thesis for magnetic bearings are the difficulty in obtaining COTS miniature magnetic bearings, the Electromagnetic Interference (EMI) emanating from these bearings based on high operating power per unit area, and the mass/complexity required to run them. As addressed in motor developments, though, these bearings will enable future ESACS performance as the system can better maintain operation throughout eclipse.

When considering bearings for ESACS, there are two main assemblies to consider and two effected parts within each assembly. The two main assemblies are the wheel motor/generator and

the gimbal motor with gearing. In terms of the wheel motor/generator, there are bearings supporting the shaft within the BLDC motor as well as bearings supporting the external shaft connecting the rotor. Clearly, to operate effectively, the external shaft connects to the internal motor shaft, but in both cases, the support bearings wear out quickly if mechanical versions are used. One should note that this is the case for the Rev A design. However, the goal of the Rev C design and its follow on instantiations is to replace both sets of bearings with magnetic varieties. Miniaturising the BLDC magnetic bearings is a more difficult issue due to the small size required. External shaft magnetic bearings exist but quite expensive when compared to the Rev A design.

Next, for the gimbal assembly, its motor and shaft have similar needs to the motor/generator except the external output shaft rotates at a much lower speed than the wheel motor generator's external shaft (e.g. less than 100 RPM as compared to 10000-50000 RPM). However, to leverage robust existing BLDC technology, the gimbal motor is selected as an EC motor whose shaft is connected to a gear box which then connects to the output shaft. The gear-box selected takes a maximum of 8000 RPM at the shaft input and transfers this relatively high speed with moderate torque to low speed, high torque output shaft motion. Clearly, one can eventually evolve the EC gimbal motor's internal input and final output shafts to magnetic bearing support assuming adequate technology is available (i.e. when finding an identical solution to the wheel motor/generator magnetic bearing problem just discussed). However, obtaining a frictionless solution to the gearbox problem is less likely. This means that a dry lubricant solution is likely the best option for gimbal motor gearing. To combat friction heat, contamination, and outgassing, one should seek a gearbox that is adequately contained/sealed, uses a wear-away lubrication approach as that for the ball bearings from before, and is built from low outgassing material (e.g. ceramic materials that meet the NASA low outgassing material rules-of-thumb [164]).

A.3 SEE and EMI/EMC

Natural radiation stemming primarily from the sun/the solar wind via ultraviolet rays, X-rays, gamma rays in addition to man-made radiation stemming primarily from nuclear detonations are prevalent in both the Low Earth Orbit (LEO) and Geosynchronous Earth Orbit (GEO) space environment regimes [114, 163, 165]. As stated in ref. [165],

In space systems, galactic cosmic rays, solar enhanced particles, or energetic pro-

tons can cause various problems when interacting with electronic systems. The results of these interactions are classified as Single Event Effects (SEE), since they are typically associated with a single energetic particle passing through the material. The most typical SEE that systems will need to address is the corruption of data within the system. This is referred to as Single Event Upset (SEU). SEUs have typically been associated with storage elements, such as memory cells and latches. SEUs can be corrected and are considered nondestructive events. With current high-speed logic, Single Event Transients (SETs) have also become a concern. SETs have been shown to lead to capture of corrupted data in storage elements and to have an impact on clock lines and set/reset signals of digital circuits. In the latter cases, multiple errors can be generated by a single ion strike. Any upset can disrupt functionality if the system is not designed to handle such events. Mitigation measures for SEEs can include design techniques (error detection and correction-EDAC), triple modular redundancy (TMR), and memory refreshing.

Ref. [165] goes on to state that SEEs can contribute to long-term degradation of spacecraft electronic systems. Due to the reliance of the ESACS on electronics (i.e. to run the motors and move power through the system), radiation hardening of the electronics is recommended for evolving the ESACS design to a space qualified version.

Here one should note that the proposed solutions to combating SEEs can significantly increase the electronics mass of the system. However, for ESACS, this effect is moderate since the ESACS mass is dominated by the wheel motor/generator, containment bowl, and support structure. Further research into radiation hardening ESACS electronics is beyond the scope of the current effort but should be pursued as the ESACS electronics are evolved in follow-on work.

A.4 Thermal Impact on Motor Performance

Motors and generators are mechanisms that are well known to build up heat rapidly through excessive use. For the Maxon motors employed in this work, such thermal heating is investigated in Appendix B, in which limits to the motor current are invoked to keep thermal heating under control. As for the case of outgassing, it is recommended that future work employ such motors in a vacuum chamber and test the operation of these devices. Regardless,

since this topic is addressed elsewhere in this thesis (as well as more extensively in [166]), this topic is not further discussed here.

A.5 Initial Start-up/Back-up Batteries and Bearings

There are several approaches one may take in implementing ESACS in space in terms of initial start-up and back-up batteries/bearings. Generating an exhaustive approach is not relevant for the current effort, but a couple of options should be addressed. First, the satellite and ESACS may be off during launch and energized at first sunlight. The solar energy can then immediately spin-up the VSCMG wheels through the motor electronics. A master ESACS controller/computer (or its functionality in the on-board computer) is required to regulate the VSCMG cluster's slewing torque and energy charge/drain using the algorithms defined in Chapter 6. Second, if deployed and turned on in eclipse, since the wheels will start at zero speed, they will require charging (i.e. spin-up) prior to power drain, most likely awaiting the first sunlight period. Here it should be noted that vibrational survivability of ESACS should be tested via normal spacecraft subsystem qualification testing prior to launch (e.g. through Random Vibe, CG/MOI, and thermal vacuum tests). Thus in the most basic case, there is no need for a back-up battery to be brought on board since the system charges directly from sunlight (this also assumes the other spacecraft subsystems can run directly from sunlight or another primary power source). It should be noted that the ESACS energy storage connections (i.e. the electronic load connections used in the thesis experiments) can be integrated into a parallel circuit with conventional secondary batteries for added spacecraft redundancy or risk reduction. This may prove beneficial for a mission that requires limited pointing and peak power that is flown on the same bus as a mission requiring precision slewing and high peak power (e.g. mini Synthetic Aperture RADAR (SAR) or precision imaging). Nevertheless, this start-up concept affords flexible implementation, leaving the choice to the satellite designer.

A.6 Other Subsystem Assumptions

When researching the ESACS design, it's important to identify some of the key assumptions made. As the ESACS research program continues, these assumptions will evolve, thus follow-on research should refine them. Nevertheless, the assumptions that follow help sculpt the

ESACS work conducted.

First, the presented arguments focus on this technology's role in fulfilling the entire energy storage mission for a satellite, however, an equally plausible alternative is to employ an ESACS on missions wherein a high-power, high-agility payload only needs the high-power properties of the ESACS during some operations, but the satellite does not need them all the time to run satellite support subsystems. Thus, a contemporary satellite ES can supply eclipse subsystem power using conventional batteries but run the payload at the high-power level with energy from the ESACS.

Second, due to its built-in redundancy and prevalence in the existing literature [13,66,74,147], it's assumed a pyramid cluster of VSCMGs is to be used in ESACS. This configuration permits all four gimbals to fail while retaining three-axis attitude control using the remaining wheels in MW mode and actuator redundancy for energy storage. However, it is recognized that there are several different plausible cluster configurations [147]. The key effect is that a different configuration will change the actuator number, N_{vc} , used as well as change the geometry-based minimum torque capability, $2 + 2\cos\beta$, term in the available torque, N_a , equation.

Third, it is assumed the initial mission employing this system will treat it as an experimentally payload and will thus fly it in concert with a secondary battery system for redundancy. However, as confidence in the system grows (as it should from the ground experiments demonstrated here), the need for such redundancy will eventually vanish. Employing the future small satellite ESACS which employs long-life magnetic-levitation, the solar panels are assumed to be the first system to fail on the satellite (after 15 years of use) from sunlight and eclipse exposure. Thus these panels are assumed to withstand 83000 orbital cycles of 95.3 min duration (i.e. in a 686 km, 95° inclination orbit) over 15 years.

Fourth, a proper VSCMG containment vessel is required for actuator use at high speeds. Clearly, the energy associated with a VSCMG-based ESACs is a personnel and systems safety risk which must be adequately accommodated. The larger the containment method used, the greater the mass impact. Future system designers must consider this fact when converting from the Rev A Alum 7075 to the post-Rev A Carbon Kevlar containment design.

Fifth, it is assumed that rotor strength to density ratio limits the maximum structurally achievable wheel speed which drives mass savings. Furthermore, subcomponent materials (magnetic wire density, Permanent Magnet and Electro-magnet materials) mass is uncertain.

The best estimates have been made, but won't be proven until a magnetic bearing-system is demonstrated. This primarily affects the magnetic bearing design for Alternatives #2 and #3 as well as the motor/generator design for Alternative #2. In addition, the magnetic bearing hardware sizing algorithm is rough/restricted as it uses Varatharajoo's very specific design geometry [78]. A better, more accurate magnetic bearing design requires Finite Element Method (FEM) analysis. In addition, an FEM analysis should also be done if using the Alternative #2 motor-generator approach.

Sixth, torque disturbance/imperfections such as Eddy currents, motor cogging, and dynamic breaking can limit the amount of actual wheel motor torque produced and thus affect the output performance of the EC motor design. Also, motor to generator switching circuits add uncertainty into the system. Plus, wheel motors are limited in the ability to achieve some of the desired maximum wheel angular accelerations for high wheel speeds limits. Modeling these assumptions has refined the motor model used to analyze experimental data. Details of this motor model as compared to experimental testing data are given in Appendix B.

Finally, the SAR target requirements, actuator fixed parameters, and baseline NiCd EPS plus MW ACS parameters and margins are valid. Obviously, changes in these values can affect the analysis results. These values have been garnered from reasonable/reliable sources, but there is still some uncertainty intrinsic to these values.

Appendix B

Motor Modelling

A significant portion of the conducted ESACS laboratory work involves the use of COTS BLDC motors, including the wheel motor/generator and the gimbal motor. Thus, it's imperative one best understands the key performance, efficiencies, and losses inherent to these motors. To address this need, the appendix that follows investigates the fundamental power theory behind the BLDC motors used, applicable modelling/parameter history prediction for the ESACS motor/generator system used, the comparison of these models to the collected laboratory data, replacement of BLDC motor components with a magnetic bearing motor drive system (assuming the draft shaft is externally magnetically levitated as well), and the thermal heating impacts of the space environment on the employed wheel and gimbal motor systems.

As shown by Stemme and Wolf in [166], brushless DC motors (BLDC), which are electrically commutated, have similar characteristics to mechanically commutated, classical brushed DC motors. Although BLDC motors are essentially three-phase AC motors that use square wave drives, the average of the oscillating three-phase behaviour closely resembles that of conventional brushed DC motors. For this reason, COTS BLDC suppliers often summarize motor specifications using conventional terms. As this is true of the maxon motors employed for the thesis, understanding these specifications helps one model and predict the ESACS performance. In addition, it's important that one understand Wilson et. al.'s work (in ref. [132]) which captures the essential motor/generator behaviour of an ESACS based on a magnetically-levitated system. Thus, the efforts on standard DC motors for ESACS investigated here synthesize the works of [132, 166]

B.1 Power Balance

Motor/generators are best characterized as energy conversion devices wherein energy is either converted from electrical to mechanical form plus losses as done in a motor or from mechanical to electrical form minus the same losses. Capturing this energy conversion is typically addressed in terms of a power balance. Defining the mechanical, electrical input, load, and loss power as P_m , P_u , P_l , and P_v yields the following power balance

$$P_m = P_u - P_l - P_v \quad (\text{B.1})$$

The losses, P_v , stem from several sources of which the primary losses are heating (joules or iron) loss, P_j , friction loss, P_r , and eddy current loss, P_{fe} [166]. The heat loss, P_j , a function of the motor resistance and current, can be expressed as $P_j = I_m^2 R_m$. The friction loss, P_r , is related to the friction torque, M_r , which is nearly constant at low speeds and speed dependent at higher speeds [166]. Thus, $M_r = k_m I_o + c_5 \Omega$ where I_o is the no-load current. Since output power is the torque multiplied by speed, $P_r = M_r \Omega$, yielding $P_r = k_m I_o \Omega + c_5 \Omega^2$. Next, the eddy current torque, M_{fe} , is quite small for contemporary motors with mechanical shaft bearings as compared to the friction torque, but as explained in [132], this effect is significant for motors with magnetic shaft bearings in which the friction and iron loss torque are negligible. [132] shows that $M_{fe} = \rho G \Phi^2 \Omega$, where ρ is the number of magnetic bearing poles, G is a constant which depends on magnetic bearing geometry, and Φ is the magnetic bearing flux bias, can be approximated as $M_{fe} = k_d \Omega$, where k_d is found experimentally via rotor spin-down tests. From this, one can see that $P_{fe} = k_d \Omega^2$. Therefore, the losses are

$$P_v = P_j + P_r + P_{fe} = I_m^2 R_m + k_m I_o \Omega + c_5 \Omega^2 + k_d \Omega^2 \quad (\text{B.2})$$

Next, the input power is the product of the input voltage and current, $P_u = U I_s$. Also, the load power is a function of the load voltage and resistance, $P_l = \frac{V_l^2}{R_l}$ where V_l is equal to the supply voltage, U , in charge and a function of the motor back EMF, $V_{m_{back}}$, in discharge. The back EMF is found as

$$V_{m_{back}} = k_m^2 \Omega^2 \quad (\text{B.3})$$

Furthermore, the mechanical power, as discussed in the thesis, is best approximated as the product of the wheel spin-axis inertia, I_{w_s} (referred to interchangeable as “J” in this appendix), the wheel angular speed, Ω , and the wheel angular acceleration, $\dot{\Omega}$. Thus, $P_m = J \Omega \dot{\Omega}$. Now,

the consolidated power balance can be expressed

$$P_m = P_u - P_l - P_j - P_r - P_{fe} \quad (\text{B.4})$$

$$J\Omega\dot{\Omega} = UI_s - \frac{V_l^2}{R_l} - I_m^2 R_m - k_m I_o \Omega - c_5 \Omega^2 - k_d \Omega^2 \quad (\text{B.5})$$

This is further simplified by noting that in charge, $I_s = \frac{V_s}{R_s}$, $R_s = R_m = R_{ph} + R_l$, $V_s = V_m = V_{m_{back}}$, $V_l = V_s = V_m$, and $I_m^2 R_m = \frac{V_m^2}{R_m} = \frac{V_{m_{back}}^2}{R_m}$, then

$$J\Omega\dot{\Omega} = U \frac{k_m \Omega}{R_m} - \frac{k m^2 \Omega^2}{R_l} - \frac{k_m^2 \Omega^2}{R_m} - k_m I_o \Omega - c_5 \Omega^2 - k_d \Omega^2 \quad (\text{B.6})$$

Note that this equation holds in discharge except the input voltage, U , is zero, and the resistance values change since the circuit transitions from a parallel construct to series. Rearranging

$$(J\dot{\Omega}) \Omega = \left(\frac{U k_m}{R_m} - k_m I_o \right) \Omega - \left(\frac{k_m^2}{R_m} + \frac{k m^2}{R_l} + c_5 + k_d \right) \Omega^2 \quad (\text{B.7})$$

Without loss of generality, one can assume that $\Omega \neq 0$, so that this becomes

$$J\dot{\Omega} = \left(\frac{U k_m}{R_m} - k_m I_o \right) - \left(\frac{k_m^2}{R_m} + \frac{k m^2}{R_l} + c_5 + k_d \right) \Omega \quad (\text{B.8})$$

Defining the following constants

$$\Delta_1 = \left(\frac{U k_m}{J R_m} - \frac{k_m I_o}{J} \right) \quad (\text{B.9})$$

$$\Delta_2 = \left(\frac{k_m^2}{J R_m} + \frac{k m^2}{J R_l} + \frac{c_5}{J} + \frac{k_d}{J} \right) \quad (\text{B.10})$$

the differential equation that characterizes the motor velocity - acceleration relationship is

$$\dot{\Omega} = \Delta_1 - \Delta_2 \Omega \quad (\text{B.11})$$

Taking the Laplace transform of both sides (and substituting $\Omega_0 = \Omega(0)$)

$$s\Omega(s) - s\Omega_0 = \frac{\Delta_1}{s} - \Delta_2 \Omega(s) \quad (\text{B.12})$$

$$\Omega(s) = \frac{\Omega_0}{(s + \Delta_2)} + \frac{\Delta_1}{s(s + \Delta_2)} \quad (\text{B.13})$$

$$\Omega(s) = \frac{\Omega_0}{(s + \Delta_2)} + \frac{\Delta_1}{s} - \frac{\Delta_1}{(s + \Delta_2)} \quad (\text{B.14})$$

$$\Omega(s) = \frac{\Omega_0 - \frac{\Delta_1}{\Delta_2}}{(s + \Delta_2)} + \frac{\Delta_1}{s} \quad (\text{B.15})$$

$$\Omega(t) = \left(\Omega_0 - \frac{\Delta_1}{\Delta_2} \right) \exp(-\Delta_2 t) + \frac{\Delta_1}{\Delta_2} \quad (\text{B.16})$$

Eq. B.16 is the speed equation of the motor and is a function of time. Note that this equation can be used for charge or discharge, but the initial speed, Ω_0 , changes with a change in charge state as do Δ_1 and Δ_2 . Δ_1 changes since the supply voltage, U , goes to zero. Meanwhile, Δ_2 changes since the resistance characteristics of the motor circuit change in discharge. Also, since the eddy current loss is extremely small compared to friction and heating losses, the k_d term can be taken as zero when using mechanical rotor bearings to support the motor/generator shaft. When applying these equations to the magnetically levitated case, the no-load current, I_o , and the speed-induced friction constant, c_5 , can be set to 0. Furthermore, the joules loss term can also be eliminated from the equations in such a case. Continuing on, one can determine the motor angular acceleration from the time derivative of the motor speed equation (Eq. B.16) as

$$\dot{\Omega}(t) = -\Delta_2 \left(\Omega_0 - \frac{\Delta_1}{\Delta_2} \right) \exp(-\Delta_2 t) \quad (\text{B.17})$$

which can be rearranged as

$$\dot{\Omega}(t) = (\Delta_1 - \Delta_2 \Omega_0) \exp(-\Delta_2 t) \quad (\text{B.18})$$

Next, one can use the relationship between motor torque, the torque constant, and the motor current to calculate the motor current from acceleration:

$$k_m I_m = J \dot{\Omega} \quad (\text{B.19})$$

which yields

$$I_m = \frac{k_m}{J} \dot{\Omega} \quad (\text{B.20})$$

Recall that one can find the motor power as the product of the spin-axis inertia, motor acceleration, and motor speed as $P_m = J \Omega \dot{\Omega}$. Similarly, the motor capacity is $C_m = \frac{1}{2} \Omega^2$. Next, the supply power during discharge is assumed to be 0 as its capacity, but the charge supply power is found from the supply voltage, U , and resistance, R_s as

$$P_{s_c} = \frac{U^2}{R_s} \quad (\text{B.21})$$

and the associated capacity is the integral of the power, which becomes

$$C_{s_c} = \frac{U^2}{R_s} t \quad (\text{B.22})$$

The load power, is characterized differently in charge and discharge due to the changing state of the supply. In charge, the load power is run from the supply in parallel and is found as

$$P_{l_c} = \frac{U^2}{R_l} \quad (\text{B.23})$$

where in discharge, the load power is run from the motor and is therefore

$$P_{l_d} = \frac{k_m^2 \Omega^2}{R_l} \quad (\text{B.24})$$

The associated capacities are

$$C_{l_c} = P_{l_c} t \quad (\text{B.25})$$

$$C_{l_d} = P_{l_d} t \quad (\text{B.26})$$

B.2 Calculating the ESACS Benefits Related to Motor Data

Carrying this theoretical development further, one can calculate the anticipated benefits values (i.e. energy and power density, transmission efficiency, and depth of discharge) from the motor model just described. First, the load power during discharge and its associated capacity when coupled with the actuator mass, M_{a_1} , yields several equations for these benefits

$$P_{min} = \min P_{l_d} \quad (\text{B.27})$$

$$P_{max} = \max P_{l_d} \quad (\text{B.28})$$

$$P_{avg} = \frac{\sum(P_{l_d})}{n_c} \quad (\text{B.29})$$

$$P_{d1min} = \frac{P_{min}}{M_{a_1}} \quad (\text{B.30})$$

$$P_{d1max} = \frac{P_{max}}{M_{a_1}} \quad (\text{B.31})$$

$$P_{d1avg} = \frac{P_{avg}}{M_{a_1}} \quad (\text{B.32})$$

$$E_{d1} = \frac{C_{l_d}}{M_{a_1}} \quad (\text{B.33})$$

where n_c is the number of P_{l_d} data points for averaging P_{l_d} . Then, the efficiency values (round-trip efficiency, η_e , transmission efficiency, η_{msn} , and depth-of-discharge, dod) are found

$$\eta_e = \frac{C_{l_d}}{C_{s_c}} \times 100\% \quad (\text{B.34})$$

$$\eta_{msn} = \frac{C_{l_d}}{C_{m_d}} \times 100\% \quad (\text{B.35})$$

$$dod = \frac{\Omega_{limit} - \Omega_{min}}{\Omega_{limit}} \times 100\% \quad (\text{B.36})$$

where Ω_{limit} is assumed to be the maximum operating value of the wheel speed from the motor specifications.

B.3 Comparison to Laboratory Data

Having developed the theory behind the motor model, the next step is to compare collected motor data to the model. The plots that follow capture this comparison.

Table B.1: Selected EC-45 Motor Parameters

Parameter	Value
Torque Constant, k_m , Nm/A	0.0433
Wheel Spin-axis Inertia, $J = I_{ws}$, kg m ²	0.009946
No-load Current, I_o , A	0.435
Starting Current, I_A , A	55.9
Phase-to-Phase Resistance, R_{ph} , Ohm	0.43
Bus Voltage for Motor Table, V_{bus} , V	24.0
No-load Speed, n_0 , RPM	5250
Stall Torque, M_h , Nm	2.421
Speed-Torque Gradient, $\Delta n \Delta M$, RPM/mNm	2.19

Table B.2: Motor Model Parameters

Parameter	Value
Input Voltage, U_{inreqd} , V	??
Discharge Voltage Drop, V_{drop} , V	2.0
Desired Operating Speed, Ω_b , RPM	9000.0
Min Operating Voltage, V_{min} , V	7.6
Load Resistance, R_l , Ohm	40
No-load Load Resistance, R_{l_0} , Ohm	1e-6
Initial Speed, Ω_0 , RPM	0.0
Input Voltage Losses, $V_{inlosses}$	2.5
Pulse Width Modulation (PWM) Efficiency, η_{PWM}	0.95
Wilson's Spin-axis Inertia, J_{wilson} , kgm ²	0.5
Wilson's Eddy Current Damping, $k_{d_{wilson}}$, μ w RPM ²	0.16
Speed-based Friction Torque Constant, c_5	0.000025
Load Discharge Resistance, $R_{r\dot{t}_d}$, Ohm	1.35
No-load Discharge Resistance, $R_{r\dot{t}_d}$, Ohm	6.0

B.4 BLDC Motor Thermal Heating in Space Vacuum

In addition to the laboratory performance of the motor modelled, tested, and analyzed throughout this appendix, there are heating limits that infringe upon smooth operation of the motor – a concept amplified in operation outside the Earth's atmosphere. As one may know, the primary means a system has for heat transfer are conduction, convection, and radiation. Most of the EC motor's heat in the laboratory is transferred via convection [167]. However in space, the ultimate method for transferring heat is via radiation. This means that motors

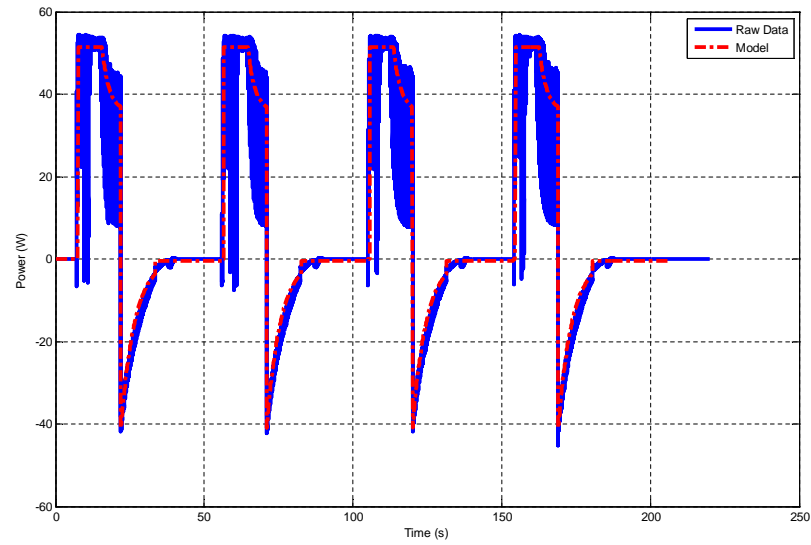


Figure B.1: Net Load Power Data versus Model

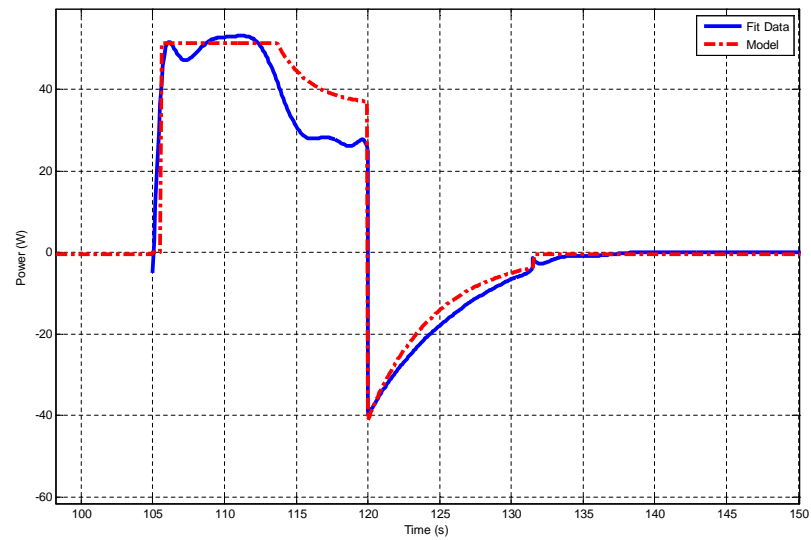


Figure B.2: Net Fit Data

designed for operation in the Earth's atmosphere have different thermal properties in the orbital vacuum of space when attempting to reject heat. The following discussion investigates the process and limitations of transferring heat for effective Maxon EC motor operation. As it turns out, radiation heat transfer limits can be directly translated to maximum continuous current operation of the motor. Although the motor can be briefly overloaded outside this regime (i.e. in charge and discharge modes where motor current magnitude is greatest), there is a recovery period from such overloading. This action also reduces the motor lifetime. Therefore, for continued smooth operation, it is important to target current loading below the maximum.

Developing these current limits begins with a worst case calculation of thermal losses as defined by Maxon Motor's Dr. Urs Kefauver [167]. As one may recall from the power balance developed earlier, the mechanical output power is comprised of the difference between the input electrical power, the subsystem load power, and significant power losses (i.e. joules loss, friction loss, eddy current loss, etc.). Assuming the power loss is only manifested as joules loss and there is no electronic load, the power balance is

$$P_m = P_u - P_l - P_v = P_u - P_v \quad (\text{B.37})$$

which, when rearranged, becomes

$$P_v = P_u - P_m \quad (\text{B.38})$$

Next, assume that the loss power is transferred to heat via one of the heat transfer mechanisms described earlier

$$P_v = \alpha' c A (T_{max}^4 - T_a^4) \quad (\text{B.39})$$

where c is the Stefan-Boltzmann constant as $5.67 \times 10^{-8} \frac{W}{m^2 K^4}$, A is the cylindrical surface area of the motor case, T_a is the assumed ambient temperature (which oscillates widely in Earth orbit depending upon spacecraft sun vector). Substituting the equation for joules loss for the total losses yields

$$P_v = P_j = I_m^2 R_m \quad (\text{B.40})$$

where I_m is the motor current and R_m is the motor resistance. Now, combining Eq. B.39 and Eq. B.40 yields a conservative continuous current limit equation

$$I_m = \sqrt{\frac{\alpha' c A (T_{max}^4 - T_a^4)}{R_m}} \quad (\text{B.41})$$

Assuming the absorptivity of the system is given as $\alpha' = 0.9$ and the maximum rated permissible temperature for Maxon EC motors is $T_{max} = 125C = 398K$, one can assess the determine the current limit, I_m , for different ambient temperatures, T_a , from the motor data. Computing such limits for the EC-45 250W, EC-16 40 W, EC-22 50 W, and EC-16 max 8W, yields the data in Table B.3. As one can see from Table B.3, the maximum continuous

Table B.3: Motor Heating Limits

Parameter	EC-16	EC-16 max	EC-22	EC-45
Surface Area, A , m ²	0.0028	0.0018	0.0043	0.0143
Max Ambient Temp, T_{amax} , K	373	373	373	373
Min Ambient Temp, T_{amin} , K	248	248	248	248
Max Operating Temp, T_{max} , K	398	398	398	398
Thermal Resistance, R_m , Ohm	0.716	20.5	0.363	0.43
Rated Cont Current, I_{cont} , A	2.71	0.461	4.16	7.47
Max Cont Current Max, $I_{cont_{max}}^s$, A	2.07	0.31	3.60	6.02 [‡]
Max Cont Current Min, $I_{cont_{min}}$, A	1.07	0.16	1.87	3.13

^S The max continuous current occurs at the min ambient temperature and vice versa.

[‡] This current is above the servo-amplifier limit of 5A, thus it can only reach 5A.

current calculated in Low Earth Orbit for a min temperature of $-25C$ and a max temperature of $100C$ yields a permissible regime of current values that is at minimum, about a third of the allowable continuous current. However, it should be highlighted that the continuous current in the laboratory runs was much less than the maximum continuous permitted at high temperature in orbit. Therefore, the thermal heating limits of the EC motors is reasonable for ESACS but these limits do constrain the permissible load. A more favourable approach of the future will be to employ a magnetically levitated shaft and magnetic motor bearings which will not only reduce the friction loss but also drastically reduce the joules loss thereby permitting higher charge and discharge operating currents (thus power). Similarly to the other space environment calculations found in Appendix A, these current limits should be tested in a thermal vacuum chamber to validate these predicted characteristics.

Appendix C

Testing Supplement

C.1 Test Article Design

Having identified the goals and requirements of the test-campaign, it's important to understand the key facets of the test article. In the present work, this test article consists of a multiple-subsystem air-bearing structure derived from the work by Prassinis in [162] wherein several typical satellite subsystems are employed to simulate spacecraft motion in earth orbital free-fall. More specifically, this test article permits one to simulate in the laboratory three-dimensional attitude rotation maneuvers, remote ground to satellite communication, and on-board computer drive of the system, the latter of which is especially critical in controlling the ESACS-based VSCMG system. The subsystems, listed in Table C.1, also permit handling of collected experimental data and transmission of this data to the ground (host) computer for data logging imperative to follow on test analysis. As one can see from the data in Table C.1 and the photograph in Figure 8.2(a), the air-bearing subsystems include those of a typical satellite – electrical power (EPS), data handling (DH), communications (Comm), propulsion (Prop), attitude determination and control (ADCS), and mechanical structures (Mech).

The electrical power subsystem consists of three 4-cell, lead-acid battery packs rated as 24V at 7.5A per pack that provide primary power (each cell is 6V at 7.5A); two 24-Volt regulators which can each provide 24-Volts to the air-bearing circuits or be connected in series thereby providing 48-Volts; a power interface hub that provides diode protection to the subsystems and interconnects supply sources and systems much like a satellite electronics bus; a wiring harness which consists of all cabling interconnecting the subsystems; a solar sim that simulates

Table C.1: Air-Bearing Subsystems

Syst	Component	Qty	Description
EPS	Solar Sim	1	OBC-driven relay that regulates power supply flow
EPS	Electronic Load	1	Series-connected bulbs as power bus simulator
EPS	Voltage Regulator	2	Regulates input supply to 24-V output
EPS	Lead Acid Battery Packs	3	Primary supply via 4-cell packs at 24-V, 7.5A
EPS	ACE OBC Power Supply	1	OBC power supply with fan
EPS	Power Interface Hub	1	Safety bridge for 24-V, 48-V lines
EPS	Wiring Harness	1	Several cables providing adequate connections
ADCS	Cross-bow IMU	1	Measures body angular rates, linear accel.s
ADCS	On-board laptop	1	Stores IMU data for post experiment processing
ESACS	VSCMG Assembly Rev A	1	Described in chapter 7
DH	OBC (target PC)	1	On-board Computer with ADLINK processor
DH	Telemetry	1	Data Acq Boards for performance data logging
DH	Command	2	Data Cmd Board to direct controlled components
Comm	D-Link Transceiver	1	Provides OBC(target)-Ground(host) data network
Prop	Inert Propulsion Tanks	2	For propulsion subsystem research
Mech	Air-bearing Platform Disk	1	Test article primary structure
Mech	Air-bearing Pedestal	1	Support base, air channel for spherical bearing
Mech	Ballast Bricks	3	Balances, keeps test article mass center low
Mech	Miscellaneous Ballast	V	Various items for system balance

switching between sunlight and eclipse via a simple, Normally Open 5V relay; and the On-board Computer (OBC)'s ACE power supply, which distributes power to both the D-link transceiver and the OBC. An electrical schematic demonstrating the inter-connectivity of equipment for the Air-bearing system is included as Figure 8.2(b).

The D-link transceiver mentioned earlier serves as the communication subsystem on-board and provides a wireless link between the target PC and the host PC. This inter-connectivity permits system scenarios to be crafted via MATLAB XPC Target software as a real-time SIMULINK model, compiled, and tested on the host before being downloaded to the on-board computer via the transceiver. Then, once a run is completed, the D-link transmits test run data back to the host for pre-processing and initial analysis.

Closely related to the communications subsystem, data handling consists of the MATLAB XPC Target software on the host and target PCs; the data acquisition circuit boards (NI-6023E), data interface cards (NI CB-68LP), and data command circuit boards (NI-6703) on the target PC; the data connection from the IMU to the on-board IMU-processing computer; the command interfaces of the DECV 50/5 for gimbal and wheels as well as the solar sim command inputs; and the current and voltage sensors on the SSC FES and DECV 50/5 boards.

The Attitude Determination and Control Subsystem is best characterized (at least in terms of attitude determination) by the Crossbow Inertial Measurement Unit (IMU) and by the VSCMG (ESACS) actuator's attitude control function. The IMU uses three-axis accelerometers and three-axis angular rate sensors to determine the test article's three-dimensional linear acceleration and angular rotation velocity. By eliminating the parasitic biases discussed later, one can find a fairly accurate attitude position estimate. This is important when characterizing the attitude performance of the VSCMG prototype.

In addition to DH, EPS, Comm, and ADCS, the mechanical structures system serves an important role – holding all the subsystems together as well as giving a stable, balanced platform on which to execute the maneuvers.

A subsystem that has not been fully exploited herein is the propulsion system. Its primary role here is to provide ballast mass and demonstrate the utility of the air-bearing structure to accommodate several key technologies on one platform, all of which are important to a space mission. However, its function may serve a more prominent role in future work if the propellant tanks are used via control thrusters to slew the air-bearing in concert with the VSCMG or used for wheel de-saturation. One can also envision comparing/contrasting wheel de-saturation using thrusters vice power regulation. In that case, use of the propellant tanks would serve a greater role.

C.2 Rotor Balancing

After development testing with Engineering Model-level components on the laboratory bench, but prior to full integration testing, it was necessary to balance the Rev A prototype Carbon Fibre rotor. The need for such testing, quantitative requirements, procedure followed, and test results are addressed in the ensuing discussion.

C.2.1 Need for Balancing

To get most efficient power and attitude control performance out of the VSCMG high speed rotor, there's clearly a need for a balanced rotor that is properly supported to reduce wear-and-tear on the motor's ball-bearings and any bearings on the wheel's drive shaft. Note that even if these motor ball bearings (and other wheel shaft bearings) are replaced by magnetic ones, these magnetic bearings will increase in power draw/energy drain if the rotor isn't

properly balanced. Not only does balancing ensure the rotor inertia is evenly distributed about the spin-axis, but it also makes the motor much more efficient as imbalance losses are minimized. This factor is especially important when designing a rotor to spin to high speeds where imbalances equate to amplified inefficiency in the system. In other words, inefficiencies in round-trip power conversion as well as accurate attitude control may result.

C.2.2 Defining the Key Balance Requirements

The needs for accurate balancing actually can be specified via quantitative requirements. In fact, an excellent source for defining such requirements in terms of static balancing (where the rotor's spin center is adjusted to align with its geometric center to prevent 'hammering' [168], where the wheel attempts to rotate about its mass center which is not at its rotation center) and dynamic balancing (where both the rotor's top and bottom axial surfaces are adjusted to avoid "wobble" about a transverse axis) is given in Ref. [169]. It describes three different approaches to identifying requirements: using an empirical quality grade, using an experimental indicator most closely associated with manufacturing and production, and applying a known bearing imbalance tolerance [168]. For the purposes of the present work, the third of these is applied as the motor/generator bearing imbalance tolerance for each of the motor options has been given in the motor specification data.

In Fig. C.1(a) taken from the BILTENSAT RW test report (Ref. [168]), the three primary types of imbalance (hammering, wobble, and a combination of both is shown). On the other hand, the wobbling effect shown in Fig. C.1(a) is more of a dynamic issue where mass difference at the axial tips of the rotor in different locations causes the rotor to wobble when viewed radially inward. This dynamic imbalance issue is best resolved by adding (or deleting) mass in two planes simultaneously (i.e. along the axial top and bottom of the wheel) at a significant axial distance. Note that if this distance is too small, the dynamic benefits of adding this mass can be neutralized. Applying the results from ISO 1940 [169] to the problem, one can determine an allowable unbalance of the rotor which directly corresponds to the mass center tolerance alluded to above. The process begins by identifying the allowable bearing loading as illustrated in Figure C.1(b). Here one can see that the loading shown (which comes from the motor data specifications) is defined by the motor manufacturer and relates to the allowable shaft bending moment impacting the motor's shaft ball bearings. The purpose of this specification is such that implementation of the motor does not involve exceeding this loading.

When implemented with a rotor, the actual loading occurs as shown in Figure C.1(d). Notice that this loading requires the distance between the rotor center line and the motor's flange conservatively assumed to be the location of the ball bearings even though there are two ball bearings sets near both motor flanges. The longer the motor, the greater the presumed separation between ball bearing sets. To glean a requirement for rotor balancing, one needs to determine the actual loading and cast this loading in relation to the maximum allowable loading per the given specification. However, reporting this requirement can be confusing if the value is misunderstood. This will be highlighted in the following example. In this example, an inconsistency arose when an allowable unbalance requirement of 0.449 g cm or 0.449 g was determined via following ISO 1940 prior to testing the Rev A prototype on SSTL's dynamic balance machine. When SSTL determined the requirement for this same motor, it was found that the requirement was really 3.56 g cm or an allowable 0.712 g of unbalance to conservatively meet the given motor specification. SSTL's value was consistent with experience garnered from several smaller momentum wheels developed that routinely allowed a mass unbalance of 0.2 - 0.3 g. As it turns out, both of these assessments are consistent once one understands the process and assumptions each organization used to determine the associated requirement.

First, the process each used yields the same equation for mass unbalance when assuming the acceleration due to gravity's (g_0) affect is negligible as compared to the centripetal acceleration experienced by the rotor in test. In this case, it was conservatively assumed the Maxon EC-45 can not exceed 12000 RPM (consistent with the maximum allowable speed permitted for the EC-45) and would be balanced to that level. In so doing, it turns out that g_0 is actually 0.01 % of the centripetal acceleration and thus the g_0 assumption is a good one. Next, it was also assumed by both groups that there should be a safety factor of 2 in the bearing specification.

Given these common assumptions, each organization applied its process. In doing so, there were actually two additional assumptions each made differently. The first of these was that SSTL assumed the shaft bending moment arm, d_{act} , was 8 mm. This value was actually reported as to SSTL as a more accurate value after the SSC version of the balance requirement was calculated with a more conservative value of 10 mm. The second disparate assumption was that the rotor radius location for which the unbalance requirement applies was different. The SSC assumed this location was for the outer radius of the rotor as that would encompass the entire rotor $r = r_0 = 63.5$ mm. On the other hand, SSTL assumed the applicable radius

is at the rotor's inner wall ($r = r_i = 50.0$ mm) since that is the location at which mass would be added in the imbalance correction step of the balance testing process.

Now that the similar and differing assumptions have been identified, one should review the two balancing methods used as depicted in Figure C.1(c). The variables used in this figure are the maximum allowable bending force, F_{bx} , maximum allowable bending moment arm, d_{bx} , maximum allowable bending moment, M_{bx} , unbalance location, r , balance wheel speed, Ω_x , total acceleration, a_t , permissible unbalance moment, U_{per} , permissible specific balance moment, e_{per} , safety factor, FS , actual bending moment arm, d_{act} , allowable mass unbalance, m_{unbal} , actual shaft force, F_A , shaft force with safety margin, F'_A , and unbalance moment at location of interest, U_{bal} . As one can see from Figure C.1(c), the total unbalance mass can be expressed generally as

$$m_{unbal} = \frac{U'_{per}}{d_{act}} = \frac{U_{bal}}{r} = \frac{F_{bx} d_{bx}}{FS d_{act} (r \Omega_x^2 + g_0)} \quad (C.1)$$

Next, revisiting the values addressed earlier, if the same d_{act} is used as 8 mm, gravity is neglected, and the rotor's inner radius is taken as the reporting location $r = r_i = 0.05$ m, one finds that m_{unbal} does equal 0.712 g or 712 mg. In addition, U'_{per} is 0.570 g cm, U_{bal} is 3.562 cm. Thus, the requirement for the balance test was taken to be a slightly rounded 710 mg.

From this analysis, it should be noted that both methods yield the same allowable mass unbalance provided the same assumptions are used. A key discrepancy arises if one in reporting the allowable unbalance moment. This requires that one understands whether U'_{per} is reported per ISO 1940 or if a value more typical of standard engineering practice such as U_{bal} is used.

C.2.3 Balance Test Results

Implementation of the balance procedure is reflected in the test rig with Rev A VSCMG photograph in Fig. C.2(a). Here one can see that a supporting L-bracket holding the VSCMG wheel assembly (i.e. the containment bowl, carbon fibre rotor, drive shaft, and motor) is mounted to four legs. These legs are connected to linear force transducers which help precisely identify the axial forces of the system while the rotor rotates. From it and defined measurements inserted into the program, the balancing machine (reflected in Fig. C.2(b)) uses the difference in forces to determine imbalance of the wheel. In addition when mass changes are made and re-tested, the machine can accurately predict where to add mass to

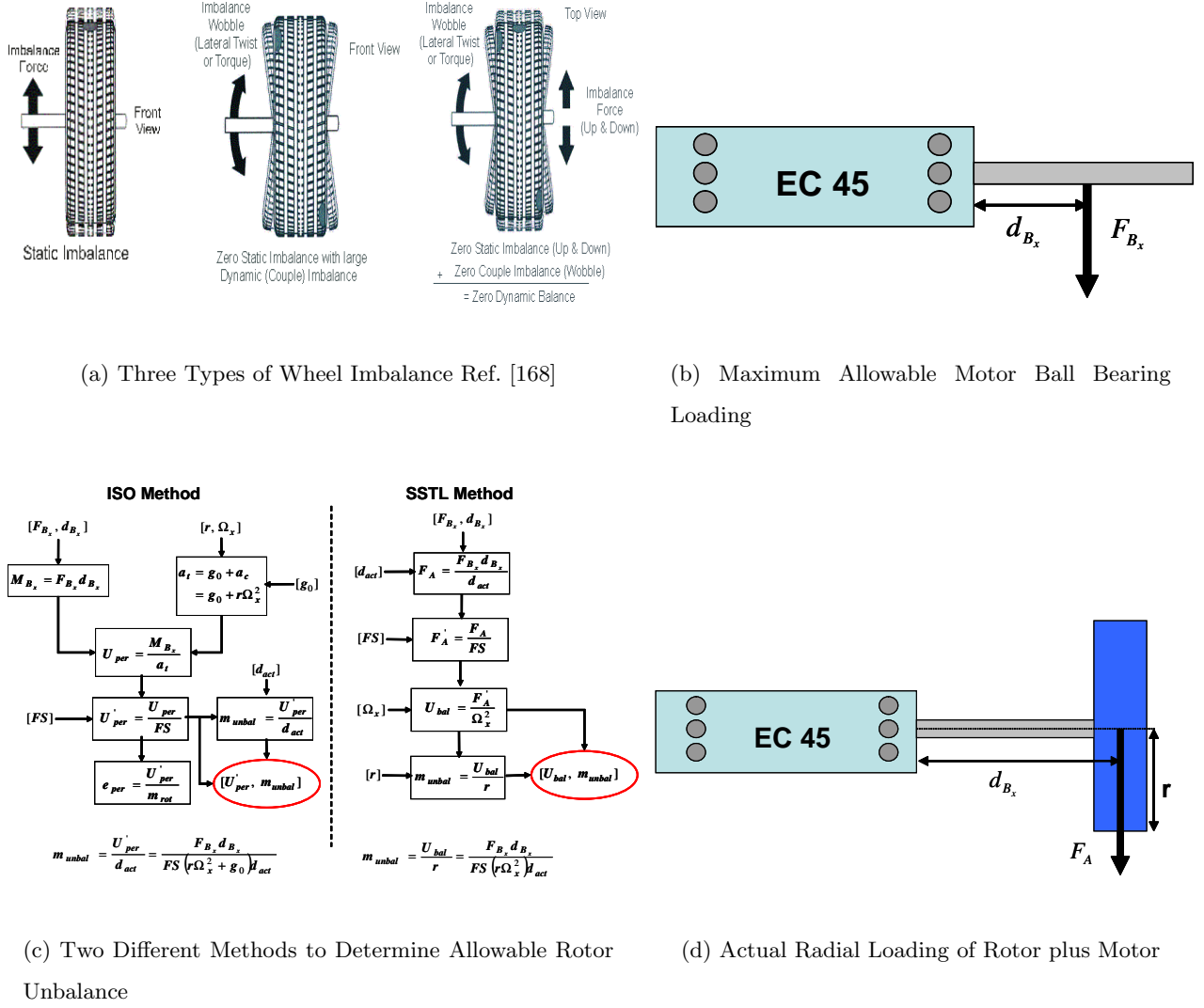


Figure C.1: Preliminary Rotor Balancing Concepts and Requirements

combat both static and dynamic unbalance. It should be noted here that there is typically more vibration in wheel rotors at lower speeds, thus as the wheel spins faster, its dynamic balance typically improves unless undergoing vibrational modes. This is akin to the improved ride over dirt road bumps when an automobile speed is increased. The bulk of time spent in balance testing lies in configuring the equipment. Once configured, the machine is calibrated. Calibration involves taking an initial unbalance measurement, then adding (or subtracting) mass from the system at known locations and in known quantities. The machine then reports this imbalance. Then, an undefined amount of mass is added to a location unbeknownst to the system. It then fairly accurately identifies the imbalance. Now, these additional masses are removed. Interestingly, blue tack is actually the best method to add this temporary mass

as it is easy to add and delete. Always keeping the maximum speed constant for balance measuring, the equipment is then iteratively run where the machine gives rotational locations to add mass and then using the actual masses, is added to determine the mass and location for additional mass. Entering mass values involves using an accurate scale to get accurate additional masses.

In the case of Carbon Fibre rotor balancing (as opposed to Aluminium wheels which typically use small set screws threaded into drilled holes for controlled mass addition), mass either needs to be attached (glued preferably to the inner radius such that rotation pushes it against its inner wall) or shaved from the structure as drilled holes disrupt the uni- and multi-directional rigidity of the composite structure.

For Rev A, mass was glued. It took four iterations of assessment to reach an accurate state of static and dynamic imbalance based on balancing at 5000 RPM. A summary of this imbalance is illustrated in Figure C.2(c). This figure shows a static imbalance of 4.03 mg and average dynamic imbalance of 37.45. Recall that the requirement was for 710 mg from the given requirements.

Further balancing was also conducted up to 9000 RPM in which the balance state did greatly improve as predicted (the static unbalance was 2.12 mg and dynamic unbalance 27.5 mg). Here one should note that the test equipment employed can only be used up to 14000 RPM. This is acceptable for the normal development of ESACS, but for future operation (perhaps in Rev B or Rev C), which will be primarily used in the 40000 RPM range, at least one test day on a faster capability machine should be completed in order to determine if there is any Carbon Fibre rotor deformation at high speeds which may impact the balance.

C.3 Sensor Calibration

Two sets of sensors fundamental to the operation of the energy charge/discharge system are those of the supply and the load. These sensors measure the voltage and current of each of these sensors. The voltage is measured through two resistor voltage dividers (included in the SSC FES board from Chapter 7), whereas the current is measured via one of two Integrated Circuit (IC) current sensor chips.

Calibrating the voltage dividers occurred in three stages. First, the rounded magnitude of the resistances of each resistor was employed in a ratio multiplied by the measured voltage to

determine the output potential. However, measurements calibrated this way were somewhat errant. Next, to correct this problem, the circuit was dismantled and these resistors were accurately measured with the resistance function of a hand-held digital multi-meter. This action slightly improved the results, but as it turns out, this change did not capture all the resistance between the voltage dividers, their measured inputs, and the computer output. For this reason, a third and final approach was taken which was the most accurate method implemented. Herein, known voltages were input to the system via a power supply (which itself was connected to a Digital Multi-Meter (DMM)), measured by the target computer, then transmitted to the ground host computer. This method involved turning the supply on after the scenario was started on XPC Target. Interestingly, the resulting data accurately captured the switch on of the power supply as well as the calibration value. Using several different inputs, a calibration curve was formed for both the supply and load. Then a linear curve was fit to the calibration data via a least-squares curve fitting process. The ensuing calibration curves are included as Figure C.3(a). After this calibration step, these measurements were found to be quite accurate. However, it was deemed that the currents should also be calibrated via this method after several errors were found in data analysis using wrong calibration values (a mistake in using the initial calibration ratio reported in the specification sheet for the sensor was found. This value was unravelled from the test data, then a generic ratio was used. However, this ratio still contained errors). Since these values seemed in error, the process turned to making a current-to-measured voltage calibration curve. The initial linear calibration curves vastly improved the quantities for both measurements. Thus, the power values of the supply and load improved greatly after this correction. However, in both curves, the initial data yielded a single outlier point at a high voltage that didn't follow the linear fit from the other nine points. In each case, this rogue point was initially cut. The new calibration ratios were used, but these values still contained error. It was discovered these errors stemmed from the region of error between the rogue point and the curve fit from calibration. For this reason, several more calibration data points were collected in this region and added to the curve. The data for each case was now fit to the second order curves shown in Figure C.3(b). Once the new second order calibration curve was employed for both the supply and load currents, the measured values yielded much cleaner results for calibrating supply and load voltage.

Here one should note that the calibrations of both the voltage dividers and current sensors were found by inputting different power supply voltages first at the supply leads (for the

supply measurement) and then at the motor leads (for the load measurement). The latter of these was used to get the load to turn on. The power supply was adjusted in increments of 4V (i.e. from 8-12-16-20-24-28-32-36-40-44-48 V) for each case. Although this idea is intuitive for the voltage calibration, it actually worked well for current sensing wherein the DMM was added in series to the power supply to accurately measure the current. This success occurred since the light-bulbs of the load increased current when voltage increased as bulb resistance remained constant. This meant that increasing input voltage also increased current usage, which was the goal. That is, the current measurement calibration required that different current values in the circuit be translated in to computer voltages. Interestingly, the region of non-linearity occurred when operating the current sensors in the 40+ V region. This makes sense as the data sheet for the current sensors claims the sensors' operating range to be 3-36V. It appears that this range is a conservative range in which the calibration is linear, although the sensors can operate outside it fairly effectively once the second order calibration curve has been determined.

C.4 Additional Test Results

The results of the experiments help demonstrate the effectiveness of the technology. Understanding these results is best when presented in a logical order as is done here. First, a test matrix is given which summarizes the test runs and the key settings used during each of these runs. Then, the test procedure followed during each run to exercise the test article and ultimately generate results data is briefly addressed. Using this test procedure to generate data, the actual results are broken into results relating to power parameters (voltage and current of the motor, power supply, and load) and results relating to attitude parameters (i.e. slew angle time history as derived from roll, pitch, and yaw Euler angle rates). Within each of these two divisions of data, summary tables and time plots of the key parameters as well as software processes followed and critical equations are presented. Taken as a whole, these sections help organize the experimental data for further analysis in this section's sequel.

C.4.1 Test Matrix

In order to test the performance of the initial prototype in an integrated system, a test matrix was constructed to exercise variable conditions and detect effects of these different conditions. Also, a few strategic test runs were repeated multiple times to demonstrate repeatability in

the results. This test matrix is given in Table C.2. The coding of this matrix is broken into the test number (33 test runs in all) in the first column, a three digit coded pattern in the second column, and the actual values of each coded digit in the last three columns. Note that the first digit corresponds to subsystem loadings (1 = no load, 2 = small load of coloured 12-V LEDs, and 3= bigger load of eight 20-W, 12-V light bulbs wired in series), the second digit corresponds to command gimbal rate voltages ($3V = 5.88 \text{ deg/s}$, $5V = 9.80 \text{ deg/s}$), and the third digit corresponds to wheel speed command settings (5000, 7000, or 9000 RPM). This matrix helped organize the test runs into a logical sequence to eliminate as many errors as possible in a small sample space.

Table C.2: Experiment Test Matrix

Run	Pattern	Bus Condition	(V) Command Gimbal Rate	(RPM) Command Wheel Speed
1	213	1	3.0	9000
2	111	-1	3.0	5000
3	122	-1	5.0	7000
4	221	1	5.0	5000
5	212	1	3.0	7000
6	223	1	5.0	9000
7	123	-1	5.0	9000
8	222	1	5.0	7000
9	112	-1	3.0	7000
10	113	-1	3.0	9000
11	211	1	3.0	5000
12	121	-1	5.0	5000
13	313	1+	3.0	9000
14	321	1+	5.0	5000
15	312	1+	3.0	7000
16	323	1+	5.0	9000
17	322	1+	5.0	7000
18	311	1+	3.0	5000
19	123	-1	5.0	9000
20	111	-1	3.0	5000
21	123	-1	5.0	9000
22	111	-1	3.0	5000
23	223	1	5.0	9000
24	211	1	3.0	5000
25	123	-1	5.0	9000
26	111	-1	3.0	5000
27	211	1	3.0	5000
28	211	1	3.0	5000
29	223	1	5.0	9000
30	223	1	5.0	9000
31	323	1+	5.0	9000
32	323	1+	5.0	9000
33	323	1+	5.0	9000

C.4.2 Test Run Procedure

To best control the testing environment in implementing the test run settings mentioned in Table C.2, a checklist procedure was identified and implemented. The tests were run in three groups, the first of which used single repetition runs of all the choices in random order for the cases of no load and small load. However, a quick look data analysis showed that the small load runs had a much smaller effect than predicted (due to its 0.8W power consumption), thus a larger load was procured. Then, all the small load runs were re-accomplished with this bigger load in the second test set. Finally, the third group of runs was conducted in which three replications of the two extreme cases in command wheel speed and command gimbal rate (5000 RPM, 3V and 9000 RPM, 5V) were accomplished for the no load and small load cases followed by three replications for the big load with the 9000 RPM, 5V settings. The aim herein was to minimize the number of tests while maximizing the test utility. A MATLAB XPC Target Graphical User Interface was used to run the scenarios from the host computer. Next, a key attribute of these tests is presented – data marking recorded attitude data.

C.4.3 Data Marking

During testing, IMU data was recorded on a portable laptop kept on-board the air-bearing structure. In order to maintain the mechanical air-bearing balance as accurately as possible once the laptop was placed, this recorded data was kept in a continuous log during each group rather than continuously, manually downloading the data after each run. The drawback of this approach is that it is very difficult to link data streams of collected OBC data with the on-board laptop data as such data is recorded on systems with different time stamps. To solve this problem, each scenario was “marked” by tapping three times on one of the ballast posts on the air-bearing structure at the appropriate step in the test run procedure to correlate IMU data with the OBC-acquired data. These three taps showed up clearly in the z-axis acceleration z_{dd} data as three grouped spikes as depicted in Figure C.3(c). Simultaneously, the time was recorded via a wristwatch to log the tapping time in real time. From the wrist-watch time and the IMU time, one can determine the timing delay between the on-board computer and the wrist-watch time. In addition, both the test start time and test stop times were also recorded from the wrist watch such that the OBC data could also be synchronized with the IMU data. Note the time shift in Figure C.3(c) was found by comparing the “whack” or “tapping” time logged from the watch with the spikes in the IMU acceleration data for

the Z-channel.

C.4.4 Preliminary Attitude Performance Data

Similarly to the power performance data presented in Appendix B, the preliminary attitude data can be best captured by test run in tabular format. Recall that this data is inconclusive and slew performance will be further studied in follow-on efforts. However, it is valuable for a glimpse into the anticipated performance of a VSCMG at reduced ESACS maximum speeds. Table C.3 presents the slew maneuver time, t_f , and maneuver angle, θ_f , captured from the Euler rotational angle time history when integrating the roll, pitch, and yaw rates and converting these angles to an Euler axis plus rotation angle representation at each time step. This table also shows the time delay between the Inertial Measurement Unit (IMU) and wrist-watch time used to synchronize key events (scenario start, scenario stop) via the data marking process described earlier. In addition, the estimated roll, pitch, and yaw biases are listed as well as the peak gimbal motor speed (pre-gearing) and resulting gimbal rate after gearing are presented in Table C.3.

Table C.3: Selected Experimental Results: Attitude Performance Data

Test Run	(s) Man. Time	(deg) Man. Angle	(deg/s) Man. Rate	(s) Time Delay	(rad/s) Roll Bias	(rad/s) Pitch Bias	(rad/s) Yaw Bias	(RPM) Gimbal Speed	(deg/s) Gimbal Rate
6	9.45	16.76	1.77	26.9	-0.0046	-0.0034	-0.005	7536.6	9.85
7	9.57	9.93	1.04	29.2	-0.0046	-0.0035	-0.005	7543.9	9.86
16	7.75	24.65	3.18	29.0	-0.0046	-0.0034	-0.005	7543.9	9.86
19	9.69	39.09	4.03	-2.5	-0.0046	-0.0038	-0.005	7522.0	9.83
21	9.72	38.88	4.00	-2.5	-0.0045	-0.0035	-0.005	7478.0	9.77
23	9.67	37.14	3.84	-2.3	-0.0046	-0.0034	-0.005	7492.7	9.79
25	9.10	19.43	2.02	26.9	-0.0047	-0.0034	-0.005	7492.7	9.79
3	11.82	22.70	1.92	27.6	-0.0045	-0.0038	-0.005	7558.6	9.88
8	11.68	7.78	0.67	29.1	-0.0045	-0.0034	-0.005	7522.0	9.83
17	7.98	22.74	2.85	29.2	-0.0046	-0.0034	-0.005	7543.9	9.86
4	2.97	6.36	2.14	31.0	-0.0045	-0.0035	-0.005	7631.8	9.97
12	2.91	2.48	0.85	48.9	-0.0045	-0.0035	-0.005	7507.3	9.81

As with power data, this data only tells part of the story. Plotted data from the test runs help further capture the performance. First, figure 8.4(a) shows the time history of the Euler axis for one of the runs. This is followed by figure C.3(d) which shows the raw roll, pitch, and yaw rate data prior to bias adjustment and subsequent integration, which yields the roll,

pitch yaw angles converted to euler axis and rotation angle. Closely associated with this plot is figure C.3(e) which contrasts what happens when the biases are and are not eliminated.

Next, the key equations used in this process to get from roll, pitch, and yaw derivatives to maneuver angle and time are important to understand. Having noted that the bias selection is an interactive process whereby each rate is integrated and plotted, followed by iteratively setting gains on the rate signal to zero centered angular motion when the structure only oscillates about zero (i.e. such that there is not a ramp of the angular sinusoid if the body's motion is oscillating about this fixed angle). The integrated values of these biases found by hand, then converted to Euler axis and roll angle. In other words, before conversion, calibrated Euler angles are available that are then transformed to Euler axis and angle. The conversion is conducted in two steps: first the Euler angles are translated to quaternions, then the quaternions are transformed. Then, the third cycle freewheel times plus delay times are used to synchronize the chopping of the Euler rotation angle during this third cycle freewheel time period. The chapped angle values at the beginning and end are captured and the difference found to determine the maneuver angle θ_f and the time period of this third cycle freewheel period is used as t_f .

As one can see, the primary calculation to present here in relation to the output parameters is that of converting Euler angles to Euler axis and rotation angle via quaternions. This was implemented as follows

$$c_1 = \cos\left(\frac{\phi}{2}\right) \quad c_2 = \cos\left(\frac{\theta}{2}\right) \quad c_3 = \cos\left(\frac{\psi}{2}\right) \quad (C.2)$$

$$s_1 = \sin\left(\frac{\phi}{2}\right) \quad s_2 = \sin\left(\frac{\theta}{2}\right) \quad s_3 = \sin\left(\frac{\psi}{2}\right) \quad (C.3)$$

$$q_1 = c_1 c_2 c_3 + s_1 s_2 s_3 \quad q_2 = c_1 c_2 s_3 - s_1 s_2 c_3 \quad (C.4)$$

$$q_3 = c_1 s_2 c_3 + s_1 c_2 s_3 \quad q_4 = s_1 c_2 c_3 - c_1 s_2 s_3 \quad (C.5)$$

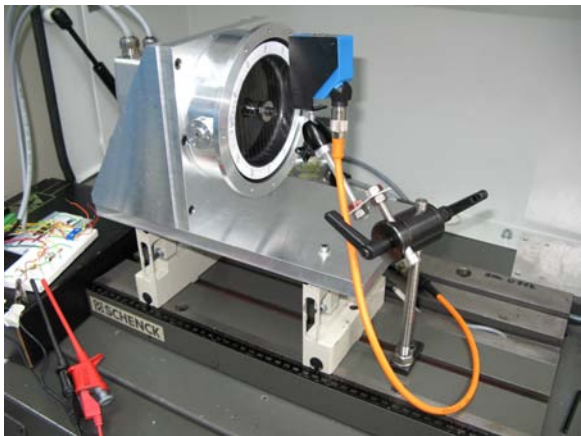
$$q = [q_1 \quad q_2 \quad q_3 \quad q_4]^T \quad (C.6)$$

$$\alpha = 2 \cos^{-1}(q_1) \quad s_a = \sin\left(\frac{\alpha}{2}\right) \quad (C.7)$$

$$e_1 = \frac{q_2}{s_a} \alpha \quad e_2 = \frac{q_3}{s_a} \alpha \quad e_3 = \frac{q_4}{s_a} \alpha \quad (C.8)$$

where α is the euler rotation angle and ϕ , θ , and ψ are the input roll, pitch, and yaw angles, respectively. Also, it is handy to recall how the calculations of gimbal rate and gimbal motor speed are found as presented in Chapter 7. First, the gimbal motor speed has been recorded in units of rad/s . This value is first converted to RPM by multiplying by $\frac{60}{2\pi}$. Then, this motor speed in RPM is converted to gimbal geared output speed by dividing the gimbal

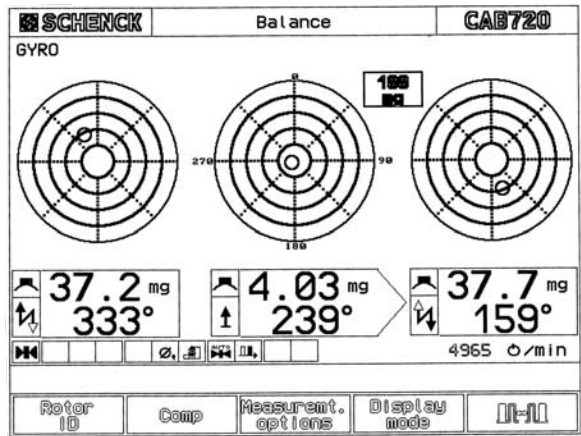
motor speed by the gear ratio (4592:1). This, then, yields both gimbal motor parameters presented in the table.



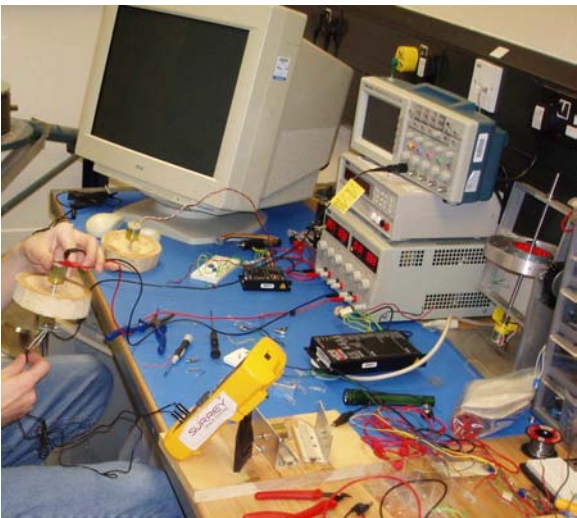
(a) Rotor on Balancing Test Rig



(b) Balancing Machine Software Interface

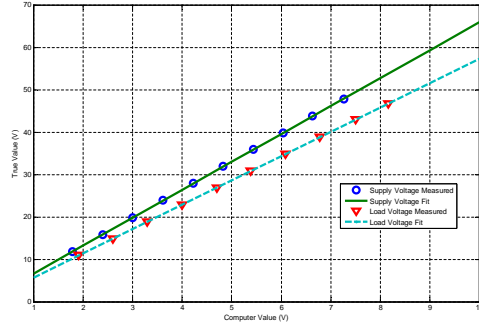


(c) Balancing Data

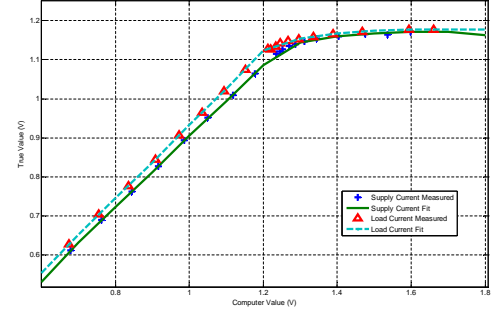


(d) Early Developmental Bench Testing

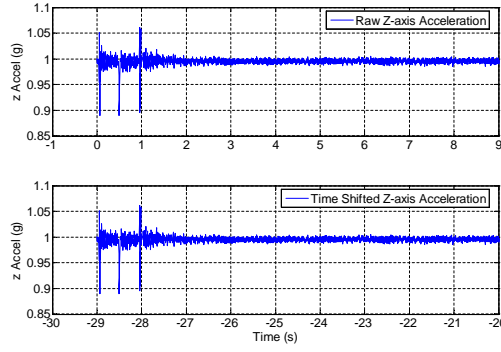
Figure C.2: Rotor Balancing and Other Developmental Testing



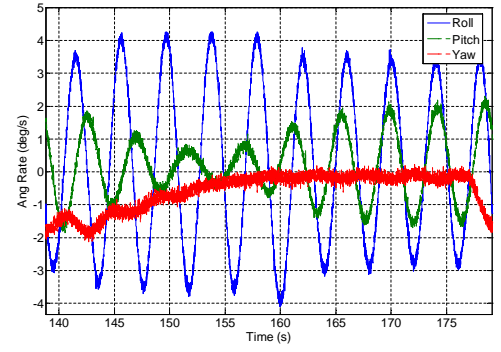
(a) Supply, Load Voltage Calibration Curves



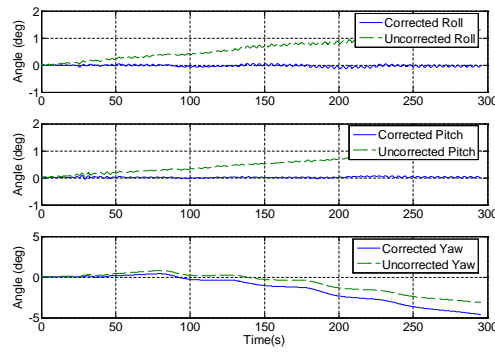
(b) Supply, Load Current Calibration Curves



(c) Z-axis Accel With and Without Time Delay



(d) Raw Roll, Pitch, and Yaw Rates



(e) RPY Corrected-Uncorrected Bias Comparison

Figure C.3: Power and Attitude Calibration Curves

Appendix D

Attitude and Power Equations

This appendix presents the derivation of the attitude and power tracking dynamics. Much of these derivations is summarized from refs. [153] and [107]. The discussion begins with a few preliminary mathematical definitions. Then, the kinematics, dynamics, simplified dynamics, dynamics summary, stable attitude tracking controller, attitude equation proof, practical small satellite attitude assumptions, and numerical supplement are addressed. These sections provide foundation support to the attitude equations given in Chapter 4.

D.1 Kinematics

One can represent the spacecraft orientation using Euler parameters corresponding to the transformation from the inertial reference frame, \mathcal{N} , to the vehicle body frame, \mathcal{B} , as:

$$\beta \triangleq \begin{bmatrix} \beta_0 \\ \beta_1 \\ \beta_2 \\ \beta_3 \end{bmatrix} \quad (\text{D.1})$$

Defining the operator $q(\beta)$ as:

$$q(\beta) \triangleq \begin{bmatrix} -\beta_1 & -\beta_2 & -\beta_3 \\ \beta_0 & -\beta_3 & \beta_2 \\ \beta_3 & \beta_0 & -\beta_1 \\ -\beta_2 & \beta_1 & \beta_0 \end{bmatrix} \quad (\text{D.2})$$

then the spacecraft's kinematic differential equation is:

$$\dot{\beta} \triangleq \frac{1}{2}q(\beta)\omega \quad (\text{D.3})$$

D.2 Attitude Dynamics

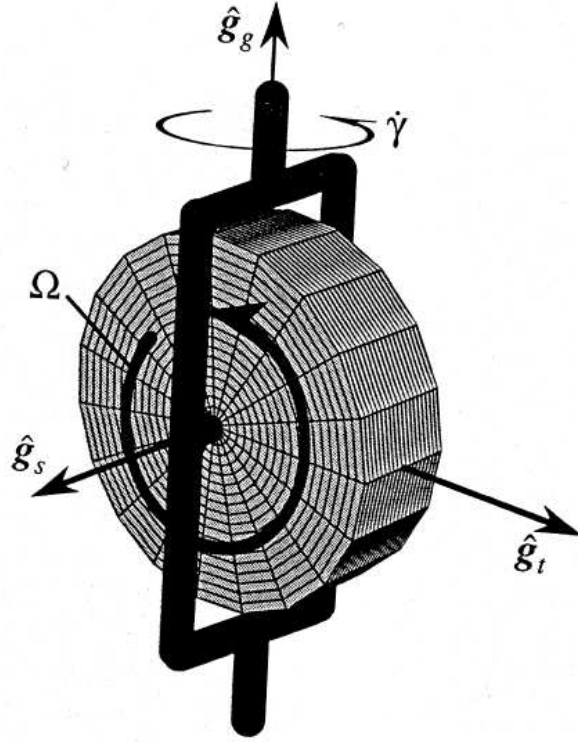


Figure D.1: Variable Speed Control Moment Gyro

In order to derive the dynamic equations of motion presented in Chapter 4, one should first analyze the motion of a single VSCMG and then extend the results to the multiple VSCMG case. This is done by deriving the angular momentum first and then finding the torque acting on the spacecraft from the angular momentum.

The relevant bodies for this 1-VSCMG system are defined to be the platform, P , which is the spacecraft without VSCMGs, the flywheel wheel, W , the gimbal structure, G , the reaction body, B , which is the portion of P that reacts to the motion of the VSCMG actuator (i.e. bodies W plus G), and the entire system, SYS , which includes P , W , and G . Each body has an orthogonal coordinate reference frame at its mass center (P^* , W^* , G^* , B^* , and SYS^*). For instance, Figure D.1 illustrates the G -frame of a VSCMG, with its axes: \hat{g}_s , \hat{g}_t , and \hat{g}_g ,

which are defined as the wheel spin-axis, the transverse output axis, and the gimbal axis, all three of which are assumed to intersect at the mass center of both the W -frame and the G -frame. It is assumed both the wheel and gimbal support structure are distributed such that the G -frame axis are principle axes for both G and W , thus the W frame is aligned with G . The wheel spin axis spins along \hat{g}_s . The N -frame is defined to be a sufficiently inertial reference frame which does not rotate with the system.

Having defined the key bodies, mass centers, and coordinate reference frames, the next step is to define relevant inertia matrices, angular velocities, and other factors. Inline with the principal axis theorem, the angular momentum of the system about an arbitrary point O is found as the sum of each body angular momentum about its mass center and each body point mass angular momentum about point O .

$$\vec{h}^{SYS/O} = \vec{h}^{P/P^*} + \vec{h}^{P^*/O} + \vec{h}^{G/G^*} + \vec{h}^{G^*/O} + \vec{h}^{W/W^*} + \vec{h}^{W^*/O} \quad (D.4)$$

One can now combine the angular momenta that rotates together as the spacecraft body to counteract actuator motion within the system, these terms constitute the platform about its mass center, the platform point mass inertia about O , the wheel point mass inertia about O , and the gimbal support structure about O .

$$\vec{h}^{B/O} = \vec{h}^{P/P^*} + \vec{h}^{P^*/O} + \vec{h}^{G^*/O} \quad (D.5)$$

Likewise, the associated inertia for body B , also known as the spacecraft inertia, is found as $[\mathbf{I}^{SC/O}]_B$. This represents the spacecraft body inertia with the wheels and gimbals locked.

Assume $\hat{g}_s, \hat{g}_t, \hat{g}_g$ are central principal axes of bodies W and G for point O . Then the inertia matrices of body G about G^* and body W about G^* , both written as components in \mathcal{G} are

$$[\mathbf{I}^{G/G^*}]_G = \begin{bmatrix} \mathbf{I}_{G_s} & 0 & 0 \\ 0 & \mathbf{I}_{G_t} & 0 \\ 0 & 0 & \mathbf{I}_{G_g} \end{bmatrix} \quad (D.6)$$

$$[\mathbf{I}^{W/G^*}]_G = \begin{bmatrix} \mathbf{I}_{W_s} & 0 & 0 \\ 0 & \mathbf{I}_{W_t} & 0 \\ 0 & 0 & \mathbf{I}_{W_g} \end{bmatrix} \quad (D.7)$$

Now, let \mathbf{L}_{BG} represent the coordinate transformation from \mathcal{G} to \mathcal{B} and $\mathbf{L}_{GB} = \mathbf{L}_{BG}^T$ be the coordinate transformation from \mathcal{B} to \mathcal{G} . Additionally, per the angular velocity addition

theorem

$$\vec{\omega}_{G/N} = \vec{\omega}_{G/B} + \vec{\omega}_{B/N} \quad (\text{D.8})$$

$$\vec{\omega}_{W/N} = \vec{\omega}_{W/G} + \vec{\omega}_{G/B} + \vec{\omega}_{B/N} \quad (\text{D.9})$$

where the gimbal structure rotates about G^* and the \hat{g}_g - axis with angular speed $\dot{\delta}$. The wheel rotates about \hat{g}_s with angular speed Ω . Thus,

$$\vec{\omega}_{G/B} = \dot{\delta} \hat{g}_g \quad (\text{D.10})$$

$$\vec{\omega}_{W/G} = \Omega \hat{g}_s \quad (\text{D.11})$$

Expressing these two quantities in \mathcal{G}

$$(\vec{\omega}_{G/B})_G = \begin{bmatrix} 0 \\ 0 \\ \dot{\delta} \end{bmatrix} \quad (\text{D.12})$$

$$(\vec{\omega}_{W/G})_G = \begin{bmatrix} \Omega \\ 0 \\ 0 \end{bmatrix} \quad (\text{D.13})$$

yields

$$(\vec{\omega}_{W/B})_G = \begin{bmatrix} \Omega \\ 0 \\ \dot{\delta} \end{bmatrix} \quad (\text{D.14})$$

Next,

$$(\vec{\omega}_{W/N})_B = L_{BG} (\vec{\omega}_{W/B})_G + (\vec{\omega}_{B/N})_B \quad (\text{D.15})$$

$$(\vec{\omega}_{G/N})_B = L_{BG} (\vec{\omega}_{G/B})_G + (\vec{\omega}_{B/N})_B \quad (\text{D.16})$$

Thus,

$$(\vec{\omega}_{W/N})_B = L_{BG} (\vec{\omega}_{W/B})_G + (\vec{\omega}_{B/N})_B = L_{BG} \begin{bmatrix} \Omega \\ 0 \\ \dot{\delta} \end{bmatrix} + (\vec{\omega}_{B/N})_B \quad (\text{D.17})$$

$$(\vec{\omega}_{G/N})_B = L_{BG} (\vec{\omega}_{G/B})_G + (\vec{\omega}_{B/N})_B = L_{BG} \begin{bmatrix} 0 \\ 0 \\ \dot{\delta} \end{bmatrix} + (\vec{\omega}_{B/N})_B \quad (\text{D.18})$$

Now,

$$[\mathbf{I}^{G/G^*}]_B = L_{BG} [\mathbf{I}^{G/G^*}]_G L_{BG}^T \quad (\text{D.19})$$

$$[\mathbf{I}^{W/G^*}]_B = L_{BG} [\mathbf{I}^{W/G^*}]_G L_{BG}^T \quad (\text{D.20})$$

Now, one can find the angular momentum of the system about point O using the inertial angular velocity of body B in N written as components in the B -frame, $(\vec{\omega}_{B/N})_B$, and the inertial angular velocity of bodies W and G in the B -frame as $(\vec{\omega}_{G/N})_B$ and $(\vec{\omega}_{W/N})_B$, respectively. This yields

$$\left(\vec{h}^{\text{sys/O}}\right)_B = [\mathbf{I}^{\text{sc/O}}]_B (\vec{\omega}_{B/N})_B + [\mathbf{I}^{G/G^*}]_B (\vec{\omega}_{G/N})_B + [\mathbf{I}^{W/W^*}]_B (\vec{\omega}_{W/N})_B \quad (\text{D.21})$$

Now, the total external torque of the system about point O with one VSCMG is found from the angular momentum as

$$\overline{\mathbf{N}}_d^{\text{sys/O}} = N \frac{d}{dt} \left(\vec{h}^{\text{sys/O}} \right) = {}^B \frac{d}{dt} \left(\vec{h}^{\text{sys/O}} \right) + (\vec{\omega}_{B/N})_B \times \vec{h}^{\text{sys/O}} \quad (\text{D.22})$$

Expanding this result in terms of defined matrices using two skew symmetric matrices, $\tilde{\omega}_{B/N}$, and $\tilde{\omega}_{G/B}$, leaves

$$\begin{aligned} \overline{\mathbf{N}}_d^{\text{sys/O}} &= N \frac{d}{dt} \left(\vec{h}^{\text{sys/O}} \right) = {}^B \frac{d}{dt} \left(\vec{h}^{\text{sys/O}} \right) + (\vec{\omega}_{B/N})_B \times \vec{h}^{\text{sys/O}} = [\mathbf{I}^{\text{sc/O}}]_B \left(\dot{\vec{\omega}}_{B/N} \right)_B \\ &+ \left(L_{BG} \begin{bmatrix} I_{G_s} & 0 & 0 \\ 0 & I_{G_t} & 0 \\ 0 & 0 & I_{G_g} \end{bmatrix} \begin{bmatrix} 0 \\ 0 \\ \ddot{\delta} \end{bmatrix} \right) + \left(L_{BG}(\tilde{\delta}) \begin{bmatrix} I_{G_s} & 0 & 0 \\ 0 & I_{G_t} & 0 \\ 0 & 0 & I_{G_g} \end{bmatrix} L_{BG}^T (\vec{\omega}_{B/N})_B \right) \\ &+ \left(L_{BG} \begin{bmatrix} I_{G_s} & 0 & 0 \\ 0 & I_{G_t} & 0 \\ 0 & 0 & I_{G_g} \end{bmatrix} (-\tilde{\delta}) L_{BG}^T (\vec{\omega}_{B/N})_B \right) + \left(L_{BG} \begin{bmatrix} I_{G_s} & 0 & 0 \\ 0 & I_{G_t} & 0 \\ 0 & 0 & I_{G_g} \end{bmatrix} L_{BG}^T (\dot{\vec{\omega}}_{B/N})_B \right) \\ &+ \left(L_{BG}(\tilde{\delta}) \begin{bmatrix} I_{W_s} & 0 & 0 \\ 0 & I_{W_t} & 0 \\ 0 & 0 & I_{W_g} \end{bmatrix} \begin{bmatrix} \Omega \\ 0 \\ \dot{\delta} \end{bmatrix} \right) + \left(L_{BG} \begin{bmatrix} I_{W_s} & 0 & 0 \\ 0 & I_{W_t} & 0 \\ 0 & 0 & I_{W_g} \end{bmatrix} \begin{bmatrix} \dot{\Omega} \\ 0 \\ \ddot{\delta} \end{bmatrix} \right) \\ &+ \left(L_{BG}(\tilde{\delta}) \begin{bmatrix} I_{W_s} & 0 & 0 \\ 0 & I_{W_t} & 0 \\ 0 & 0 & I_{W_g} \end{bmatrix} L_{BG}^T (\vec{\omega}_{B/N})_B \right) + \left(L_{BG} \begin{bmatrix} I_{W_s} & 0 & 0 \\ 0 & I_{W_t} & 0 \\ 0 & 0 & I_{W_g} \end{bmatrix} (-\tilde{\delta}) L_{BG}^T (\vec{\omega}_{B/N})_B \right) \\ &+ \left(L_{BG} \begin{bmatrix} I_{W_s} & 0 & 0 \\ 0 & I_{W_t} & 0 \\ 0 & 0 & I_{W_g} \end{bmatrix} L_{BG}^T (\dot{\vec{\omega}}_{B/N})_B \right) + \tilde{\omega}_{B/N} \mathbf{L}_{BG} \begin{bmatrix} I_{G_s} & 0 & 0 \\ 0 & I_{G_t} & 0 \\ 0 & 0 & I_{G_g} \end{bmatrix} \begin{bmatrix} 0 \\ 0 \\ \dot{\delta} \end{bmatrix} \\ &+ \tilde{\omega}_{B/N} \mathbf{L}_{BG} \begin{bmatrix} J_s & 0 & 0 \\ 0 & J_t & 0 \\ 0 & 0 & J_g \end{bmatrix} \mathbf{L}_{BG}^T \tilde{\omega}_{B/N} + \tilde{\omega}_{B/N} \mathbf{L}_{BG} \begin{bmatrix} I_{W_s} & 0 & 0 \\ 0 & I_{W_t} & 0 \\ 0 & 0 & I_{W_g} \end{bmatrix} \begin{bmatrix} \Omega \\ 0 \\ \dot{\delta} \end{bmatrix} + \tilde{\omega}_{B/N} [\mathbf{I}_{sc}]_B (\vec{\omega}_{B/N})_B \end{aligned}$$

D.2.1 Simplifying the Torque Equation

Using the VSCMG unit vector, combined unit vector, and combined inertia matrices from [12, 107], one can define the following terms

$$\begin{aligned}
 \mathbf{B}_1 \begin{bmatrix} \ddot{\delta}_1 \\ \ddot{\delta}_2 \\ \dots \\ \ddot{\delta}_n \end{bmatrix} &= \left(\sum_{i=1}^n L_{BG_i} [\mathbf{I}^{G_i/G_i^*}]_{G_i} \begin{bmatrix} 0 \\ 0 \\ \ddot{\delta}_i \end{bmatrix} \right) = \mathbf{G}_g \mathbf{I}_{G_{gd}} \\
 \mathbf{B}_2 \begin{bmatrix} \ddot{\delta}_1 \\ \ddot{\delta}_2 \\ \dots \\ \ddot{\delta}_n \end{bmatrix} &= \left(\sum_{i=1}^n L_{BG_i} [\mathbf{I}^{W_i/G_i^*}]_{G_i} \begin{bmatrix} 0 \\ 0 \\ \ddot{\delta}_i \end{bmatrix} \right) = \mathbf{G}_g \mathbf{I}_{W_{gd}} \\
 \mathbf{D}_1 \begin{bmatrix} \dot{\delta}_1 \\ \dot{\delta}_2 \\ \dots \\ \dot{\delta}_n \end{bmatrix} &= \left(\sum_{i=1}^n L_{BG_i}(\tilde{\delta}_i) [\mathbf{I}^{W_i/G_i^*}]_{G_i} \left(\begin{bmatrix} \Omega_i \\ 0 \\ \dot{\delta}_i \end{bmatrix} + L_{G_i B} (\vec{\omega}_{B/N})_B \right) \right) \\
 &= \mathbf{G}_t \mathbf{I}_{W_{sd}} \Omega_d + (\mathbf{G}_t \mathbf{G}_{sd}^T \mathbf{I}_{W_{sm}} - \mathbf{G}_s \mathbf{G}_{td}^T \mathbf{I}_{W_{tm}}) \omega_d \\
 \mathbf{D}_2 \begin{bmatrix} \dot{\delta}_1 \\ \dot{\delta}_2 \\ \dots \\ \dot{\delta}_n \end{bmatrix} &= (\tilde{\vec{\omega}}_{B/N})_B \left(\sum_{i=1}^n L_{BG_i} \left([\mathbf{I}^{G_i/G_i^*}]_{G_i} + [\mathbf{I}^{W_i/G_i^*}]_{G_i} \right) \begin{bmatrix} 0 \\ 0 \\ \dot{\delta}_i \end{bmatrix} \right) = \tilde{\omega} \mathbf{G}_g \mathbf{J}_{gd} \\
 \mathbf{D}_3 \begin{bmatrix} \dot{\delta}_1 \\ \dot{\delta}_2 \\ \dots \\ \dot{\delta}_n \end{bmatrix} &= \left(\sum_{i=1}^n L_{BG_i}(\tilde{\delta}_i) [\mathbf{I}^{G_i/G_i^*}]_{G_i} L_{G_i B} - L_{BG_i} \left([\mathbf{I}^{G_i/G_i^*}]_{G_i} + [\mathbf{I}^{W_i/G_i^*}]_{G_i} \right) (\tilde{\delta}_i) L_{G_i B} \right) (\vec{\omega}_{B/N})_B \\
 &= [(\mathbf{G}_t \mathbf{G}_{sd}^T \mathbf{I}_{G_{sm}} - \mathbf{G}_s \mathbf{G}_{td}^T \mathbf{I}_{G_{tm}}) - (\mathbf{G}_t \mathbf{G}_{sd}^T \mathbf{J}_{tm} - \mathbf{G}_s \mathbf{G}_{td}^T \mathbf{J}_{sm})] \omega_d \\
 \mathbf{E} \begin{bmatrix} \dot{\Omega}_1 \\ \dot{\Omega}_2 \\ \dots \\ \dot{\Omega}_n \end{bmatrix} &= \left(\sum_{i=1}^n L_{BG_i} [\mathbf{I}^{W_i/G_i^*}]_{G_i} \begin{bmatrix} \dot{\Omega}_i \\ 0 \\ 0 \end{bmatrix} \right) = \mathbf{G}_s \mathbf{I}_{W_{sd}} \\
 \mathbf{F} \begin{bmatrix} \Omega_1 \\ \Omega_2 \\ \dots \\ \Omega_n \end{bmatrix} &= (\tilde{\vec{\omega}}_{B/N})_B \left(\sum_{i=1}^n L_{BG_i} [\mathbf{I}^{W_i/G_i^*}]_{G_i} \begin{bmatrix} \Omega_i \\ 0 \\ 0 \end{bmatrix} \right) = \tilde{\omega} \mathbf{G}_s \mathbf{I}_{W_{sd}}
 \end{aligned}$$

This yields the system dynamic motion equations

$$\begin{aligned} \left(\overline{\mathbf{N}}_d^{\text{sys/O}} \right)_B &= [\mathbf{I}^{\text{TOT/O}}]_B \left(\dot{\vec{\omega}}_{B/N} \right)_B + \left(\ddot{\vec{\omega}}_{B/N} \right)_B [\mathbf{I}^{\text{TOT/O}}]_B \left(\vec{\omega}_{B/N} \right)_B \\ &+ (\mathbf{D}_1 + \mathbf{D}_2 + \mathbf{D}_3) \begin{bmatrix} \dot{\delta}_1 \\ \dot{\delta}_2 \\ \dots \\ \dot{\delta}_n \end{bmatrix} + (\mathbf{B}_1 + \mathbf{B}_2) \begin{bmatrix} \ddot{\delta}_1 \\ \ddot{\delta}_2 \\ \dots \\ \ddot{\delta}_n \end{bmatrix} + \mathbf{E} \begin{bmatrix} \dot{\Omega}_1 \\ \dot{\Omega}_2 \\ \dots \\ \dot{\Omega}_n \end{bmatrix} + \mathbf{F} \begin{bmatrix} \Omega_1 \\ \Omega_2 \\ \dots \\ \Omega_n \end{bmatrix} \end{aligned}$$

where $[\mathbf{I}^{\text{TOT/O}}]_B = [\mathbf{I}^{\text{SC/O}}]_B + \left(\sum_{i=1}^n L_{BG_i} \left([\mathbf{I}^{G_i/G_i^*}]_{G_i} + [\mathbf{I}^{W_i/G_i^*}]_{G_i} \right) L_{G_i B} \right)$ Defining the gimbal rate, $\dot{\delta}$, gimbal acceleration, $\ddot{\delta}$, wheel speed, Ω , and wheel acceleration, $\dot{\Omega}$ as

$$\dot{\delta} = \begin{bmatrix} \dot{\delta}_1 \\ \dot{\delta}_2 \\ \dots \\ \dot{\delta}_n \end{bmatrix} \quad \ddot{\delta} = \begin{bmatrix} \ddot{\delta}_1 \\ \ddot{\delta}_2 \\ \dots \\ \ddot{\delta}_n \end{bmatrix} \quad \dot{\Omega} = \begin{bmatrix} \dot{\Omega}_1 \\ \dot{\Omega}_2 \\ \dots \\ \dot{\Omega}_n \end{bmatrix} \quad \Omega = \begin{bmatrix} \Omega_1 \\ \Omega_2 \\ \dots \\ \Omega_n \end{bmatrix} \quad (\text{D.23})$$

one can summarize the simplified equations for the vehicle dynamics as

$$\vec{h}^{\text{sys/O}} = \vec{h}^{\text{P/P}^*} + \vec{h}^{\text{P}^*/\text{O}} + \vec{h}^{\text{W/W}^*} + \vec{h}^{\text{W}^*/\text{O}} + \vec{h}^{\text{G/G}^*} + \vec{h}^{\text{G}^*/\text{O}} \quad (\text{D.24})$$

$$\overline{\mathbf{N}}_d^{\text{sys/O}} = N \frac{d}{dt} \left(\vec{h}^{\text{sys/O}} \right) \quad (\text{D.25})$$

$$\overline{\mathbf{N}}_d \triangleq \left(\overline{\mathbf{N}}_d^{\text{sys/O}} \right)_B \quad (\text{D.26})$$

$$\vec{\omega} \triangleq \left(\vec{\omega}_{B/N} \right)_B \quad (\text{D.27})$$

$$\mathbf{I}_T \triangleq [\mathbf{I}^{\text{TOT/O}}]_B = [\mathbf{I}^{\text{SC/O}}]_B + \left(\sum_{i=1}^n L_{BG_i} \left([\mathbf{I}^{G_i/G_i^*}]_{G_i} + [\mathbf{I}^{W_i/G_i^*}]_{G_i} \right) L_{G_i B} \right) \quad (\text{D.28})$$

$$\overline{\mathbf{N}}_d = \mathbf{I}_T \dot{\vec{\omega}} + \tilde{\omega} \mathbf{I}_T \vec{\omega} + \mathbf{B} \ddot{\delta} + \mathbf{D}_s \dot{\delta} + \mathbf{E} \dot{\Omega} + \mathbf{F} \Omega \quad (\text{D.29})$$

$$\mathbf{B} = \mathbf{B}_1 + \mathbf{B}_2 \quad (\text{D.30})$$

$$\mathbf{B}_1 = \mathbf{G}_g \mathbf{I}_{G_{gd}} \quad (\text{D.31})$$

$$\mathbf{B}_2 = \mathbf{G}_g \mathbf{I}_{W_{gd}} \quad (\text{D.32})$$

$$\mathbf{E} = \mathbf{G}_s \mathbf{I}_{W_{sd}} \quad (\text{D.33})$$

$$\mathbf{F} = \tilde{\omega} \mathbf{G}_s \mathbf{I}_{W_{sd}} \quad (\text{D.34})$$

$$\mathbf{D}_s = \mathbf{D}_1 + \mathbf{D}_2 + \mathbf{D}_3 \quad (\text{D.35})$$

$$\mathbf{D}_1 = \mathbf{G}_t \mathbf{I}_{W_{sd}} \Omega_d + (\mathbf{G}_t \mathbf{G}_{sd}^T \mathbf{I}_{W_{sm}} - \mathbf{G}_s \mathbf{G}_{td}^T \mathbf{I}_{W_{tm}}) \omega_d \quad (\text{D.36})$$

$$\mathbf{D}_2 = \tilde{\omega} \mathbf{G}_g \mathbf{J}_{gd} \quad (\text{D.37})$$

$$\mathbf{D}_3 = [(\mathbf{G}_t \mathbf{G}_{sd}^T \mathbf{I}_{G_{sm}} - \mathbf{G}_s \mathbf{G}_{td}^T \mathbf{I}_{G_{tm}}) - (\mathbf{G}_t \mathbf{G}_{sd}^T \mathbf{J}_{tm} - \mathbf{G}_s \mathbf{G}_{td}^T \mathbf{J}_{sm})] \omega_d \quad (\text{D.38})$$

D.3 Proving Attitude Tracking Stability

Using the reference attitude quaternion, β_r , and reference attitude rate vector, ω_r , one can define a radially-unbounded lyapunov function, V ,

$$V = k(\beta - \beta_r)^T (\beta - \beta_r) + \frac{1}{2}(\omega - \omega_r)^T \mathbf{I}_{sc} (\omega - \omega_r) \quad (D.39)$$

Computing the time derivative, \dot{V} , yields

$$\dot{V} = -(\omega - \omega_r)^T \left[kq^T(\beta) \beta_r - \mathbf{I}_{sc}(\dot{\omega} - \dot{\omega}_r) - \frac{1}{2}\dot{\mathbf{I}}_{sc}(\omega - \omega_r) \right] \quad (D.40)$$

Now, define $\mathbf{K}(\omega - \omega_r) \equiv kq^T(\beta) \beta_r - \mathbf{I}_{sc}(\dot{\omega} - \dot{\omega}_r) - \frac{1}{2}\dot{\mathbf{I}}_{sc}(\omega - \omega_r)$, and assume that the given maneuver involves matching a reference attitude position and attitude rate, so that $\dot{\omega}_r = 0$ and also that the spacecraft inertia matrix, \mathbf{I}_{sc} changes very little over time. Since the VSCMG mass is much smaller than the rest of the spacecraft, $\dot{\mathbf{I}}_{sc} = 0$, reducing the attitude tracking stability constraint to $\mathbf{I}_{sc}\dot{\omega} = -\mathbf{K}(\omega - \omega_r) + kq^T(\beta) \beta_r$.

Then $\dot{V} < 0$ except when $(\omega - \omega_r)^T \mathbf{K}(\omega - \omega_r) = 0$, which implies that $(\omega - \omega_r) = 0$, hence $\omega \rightarrow \omega_r$. Furthermore, since $\omega - \omega_r = 0$, then $\dot{\omega} - \dot{\omega}_r = 0$. Now note $\dot{V} = 0$ implies that $\mathbf{K}(\omega - \omega_r) = 0 = kq^T(\beta) \beta_r - \mathbf{I}_{sc}(\dot{\omega} - \dot{\omega}_r) - \frac{1}{2}\dot{\mathbf{I}}_{sc}(\omega - \omega_r)$, which means $kq^T(\beta) \beta_r = 0$. The only way this can happen is if $q^T(\beta) \beta_r = 0$. Following this logic, one can see that

$$q^T(\beta) \beta_r = \begin{bmatrix} -\beta_1 & \beta_0 & \beta_3 & -\beta_2 \\ -\beta_2 & -\beta_3 & \beta_0 & \beta_1 \\ -\beta_3 & \beta_2 & -\beta_1 & \beta_0 \end{bmatrix} \begin{bmatrix} \beta_{0r} \\ \beta_{1r} \\ \beta_{2r} \\ \beta_{3r} \end{bmatrix} \quad (D.41)$$

$$q^T(\beta) \beta_r = \begin{bmatrix} -\beta_1\beta_{0r} + \beta_0\beta_{1r} + \beta_3\beta_{2r} - \beta_2\beta_{3r} \\ -\beta_2\beta_{0r} - \beta_3\beta_{1r} + \beta_0\beta_{2r} + \beta_1\beta_{3r} \\ -\beta_3\beta_{0r} + \beta_2\beta_{1r} - \beta_1\beta_{2r} + \beta_0\beta_{3r} \end{bmatrix} = 0 \quad (D.42)$$

$$q^T(\beta_r) \beta = \begin{bmatrix} -\beta_{1r}\beta_0 + \beta_{0r}\beta_1 + \beta_{3r}\beta_2 - \beta_{2r}\beta_3 \\ -\beta_{2r}\beta_0 - \beta_{3r}\beta_1 + \beta_{0r}\beta_2 + \beta_{1r}\beta_3 \\ -\beta_{3r}\beta_0 + \beta_{2r}\beta_1 - \beta_{1r}\beta_2 + \beta_{0r}\beta_3 \end{bmatrix} = 0 \quad (D.43)$$

Changing the order and multiplying by -1

$$q^T(\beta_r)\beta = - \begin{bmatrix} \beta_0\beta_{1r} - \beta_1\beta_{0r} - \beta_2\beta_{3r} + \beta_3\beta_{2r} \\ \beta_0\beta_{2r} + \beta_1\beta_{3r} - \beta_2\beta_{0r} - \beta_3\beta_{1r} \\ \beta_0\beta_{3r} - \beta_1\beta_{2r} + \beta_2\beta_{1r} - \beta_3\beta_{0r} \end{bmatrix} = 0 \quad (\text{D.44})$$

Rearranging

$$q^T(\beta_r)\beta = - \begin{bmatrix} -\beta_1\beta_{0r} + \beta_0\beta_{1r} + \beta_3\beta_{2r} - \beta_2\beta_{3r} \\ -\beta_2\beta_{0r} - \beta_3\beta_{1r} + \beta_0\beta_{2r} + \beta_1\beta_{3r} \\ -\beta_3\beta_{0r} + \beta_2\beta_{1r} - \beta_1\beta_{2r} + \beta_0\beta_{3r} \end{bmatrix} = 0 \quad (\text{D.45})$$

Next notice that $q^T(\beta_r)\beta = 0 = q^T(\beta)\beta_r$ from eqs. D.42 and D.43. On the other hand, $q^T(\beta_r)\beta = 0 = -q^T(\beta)\beta_r$ from eqs. D.44 and D.45. Both conditions only hold when $\beta = \beta_r$. Thus, $\dot{\mathbf{V}} = 0 \Rightarrow \omega = \omega_r, \beta = \beta_r$.

Rearranging eq. 4.16 yields $\overline{\mathbf{N}}_d - \mathbf{I}_{sc}\dot{\omega} - \tilde{\omega}\mathbf{I}_{sc}\omega = \mathbf{B}\ddot{\delta} + \mathbf{E}\dot{\Omega} + \mathbf{D}\dot{\delta} + \mathbf{F}\Omega$ and eq. 4.18 yields $\overline{\mathbf{N}}_r = \mathbf{K}(\omega - \omega_r) - kq^T(\beta)\beta_r - \tilde{\omega}\mathbf{I}_{sc}\omega$, combining to yield eq. 4.20 as $\overline{\mathbf{N}}_r + \overline{\mathbf{N}}_d = \mathbf{B}\ddot{\delta} + \mathbf{E}\dot{\Omega} + \mathbf{D}\dot{\delta} + \mathbf{F}\Omega$. Assuming there is no disturbance torque on the system, $\overline{\mathbf{N}}_d = 0$, then $\omega \rightarrow \omega_r$ and $\beta \rightarrow \beta_r$ asymptotically as long as the condition

$$\overline{\mathbf{N}}_r = \mathbf{K}(\omega - \omega_r) - kq^T(\beta)\beta_r - \tilde{\omega}\mathbf{I}_{sc}\omega \quad (\text{D.46})$$

holds. From this, one can find the required torque for stability, $\overline{\mathbf{N}}_r$ as

$$\overline{\mathbf{N}}_r = \mathbf{B}\ddot{\delta} + \mathbf{E}\dot{\Omega} + \mathbf{D}\dot{\delta} + \mathbf{F}\Omega \quad (\text{D.47})$$

Then, assuming that $\ddot{\delta} \rightarrow 0$, this equation can be further refined as

$$\mathbf{E}\dot{\Omega} + \mathbf{D}\dot{\delta} = \overline{\mathbf{N}}_r - \mathbf{F}\Omega = \mathbf{N}_c \quad (\text{D.48})$$

which is identical to eq. 4.21. Note that $\mathbf{Q}u = \mathbf{E}\dot{\Omega} + \mathbf{D}\dot{\delta}$ where u is any of the control laws for $\begin{bmatrix} \dot{\Omega} \\ \dot{\delta} \end{bmatrix}_c$ presented earlier. Therefore, provided this equation holds, $\omega \rightarrow \omega_r$ and $\beta \rightarrow \beta_r$ which demonstrates global asymptotically stable attitude tracking of the reference attitude position and rate.

D.4 Projected Power in Null Space of \mathbf{Q}

Define $u_n = \begin{bmatrix} \dot{\Omega} \\ \dot{\delta} \end{bmatrix}_{null}$ and the operator, P_n , which projects a vector, ν onto the nullspace of \mathbf{Q} . Then, one can use the step-by-step equation set below to derive the simultaneous

wheel and gimbal steering law, u . Notice that in this equation set, \mathbf{Q}^\dagger represents any suitable generalized inverse, including \mathbf{Q}^\star or \mathbf{Q}^\diamond .

$$\mathbf{Q}u = \mathbf{N}_c \quad (\text{D.49})$$

$$\mathbf{Q}u_n = 0 \quad (\text{D.50})$$

$$u_n = P_n \nu \quad (\text{D.51})$$

$$P_n = P_n P_n^T = I_n - \mathbf{Q}^\dagger \mathbf{Q} \quad (\text{D.52})$$

$$u = \mathbf{Q}^\dagger N_c + u_n \quad (\text{D.53})$$

$$\mathbf{S}u = \mathbf{S}(\mathbf{Q}^\dagger N_c + u_n) = P_c \quad (\text{D.54})$$

$$\mathbf{S}u_n = \mathbf{S}P_n \nu = P_c - \mathbf{S}\mathbf{Q}^\dagger N_c \quad (\text{D.55})$$

$$(\mathbf{S}P_n)\nu = P_c - \mathbf{S}\mathbf{Q}^\dagger N_c, \mathbf{S}P_n \neq [0 \dots 0_n]^T \quad (\text{D.56})$$

$$\nu = (\mathbf{S}P_n)^\dagger (P_c - \mathbf{S}\mathbf{Q}^\dagger N_c) \quad (\text{D.57})$$

$$\nu = P_n^T \mathbf{S}^T (\mathbf{S}P_n P_n^T \mathbf{S}^T)^{-1} (P_c - \mathbf{S}\mathbf{Q}^\dagger N_c) \quad (\text{D.58})$$

$$u_n = P_n P_n^T \mathbf{S}^T (\mathbf{S}P_n P_n^T \mathbf{S}^T)^{-1} (P_c - \mathbf{S}\mathbf{Q}^\dagger N_c) \quad (\text{D.59})$$

$$u_n = P_n \mathbf{S}^T (\mathbf{S}P_n \mathbf{S}^T)^{-1} (P_c - \mathbf{S}\mathbf{Q}^\dagger N_c) \quad (\text{D.60})$$

$$u = \mathbf{Q}^\dagger N_c + P_n \mathbf{S}^T (\mathbf{S}P_n \mathbf{S}^T)^{-1} (P_c - \mathbf{S}\mathbf{Q}^\dagger N_c) \quad (\text{D.61})$$

D.5 Proving Power Tracking

Having shown the control laws presented track the attitude as shown in subsection D.3, the next step is to show that the desired power is adequately tracked. So as long as $\mathbf{Q}u = N_c$, if one can show that $\mathbf{Q}u_n = 0$, thus $\mathbf{Q}u + \mathbf{Q}u_n = N_c$, he or she can show that $\mathbf{Q}u_n$ can be used for tracking power. So here, we check this result and examine $\mathbf{Q}u_{new}$.

$$\mathbf{Q}u_{new} = \mathbf{Q}\mathbf{Q}^\diamond N_c + \mathbf{Q}P_n \mathbf{S}^T (\mathbf{S}P_n \mathbf{S}^T)^{-1} (P_c - \mathbf{S}\mathbf{Q}^\diamond N_c) \quad (\text{D.62})$$

Noting that $\mathbf{Q}\mathbf{Q}^\diamond N_c \rightarrow N_c$ by definition, it must be shown that $\mathbf{Q}P_n \mathbf{S}^T (\mathbf{S}P_n \mathbf{S}^T)^{-1} (P_c - \mathbf{S}\mathbf{Q}^\diamond N_c) = 0$ as reflected in the following steps (and noting that by definition $\mathbf{Q}\mathbf{Q}^\dagger \rightarrow I_n$)

$$\mathbf{Q}u_n = \mathbf{Q}P_n \mathbf{S}^T (\mathbf{S}P_n \mathbf{S}^T)^{-1} (P_c - \mathbf{S}\mathbf{Q}^\diamond N_c) \quad (\text{D.63})$$

$$\mathbf{Q}u_n = \mathbf{Q} (I_n - \mathbf{Q}^\dagger \mathbf{Q}) \mathbf{S}^T (\mathbf{S}P_n \mathbf{S}^T)^{-1} (P_c - \mathbf{S}\mathbf{Q}^\diamond N_c) \quad (\text{D.64})$$

$$\mathbf{Q}u_n = (\mathbf{Q} - \mathbf{Q}\mathbf{Q}^\dagger \mathbf{Q}) \mathbf{S}^T (\mathbf{S}P_n \mathbf{S}^T)^{-1} (P_c - \mathbf{S}\mathbf{Q}^\diamond N_c) = 0 \quad (\text{D.65})$$

Thus, $\mathbf{Q}u_{new} = N_c + 0 = N_c$ and all encompassing control law, u_{new} , can be used to simultaneously track power and attitude.

Appendix E

Rotor Stress Analysis

The following appendix captures the orthotropic rotor stress equation derivation used to define the equation for maximum structural speed presented in the thesis. These equations have been adapted from the work found in [78, 149, 170, 171].

An orthotropic composite wheel rotor constructed primarily of unidirectional fibres can be modeled as several concentric rings of material as depicted in Fig E.1.

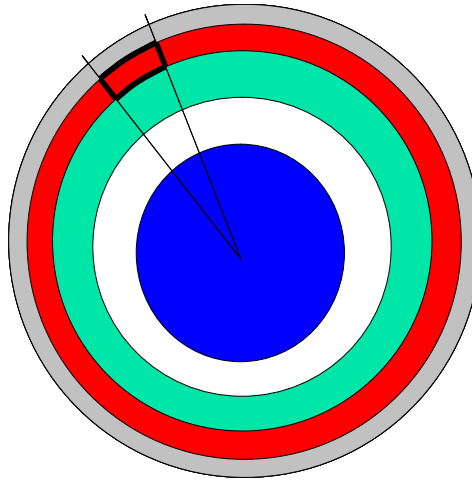


Figure E.1: Wheel Rotor Representation

The analysis begins with a differential mass as depicted in Fig. E.2 with constant axial thickness t . It is assumed for the initial portion of the analysis that the rotor is in static equilibrium.

Next, as stress is force per unit area, the forces on the mass are developed leading to the appropriate stress equations. Using the polar definitions above, the forces can be summed in

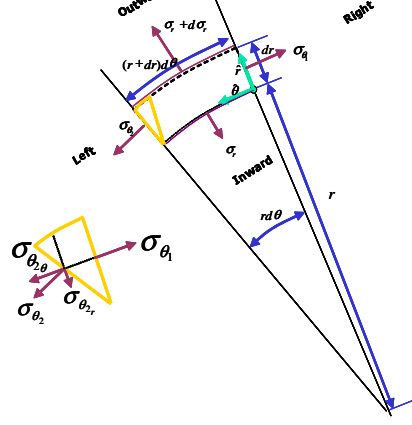


Figure E.2: Rotor Differential Mass Free Body Diagram

both the radial and tangential directions as

$$\sum F_r = \sum F_{outward} - \sum F_{inward} = 0 \quad (E.1)$$

$$\sum F_\theta = \sum_{left} - \sum_{right} = 0 \quad (E.2)$$

Radially, for a differential mass in tension (using Fig. E.2)

$$\sum F_r = \sum F_{outward} - \sum F_{inward} = 0 \quad (E.3)$$

$$\sum dF_r = \sum dF_{outward} - \sum dF_{inward} = 0 \quad (E.4)$$

$$\sum dF_{inward} = (\sigma_r r d\theta) t - dF_{\sigma_{\theta_2}} \quad (E.5)$$

$$\sum dF_{outward} = (\sigma_r + d\sigma_r) ((r + dr) d\theta) t \quad (E.6)$$

$$dF_{\sigma_{\theta_2}} = (\sigma_{\theta_2} dr d\theta) t \quad (E.7)$$

$$dF_{\sigma_{\theta_2}} = (\sigma_{\theta_2} dr d\theta) t \quad (E.8)$$

This yields

$$\sum dF_r = (\sigma_r + d\sigma_r) ((r + dr) d\theta) t - (\sigma_r r d\theta) t - (\sigma_{\theta_2} dr d\theta) t = 0 \quad (E.9)$$

Tangentially, the differential mass tension equations become

$$\sum dF_{\sigma_\theta} = dF_{\sigma_{\theta_1}} - dF_{\sigma_{\theta_2}} = 0 \quad (E.10)$$

$$\sum dF_{\sigma_\theta} = dF_{\sigma_{\theta_1}} - dF_{\sigma_{\theta_2\theta}} = 0 \quad (E.11)$$

$$\sum dF_{\sigma_\theta} = \sigma_{\theta_1} dr t - \sigma_{\theta_2\theta} dr t = 0 \quad (E.12)$$

Noting from Fig. E.2

$$\| \sigma_{\theta_2\theta} \| \approx \| \sigma_{\theta_2} \| \quad (E.13)$$

and that

$$\| \sigma_{\theta_2} \| = \| \sigma_{\theta_1} \| = \sigma_{\theta} \quad (\text{E.14})$$

Thus, trivially,

$$\sum dF_{\sigma_{\theta}} = \sigma_{\theta} drt - \sigma_{\theta} drt = 0 \quad (\text{E.15})$$

Examining radial force equilibrium following eqn. E.9

$$\sum dF_r = (\sigma_r + d\sigma_r) ((r + dr) d\theta) t - (\sigma_r r d\theta) t - (\sigma_{\theta} dr d\theta) t = 0 \quad (\text{E.16})$$

$$((\sigma_r + d\sigma_r) (r + dr) - \sigma_r r - \sigma_{\theta} dr) d\theta t = 0 \quad (\text{E.17})$$

$$(d\sigma_r r + d\sigma_r dr + \sigma_r dr + \sigma_r r - \sigma_r r - \sigma_{\theta} dr) d\theta t = 0 \quad (\text{E.18})$$

$$(d\sigma_r r + d\sigma_r dr + \sigma_r dr - \sigma_{\theta} dr) d\theta t = 0 \quad (\text{E.19})$$

$$\frac{1}{r dr} ((d\sigma_r r + d\sigma_r dr + \sigma_r dr - \sigma_{\theta} dr) d\theta t) = 0 \quad (\text{E.20})$$

$$\left(\frac{d\sigma_r}{dr} + \left(\frac{\sigma_r - \sigma_{\theta}}{r} \right) \right) d\theta t + \frac{d\sigma_r dr d\theta}{r dr} t = 0 \quad (\text{E.21})$$

Discarding higher order terms yields

$$t d\theta \left(\frac{d\sigma_r}{dr} + \left(\frac{\sigma_r - \sigma_{\theta}}{r} \right) \right) = 0 \quad (\text{E.22})$$

Now, further examining radial force equilibrium at constant angular velocity for one differential mass

$$\sum dF_r = (\sigma_r + d\sigma_r) ((r + dr) d\theta) t - (\sigma_r r d\theta) t - (\sigma_{\theta} dr d\theta) t = -dm a_c \quad (\text{E.23})$$

$$((\sigma_r + d\sigma_r) (r + dr) - \sigma_r r - \sigma_{\theta} dr) d\theta t = -\rho dV a_c = -\rho (tdA) a_c \quad (\text{E.24})$$

$$(d\sigma_r r + d\sigma_r dr + \sigma_r dr + \sigma_r r - \sigma_r r - \sigma_{\theta} dr) d\theta t = -\rho (tdA) \frac{v^2}{r} \quad (\text{E.25})$$

$$(d\sigma_r r + d\sigma_r dr + \sigma_r dr - \sigma_{\theta} dr) d\theta t = -\rho (tr dr d\theta) \frac{(r\Omega)^2}{r} \quad (\text{E.26})$$

$$\frac{1}{r dr} \left((d\sigma_r r + d\sigma_r dr + \sigma_r dr - \sigma_{\theta} dr) d\theta t = -\rho (tr dr d\theta) \frac{(r\Omega)^2}{r} \right) \quad (\text{E.27})$$

$$\left(\frac{d\sigma_r}{dr} + \left(\frac{\sigma_r - \sigma_{\theta}}{r} \right) \right) d\theta t + \frac{d\sigma_r dr d\theta}{r dr} t = -\rho t d\theta r \Omega^2 \quad (\text{E.28})$$

Discarding higher order terms yields

$$t d\theta \left(\frac{d\sigma_r}{dr} + \left(\frac{\sigma_r - \sigma_{\theta}}{r} \right) + \rho r \Omega^2 \right) = 0 \quad (\text{E.29})$$

Integrating for one dm ring and re-arranging

$$\int_0^{2\pi} t \left(\frac{d\sigma_r}{dr} + \left(\frac{\sigma_r - \sigma_\theta}{r} \right) + \rho r \Omega^2 \right) d\theta = 2\pi t \left(\frac{d\sigma_r}{dr} + \left(\frac{\sigma_r - \sigma_\theta}{r} \right) + \rho r \Omega^2 \right) = 0 \quad (\text{E.30})$$

$$\left(\frac{d\sigma_r}{dr} + \left(\frac{\sigma_r - \sigma_\theta}{r} \right) + \rho r \Omega^2 \right) = 0 \quad (\text{E.31})$$

Next, the focus turns to strain analysis based on the differential mass illustration in Fig. E.3. Since strain is defined by the amount of elongation ΔL induced in a material from stress, one should note that the differential mass is assumed to be free to elongate in the radial direction but due to its circular geometry, not free to have a net elongation tangentially. The strain is thus

$$\epsilon = \frac{\Delta L}{L} \quad (\text{E.32})$$

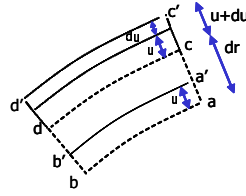


Figure E.3: Differential Mass Strain Diagram

Or, in terms of radial strain (based on Figure E.3)

$$\epsilon_r = \frac{\Delta L_r}{L_r} = \frac{\Delta dr}{dr} = \frac{(u + du) - u}{dr} = \frac{du}{dr} \quad (\text{E.33})$$

Even though there is no tangential displacement, arc $a'b'$ is greater than ab , thus

$$L_\theta = L_{ab} = r d\theta \quad (\text{E.34})$$

$$\Delta L_\theta = L_{a'b'} - L_{ab} = (r + u) d\theta - r d\theta \quad (\text{E.35})$$

$$\epsilon_\theta = \frac{\Delta L_\theta}{L_\theta} = \frac{(r + u) d\theta - r d\theta}{r d\theta} \quad (\text{E.36})$$

$$= \frac{(r d\theta + u d\theta - r d\theta)}{r d\theta} = \frac{u d\theta}{r d\theta} = \frac{u}{r} \quad (\text{E.37})$$

Thus

$$\epsilon_r = \frac{du}{dr} \quad (\text{E.38})$$

$$\epsilon_\theta = \frac{u}{r} \quad (\text{E.39})$$

Hooke's Law for principal stress of an elastic material in a 2-dimensional system (as explained by Case and Chiver [] on p. 79)

$$E\epsilon_r = \sigma_r - \nu\sigma_\theta \quad (\text{E.40})$$

$$E\epsilon_\theta = \sigma_\theta - \nu\sigma_r \quad (\text{E.41})$$

Solving this simultaneous system

$$E\epsilon_r = \sigma_r - \nu\sigma_\theta \quad (\text{E.42})$$

$$\nu E\epsilon_\theta = -\nu^2\sigma_r + \nu\sigma_\theta \quad (\text{E.43})$$

$$(E\epsilon_r + \nu E\epsilon_\theta) = (1 - \nu^2)\sigma_r \quad (\text{E.44})$$

$$\sigma_r = \frac{E}{(1 - \nu^2)}(\epsilon_r + \nu\epsilon_\theta) \quad (\text{E.45})$$

$$E\epsilon_\theta = -\nu\sigma_r + \sigma_\theta \quad (\text{E.46})$$

$$\sigma_\theta = E\epsilon_\theta + \nu\sigma_r = E\epsilon_\theta + \frac{E\nu}{(1 - \nu^2)}(\epsilon_r + \nu\epsilon_\theta) \quad (\text{E.47})$$

$$\sigma_\theta = \frac{E}{(1 - \nu^2)}((1 - \nu^2)\epsilon_\theta + \nu\epsilon_r + \nu^2\epsilon_\theta) \quad (\text{E.48})$$

Yields

$$\sigma_r = \frac{E}{(1 - \nu^2)}(\epsilon_r + \nu\epsilon_\theta) \quad (\text{E.49})$$

$$\sigma_\theta = \frac{E}{(1 - \nu^2)}(\epsilon_\theta + \nu\epsilon_r) \quad (\text{E.50})$$

Or, in terms of u , du

$$\sigma_r = \frac{E}{(1 - \nu^2)}\left(\frac{du}{dr} + \nu\frac{u}{r}\right) \quad (\text{E.51})$$

$$\sigma_\theta = \frac{E}{(1 - \nu^2)}\left(\frac{u}{r} + \nu\frac{du}{dr}\right) \quad (\text{E.52})$$

Substituting the stress terms into the radial force equilibrium equation for one differential mass, dm , yields

$$0 = \left(\frac{d\sigma_r}{dr} + \left(\frac{\sigma_r - \sigma_\theta}{r}\right) + \rho r\Omega^2\right) \quad (\text{E.53})$$

$$0 = \left(\frac{d\left(\frac{E}{(1 - \nu^2)}\left(\frac{du}{dr} + \nu\frac{u}{r}\right)\right)}{dr}\right) + \left(\frac{\left(\frac{E}{(1 - \nu^2)}\left(\frac{du}{dr} + \nu\frac{u}{r}\right)\right) - \left(\frac{E}{(1 - \nu^2)}(\epsilon_\theta + \nu\epsilon_r)\right)}{r}\right) + \rho r\Omega^2 \quad (\text{E.54})$$

$$0 = \frac{E}{(1 - \nu^2)}\left(\frac{d^2u}{dr^2} + \frac{du}{rdr} - \frac{u}{r^2} + \frac{(1 - \nu^2)}{E}\rho r\Omega^2\right) \quad (\text{E.55})$$

The results above match the thick-walled cylinder derivation from the Univ of Washington [172], but do not have necessary granularity to match Danfelt's results from [149]. Continuing on ... Hooke's Law for principal stress of an elastic material in a 2-dimensional rotor in polar coordinates (as explained in [149]) gives

$$E\epsilon_r = \sigma_r - \nu\sigma_\theta \rightarrow \epsilon_r = \frac{\sigma_r}{E_r} - \nu_{\theta r} \frac{\sigma_\theta}{E_\theta} \quad (\text{E.56})$$

$$E\epsilon_\theta = \sigma_\theta - \nu\sigma_r \rightarrow \epsilon_\theta = \frac{\sigma_\theta}{E_\theta} - \nu_{r\theta} \frac{\sigma_r}{E_r} \quad (\text{E.57})$$

Solving the simultaneous system

$$\epsilon_r = \frac{\sigma_r}{E_r} - \nu_{\theta r} \frac{\sigma_\theta}{E_\theta} \quad (\text{E.58})$$

$$\epsilon_\theta = -\nu_{r\theta} \frac{\sigma_r}{E_r} + \frac{\sigma_\theta}{E_\theta} \quad (\text{E.59})$$

Note that $E_r\nu_{\theta r} = E_\theta\nu_{r\theta}$, so this becomes

$$E_r\epsilon_r = \sigma_r - \nu_{\theta r} \frac{E_r}{E_\theta} \sigma_\theta = \sigma_r - \nu_{r\theta} \sigma_\theta \quad (\text{E.60})$$

$$E_\theta\epsilon_\theta = -\nu_{r\theta} \frac{E_\theta}{E_r} \sigma_r + \sigma_\theta = -\nu_{\theta r} \sigma_r + \sigma_\theta \quad (\text{E.61})$$

$$\nu_{r\theta} E_\theta \epsilon_\theta = -\nu_{r\theta} \nu_{\theta r} \sigma_r + \nu_{r\theta} \sigma_\theta \quad (\text{E.62})$$

$$\sigma_\theta = \frac{E_\theta \epsilon_\theta}{(1 - \nu_{\theta r} \nu_{r\theta})} + \frac{E_\theta \nu_{r\theta} \epsilon_r}{(1 - \nu_{\theta r} \nu_{r\theta})} = \frac{E_\theta}{(1 - \nu_{\theta r} \nu_{r\theta})} (\epsilon_\theta + \nu_{r\theta} \epsilon_r) \quad (\text{E.63})$$

Yields

$$\sigma_r = \frac{E_r}{(1 - \nu_{\theta r} \nu_{r\theta})} (\epsilon_r + \nu_{\theta r} \epsilon_\theta) \quad (\text{E.64})$$

$$\sigma_\theta = \frac{E_\theta}{(1 - \nu_{\theta r} \nu_{r\theta})} (\epsilon_\theta + \nu_{r\theta} \epsilon_r) \quad (\text{E.65})$$

Or in terms of u , du

$$\sigma_r = \frac{E_r}{(1 - \nu_{\theta r} \nu_{r\theta})} \left(\frac{du}{dr} + \nu_{\theta r} \frac{u}{r} \right) \quad (\text{E.66})$$

$$\sigma_\theta = \frac{E_\theta}{(1 - \nu_{\theta r} \nu_{r\theta})} \left(\frac{u}{r} + \nu_{r\theta} \frac{du}{dr} \right) \quad (\text{E.67})$$

Substituting the stress terms into the radial force equilibrium equation for one differential

mass, dm , yields

$$0 = \left(\frac{d\sigma_r}{dr} + \left(\frac{\sigma_r - \sigma_\theta}{r} \right) + \rho r \Omega^2 \right) \quad (\text{E.68})$$

$$0 = \left(\frac{d \left(\frac{E}{(1 - \nu_{r\theta}\nu_{\theta r})} \left(\frac{du}{dr} + \nu_{\theta r} \frac{u}{r} \right) \right)}{dr} \right) + \left(\frac{\left(\frac{E}{(1 - \nu_{r\theta}\nu_{\theta r})} \left(\frac{du}{dr} + \nu_{\theta r} \frac{u}{r} \right) \right) - \left(\frac{E}{(1 - \nu_{r\theta}\nu_{\theta r})} \left(\frac{u}{r} + \nu_{r\theta} \frac{du}{dr} \right) \right)}{r} \right) + \rho r \Omega^2 \quad (\text{E.69})$$

$$0 = \frac{d^2 u}{dr^2} + \frac{du}{r dr} - \frac{E_\theta}{E_r} \frac{u}{r^2} + \frac{(1 - \nu_{r\theta}\nu_{\theta r}) \rho \Omega^2}{E_r} r \quad (\text{E.70})$$

Let $\lambda = \left(\frac{E_\theta}{E_r} \right)^{0.5}$ and note that $\lambda^2 = \frac{E_\theta}{E_r}$. In addition, let $\gamma = \left(\frac{(1 - \nu_{r\theta}\nu_{\theta r})}{E_r} \rho \Omega^2 \right)$, then the stress differential equation becomes

$$0 = \frac{d^2 u}{dr^2} + \frac{1}{r} \frac{du}{dr} - \lambda^2 \frac{u}{r^2} + \gamma r \quad (\text{E.71})$$

Recognizing that the left hand side of eq. E.71 is an Euler-Cauchy equation, if set equal to zero, of the form

$$x^2 y'' + ax y' + by = 0 \quad (\text{E.72})$$

whose solution (i.e. the homogeneous solution) is $y_h = c_1 x^{m_1} + c_2 x^{m_2}$ and $m = m_1, m_2$ are the solutions to the equation $m^2 + (a - 1)m + b = 0$, then one can use the equation

$$x^2 y'' + ax y' + by = -\gamma x^3 \quad (\text{E.73})$$

to find the particular solution of this equation, $y_p = \alpha_1 x^3 + \alpha_2 x^2 + \alpha_3 x + \alpha_4$, with $\alpha_2 = \alpha_3 = \alpha_4 = 0$ and

$$\alpha_1 = \frac{-\gamma}{9 - b} \quad (\text{E.74})$$

where $a = 1$, $b = -\lambda^2$, $x = r$, $u = y$, $m_1 = \lambda$, and $m_2 = -\lambda$. Thus

$$u_h = c_1 r^\lambda + c_2 r^{-\lambda} \quad (\text{E.75})$$

$$u_p = \frac{-\gamma}{9 - \lambda^2} r^3 = -\frac{(1 - \nu_{r\theta}\nu_{\theta r})}{9E_r - E_\theta} \rho \Omega^2 r^3 \quad (\text{E.76})$$

Combining u_h and u_p yields

$$u = c_1 r^\lambda + c_2 r^{-\lambda} - \frac{(1 - \nu_{r\theta}\nu_{\theta r})}{9E_r - E_\theta} \rho \Omega^2 r^3 \quad (\text{E.77})$$

$$du = \lambda c_1 r^{\lambda-1} - \lambda c_2 r^{-\lambda-1} - \frac{3(1 - \nu_{r\theta}\nu_{\theta r})}{9E_r - E_\theta} \rho \Omega^2 r^2 \quad (\text{E.78})$$

And one can substitute the values u and du to get the final stress equations for σ_r and σ_θ

$$\sigma_r = c_1 \frac{E_r (\lambda + \nu_{\theta r})}{(1 - \nu_{\theta r} \nu_{r\theta})} r^{\lambda-1} + c_2 \frac{E_r (-\lambda + \nu_{\theta r})}{(1 - \nu_{\theta r} \nu_{r\theta})} r^{-\lambda-1} - \frac{(3 + \nu_{\theta r}) E_r}{9E_r - E_\theta} \rho \Omega^2 r^2 \quad (\text{E.79})$$

$$\sigma_\theta = c_1 \frac{E_\theta (1 + \lambda \nu_{r\theta})}{(1 - \nu_{\theta r} \nu_{r\theta})} r^{\lambda-1} + c_2 \frac{E_\theta (1 - \lambda \nu_{r\theta})}{(1 - \nu_{\theta r} \nu_{r\theta})} r^{-\lambda-1} - \frac{(1 + 3\nu_{r\theta}) E_\theta}{9E_r - E_\theta} \rho \Omega^2 r^2 \quad (\text{E.80})$$

One can now apply appropriate boundary conditions to find relationships for the constants c_1 and c_2 an example of which is found in [78]. However, with these values, one can calculate the radial and tangential stresses at different radii in the rotor and compare the results to the limits for tensile and compressive stress for a given material. These materials are compared in Chapter 5. Continuing on to the boundary conditions, the radial stress at the outer radius is 0, so $\sigma_r = 0$ at $r = R_o$ and can thus be written

$$0 = \alpha_1 R_o^{\lambda-1} c_1 + \beta_1 R_o^{-\lambda-1} c_2 - D_1 R_o^2 \quad (\text{E.81})$$

At the inner radius, the radial stress is equal to the internal radial pressure, P_i , so $\sigma_r = -P_i$ and this pressure can be found as

$$-P_i = \frac{F_c}{A} = \frac{m_{rot} a_c}{A} = \frac{\rho V R_i \Omega^2}{A} = \frac{\rho l_r A R_i \Omega^2}{A} = \rho l_r R_i \Omega^2 \quad (\text{E.82})$$

Thus, this radial stress condition is

$$-P_i = \alpha_1 R_i^{\lambda-1} c_1 + \beta_1 R_i^{-\lambda-1} c_2 - D_1 R_i^2 \quad (\text{E.83})$$

So, in summary, the flywheel rotor radial and tangential orthotropic stress equations are

$$\sigma_r = c_1 \frac{E_r (\lambda + \nu_{\theta r})}{(1 - \nu_{\theta r} \nu_{r\theta})} r^{\lambda-1} + c_2 \frac{E_r (-\lambda + \nu_{\theta r})}{(1 - \nu_{\theta r} \nu_{r\theta})} r^{-\lambda-1} - \frac{(3 + \nu_{\theta r}) E_r}{9E_r - E_\theta} \rho \Omega^2 r^2 \quad (\text{E.84})$$

$$\sigma_\theta = c_1 \frac{E_\theta (1 + \lambda \nu_{r\theta})}{(1 - \nu_{\theta r} \nu_{r\theta})} r^{\lambda-1} + c_2 \frac{E_\theta (1 - \lambda \nu_{r\theta})}{(1 - \nu_{\theta r} \nu_{r\theta})} r^{-\lambda-1} - \frac{(1 + 3\nu_{r\theta}) E_\theta}{9E_r - E_\theta} \rho \Omega^2 r^2 \quad (\text{E.85})$$

and the boundary conditions yield the following equations for the constants c_1 and c_2

$$c_1 = \frac{(3 + \nu_{\theta r}) (1 - \nu_{\theta r} \nu_{r\theta})}{(9E_r - E_\theta) (\lambda + \nu_{\theta r})} \left(R_o^{3-\lambda} - R_o^{-2\lambda} \left(\frac{R_i R_o^{\lambda-1} - \frac{R_i R_o^{\lambda-1} l_r}{E_r \Omega (3 + \nu_{\theta r})} - R_i^{\lambda-1} R_o \right) \right) \quad (\text{E.86})$$

$$c_2 = \frac{(3 + \nu_{\theta r}) (1 - \nu_{\theta r} \nu_{r\theta}) \rho \Omega^2}{(-\lambda + \nu_{\theta r}) (9E_r - E_\theta)} \left(\frac{R_i R_o^{\lambda-1} - \frac{R_i R_o^{\lambda-1} l_r}{E_r \Omega (3 + \nu_{\theta r})} - R_i^{\lambda-1} R_o}{R_o^{\lambda-1} R_i^{-\lambda-1} - R_o^{-\lambda-1} R_i^{\lambda-1}} \right) \quad (\text{E.87})$$

where $\lambda = \left(\frac{E_\theta}{E_r} \right)^{0.5}$, the values E_r , E_θ , $\nu_{r\theta}$, $\nu_{\theta r}$, and ρ are rotor material properties, l_r , R_o , and R_i are features of the rotor design, and Ω is the rotor speed. Comparing the stress equations to the material ultimate compressive and ultimate tensile stress limits, one can analyze/plot the rotor stress performance versus wheel speed. Such analysis is plotted in Chapter 5.